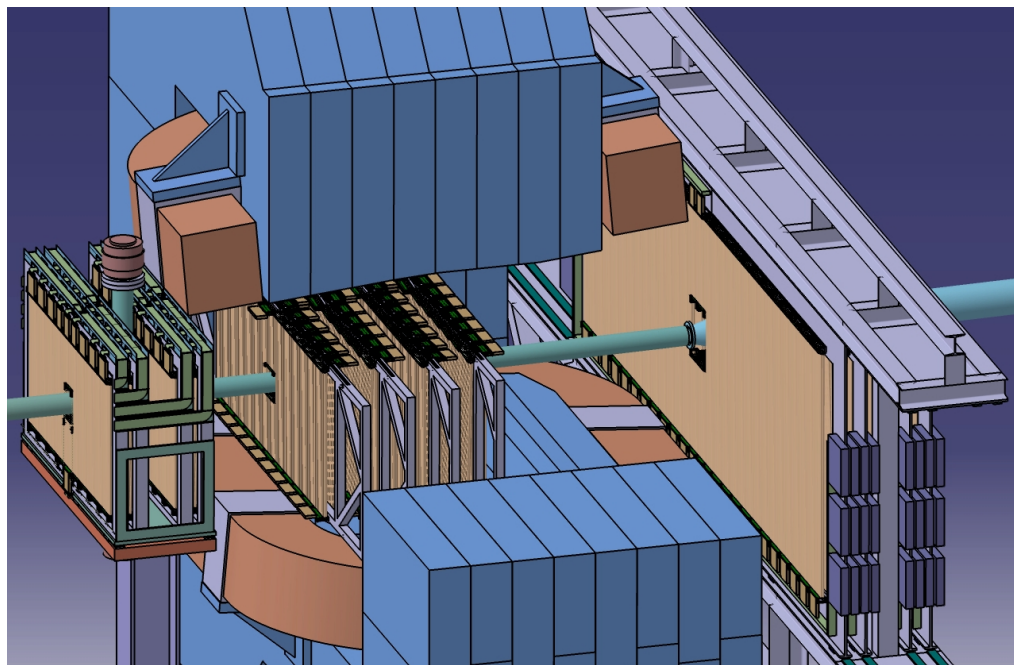


Technical Design Report

for the $\bar{\text{P}}\text{ANDA}$ Forward Tracker

$\bar{\text{P}}\text{ANDA}$ Collaboration

October 17, 2018



The **PANDA** Collaboration

Università Politecnica delle Marche-Ancona, **Ancona**, Italy

F. Davì

Universität Basel, **Basel**, Switzerland

W. Erni, B. Krusche, M. Steinacher, N. Walford

Institute of High Energy Physics, Chinese Academy of Sciences, **Beijing**, China

B. Liu, H. Liu, Z. Liu, X. Shen, C. Wang, J. Zhao

Ruhr-Universität Bochum, Institut für Experimentalphysik I, **Bochum**, Germany

M. Albrecht, T. Erlen, F. Feldbauer, M. Fink, V. Freudenreich, M. Fritsch, F.H. Heinsius, T. Held,
T. Holtmann, I. Keshk, H. Koch, B. Kopf, M. Kuhlmann, M. Kümmel, S. Leiber, P. Musiol,
A. Mustafa, M. Pelizäus, A. Pitka, G. Reicherz, M. Richter, C. Schnier, T. Schröder, S. Sersin, L. Sohl,
C. Sowa, M. Steinke, T. Triffterer, U. Wiedner

Rheinische Friedrich-Wilhelms-Universität Bonn, **Bonn**, Germany

R. Beck, C. Hammann, J. Hartmann, B. Ketzer, M. Kube, M. Rossbach, C. Schmidt, R. Schmitz,
U. Thoma, M. Urban

Università di Brescia, **Brescia**, Italy

A. Bianconi

Institutul National de C&D pentru Fizica si Inginerie Nucleara "Horia Hulubei", **Bukarest-Magurele**,
Romania

M. Bragadireanu, D. Pantea

University of Technology, Institute of Applied Informatics, **Cracow**, Poland

W. Czyżycski, M. Domagała, G. Filo, J. Jaworowski, M. Krawczyk, E. Lisowski, F. Lisowski,
M. Michałek, J. Płażek

IFJ, Institute of Nuclear Physics PAN, **Cracow**, Poland

K. Korcyl, A. Kozela, P. Kulessa, P. Lebiedowicz, K. Pysz, W. Schäfer, A. Szczurek

AGH, University of Science and Technology, **Cracow**, Poland

T. Fiutowski, M. Idzik, B. Mindur, K. Swientek

Instytut Fizyki, Uniwersytet Jagiellonski, **Cracow**, Poland

J. Biernat, S. Jowzaee, G. Korcyl, R. Lalik, A. Malige, P. Moskal, K. Nowakowski, W. Przygoda,
N. Rathod, Z. Rudy, P. Salabura, J. Smyrski, P. Strzempek, A. Wrońska

FAIR, Facility for Antiproton and Ion Research in Europe, **Darmstadt**, Germany

I. Augustin, R. Böhm, I. Lehmann, D. Nicmorus Marinescu, L. Schmitt, V. Varentsov

GSI Helmholtzzentrum fr Schwerionenforschung GmbH, **Darmstadt**, Germany

M. Al-Turany, A. Belias, H. Deppe, N. Divani Veis, R. Dzhygadlo, H. Flemming, A. Gerhardt,
K. Götzen, R. Karabowicz, U. Kurilla, D. Lehmann, S. Löchner, J. Lühning, U. Lynen, S. Nakhoul,
H. Orth, K. Peters, T. Saito, G. Schepers, C.J. Schmidt, C. Schwarz, J. Schwiening, A. Täschner,
M. Traxler, B. Voss, P. Wieczorek, A. Wilms,

Joint Institute for Nuclear Research, **Dubna**, Russia

V. Abazov, G. Alexeev, V. A. Arefiev, V. Astakhov, M. Yu. Barabanov, B. V. Batyunya,
V. Kh. Dodokhov, A. Efremov, A. Fechtchenko, A. Galoyan, G. Golovanov, E. K. Koshurnikov,
Y. Yu. Lobanov, V. I. Lobanov, V. Malyshev, A. G. Olshevskiy, A. A. Piskun, A. Samartsev,
M. G. Sapozhnikov, N. B. Skachkov, A. N. Skachkova, E. A. Strokovsky, V. Tokmenin, V. Uzhinsky,
A. Verkheev, A. Vodopianov, N. I. Zhuravlev, A. Zinchenko

University of Edinburgh, **Edinburgh**, United Kingdom

D. Branford, D. Glazier, D. Watts

Friedrich Alexander Universität Erlangen-Nürnberg, **Erlangen**, Germany
 M. Böhm, W. Eyrich, A. Lehmann, D. Miehling, M. Pfaffinger, S. Stelter, F. Uhlig

Northwestern University, **Evanston**, U.S.A.
 S. Dobbs, K. Seth, A. Tomaradze, T. Xiao

Università di Ferrara and INFN Sezione di Ferrara, **Ferrara**, Italy
 D. Bettoni, E. Fioravanti, I. Garzia, M. Savrie

Goethe Universität, Institut für Kernphysik, **Frankfurt**, Germany
 A. Ali, A. Hamdi, M. Krebs, F. Nerling

Frankfurt Institute for Advanced Studies, **Frankfurt**, Germany
 V. Akishina, S. Gorbunov, I. Kisel, G. Kozlov, M. Pugach, M. Zyzak

INFN Laboratori Nazionali di Frascati, **Frascati**, Italy
 N. Bianchi, P. Gianotti, C. Guaraldo, V. Lucherini

Dept of Physics, University of Genova and INFN-Genova, **Genova**, Italy
 G. Bracco

Justus Liebig-Universität Gießen II. Physikalisches Institut, **Gießen**, Germany
 S. Bodenschatz, K.T. Brinkmann, V. Di Pietro, S. Diehl, V. Dormenev, M. Düren, E. Etzelmüller,
 K. Föhl, M. Galuska, T. Gessler, E. Gutz, C. Hahn, A. Hayrapetyan, M. Kesselkau, W. Kühn,
 T. Kuske, J. S. Lange, Y. Liang, V. Metag, M. Moritz, M. Nanova, R. Novotny, T. Quagli, A. Riccardi,
 J. Rieke, M. Schmidt, R. Schnell, H. Stenzel, M. Strickert, U. Thöring, T. Wasem, B. Wohlfahrt,
 H.G. Zaunick

IRFU, CEA, Université Paris-Saclay, **Gif-sur-Yvette Cedex**, France
 E. Tomasi-Gustafsson

University of Glasgow, **Glasgow**, United Kingdom
 D. Ireland, G. Rosner, B. Seitz

Birla Institute of Technology and Science, Pilani , K K Birla Goa Campus, **Goa**, India
 P.N. Deepak, A. Kulkarni

KVI-Center for Advanced Radiation Technology (CART), University of Groningen, **Groningen**,
 Netherlands
 A. Apostolou, M. Babai, M. Kavatsyuk, H. Loehner, J. Messchendorp, P. Schakel, M. Tiemens,
 J. C. van der Weele, S. Vejdani

Gauhati University, Physics Department, **Guwahati**, India
 K. Dutta, K. Kalita

Fachhochschule Südwestfalen, **Iserlohn**, Germany
 H. Sohlbach

Forschungszentrum Jülich, Institut für Kernphysik, **Jülich**, Germany
 M. Bai, L. Bianchi, M. Büscher, A. Derichs, R. Dosdall, A. Erven, V. Fracassi, A. Gillitzer,
 F. Goldenbaum, D. Grunwald, L. Jokhovets, G. Kemmerling, H. Kleines, A. Lai, A. Lehrach,
 M. Mikirtychyants, S. Orfanitski, D. Prasuhn, E. Prencipe, J. Pütz, J. Ritman, E. Rosenthal,
 S. Schadmand, T. Sefzick, V. Serdyuk, G. Sterzenbach, T. Stockmanns, P. Wintz, P. Wüstner, H. Xu,
 Y. Zhou

Chinese Academy of Science, Institute of Modern Physics, **Lanzhou**, China
 Z. Li, X. Ma, H. Xu

INFN Laboratori Nazionali di Legnaro, **Legnaro**, Italy
 V. Rigato

Lunds Universitet, Department of Physics, **Lund**, Sweden
 L. Isaksson

Johannes Gutenberg-Universität, Institut für Kernphysik, **Mainz**, Germany
 P. Achenbach, A. Aycock, O. Corell, A. Denig, M. Distler, M. Hoek, W. Lauth, Z. Liu, H. Merkel,
 U. Müller, J. Pochodzalla, S. Sanchez, S. Schlimme, C. Sfienti, M. Thiel, M. Zambrana

Helmholtz-Institut Mainz, **Mainz**, Germany

H. Ahmadi, S. Ahmed , S. Bleser, L. Capozza, M. Cardinali, A. Dbeissi, A. Ehret, B. Fröhlich, P. Grasemann, S. Haasler, D. Izard, J. Jorge, D. Khanef, R. Klasen, R. Kliemt, J. Kübler, H. Leithoff, D. Lin, F. Maas, S. Maldaner, M. Michel, M. C. Mora Espí, C. Morales Morales, C. Motzko, O. Noll, S. Pfleiderer, D. Rodriguez Piñeiro, M. Steinen, E. Walaa, S. Wolff, I. Zimmermann

Research Institute for Nuclear Problems, Belarus State University, **Minsk**, Belarus
A. Fedorov, M. Korjik, O. Mishevitch

Institute for Theoretical and Experimental Physics, **Moscow**, Russia

P. Balanutsa, V. Chernetsky, A. Demekhin, A. Dolgolenko, P. Fedorets, A. Gerasimov, V. Goryachev, D. Y. Kirin, V. A. Matveev, A. V. Stavinskiy

Moscow Power Engineering Institute, **Moscow**, Russia
A. Balashoff, A. Boukharov, O. Malyshev, I. Marishev

Nuclear Physics Division, Bhabha Atomic Research Centre, **Mumbai**, India

V. Chandratre, V. Datar, V. Jha, H. Kumawat, A.K. Mohanty, A. Parmar, A. K. Rai, B. Roy, G. Sonika

Westfälische Wilhelms-Universität Münster, **Münster**, Germany

C. Fritzsch, S. Grieser, A.K. Hergemöller, B. Hetz, N. Hüskens, A. Khoukaz, J. P. Wessels

Suranaree University of Technology, **Nakhon Ratchasima**, Thailand

C. Herold, K. Khosonthongkee, C. Kobdaj, A. Limphirat, P. Srisawad, Y. Yan

Novosibirsk State University, **Novosibirsk**, Russia
A. E. Blinov, S. Kononov, E. A. Kravchenko

Budker Institute of Nuclear Physics, **Novosibirsk**, Russia

E. Antokhin, A.Yu. Barnyakov, M. Barnyakov, K. Beloborodov, V.E. Blinov, V.S. Bobrovnikov, I.A. Kuyanov, A.P. Onuchin, S. Pivovarov, E. Pyata, S. Serednyakov, Y. Tikhonov

Institut de Physique Nucléaire, CNRS-IN2P3, Univ. Paris-Sud, Université Paris-Saclay, 91406, **Orsay cedex**, France

R. Kunne, D. Marchand, B. Ramstein, J. van de Wiele, Y. Wang

Dipartimento di Fisica, Università di Pavia, INFN Sezione di Pavia, **Pavia**, Italy
G. Boca

Charles University, Faculty of Mathematics and Physics, **Prague**, Czech Republic

V. Burian, M. Finger, M. Finger, A. Nikolovova, M. Pesek, M. Peskova, M. Pfeffer, I. Prochazka, M. Slunecka

Czech Technical University, Faculty of Nuclear Sciences and Physical Engineering, **Prague**, Czech Republic

P. Gallus, V. Jary, J. Novy, M. Tomasek, M. Virius, V. Vrba

Institute for High Energy Physics, **Protvino**, Russia

V. Abramov, N. Belikov, S. Bukreeva, A. Davidenko, A. Derevschikov, Y. Goncharenko, V. Grishin, V. Kachanov, V. Kormilitsin, A. Levin, Y. Melnik, N. Minaev, V. Mochalov, D. Morozov, L. Nogach, S. Poslavskiy, A. Ryazantsev, S. Ryzhikov, P. Semenov, I. Shein, A. Uzunian, A. Vasiliev, A. Yakutin

Siksha-Bhavana, Visva-Bharati, WB, **Santiniketan**, India
U. Roy

University of Sidney, School of Physics, **Sidney**, Australia
B. Yabsley

National Research Centre "Kurchatov Institute" B. P. Konstantinov Petersburg Nuclear Physics Institute, Gatchina, **St. Petersburg**, Russia

S. Belostotski, G. Gavrilov, A. Izotov, S. Manaenkov, O. Miklukho, D. Veretennikov, A. Zhdanov

Kungliga Tekniska Högskolan, **Stockholm**, Sweden
T. Bäck, B. Cederwall

Stockholms Universitet, **Stockholm**, Sweden
K. Makonyi, M. Preston, P.E. Tegner, D. Wölbing

Veer Narmad South Gujarat University, Department of Physics, **Surat**, India
S. Godre

Università di Torino and INFN Sezione di Torino, **Torino**, Italy
M. P. Bussa, S. Marcello, S. Spataro

Politecnico di Torino and INFN Sezione di Torino, **Torino**, Italy
F. Iazzi, R. Introzzi, A. Lavagno

INFN Sezione di Torino, **Torino**, Italy
D. Calvo, P. De Remigis, A. Filippi, G. Mazza, A. Rivetti, R. Wheaton

Università di Trieste and INFN Sezione di Trieste, **Trieste**, Italy
A. Martin

Uppsala Universitet, Institutionen för fysik och astronomi, **Uppsala**, Sweden
H. Calen, W. Ikegami Andersson, T. Johansson, A. Kupsc, P. Marciniewski, M. Papenbrock,
J. Pettersson, J. Regina, K. Schönning, M. Wolke

Instituto de Física Corpuscular, Universidad de Valencia-CSIC, **Valencia**, Spain
J. Diaz

Sardar Patel University, Physics Department, **Vallabh Vidynagar**, India
V. Pothodi Chackara

National Centre for Nuclear Research, **Warsaw**, Poland
A. Chlopik, G. Kesik, D. Melnychuk, B. Slowinski, A. Trzcinski, M. Wojciechowski, S. Wronka,
B. Zwieglinski

Österreichische Akademie der Wissenschaften, Stefan Meyer Institut für Subatomare Physik, **Wien**,
Austria
P. Bühler, J. Marton, D. Steinschaden, K. Suzuki, E. Widmann, S. Zimmermann, J. Zmeskal

Editors:	Elisa Fioravanti Grzegorz Korcyl Krzysztof Korcyl Piotr Salabura Jerzy Smyrski Peter Wintz	Email: fioravanti@fe.infn.it Email: grzegorz.korcyl@uj.edu.pl Email: Krzysztof.Korcyl@ifj.edu.pl Email: piotr.salabura@uj.edu.pl Email: jerzy.smyrski@uj.edu.pl Email: p.wintz@fz-juelich.de
Technical Coordinator:	Lars Schmitt	Email: l.schmitt@gsi.de
Deputy:	Anastasios Belias	Email: A.Belias@gsi.de

Spokesperson:	Klaus Peters	Email: k.peters@gsi.de
Deputy:	Tord Johansson	Email: tord.johansson@physics.uu.se

Preface

This document presents the technical layout and the expected performance of the Forward Tracker (FT), a tracking detector for the $\bar{\text{P}}\text{ANDA}$ Forward Spectrometer (FS). The FT consists of a set of planar tracking stations measuring deflection of particle trajectories in the magnetic field of the FS dipole magnet, providing the information about the particle momenta. The design of the stations is based on self-supporting straw tube detectors which will be also used in the $\bar{\text{P}}\text{ANDA}$ central Straw Tube Tracker (STT) described in a separate TDR, submitted and accepted earlier.

The use of registered names, trademarks, *etc.* in this publication does not imply, even in the absence of specific statement, that such names are exempt from the relevant laws and regulations and therefore free for general use.

Contents

Preface	vii			
1 Executive Summary	xi	4.3.2	Platform with Movable Tables	28
		4.3.3	Supply Lines	28
		4.3.4	Installation	29
2 The $\bar{\text{P}}\text{ANDA}$ Experiment and its Tracking Concept	1	4.4	Tracking Stations inside the Dipole Magnet Gap	29
2.1 The $\bar{\text{P}}\text{ANDA}$ Experiment	1	4.4.1	Space Available for the Tracking Stations	29
2.1.1 The Scientific Program	1	4.4.2	Support Frames with Straw Tube Modules	29
2.1.2 High Energy Storage Ring – HESR	1	4.4.3	Base Frame	30
2.1.3 Targets	2	4.4.4	Installation Procedure	30
2.2 The $\bar{\text{P}}\text{ANDA}$ Detector	2	4.5	Tracking Stations after the Dipole Magnet	31
2.2.1 Target Spectrometer	2	4.5.1	Support Frames for Straw Tube Modules	31
2.2.2 Forward Spectrometer	4	4.5.2	Stand for the Stations	32
2.2.3 Data Acquisition	4	4.5.3	Concept of Self-supporting Half-frame	32
2.3 The Charged Particle Tracking System	5	4.5.4	Module Exchange Procedure	33
2.3.1 General Layout	5	4.6	The Readout Electronics	34
2.3.2 Micro Vertex Detector	5	4.6.1	Requirements and General Concept	34
2.3.3 Straw Tube Tracker (STT)	6	4.6.2	Analog Front-End Electronics	36
2.3.4 Forward GEM Detectors	6	4.7	The Readout System	40
2.3.5 Forward Tracker	6	4.7.1	Development Policy	40
3 Overview of the Forward Tracker	8	4.7.2	Time-to-digital Converters and TRBv3	41
3.1 Basic Requirements	8	4.7.3	High Resolution Mode Data Rates	42
3.2 General Layout	10	4.7.4	High Luminosity Mode Readout Scheme	42
4 Technical Design	18	4.7.5	System Integration and Synchronization	44
4.1 Straw Tube Detectors	18	4.8	Quality Control	44
4.1.1 Straw Tubes	18	4.8.1	Gas Tightness	44
4.1.2 Gas Mixture	18	4.8.2	Wire Tension	45
4.1.3 End-plugs	19	4.8.3	Control of the Module Geometry	46
4.2 Straw Tube Modules	22	4.9	Detector Integration	51
4.2.1 Assembly of Straw Modules	22	4.10	Infrastructure	51
4.2.2 Module Description	22	4.10.1	The Gas System	51
4.2.3 Layer Arrangement	24	4.10.2	The Power Systems	53
4.2.4 Precision of Positioning Anode Wires	25	4.10.3	Detector Control System	54
4.2.5 The Grounding Scheme	25			
4.3 Tracking Stations before the Dipole Magnet	26			
4.3.1 Support Frames	26			

4.11 Alignment and Calibration Methods	55	6.4 Physics Channels Analysis	102
4.11.1 Alignment	55	6.4.1 Benchmark Channels	102
4.11.2 $r(t)$ Calibration Curve	55	6.4.2 $\bar{p}p \rightarrow \Psi(4040) \rightarrow D^{*+}D^{*-}$	102
6.4.3 $\bar{p}p \rightarrow \Lambda\bar{\Lambda}$	102		
5 Prototype Results	60		
5.1 Test Systems	60	7 Organization	106
5.2 The COSY-TOF Straw Tube Tracker	61	7.1 Production Logistics	106
5.3 Aging Tests	64	7.2 Timeline	106
5.4 Laboratory Tests with ^{55}Fe	67	7.3 Work Packages and Contributing Institutes	107
5.4.1 Signal-to-Noise Ratio	67	7.4 Infrastructure needed at FAIR	108
5.4.2 Signal Amplitude Variation Along Straw	69	7.5 Safety	108
5.4.3 Cross-Talk	69		
5.4.4 Gain Drop due to Space Charge	70	A Appendix: Wire Tension vs. Over-pressure	110
5.5 Tests with Proton Beams	71		
5.5.1 Experimental Setup	71	B Appendix: FEE Cards with CARI-OCA Chips	111
5.5.2 Adjustment of Baselines and Threshold in FEE	72		
5.5.3 Drift Time Spectra	73	Acknowledgements	113
5.5.4 Track Reconstruction	74		
5.5.5 PID Based on the TOT Measurement	77	List of Acronyms	115
		List of Figures	117
6 Computer Simulations and Expected Performance	81		
		List of Tables	123
6.1 The Single Straw Tube Simulation	81		
6.1.1 The Charge Released into the Tube	81		
6.1.2 Simulation of the Electron Drift	81		
6.1.3 The Gas Gain	83		
6.1.4 Detector Pulses	83		
6.1.5 Performance in Magnetic Field	84		
6.2 Track Reconstruction in the Forward Tracker	86		
6.2.1 Simulation and Reconstruction Software	86		
6.2.2 Pattern Recognition in the Forward Tracker	88		
6.2.3 Momentum Reconstruction	94		
6.3 Optimization of the Tracking System	97		
6.3.1 Short versus Long Distance Scenario for Arrangement of FT5-FT6	97		
6.3.2 Inclination Angle of Skewed Modules	98		
6.3.3 Active Areas of Tracking Stations	99		

1 Executive Summary

This report presents the design and the expected performance of the Forward Tracker for the **PANDA** experiment.

The **PANDA** detector at FAIR, Darmstadt, is designed for measurements of reactions induced by high intensity antiproton beams with a momentum between 1.5 GeV/c and 15 GeV/c interacting with hydrogen as well as nuclear targets. The main topics of the experiment are hadron spectroscopy, in particular the search of exotic states in the charmonium mass region and spectroscopy of multi-strange baryons, investigation of properties of mesons embedded in nuclear medium, spectroscopy of double hypernuclei and study of the nucleon structure.

Application of a fixed target at **PANDA** results in a forward peaking of the reaction products. Therefore, to ensure a geometrical acceptance close to 4π and a good momentum resolution in a wide range, the chosen setup consists of two spectrometers: the Target Spectrometer (TS) based on a 2 T solenoid magnet surrounding the interaction point and the Forward Spectrometer (FS) using a large gap 2 Tm dipole magnet for momentum analysis of particles emitted at the most forward angles. The FS covers an angular range of $\pm 10^\circ$ in the horizontal plane and $\pm 5^\circ$ in the vertical plane.

For measurement of particles momenta based on deflection of their trajectories in the magnetic field of the FS dipole magnet, the Forward Tracker (FT) is foreseen. The FT has to fulfill several basic requirements: high momentum resolution of 1-2%, momentum acceptance extending down to at least $0.03 \cdot p_{beam}$, high rate capability corresponding to $5 \cdot 10^7$ tracks/s and resistance against aging effects expected during a lifetime of the experiment of 10 years.

The design of the FT is based on self-supporting straw tubes, with 10 mm diameter, similar to those used in the **PANDA** Straw Tube Tracker (STT). Development of the Forward Tracker benefits from numerous synergies with the STT project.

The FT consists of three pairs of tracking stations: one pair (FT1, FT2) is placed upstream of the FS dipole magnet, the second pair (FT5, FT6) - downstream of the magnet, and the third pair (FT3, FT4) is placed inside the magnet gap in order to track also low momentum particles hitting the magnet yoke.

The FT has a modular structure. It consists of

modules comprising 32 straw tubes arranged in two staggered layers. Modules closely arranged next to each other and mounted on the same support frame form a double layer of straw tubes. Each tracking station consists of four double layers: the first and the fourth one contain vertical straws and the two intermediate - the second and the third one - are composed of straws inclined at $+5^\circ$ and -5° , respectively. The total number of the straw tube modules in all tracking stations equals 400 and the number of straw tubes equals 12 224. The active area of the tracking stations ranges from $x \times y = 134 \times 64 \text{ cm}^2$ in FT1, FT2 to $392 \times 120 \text{ cm}^2$ in FT5, FT6.

The pulses from the straw tubes are amplified and discriminated in front-end electronics cards based on an especially designed ASIC called PASTTREC. The time of the leading and trailing edges of the PASTTREC discriminator pulses are measured using multichannel TDCs based on FPGAs and equipped with Gbit optical links for the data transmission to the **PANDA** DAQ system.

This document is organized in the following way: In the next (2nd) chapter, an outline of the **PANDA** physics program is presented, and a layout of the **PANDA** detection system is described with a special emphasis on the tracking systems.

In chapter 3, basic requirements for the **PANDA** Forward Tracker are formulated and a general concept of the tracker is proposed.

Technical details of the tracker and the readout electronics including the front-end boards and the digitizing electronics are described in chapter 4. Also the tracker supplies and the integration in the **PANDA** setup are covered.

In chapter 5, prototypes of the straw tube detectors and the results of their tests with the proton beam from the COSY-Juelich accelerator are described.

Chapter 6 presents results of computer simulations of the FT including studies of a single straw tube response, pattern recognition and track reconstruction for simulated tracks as well as studies of physics performance for selected benchmark channels. The optimization of some of the tracker parameters is also discussed.

The last chapter is devoted to organizational issues including production logistics of the FT, time-lines, work packages and safety aspects.

2 The $\bar{\text{P}}\text{ANDA}$ Experiment and its Tracking Concept

The following sections contain a general introduction to the $\bar{\text{P}}\text{ANDA}$ experiment and, in particular, a short description of the implemented overall tracking concept.

2.1 The $\bar{\text{P}}\text{ANDA}$ Experiment

2.1.1 The Scientific Program

The $\bar{\text{P}}\text{ANDA}$ (anti-Proton ANnihilation at DArmstadt) collaboration [1] envisages a physics core program [2] that comprises:

- charmonium spectroscopy with precision measurements of mass, width, and decay branches;
- the investigation of states that are assumed to have more exotic configurations like multi-quark states, charmed hybrids, and glueballs;
- spectroscopy of (multi-)strange and charmed baryons;
- the search for medium modifications of charmed hadrons in nuclear matter;
- the γ -ray spectroscopy of hypernuclei, in particular double Λ states.

In the charmonium and open-charm regions, many new states have been observed in the last years, that do not match the patterns predicted in those regimes [3]. There are even several states unambiguously being of exotic nature, rising the question about the underlying mechanism to form such kind of states [4]. The production of charmonium and open-charm states in e^+e^- interactions are restricted to initial spin-parities of $J^{PC} = 1^{--}$. This limits the possibility to precisely scan and investigate these resonances in formation reactions. The use of $\bar{p}p$ annihilation does not suffer from this limitation. Combined with the excellent energy resolution of down to about 25 keV, this kind of reactions offer unique opportunity to perform hadron and charmonium spectroscopy in the accessible energy range.

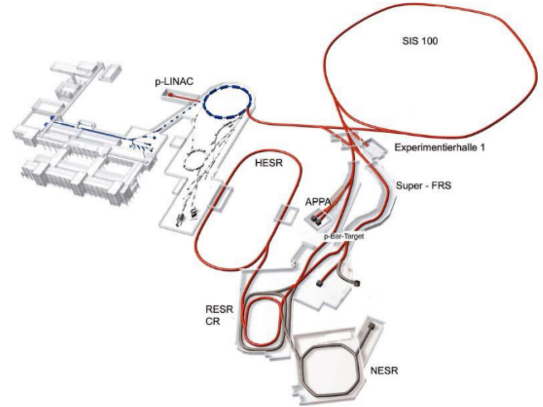


Figure 2.1: Schematic of the future FAIR layout incorporating the current GSI installations on the left; on the right the future installations, the SIS 100 synchrotron the storage and cooler ring complex including CR and HESR and the Super FRS experiment being some of the new parts.

2.1.2 High Energy Storage Ring – HESR

The $\bar{\text{P}}\text{ANDA}$ experiment is one of the key projects at the future Facility for Antiproton and Ion Research (FAIR) [5, 6] which is currently under construction at GSI, Darmstadt. The basic machine of the FAIR complex shown schematically in Fig. 2.1 will be the SIS100 synchrotron which will accelerate high intensity proton beams up to energy of 30 GeV and heavy ion beams e.g. U^{28+} up to 2.7 GeV/u. The antiprotons will be produced using 30 GeV proton beam from SIS100 hitting a production target. The produced antiprotons with momentum around 3 GeV/c will be collected, pre-cooled and accumulated in the CR/RESR rings. After accumulation of $10^{10}\text{-}10^{11}$ antiprotons, they will be injected in the High Energy Storage Ring (HESR) where the $\bar{\text{P}}\text{ANDA}$ detector will be installed as an internal target experiment (see Fig. 2.2).

The combination of HESR and $\bar{\text{P}}\text{ANDA}$ aims at both high reaction rates and high resolution to be able to study rare production processes and small branching ratios. With a design value of 10^{11} stored antiprotons for beam momenta from 1.5 GeV/c to

15 GeV/c and high density targets the anticipated antiproton production rate of $2 \cdot 10^7 \text{ s}^{-1}$ governs the experiment interaction rate in the order of cycle-averaged $1 \cdot 10^7 \text{ s}^{-1}$. The stored antiprotons do not have a bunch structure, and with 10% to 20% allocated to a barrier bucket, the antiprotons are continuously spread over about 80% of the HESR circumference.

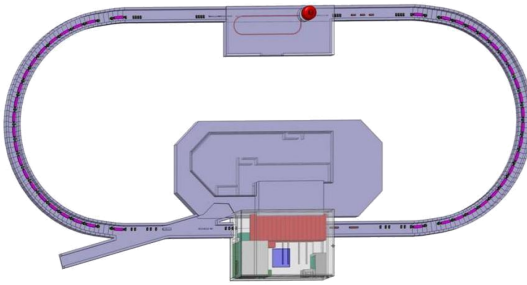


Figure 2.2: The HESR ring with the \bar{P} **A**ND**A** experimental area at the bottom and the electron cooler installation at the top. Standard operation has the antiproton injection from RESR (during the modularized startup phase from CR) from the left, or protons at reversed field polarities.

Two complementary operating modes are planned for the HESR, named *high luminosity* mode and *high resolution* mode. The high luminosity mode with $\Delta p/p = 10^{-4}$ and a pellet target density of $4 \cdot 10^{15} \text{ cm}^{-2}$ will produce an average luminosity of up to $L = 1.6 \cdot 10^{32} \text{ cm}^{-2}\text{s}^{-1}$. In the high resolution mode $\Delta p/p = 5 \cdot 10^{-5}$ will be achieved with electron cooling and stochastic cooling of the antiproton beam. A cluster jet target will be used to limit the energy broadening caused by the target. The cycle-averaged luminosity is expected to be $L = 1.6 \cdot 10^{31} \text{ cm}^{-2}\text{s}^{-1}$.

The values described here are the design values for the HESR and the \bar{P} **A**ND**A** experiment. In the modularized start version the Recycled Experimental Storage Ring (RESR) will not be available to accumulate the antiprotons. Instead, the accumulation process has to be done with the HESR itself. The absence of the dedicated RESR has the implication that, on one hand, the maximum number of antiprotons is reduced by one order of magnitude to $N_{max} = 10^{10}$ compared to the high luminosity mode. On the other hand the accumulation process, which takes a finite time, cannot be performed in parallel and further worsens the duty cycle (for more detail see [7]). However, since the full version of FAIR will be built, the requirements for the detectors of the \bar{P} **A**ND**A** experiment have to be set up

regarding the original design values.

2.1.3 Targets

The \bar{P} **A**ND**A** spectrometer is designed to allow the installation of different targets. For hydrogen as target material both Cluster Jet Targets and Pellet Targets are being prepared [8, 9]. One main technical challenge is the distance of 2 m between the target injection point and the dumping region.

The cluster jet target can maintain a constant thickness as a function of time, whereas a pellet target, with average velocities of around 50 m/s and average pellet spacing of 3 mm, produces target density variations on the 10-100 μs timescale.

An extension of the targets to heavier gases such as deuterium, nitrogen, or argon is planned for complementary studies with nuclear targets. In addition wire or foil targets are used in a dedicated setup for the production of hypernuclei.

2.2 The \bar{P} **A**ND**A** Detector

Fig. 2.3 shows a longitudinal section of the \bar{P} **A**ND**A** detector. As a fixed target experiment, it is asymmetric having two parts, the Target Spectrometer (TS) and the Forward Spectrometer (FS). The antiproton beam is scattered off a pellet or cluster jet target (left side in Fig. 2.3). \bar{P} **A**ND**A** will measure $\bar{p}p$ reactions comprehensively and exclusively, which requires simultaneous measurements of leptons and photons as well as charged and neutral hadrons. The physics requirements for the detectors are:

- to cover the full solid angle of the final state particles,
- to detect momenta of the reaction products, and
- to identify particle types over the full range of momenta of the reaction products.

2.2.1 Target Spectrometer

The TS, which is almost hermetically sealed to avoid solid angle gaps and which provides little spare space inside, consists of a solenoid magnet with a field of 2 T [10] and a set of detectors for the energy determination of neutral and charged particles as well as for the tracking and PID for charged tracks housed within the superconducting

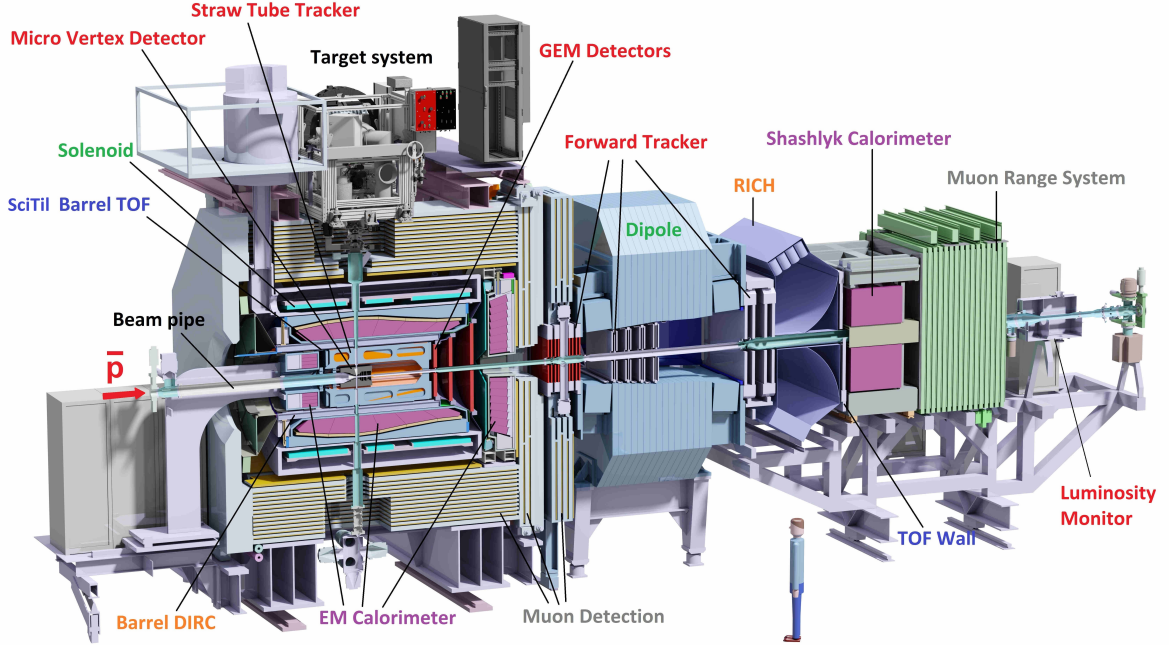


Figure 2.3: Longitudinal section of the \bar{p} ANDA setup with the Target Spectrometer (TS) on the left side, and the Forward Spectrometer (FS) starting with the dipole magnet on the right. The antiproton beam enters from the left.

solenoid magnet. The silicon Micro Vertex Detector (MVD) closely abuts the beam pipe surrounding the target area and provides secondary vertex sensitivity for particles with decay lengths on the order of $100\ \mu\text{m}$. Surrounding the MVD the main tracker is the Straw Tube Tracker (STT). In addition, in the forward direction, there will be three tracking stations based on Gaseous Electron Multiplier foils (GEM) as gas amplification stage. The tracking detectors like MVD and STT also provide information on the specific energy loss in their data stream.

Two Detectors for Internally Reflected Cherenkov light (DIRC) are to be located within the TS. Compared to other types of Ring Imaging Cherenkov (RICH) counters the possibility of using thin radiators and placing the readout elements outside the acceptance favors the use of DIRC designs as Cherenkov imaging detectors for PID. The Barrel DIRC covers polar angles θ from 22° to 140° inside the \bar{p} ANDA TS with at least a 3 s.d. π -K separation up to $3.5\ \text{GeV}/c$. The Endcap Disc DIRC covers polar angles θ from 10° to 22° in the horizontal plane and 5° to 22° in the vertical plane. For the analysis of the DIRC data the tracking information is needed, as the Cherenkov angle is measured between the Cherenkov photon direction and the momentum vector of the radiating particle. The

error of the measurement of the polar angle from the tracking system is expected to be 2-3 mrad.

The Scintillation Tile (SciTil) detector consisting of small scintillator tiles ($3\ \text{cm} \times 3\ \text{cm}$), read out by Silicon PhotoMultipliers (SiPMs), and situated in the support frame outside the Barrel DIRC will have a time precision of 100 ps or less. In the absence of a start detector the SciTil will provide in combination with the forward time of flight system a good relative timing and event start time.

The lead tungstate (PWO) crystals of the Electromagnetic Calorimeter (EMC) are read out with Avalanche Photo Diodes (APD) or vacuum tetrodes. Both the light output and the APD performance improve with lower temperature. Thus the plan is to operate the EMC detectors at $T=-25^\circ\text{C}$. The EMC is subdivided into barrel detector, backward and forward endcaps, all housed within the solenoid magnet return yoke.

Besides the detection of photons, the EMC [11] is also the most powerful detector for the identification of electrons. The identification and measurement of this particle species will play an essential role for the physics program of \bar{p} ANDA.

The return yoke for the solenoid magnet in the \bar{p} ANDA TS is laminated to accommodate layers of

muon detectors. They form a range stack, with the inner muon layer being able to detect low energy muons and the cumulated iron layer thickness in front of the outer layers providing enough hadronic material to stop the high energy pions produced in $\bar{\text{P}}\text{ANDA}$.

2.2.2 Forward Spectrometer

The FS angular acceptance has an ellipsoidal form with a maximum value of ± 10 degrees horizontally and ± 5 degrees vertically w.r.t. the beam direction.

The FS starts with a 2 Tm dipole magnet to provide bending power with a B-field perpendicular to the forward tracks. The magnet has a window frame with about a 1 m gap, a 3.1 m width and a 1.6 m length in the beam direction starting from 3.9 m downstream of the target. The dipole field will be ramped during acceleration in the HESR and the final ramp maximum scales with the selected beam momentum. The magnetic field of the dipole magnet causes a deflection of the antiproton beam by an angle of 2.2° . The beam deflection will be compensated by two correcting dipole magnets, placed one upstream and the other downstream of the $\bar{\text{P}}\text{ANDA}$ detection system.

The Forward Tracker (FT), which is the topic of this document, is designed for momentum analysis of charged particles deflected in the field of the dipole magnet. The FT comprises 24 planar double layers of straw tube detectors grouped in six tracking stations placed around the dipole magnet.

Most of the detectors of the FS (except parts of the tracking detectors) are located downstream the dipole magnet.

In the FS, the Forward EMC of a Shashlyk-type, consisting of 1512 channels of $55 \times 55 \text{ mm}^2$ cell size, covers an area of $4.9 \times 2.2 \text{ m}^2$.

An aerogel RICH detector will be located between the dipole magnet and the Forward EMC. A Time-of-Flight Wall covers the identification of slow particles below the Cherenkov light threshold.

For the determination of the luminosity, a detector based on four layers of monolithic active pixel sensors close to the beam pipe detects hits from the tracks of elastically scattered antiprotons.

2.2.3 Data Acquisition

The $\bar{\text{P}}\text{ANDA}$ detector is located in an experimental hall, encased in a smaller tunnel-like concrete structure for radiation protection. Most subsystems con-

nect their Front End Electronics (FEE) components via cables and tubes placed in movable cable ducts to the installations in the counting house, where three levels are foreseen to accommodate cooling, gas supplies, power supplies, electronics, and worker places. Only subcomponents, where cables must be as short as possible, will place racks or crates directly on the outside of the TS.

The data flow and processing is spatially separated into the FEE part located on the actual detector subsystems and the Data Acquisition (DAQ), located off-detector in the counting room.

The FEE comprises analog electronics, digitization, low level pre-processing and optical data transmission to the DAQ system.

While each sub-detector implements detector specific FEE systems the DAQ features a common architecture and hardware for the complete $\bar{\text{P}}\text{ANDA}$ detector.

Operating the $\bar{\text{P}}\text{ANDA}$ detector at interaction rates of $2 \times 10^7/\text{s}$, typical event sizes of 4-20 kB lead to mean data rates of $\sim 200 \text{ GB/s}$. The $\bar{\text{P}}\text{ANDA}$ DAQ design does not use fixed hardware based triggers but features a continuously sampling system where the various subsystems are synchronized with a precision time stamp distribution system.

Event selection is based on real time feature extraction, filtering and high level correlations.

The main elements of the $\bar{\text{P}}\text{ANDA}$ DAQ are the data concentrators, the compute nodes, and high speed interconnecting networks. The data concentrators aggregate data via point-to-point links from the FEE and the compute nodes provide feature extraction, event building and physics driven event selection.

A data rate reduction of about 1000 is envisaged in order to write event data of interest to permanent storage.

Peak rates above the mean data rate of $\sim 200 \text{ GB/s}$ and increased pile-up may occur due to antiproton beam time structure, target density fluctuations (in case of pellet target) and luminosity variations during the HESR operation cycle.

FPGA based compute nodes serve as basic building blocks for the $\bar{\text{P}}\text{ANDA}$ DAQ system exploiting parallel and pipelined processing to implement the various real-time tasks, while multiple high speed interconnects provide flexible scalability to meet the rate demands.

2.3 The Charged Particle Tracking System

2.3.1 General Layout

There are different tracking systems for charged particles at $\bar{\text{P}}\text{ANDA}$, positioned inside the Target Spectrometer and in the forward region around the dipole magnet. Main tasks of the global tracking system are the accurate determination of the particle momenta, a high spatial resolution of the primary interaction vertex and the detection of displaced secondary vertices. Therefore, measurements of different sub-detectors have to be merged in order to access the full tracking information.

The magnetic solenoid field in the Target Spectrometer produces a circular transverse motion of the charged particles with non-zero transverse momentum. The particle momentum then can be extracted via the determination of the bending radius. However, tracks with a small polar angle have small transverse momentum and hence can not be curved enough to be momentum analyzed in the TS.

For this case, the particle deflection induced by the subsequent dipole magnet is used to measure the particle momentum. Basically it can be deduced from a combined straight line fit before and after the dipole magnet.

Central tracks are reconstructed by combining hit points in the MVD layers with the hits of the STT or the GEM stations. The MVD detector covers a range of 3° to 150° in polar angle. This range is also almost fully covered by the combination of the STT (10° - 140°) and the GEM stations (3° - 22°). The momentum resolution of the TS tracking system is about 1-2%.

For the reconstruction of the small angle tracks, the straw tube layers in the FT have to be used. The FT angular range of $\pm 10^\circ$ horizontally and $\pm 5^\circ$ vertically overlaps partly with the range of the MVD and of the GEM stations (polar angles $> 3^\circ$). In the overlap region the MVD and the GEM stations can contribute to the forward tracking because the delivery of an additional track point closer to the IP significantly improves the precision of the fitting results.

After the global identification of individual tracks an event mapping has to be performed to match different tracks of the same event to a common vertex which either corresponds to the primary interaction vertex or a delayed decay of short-lived particles.

In the following four subsections, the components

of the $\bar{\text{P}}\text{ANDA}$ tracking system, namely the Micro Vertex Detector, the Straw Tube Tracker, the GEM Detectors and the Forward Tracker, are described in more detail.

2.3.2 Micro Vertex Detector

The design of the Micro Vertex Detector (MVD) [12] for the Target Spectrometer is optimised for the detection of secondary decay vertices from charmed and strange hadrons and for a maximum acceptance close to the interaction point. It will also strongly improve the transverse momentum resolution. The setup is depicted in Fig. 2.4.

The concept of the MVD is based on radiation hard silicon pixel detectors with fast individual pixel readout circuits and silicon strip detectors. The layout foresees a four layer barrel detector with an inner radius of 2.5 cm and an outer radius of 13 cm. The two innermost layers will consist of pixel detectors and the outer two layers will be equipped with double-sided silicon strip detectors.

Six detector wheels arranged perpendicular to the beam will achieve the best acceptance for the forward part of the particle spectrum. While the inner four layers will be made entirely of pixel detectors, the following two will be a combination of strip detectors on the outer radius and pixel detectors closer to the beam pipe.

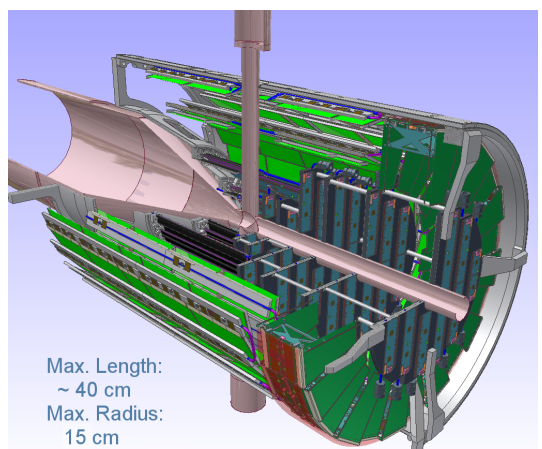


Figure 2.4: The Micro Vertex Detector (MVD) of the Target Spectrometer surrounding the beam and target pipes seen from downstream. To allow a look inside the detector a three-quarters portraits is chosen.

2.3.3 Straw Tube Tracker (STT)

The Straw Tube Tracker [13] will consist of aluminised Mylar straw tubes stiffened by operating them at an overpressure of 1 bar which makes them self-supporting. The straws are to be arranged in planar layers which are mounted in a hexagonal shape around the MVD as shown in Fig. 2.5. In total there are 27 layers of which the 8 central ones are skewed, to achieve an acceptable resolution of 3 mm also in z (parallel to the beam). The gap to the surrounding detectors will be filled with further individual straws. In total there will be 4636 straws around the beam pipe at radial distances between 15 cm and 41.8 cm with an overall length of 150 cm. All straws have a diameter of 10 mm and are made of a 27 μm thick Mylar foil. Each straw tube is constructed with a single anode wire in the center that is made of 20 μm thick gold plated tungsten. The gas mixture used will be Argon based with CO₂ as quencher. It is foreseen to have a gas gain not greater than 10⁵ in order to warrant long term operation. With these parameters, a resolution in x and y coordinates of less than 150 μm is expected. A thin and light space frame will hold the straws in place, the force of the wire however is kept solely by the straw itself. This overall design results in a material budget of 1.2% of one radiation length.

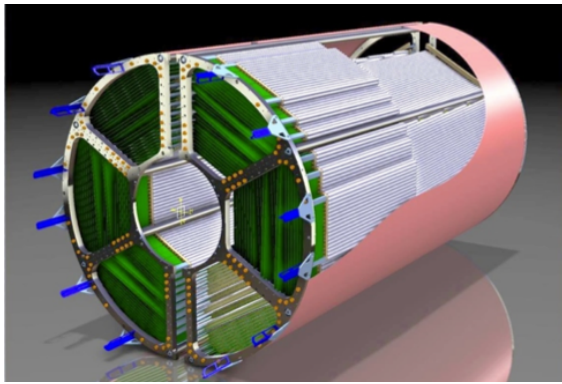


Figure 2.5: The Straw Tube Tracker (STT) of the Target Spectrometer seen from upstreams.

2.3.4 Forward GEM Detectors

Fig. 2.6 shows the components of the tracking system of the Target Spectrometer. Particles emitted at angles below 22° which are not fully accepted by the STT will be tracked by three planar Gaseous Electron Multipliers (GEM) stations placed approximately 1.1 m, 1.4 m and 1.9 m downstream of the target. Located in the middle of each station is a

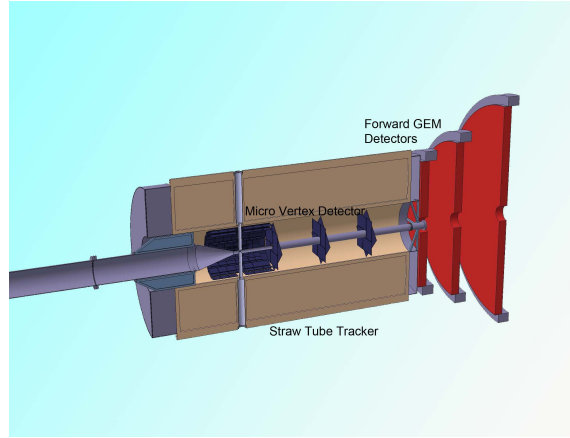


Figure 2.6: Schematic drawing of the tracking detectors of the Target Spectrometer.

double-sided read-out pad plane which allows particle track position measurement in four projections. In the front and back of the pad plane stacks of three GEM foils are used for electron amplification. The station volume is closed with one cathode plane and one window foil per side. On the perimeter of the station a ring of Front-End Electronics, cooling, support, voltage supply and shielding is formed.

The stations have to sustain a high counting rate of particles peaked at the most forward angles due to the relativistic boost of the reaction products as well as due to the small angle $\bar{p}p$ elastic scattering. The maximum expected particle flux in the first station in the vicinity of the 5 cm diameter beam pipe will be about $3 \cdot 10^4 \text{ cm}^{-2}\text{s}^{-1}$.

2.3.5 Forward Tracker

The deflection of particle trajectories in the field of the dipole magnet will be measured with the Forward Tracker (FT). The design of this tracker is a subject of the present document. The FT will consist of three pairs of tracking stations. The first pair will be placed in front, the second within and the third behind the dipole magnet. The FT will be based on self-supporting straw tubes, with a 10 mm diameter, which will be also used in the \bar{P} *ANDA* Straw Tube Tracker. Each tracking station will consist of four double-layers of straw tubes, two with vertical straws and two with straws inclined at +5° and at -5°, respectively. The planned configuration of double-layers of straws will allow to reconstruct tracks in each pair of tracking detectors, also in case of multi-track events.

References

- [1] $\bar{\text{P}}\text{ANDA}$ Collaboration, http://www-panda.gsi.de/archive/public/panda_tpr.pdf Technical Progress Report, Technical report, FAIR-ESAC, 2005, <http://www-panda.gsi.de>.
- [2] $\bar{\text{P}}\text{ANDA}$ Collaboration, Physics Performance Report, 2009, arXiv:0903.3905v1.
- [3] X. Liu, An overview of XYZ new particles, 2014, arXiv:1312.7408v2/hep-ph.
- [4] Yu. S. Kalashnikova et al., Phys. Atom. Nucl. **73**, 1592 (2010).
- [5] GSI Helmholtzzentrum für Schwerionenforschung, FAIR - An International Accelerator Facility for Beams of Ions and Antiprotons, Baseline technical report, 2006, <http://www.gsi.de/fair/reports/btr.html>.
- [6] Technical report, http://www.fair-center.de/fileadmin/fair/publications_FAIR/FAIR_GreenPaper_2009.pdf.
- [7] K. Goetzen, Average Luminosities and Event Rates at $\bar{\text{P}}\text{ANDA}$, 2009, Report of the PID TAG.
- [8] $\bar{\text{P}}\text{ANDA}$ collaboration, Targets Technical Design Report, 2012.
- [9] M. Büscher et al., Int. J. Mod. Phys. E **18**, 505 (2009).
- [10] $\bar{\text{P}}\text{ANDA}$ collaboration, Technical Design Report for the Solenoid and Dipole Spectrometer Magnets, arxiv:0907.0169v1, 2009.
- [11] $\bar{\text{P}}\text{ANDA}$ collaboration, EMC Technical Design Report, Technical report, Darmstadt, 2008, arXiv:0810.1216v1.
- [12] $\bar{\text{P}}\text{ANDA}$ collaboration, Technical Design Report for the $\bar{\text{P}}\text{ANDA}$ Micro Vertex Detector, 2011.
- [13] $\bar{\text{P}}\text{ANDA}$ collaboration, Technical Design Report for the $\bar{\text{P}}\text{ANDA}$ Straw Tube Tracker, arxiv:1205.5441v2, 2012.

3 Overview of the Forward Tracker

3.1 Basic Requirements

$\bar{\text{P}}\text{ANDA}$ is a fixed target experiment and, therefore, to assure a coverage of the 4π solid angle and a high momentum resolution for charged particles, it is split into two spectrometers: the Target Spectrometer (TS) based on a 2 T solenoid magnet surrounding the interaction point, and the Forward Spectrometer (FS) using a large gap dipole magnet for a momentum analysis of forward emitted particles. The angular range of the FS is $\pm 10^\circ$ in the horizontal plane and $\pm 5^\circ$ in the vertical one with exclusion of a central region around the beam line corresponding to polar angles below $\sim 1.2^\circ$. The angular acceptance of the FS constitutes only about 0.5% of the full solid angle, however, the FS plays an essential role in the measurement of reactions with angular distributions of produced particles strongly peaked in the forward direction. This takes place for reactions with low center of mass (CM) velocities of the reaction products, and/or with cross-sections with angular distributions peaking forward. An example of the former case is the reaction $\bar{p}p \rightarrow \Psi(4040) \rightarrow D^{*+}D^{*-} \rightarrow D_0\pi^+\bar{D}_0\pi^- \rightarrow K^+K^-\pi^+\pi^-\pi^+\pi^-$. Due to small decay energy in the channel $\Psi(4040) \rightarrow D^{*+}D^{*-}$ (19 MeV) and in the subsequent decay $D^{*+} \rightarrow D_0\pi^+$ (6 MeV), the velocities of the outgoing pions in the CM system are much lower than the velocity of the CM frame in the LAB system. Consequently, the pions are emitted at LAB angles smaller than $\sim 12^\circ$ and are predominately in the FS acceptance (see Sec. 6.4.2). An example of a reaction with a CM cross section strongly peaked in the forward direction is the production of pairs of hyperons: $\bar{p}p \rightarrow \Lambda\bar{\Lambda} \rightarrow p\pi^-\bar{p}\pi^+$ [1]. The outgoing $\bar{\Lambda}$ hyperon "takes over" the $\bar{u}-\bar{d}$ quark pair from the beam antiproton and, therefore, its angular distribution is strongly enhanced at forward angles. Additionally, due to a small decay energy of $\Lambda \rightarrow \bar{p}\pi^+$ (38 MeV), also the outgoing antiprotons and positively charged pions are emitted at small LAB angles and are almost exclusively detectable in the FS (see Sec. 6.4.3).

For tracking of charged particles in the Forward Spectrometer, the Forward Tracker (FT) is foreseen. The fundamental requirements for this tracker are based on simulations of selected benchmark channels and of background reactions expected in $\bar{p}p$ and $\bar{p}A$ collisions (see Chapter 6). To study the background processes, two different gen-

erators, based on different models, have been used: in the case of $\bar{p}p$ annihilation - the Dual Parton Model (DPM) [2], while in the case of the $\bar{p}A$ annihilations - the Ultrarelativistic Quantum Molecular Dynamics (UrQMD) [3, 4].

The momentum acceptance of the tracker should extend down to at least $0.03 \cdot p_{beam}$ where the lower limit is important for measurements of low momentum pions originating e.g. from decays of $\bar{\Lambda}$ -hyperons. The expected distributions of momenta of charged particles emitted in the angular range of the Forward Spectrometer in the collisions of 15 GeV/c antiprotons with a proton target and with a nitrogen target are shown in Fig. 3.1 (a) and (b), respectively. Both distributions have a similar shape with a pronounced peak visible at high momenta corresponding to the elastic (quasi-elastic) $\bar{p}p$ scattering, and a broad structure at low momenta. The lower limit of the momentum acceptance, equal to 3% of p_{beam} , is indicated with a red dashed line. Only a small fraction of low momentum tracks (about 1% for $\bar{p}p$ and 2.5% for $\bar{p}N$) does not fit in the momentum acceptance.

For a high invariant mass resolution, the momentum resolution of the FT should be comparable or better than the one of the Target Spectrometer which is of about 1.5%. The FT should also provide the information about track parameters in the Forward RICH detector and the Forward TOF Wall located after the dipole magnet.

The material budget should be as low as possible ($< 5\% X_0$) in order to minimize the multiple scattering and the gamma conversions.

The FT should digest high particle fluxes expected in $\bar{p}p$ collisions at the maximum interaction rate of $2 \cdot 10^7$ /s and the highest beam momentum of 15 GeV/c. These fluxes reach $25 \text{ kHz} \cdot \text{cm}^{-2}$ in the vicinity of the beam line before the dipole magnet, where the first tracking station of the FT will be placed (see Fig. 3.2.a). In $\bar{p}A$ collisions for interaction rates lying below 10^7 /s, the particles fluxes are smaller. For example, in $\bar{p}N$ collisions at 15 GeV/c at an interaction rate of $1 \cdot 10^7$ /s, the fluxes of charged particles reach $19 \text{ kHz} \cdot \text{cm}^{-2}$ in the vicinity of the beam line (see Fig. 3.2.b).

The total counting rate in the FT before the dipole magnet expected in the $\bar{p}p$ collisions at the highest beam momentum and the maximum luminosity is about $5 \cdot 10^7$ tracks/s, where $2 \cdot 10^7$ /s are primary

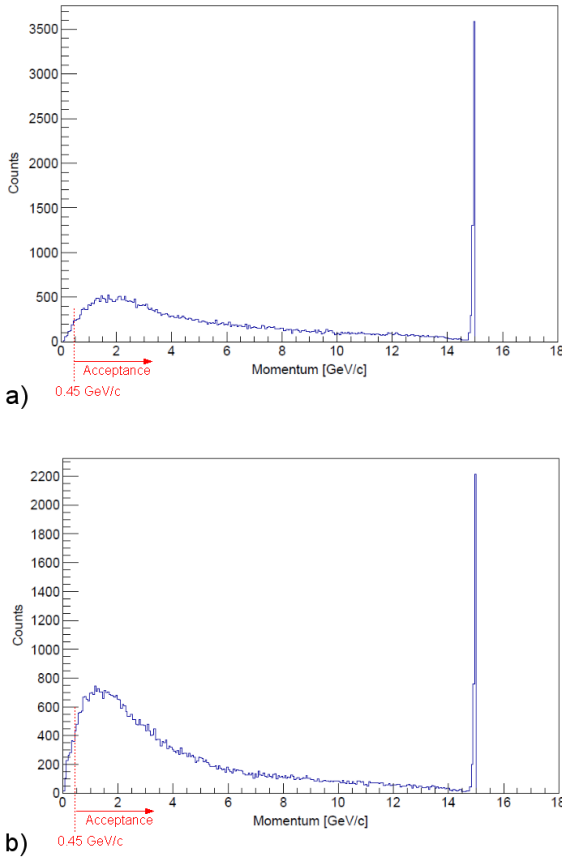


Figure 3.1: Momentum distribution of charged particles emitted in the angular range of the FS in collisions of a 15 GeV/c antiproton beam with a hydrogen (a) and a nitrogen (b) target, obtained with event generators based on the DPM and the UrQMD model, respectively. The dashed red line indicates the 3% limit of the momentum acceptance which equals 0.45 GeV/c for 15 GeV/c beam momentum.

tracks originating from the target and $3 \cdot 10^7$ /s are secondary particles produced in interaction of primary particles with the beam pipe and other elements of the \bar{P} ANDA detection system. The Forward Tracker should be resistant against aging effects expected during a lifetime of the experiment of 10 years with a foreseen data taking period of 6 months per year.

The production of secondary particles increases substantially the multiplicity of tracks entering the FS. For $\bar{p}p$ collisions at 15 GeV/c, multiplicities of primary tracks of 0, 1, 2, 3 and 4 occur with probability of about 37%, 40%, 18%, 5% and 1%, respectively. Higher multiplicities contribute by less than 1% (see Fig. 3.3.a). When the secondary tracks are included, the multiplicities 0, 1, 2, 3, 4 appear

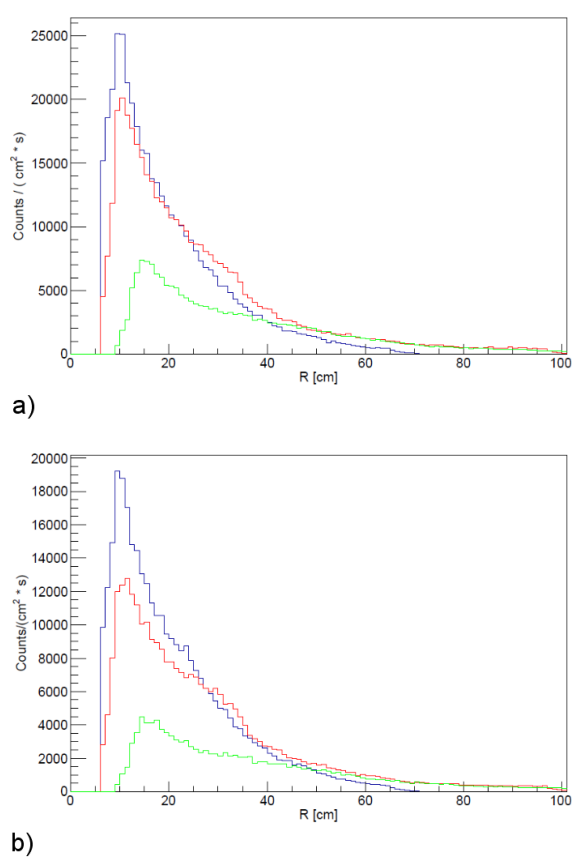


Figure 3.2: Number of charged tracks passing through a squared centimeter per second as a function of the distance from the beam axis, expected before the dipole magnet at $z = 2954$ mm where the first tracking stations of the FT will be placed (blue curve), inside the dipole magnet at $z = 3945$ mm (red curve) and after the dipole magnet at $z = 6075$ mm (green curve) in collisions of a 15 GeV/c antiproton beam with a hydrogen target (a) and with nitrogen target (b). The counts include both primary and secondary tracks and are obtained in simulations of $\bar{p}p$ and $\bar{p}-N$ collisions at the interaction rate of $2 \cdot 10^7$ s⁻¹ and 10^7 s⁻¹, respectively.

with probabilities of about 16%, 30%, 20%, 13%, 7%, respectively, and the higher multiplicities constitute about 14%. The track multiplicities are even higher in reactions on nuclear targets as illustrated in Fig. 3.3.b in the case of $\bar{p}-N$ collisions.

The FT should be equipped with a fast front-end and digitizing electronics capable to deal with these high counting rates. Efficient algorithms for on-line track reconstruction should provide the information about particle momenta required for the selection of events by the \bar{P} ANDA software trigger.

Besides the requirements discussed above, the

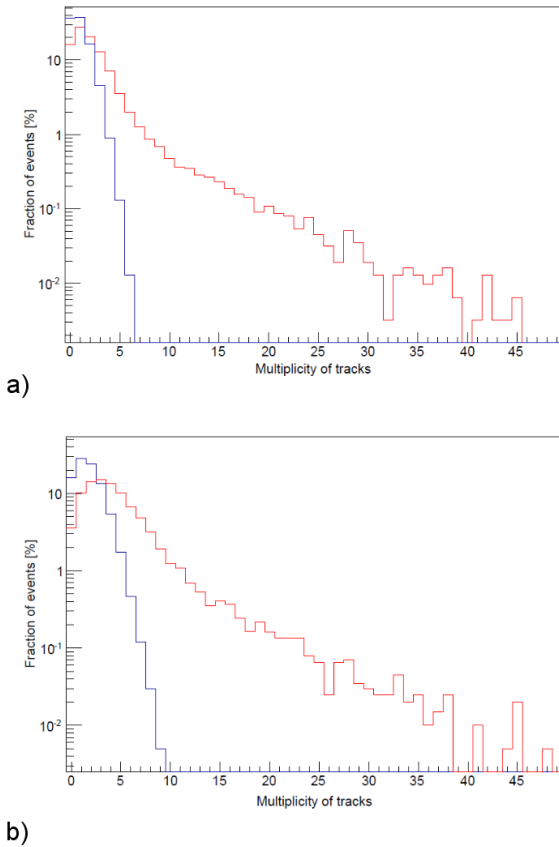


Figure 3.3: Multiplicity of primary tracks (blue line) and all tracks including the secondary ones (red line) expected in the FT at the position before the dipole magnet in collisions of 15 GeV/c antiproton beam with proton target (a) and with nitrogen target (b).

tracking detectors in the FT should fulfill also certain geometrical and mechanical conditions. First of all, the detectors should contain an opening for the beam pipe in the center of the active area. It should be also possible to split the tracking detectors, located before and after the dipole magnet, into two halves - the left and right with respect to the beam line - in order to access flange connections on the beam pipe. These flange connections are necessary in order to split (or connect) the beam pipe between the TS and FS as well as between the dipole magnet and the forward platform. This is necessary to allow the movement of the TS and the FS from the experimental to the parking position (or vice versa). A serious limitation concerns the tracking detectors located inside the dipole magnet gap. Here the space foreseen for frames and other passive elements is restricted in the vertical direction to only 5.5 cm.

3.2 General Layout

The requirements for the Forward Tracker presented in the previous section, led toward alternative options: multi-wire drift chambers and straw tube detectors. Both solutions allow to cover large active area at moderate price, and provide high position resolution with low masses.

Drift chambers offer low material budget, but their application in the FT is hampered by the necessity to split the tracking stations into two halves for installation on the beam line and the need of an opening for the beam pipe in the center of the active area. The HERMES forward tracking chambers [5] fulfill these requirements, but at the cost of massive frames passing through the center of the active area. This solution can not be adopted for the FT since it determines losses of acceptance caused by the frames and due to the production of secondary particles on the frames. The solution implemented by the COSY-11 collaboration using C-shaped frames for the chambers [6] avoids additional support structures in the active area, however, leaves a gap in the active area with a width corresponding to a beam pipe diameter.

The above mentioned problems that occur by adopting drift chambers can be easily overcome in a design based on straw tube detectors. Due to many important advantages, such detectors have been applied in numerous experiments including cylindrical tracking detectors e.g. the ATLAS TRT Barrel Detector [7] or the GlueX Central Drift Chamber [8] as well as planar detectors like the LHCb Outer Tracker [9], the COMPASS drift chamber [10] and the COSY-TOF straw tube tracker [11]. The mentioned planar trackers are dedicated to measurement of trajectories of particles emitted at forward angles around the beam direction as it is the case for the \bar{P} *ANDA* Forward Tracker. The LHCb and the COMPASS straw trackers, similarly as the \bar{P} *ANDA* FT, are used as components of forward spectrometers based on large dipole magnets and work in high rate conditions.

The LHCb Outer Tracker was built as a modular detector. A module contains 64 straw tube detectors with a diameter of 5 mm arranged in two staggered layers. The straw tubes are mounted on sandwich panels providing mechanical rigidity. The material budget of the straw module is relatively high and corresponds to $0.75\% X_0$. One tracking station comprising four layers of modules represents $3\% X_0$.

The COMPASS tracker comprises overall 15 double straw tube layers with an active area of about

$2.8 \times 3.2 \text{ m}^2$. The central parts of the straw layers, which are exposed to the highest rates, contain straws of 6.144 mm diameter and in the outer parts 9.654 mm. The material budget of one straw tube double layer is about 0.2 % X_0 . The COMPASS tracker uses large, massive frames for holding the mechanical tension of the straw tubes and the anode wires. This solution is not optimum for the $\bar{\text{P}}\text{ANDA}$ FT since we need to use detector frames of split type for the tracking stations before and after the dipole magnet. Also for tracking stations inside the dipole magnet gap, the COMPASS solution is not well suited, due to the very limited space available for the detector frames.

The COSY-TOF tracker, which is based on self supporting straw tubes, constitutes an attractive alternative to the LHCb and the COMPASS trackers. The tracker consists of 13 double layers of straw tubes with an active area of about $1 \times 1 \text{ m}^2$ and is placed inside the COSY-TOF vacuum tank. In the tracker, a gas pressure of about 1 bar gives the straws high mechanical stiffness and maintains the anode wire tension. The role of the detector frames is limited to position the straw tubes and, therefore, they are made of lightweight and compact beams of reinforced Rohacell. The straw tubes have a diameter of 10 mm and consist of thin aluminised Mylar walls of thickness $27\mu\text{m}$. The material budget of a straw tube double layer is only 0.09 % X_0 and compared to the LHCb and COMPASS straws is smaller by a factor of 8 and 2, respectively.

For the FT we chose straw tube detectors of self supporting type with a diameter of 10 mm developed for the COSY-TOF experiment, since they offer important advantages: low material budget and very compact, lightweight frames. The same straw tube detectors were also chosen for the $\bar{\text{P}}\text{ANDA}$ central Straw Tube Tracker. The gas mixture foreseen for the $\bar{\text{P}}\text{ANDA}$ FT is argon based with a percentage of 10% CO₂ as quenching component. The details that brought to this choice are discussed in Sec. 4.1.2. The most important advantages of this gas mixture are a high rate capability combined with low aging. With the chosen straw tube diameter of 10 mm, which corresponds to a maximum drift path of 5 mm, and a working pressure of the gas mixture of 2 bar, the maximum drift time is about 130 ns. At the highest expected counting rate of 1400 kHz for straws in the central region close to the beam pipe (see Fig. 3.4), the occupancy is 18%.

Unlike the COSY-TOF tracker, in our design, the tracking stations of the Forward Tracker have a modular layout. They consist of straw tube mod-

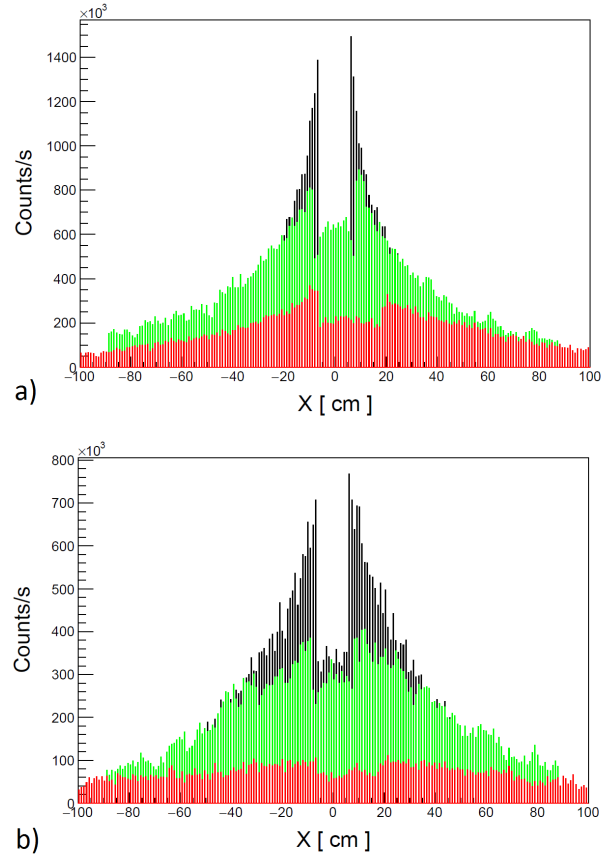


Figure 3.4: Counts per second expected in individual straw detectors placed before the dipole magnet at $z = 2954 \text{ mm}$, where the first tracking stations of the FT will be located (black histogram), inside the dipole magnet at $z = 3945 \text{ mm}$ (green histogram), and after the dipole magnet at $z = 6075 \text{ mm}$ (red histogram), for collisions of 15 GeV/c antiprotons with a hydrogen target (a) and with nitrogen target (b). The counts include both primary and secondary tracks and are obtained in simulations of $\bar{p}\text{-p}$ and $\bar{p}\text{-N}$ collisions at the interaction rate of $2 \cdot 10^7 \text{ s}^{-1}$ and 10^7 s^{-1} , respectively. Lower counting rates in the central detector region corresponds to shorter modules placed above and below the beam pipe. The displacement, with respect to $x = 0$, of the region with lower counts in the tracking station placed after the dipole magnet, is due to the bending of the beam pipe in the area between the dipole magnet poles.

ules arranged in detection planes. The standard modules contain 32 straw tube detectors placed in two staggered layers glued together. Only in the tracking stations before and after the dipole magnet, narrower modules comprising $2 \times 12 = 24$ straw tubes are mounted in the vicinity of the beam pipe. This allows to leave the needed space for the beam pipe. The arrangement of the straw tubes in a mod-

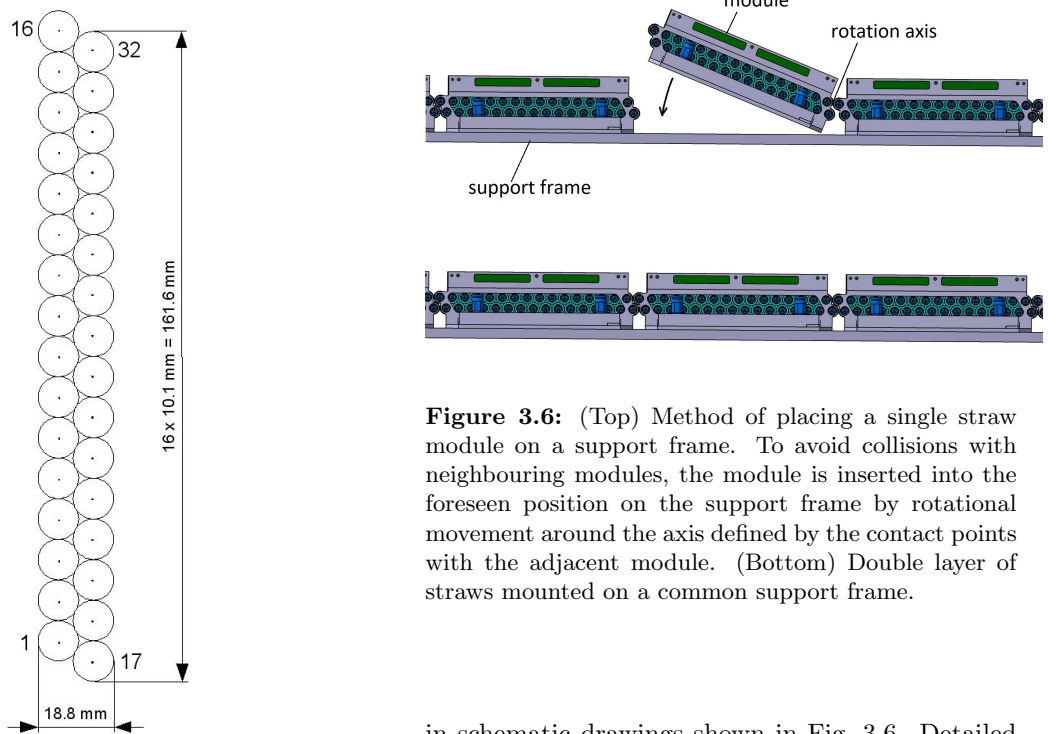


Figure 3.5: Schematic view of the cross section of a straw tubes double layer in one module. The distance between the anode wires of neighboring straws equals the straw tube diameter (10.1 mm).

ule is schematically shown in Fig. 3.5. Each module is equipped with its own preamplifier-discriminator card. It has also its own high voltage supply and gas supply lines. In this way it constitutes an autonomous mechanical and electrical unit.

The modules, arranged one beside the other, form a double layer of straw tubes. Each tracking station consists of four double-layers: the first and the fourth one contain vertical straws and the two intermediate - the second and the third one - contain straws inclined at $+5^\circ$ and -5° , respectively. This arrangement of straws allows for a three dimensional reconstruction of multi-track events. It contains also some redundancy allowing to compensate the lower detection efficiency for tracks distances from the anode wire close to the straw radius.

In the tracking stations, one support frame is used for a pair of double layers. In this way the four double layers in one tracking station are mounted on two frames. Each module can be mounted and dismounted from the support frame without the need to remove neighboring modules as it is explained

Figure 3.6: (Top) Method of placing a single straw module on a support frame. To avoid collisions with neighbouring modules, the module is inserted into the foreseen position on the support frame by rotational movement around the axis defined by the contact points with the adjacent module. (Bottom) Double layer of straws mounted on a common support frame.

in schematic drawings shown in Fig. 3.6. Detailed description of the module replacement procedure is given in Sec. 4.5.4.

An important advantage of the modular construction of the Forward Tracker is the possibility of a fast and simple repair of the detection planes by replacing the modules containing broken channels. It also allows the replacement of modules with straws showing deterioration of performance due to aging effects. This concerns especially the modules working in the high particle fluxes close to the beam pipe. The modular construction also allows to introduce modifications of the tracker to enhance its rate capabilities. If necessary, especially in the central region close to the beam pipe, it will be possible to insert modules made of straw tubes with smaller diameter. For example, the standard module containing 2x16 straw detectors with 10 mm diameter can be replaced by a module containing 2x27 straws with 6 mm diameter. It is also possible to halve the occupancy, and in this way to increase the rate capability of the modules, by segmenting the anode wire into two independent sections of equal length connected in the middle with an isolating piece, and read out from opposite ends using two electronic channels [7, 12].

The Forward Tracker consists of three pairs of tracking stations: one pair (FT1, FT2) is placed before the dipole magnet, the second pair (FT3, FT4) - inside the magnet gap, and the third pair (FT5, FT6) - after the magnet. The positions of the tracking stations along the beam line are indicated in

Fig. 3.7 and a 3-D model of the tracker is presented in Fig. 3.8. Straw tube double layers in all tracking stations are oriented parallel to the x-y plane which is perpendicular to the beam direction (z-axis). The projection of each double layer on the x-y plane is symmetric under rotation of 180° around the z-axis. The two pairs (FT1, FT2) and (FT5, FT6) allow for momentum analysis of charged particles in the range above $0.05 \cdot p_{beam}$, where the dependence on the beam momentum results from the scaling of the magnetic field in the dipole magnet. This momentum acceptance is extended towards lower values to about $0.03 \cdot p_{beam}$, by the tracking stations (FT3, FT4) which can register tracks of low momentum particles deflected in the magnetic field of the dipole magnet towards the side walls of the magnet gap. The tracking stations FT3, FT4 should be located inside the dipole magnet gap, close to the entrance in the dipole, so that the low momentum tracks can pass through all the detection planes. The space occupied by the FT3 and FT4 station along the z -axis (beam direction) equals 385 mm and is larger than 200 mm foreseen for each of the stations FT1, FT2, FT5, FT6, due to the need to leave free space between the FT3, FT4 frames for the front-end electronics cards. We checked, that the chosen arrangement of the detection planes provides momentum acceptance and resolution that meets the requirements for the FT (see Sect. 6.2.3 and 6.3.3).

The tracking stations FT1 and FT2 are identical. The arrangement of the straw tube modules in vertical and inclined double layers in these stations is presented schematically in Fig. 3.9 a) and b), respectively. A double layer with vertical straws forms a rectangular active area which is 1338 mm wide and 640 mm high. A double layer with inclined straws covers fully a rectangle with the same height but with slightly smaller width of 1287 mm (see Fig. 3.9). These dimensions are sufficient to cover, with some excess, the angular acceptance of the FS ($\pm 10^\circ$ horizontally and $\pm 5^\circ$) which can be represented as an area with a width of 1207 mm and a height of 599 mm located at the position of the last double layer of the FT2 ($z = 3424$ mm). Each double layer consists of 10 modules. The modules numerated 1,2,3 and 8,9,10 in Fig. 3.9 have a standard width of 16 straws and the central modules, numerated 4,5,6,7, have a reduced width of 12 straws. At the position of FT1 and FT2, the beam pipe has an outer diameter of 102 mm and an opening for the beam pipe in the straw tube double layer is created by using two short modules - one above and the second below the beam pipe. The width of the opening equals 116.15 mm. It cor-

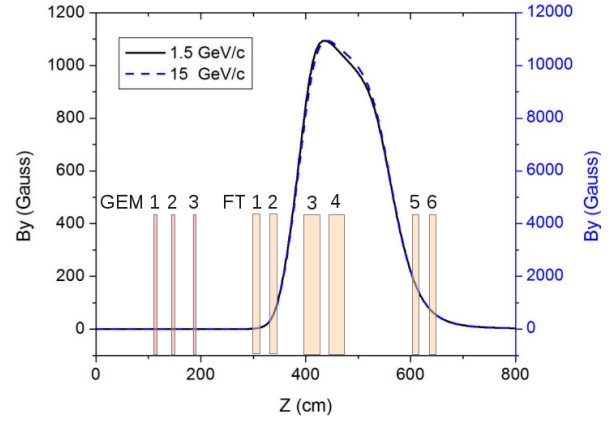


Figure 3.7: Positions of the planar GEM detectors and of the forward tracking stations along the beam line downstream of the target ($z = 0$). The GEM detectors cover polar angles larger than 3° and thus only partly overlap the acceptance of the FT. The solid and the dashed curves present the magnitude of the vertical component of the magnetic field calculated for the dipole magnet setting for $p_{beam} = 1.5$ GeV/c and 15 GeV/c, respectively.

responds to a width of 12 straw tubes in one layer (12×10.1 mm = 121.2 mm) reduced by a radius of the straw tube (5.05 mm) due to the staggering of the straws in the double layers. The height of the opening is fixed to 112 mm and it leaves a free space of 5 mm above and below the beam pipe as a safety margin for any misalignments of the beam pipe.

The tracking stations inside the dipole magnet gap - FT3 and FT4 - consist exclusively of standard "2x16" straw tube modules (see Fig. 3.10). Double layers in FT3 consist of 12 modules and in FT4 the number of modules is increased to 14 in order to accept the low momentum particles deflected in the magnetic field towards the side walls of the dipole magnet gap. Contrary to the tracking stations FT1 and FT2 which contain straw tubes double layers of equal height, FT3 and FT4 have vertical extension of the active areas which follows the $\pm 5^\circ$ vertical acceptance of the Forward Spectrometer. This is due to the fact that the vertical space for the detector frames foreseen in the dipole poles is limited to only 55 mm and it does not allow for any excesses in the active areas of the double layers. The central openings in FT3, FT4 have a width of 156.5 mm and a height of 114 mm which is sufficient for housing the beam pipe having a diameter of 104 mm.

Similarly to the FT1, FT2 pair, the stations FT5, FT6 have identical layout. Double layers in

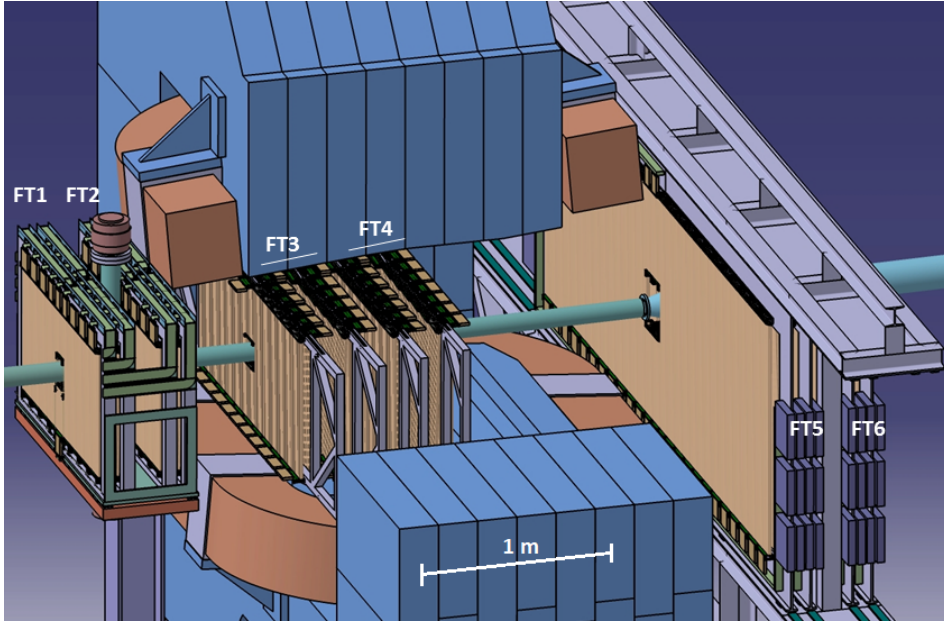


Figure 3.8: The dipole magnet shown in section and the FT stations.

these stations consist of 27 modules (see Fig. 3.11). A width of a double layer with vertical straws equals 3923 mm and exceeds by 823 mm a width of the dipole magnet aperture equal to 3100 mm. In this way most of the charged particles passing through the aperture are registered even in the case of a strong deflection in the magnetic field. An opening for the beam pipe in the double layer is created by means of two pairs of short modules located - one above and the other below the beam pipe. The modules in these pairs have a reduced width of 12 straw tubes and the resulting width of the opening is 237.35 mm. An additional module of a reduced width (number 12 in Fig. 3.11) is used in order to preserve the symmetry of the double layer with respect the z direction (symmetry corresponding to rotation by 180° around the z-axis). The center of the opening for the beam pipe is not located centrally in the double layers but is displaced horizontally to $x=+60.6$ mm in order to account for the bending of the beam pipe according to the deflection of the antiproton beam in the magnetic field of the dipole magnet. The beam pipe diameter at the position of the FT5 and FT6 equals 168 mm. At the position of the first double layer of the FT5 ($z=6075$ mm) and the last double layer of the FT6 ($z=6545$ mm) the center of the beam pipe is located at $x=+51$ mm and $x=+69$ mm, respectively.

The basic geometrical characteristics of the tracking stations are summarized in Table 3.1. The total number of the straw tube modules in all tracking

stations equals 400 and the number of straw tubes amounts to 12 224.

A table summarizing the key parameters of the Forward Tracker, allowing for comparison to other straw-based system, is presented in Table 3.2.

References

- [1] T. Johansson, AIP Conf. Proc. **796**, 95 (2005).
- [2] A. Capella et al., Phys. Rept. **236**, 225 (1994).
- [3] M. Bleicher et al., J. Phys. **G25**, 1859 (1999).
- [4] S. A. Bass et al., Prog. Part. Nucl. Phys. **41**, 225 (1998).
- [5] J. T. Brack et al., Nucl. Instrum. Methods **A469**, 47 (2001).
- [6] J. Smyrski et al., Nucl. Instrum. Methods **A541**, 574 (2005).
- [7] E. Abat et al., JINST **3**, P02014 (2008).
- [8] Y. V. Haarlem et al., arXiv:1004:3796v1 **A541**, 574 (2010).
- [9] P. R. Barbosa et al., CERN/LHCC/2001-024 (2001).

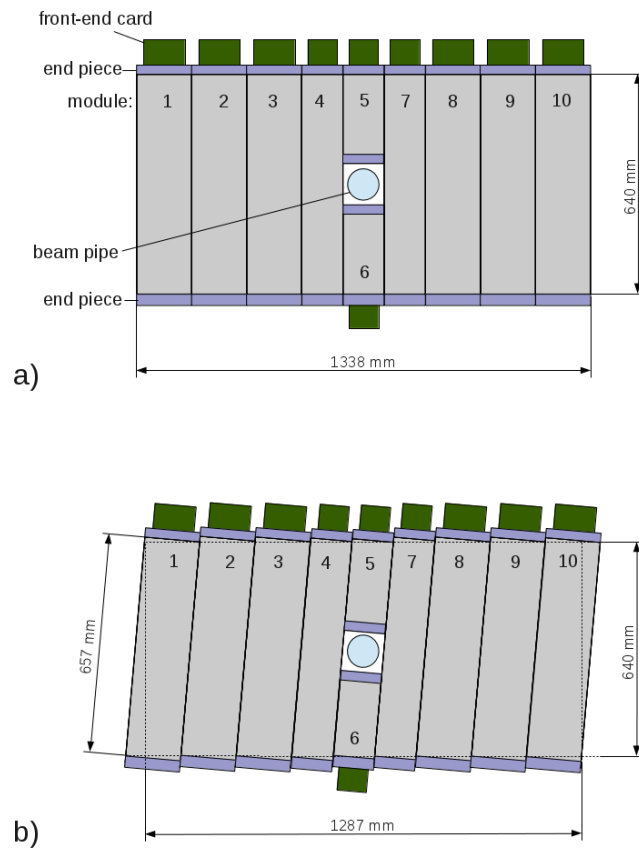


Figure 3.9: Arrangement of straw tube modules in double layers with vertical straws (a) and with straws inclined at 5° (b) for the tracking station FT1 and FT2. The central modules (4, 5, 6 and 7) have a reduced width corresponding to a double layer of 2x12 straw tubes and the remaining modules (1, 2, 3 and 8, 9, 10) have the standard width of 2x16 straw tubes.

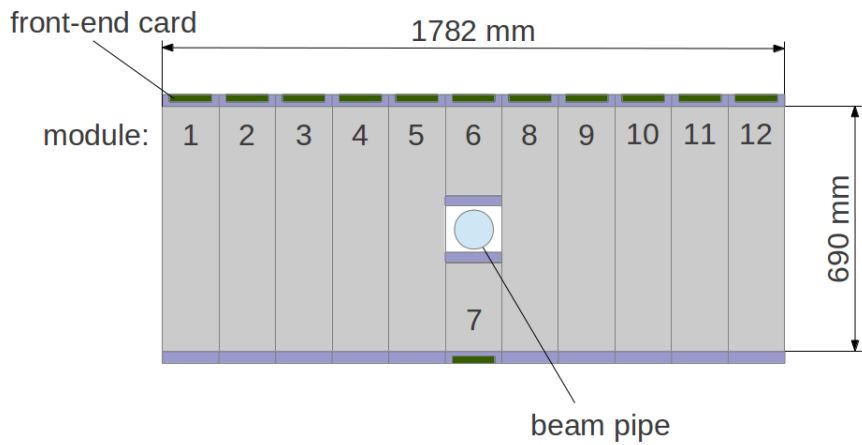


Figure 3.10: Arrangement of straw tube modules with vertical straws for FT3. The modules have a standard width of 2x16 straw tubes. The green rectangles represent the front-end electronics cards. They look different from those of Fig. 3.9 since the cards in FT3, FT4 are oriented horizontally, whereas in FT1, FT2 - vertically. The indicated vertical dimension of the active area (690 mm) corresponds to the first double layer of FT3.

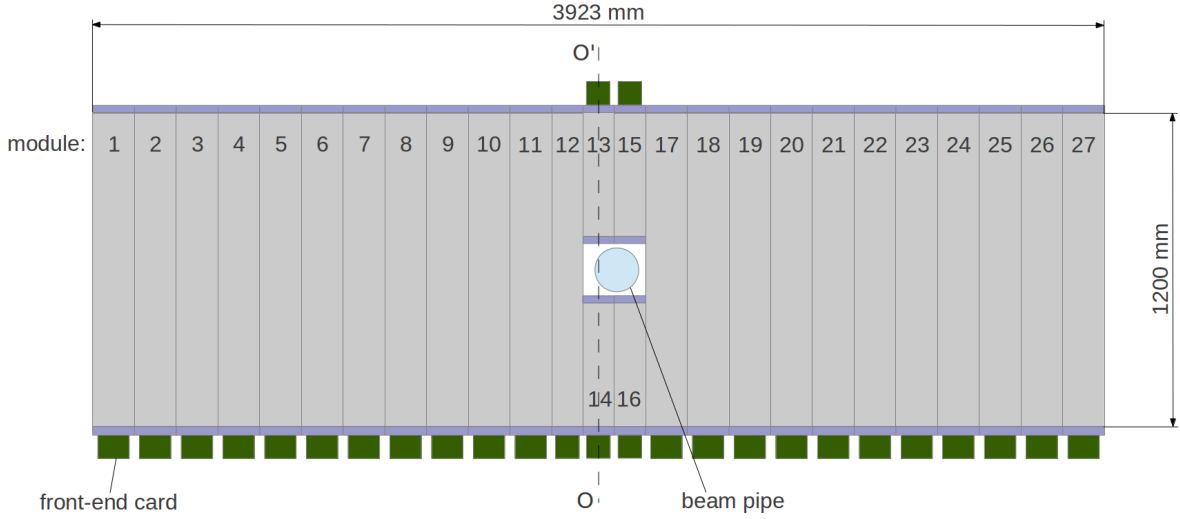


Figure 3.11: Arrangement of the straw tube modules with vertical straws of the tracking station FT5 and FT6. Five central modules (12, 13,..., 16) have a reduced width of 2x12 straw tubes and the remaining modules (1, 2,..., 11 and 17,...,27) have a standard width of 2x16 straw tubes. This arrangement is symmetric with respect to the vertical symmetry plane O-O' of the $\bar{P}ANDA$ detection system. Only the opening for the beam pipe is not symmetric with respect to O-O' due to the bending of the beam pipe according to the deflection of the antiproton beam in the magnetic field of the dipole magnet (2.2°).

Tracking station	$z_{min} - z_{max}$ [mm]	Active area		Number of modules	Number of straw tubes
		w [mm]	h [mm]		
1	2954-3104	1338	640	4x10=40	4x288=1152
2	3274-3424	1338	640	4x10=40	4x288=1152
3	3945-4245	1782	690	4x12=48	4x384=1536
4	4385-4685	2105	767	4x14=56	4x448=1792
5	6075-6225	3923	1200	4x27=108	4x824=3296
6	6395-6545	3923	1200	4x27=108	4x824=3296

Table 3.1: Positions, width and height of the active area, number of modules and number of straw tubes in the Forward Tracker stations. In the second column, z-coordinates of the first and the forth double layer are given. The indicated width and height of the active area correspond to the first double layer with vertical straws.

[10] V. N. Bychkov et al., Nucl. Instrum. Methods **A556**, 66 (2006).

[11] P. Wintz, A large tracking detector in vacuum consisting of self-supporting straw tubes, in *Intersections of Particle and Nuclear Physics: 8th Conference CIPANP2003*, volume 698 of *Issue 1*, pages 789–792, AIP Conf.Proc., (2004).

[12] K. Davkov et al., Nucl. Instrum. Methods **A584**, 285 (2008).

Straws	
Straw outer diameter	10.1 mm
Straw length	640-1250 mm
Straw wall	two layers of 12 μm Mylar
Straw metalization on the inner and outer diameter	1000 Å aluminum layer
Anode wire	20 μm gold-plated tungsten-rhenium
Drift gas	Ar:CO ₂ , 90:10
Gas pressure	2 bar
Material budget (straw+wire+gas)	$4.4 \times 10^{-4} \text{ X}/\text{X}_0$
Straw straightness (max. deviation from cylindrical shape)	0.5 mm
Maximum wire offset	0.05 mm
Working voltage	1800 V
Gas gain	$\sim 5 \cdot 10^4$
Maximum electron drift time with no magnetic field ($B = 0$)	140 ns
Maximum ion drift time	600 μs
Tracking stations	
Angular acceptance - horizontally	$\pm 10^\circ$
- vertically	$\pm 5^\circ$
Number of tracking stations	6
Active area of tracking stations	$1338 \times 640 \text{ mm}^2 - 3923 \times 1200 \text{ mm}^2$
Number of straw double-layers in tracking station	4
Inclination of straws in consecutive double layers in tracking station	$0^\circ, +5^\circ, -5^\circ, 0^\circ$
Total number of straws	12 224
Gas volume (straws only)	0.912 m ³
Operating conditions	
Total counting rate in the FT	up to $5 \cdot 10^7$ tracks/s
Maximum counting rate per straw	1400 kHz
Maximum particle flux	$25 \text{ kHz} \cdot \text{cm}^{-2}$
Maximum radiation dose in 10 years	5 krad
Maximum accumulated charge in 10 years	6.3 C/cm
Maximum current per straw	2.2 μA
Expected performance	
Discrimination threshold	$\sim 5 \text{ fC}$
Position resolution per straw	100-200 μm
Momentum resolution	$\sim 1\%$

Table 3.2: Key parameters of the Forward Tracker.

4 Technical Design

4.1 Straw Tube Detectors

4.1.1 Straw Tubes

For the Forward Tracker we adopted the self-supporting straw tube detectors which were developed for the COSY-TOF experiment [1] and which will also be used in the $\bar{\text{P}}\text{ANDA}$ Straw Tube Tracker [2]. In these straws, the applied gas overpressure of 1 bar provides their mechanical stiffness and maintains the anode wire tension. The straw tubes have 10 mm inner diameter, and a total wall thickness of 27 μm . They are made of two layers of 12 μm thick aluminized Mylar [3] films by wrapping two long film strips around a rotating mandrel and gluing the two half-overlapping strips together. Then the cylindrical film tube is stripped off. The aluminization at the inner tube wall is used as the cathode whereas the aluminization of the second, outer strip layer is used to prevent light incidence. A gold-plated tungsten-rhenium wire with 20 μm diameter is used as anode.

The wire tension depends only weakly on the gas overpressure as indicated by the result of our measurement presented in Fig. 4.1. Even in the absence of overpressure, the wire tension is about 43 g, and so is relatively large. For a quantitative description of this dependence, we calculated it with known values of the Young's modulus for the anode wire (41800 kg/mm² [4]) and for the Mylar film (418 kg/mm² [5]). Details of the calculations are described in Appendix A. The dashed line in Fig. 4.1 presents the result of the calculation with a typical value of the Poisson's ratio for Mylar equal 0.38 according to ref. [6]. An almost perfect description of the data points is obtained with a slightly lower value of the Poisson's ratio of 0.356 (see the solid line in Fig. 4.1).

Table 4.1 lists the different straw components and their thickness in radiation lengths. The chosen film tubes are the thinnest used for straw detectors, but still show sufficient mechanical stability for the assembly to self-supporting double-layers. For the proposed $\bar{\text{P}}\text{ANDA}$ FT consisting of six tracking stations, each comprising four double layers of straw tubes, the total radiation length of the straw volume is 2.1% X_0 .

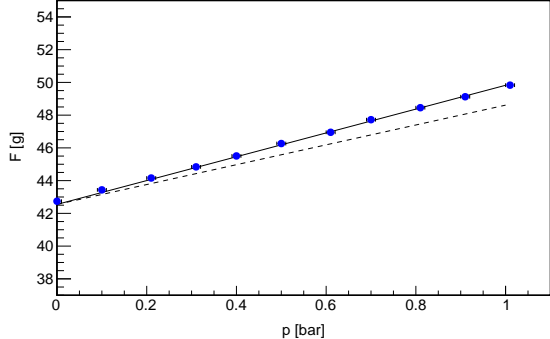


Figure 4.1: Wire tension (weight equivalent) as a function of gas overpressure. Full points represent measurement results and lines correspond to the calculations described in text.

4.1.2 Gas Mixture

The main requirements, that should be taken into account for the choice of the most suited gas mixture, are:

- good spatial resolution,
- rate capability,
- radiation hardness,
- radiation length,
- chemical inactivity,
- working voltage,
- working pressure,
- accessibility on the market and price.

For the $\bar{\text{P}}\text{ANDA}$ FT the rate capability and the radiation hardness are the most critical points and require a gas mixture with a low aging rate and a short electron drift time. For use in high radiation applications, only few gases are suited and these are noble gases, CO₂ and CF₄ [7]. For the FT straw tubes, we exclude CF₄ due to the enhanced aging observed in combination with aluminum cathode [8]. A natural choice for the FT is argon as a basic component due to its low cost and CO₂ as a quencher. We choose a mixture with a low CO₂ concentration of 10% since higher concentrations result in a longer electron drift time (see Sec. 6.1.2).

Table 4.1: Mean thickness in radiation lengths of the different straw tube components. The number for the gas mixture is evaluated at temperature of 20° and a pressure of 2 atm.

Element	Material	X[mm]	X ₀ [cm]	X/X ₀
Film Tube	Mylar, 27 μm	0.085	28.7	3.0×10 ⁻⁴
Coating	Al, 2×0.1 μm	6×10 ⁻⁴	8.9	6.7×10 ⁻⁶
Gas	Ar/CO ₂ (10 %)	7.85	6131	1.3×10 ⁻⁴
Wire	W/Re, 20 μm	3×10 ⁻⁵	0.35	8.6×10 ⁻⁶
			\sum_{straw}	4.4×10 ⁻⁴

4.1.3 End-plugs

End-plugs in the self-supporting straw tube detectors have to fulfill the following functions:

- tightly close the gas volume in the straws,
- provide gas connection to the straws,
- provide electrical contact with the inner surface of the straw acting as a cathode,
- position the anode wire on the straw axis and hold its mechanical tension,
- provide electrical contact with the anode wire and electrically isolate it from the cathode.

Due to the diversity of the listed functions, the appropriate design of end-plugs is crucial for the reliability of the straw detectors. It is also decisive for an easy assembly of the straw detectors.

The mounting of the end-plugs, which are used in the COSY-TOF as well as $\bar{\text{P}}\text{ANDA}$ STT straws, demands high manual skills and extends production times. This could make difficult to maintain the required high quality of assembly during the production of a large number of straws needed for the FT (more than 12 000). Therefore, we developed a new end-plug which allows an easy assembly of the straw detectors. In our design, for positioning and holding of the anode wire, we use a wire locator with a V-groove and a small printed circuit board (PCB) for soldering the wire, instead of the crimp pin applied in the other design. Besides, for providing the electric cathode contact, we use an aluminum ring glued inside the straw with an electrically conductive adhesive. This substitutes the contact spring inserted in small overlap at both ends of the COSY-TOF and STT straws. The use of the aluminum ring provides more solid cathode contact than the spring since it allows to avoid possible corrosion of the inner aluminum layer in the straw at the point

of contact with the spring and its mechanical damage by the spring during the course of increasing or decreasing the gas pressure in the straw.

The end-plug for the FT straws is presented in cross-section in Fig. 4.2. It consists of the following elements, which are also shown in Fig. 4.3:

- Cylindrical plastic bushing constituting the basic mechanical element of the end-plug. It has a form of a cup with a nose. The cup, having an outer diameter of 10 mm, is glued into the straw and the nose, with an outer diameter of 7 mm, is used for positioning the straw. A groove in the nose is used for holding and stretching the straw during tensioning of the anode wire.
- Aluminum ring for grounding the aluminized inner surface of the straw.
- Wire locator having a cylindrical shape with a V-groove for positioning the anode wire on the axis of the straw and a PCB for soldering the anode wire. The wire locator is inserted in $\phi = 5$ mm opening in the plastic bushing.
- Plastic plug fitting into the V-groove in the wire locator. A steel capillary tube with attached micro PVC (medical quality grade) pipe [9] is fed through a hole in the plug to provide a gas flow through the tube. The capillary tube has an outer diameter of 0.55 mm, the wall thickness of 0.09 mm and a length of 10 mm. The micro PVC tube has an inner/outer diameter of 0.5/0.8 mm.

The bushing, the wire locator and the plug are made from ABS [10] by injection molding.

The assembly of the straws proceeds in the following three steps, which are conducted on separate stands using dedicated tooling:

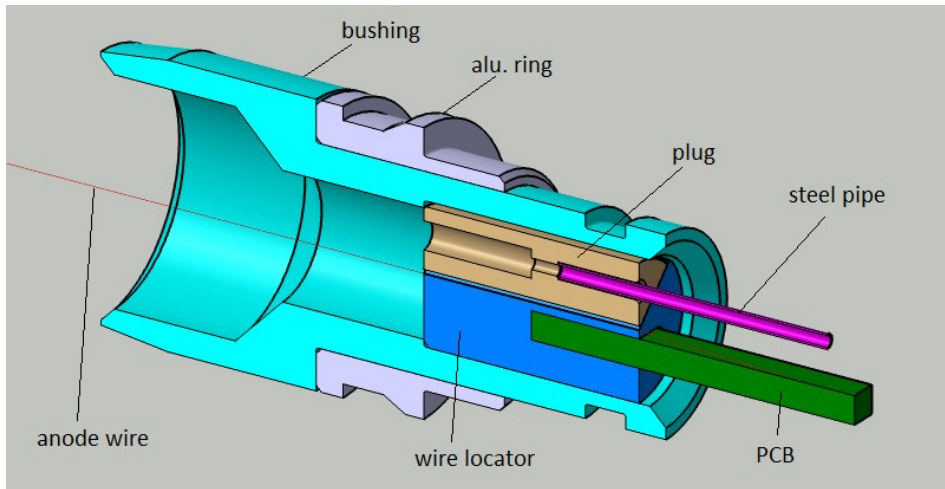


Figure 4.2: Sectional drawing of assembled end-plug.

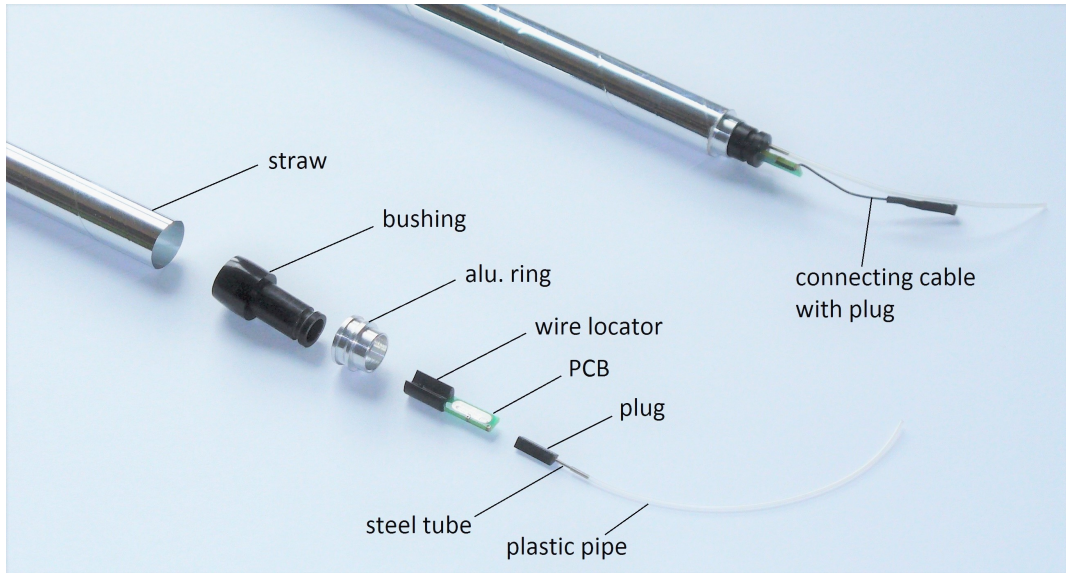


Figure 4.3: Components of end-plug (lower left) and assembled end-plug with attached connecting cable with plug (upper right).

- Gluing the plastic bushings and the aluminum rings in the straws.
- Tensioning the anode wires.
- Inserting the plugs in the V-grooves in the wire locators and sealing them with adhesive.

The plastic bushings are glued in the straws at both ends using a 2-component epoxy resin adhesive (UHU endfest 300 [11]) ensuring gas tightness. The aluminum rings are applied for grounding the inner aluminized surface of the straw only at one end of the straw, where the readout electronics is attached.

In order to ensure durability of the electrical contact between the ring and the inner straw surface, an electrically conductive adhesive (MG Chemicals 8331S [12]) is used.

For applying the two-component epoxy adhesive inside the straw in a reproducible manner, especially the amount of the adhesive, and to control the distance from the edge of the straw tube, a device shown in Fig. 4.4 was constructed. In this device, the straw is held by air under-pressure and is rotated around the symmetry axis at a predetermined speed. The adhesive is dispensed inside the straw, at the required distance from the edge, using a glue

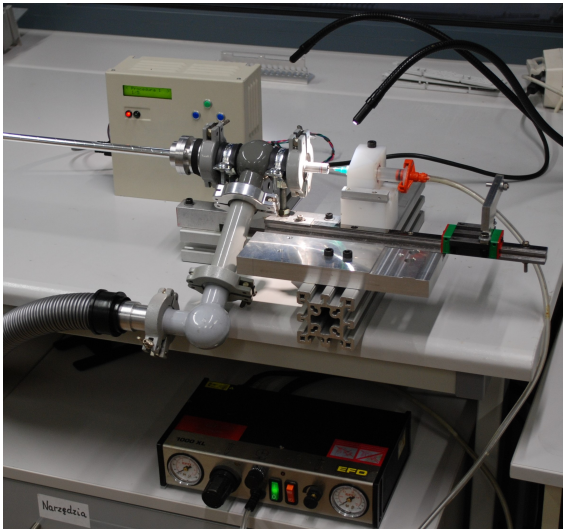


Figure 4.4: Setup for dispensing adhesive inside straws.

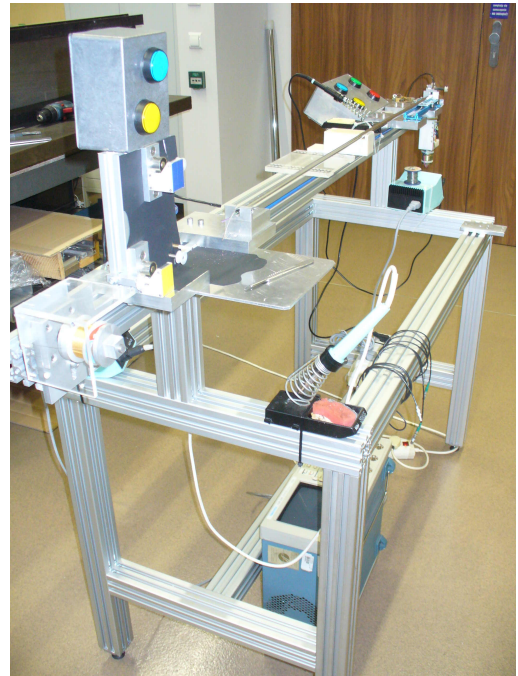


Figure 4.5: Stand for tensioning anode wires in straws.

dispenser machine. The electrically conductive adhesive is applied on the perimeter of the aluminum ring by a rubber wheel covered with the adhesive and rolling around the ring. After that, the bushing with the ring is inserted inside the straw.

Tensioning of the anode wire in the straw tube is performed on a stand shown in Fig. 4.5. The straw with plastic bushings glued on both ends is held on the stand by means of two grips inserted in the grooves in the noses of the bushings. The straw is tensioned by applying an appropriate force to one of the grips and locking the other. The force is chosen in such a way that the elongation of the straw is the same as that caused by the overpressure of 1 bar of the working gas. For the 125 cm long straws of the FT5, FT6 stations, the force equals 160 g. It is worth noting, that due to the Poisson's effect, this force is smaller than the axial force exerted by the gas overpressure of $p = 1$ bar acting on the surface of the end-plug ($S = \pi r^2 \approx 0.785 \text{ cm}^2$, $r = 0.5 \text{ cm}$) equal to $p \cdot S \approx 801 \text{ g}$.

After tensioning the straw, the wire is threaded through the straw using a carbon fiber rod with a notch to hold the wire. The operation of pulling the rod through the straw is very easy due to the relatively large diameter of the inner opening in the plastic bushings (5 mm) and the funnel shape of the bushing on the inner side of the straw. The wire is then blocked at one end and tensioned at the other by a weight of 50 g. After that, the wire locators are inserted in the $\phi = 5 \text{ mm}$ opening in the plastic bushings at both ends and the wire is soldered to the PCBs attached to the wire locators. Finally,

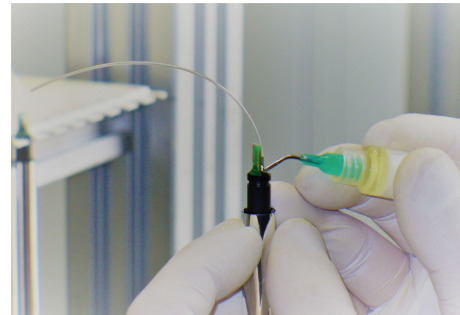


Figure 4.6: Sealing of plugs with adhesive.

the excess of wire is cut off with a sharp knife.

In the last step of the straw assembly, the plugs with steel tubes and plastic pipes are inserted in the V-groove in the wire locators and are sealed with adhesive (UHU endfest 300 [11]) as shown in Fig. 4.6.

Each of the produced straws is tested for gas leakage and correct wire tension (see Sec. 4.8). Tubes showing deviations from the nominal 50 g wire tension larger than 5 g or gas leakage exceeding $\Delta p/p/t = 0.2\%/\text{h}$ are rejected.

Mechanical properties of the materials used in the straw detectors may change due to high radiation doses. Fig. 4.7 presents a map of radiation doses, expected in the PANDA Forward Spectrometer for

one year of operation of the $\bar{P}ANDA$ experiment, with a half-year period of data taking in the high luminosity mode and with the 15 GeV/c antiproton beam [13]. The map was calculated using simulations in the PandaRoot framework [14] with the DPM event generator [15], and with realistic detector geometry and materials. In the FT1, FT2 stations, in the vicinity of the beam pipe, being the hottest region in the Forward Tracker, the absorbed dose is about 5 Gy/year. In ten years of the experiment lifetime, the expected dose is 50 Gy (5 krad). This dose is roughly two orders of magnitude smaller than the level of a few hundred krad, at which mechanical properties of various materials such as e.g. epoxy resins change in a significant way due to the radiation dose (see, for example, Refs. [16, 17]). Therefore we conclude, that the radiation doses expected in the Forward Tracker can be neglected, when considering the mechanical properties of the applied materials.

Selection of materials for the construction of the straw detectors, characterized by low outgassing properties, is very important for minimizing the aging effects in the straws expected at high accumulated charges. Table 4.2 presents a list of materials in contact with the gas mixture in our straw detectors, outgassing properties of these materials and other experiments/detectors in which they were used in straws. We don't have data on outgassing for all the materials used in particular for the 2-component epoxy adhesive UHU endfest 300 and for the medical grade PVC pipes. The aging tests, presented in Sec. 5.3, indicate, that the applied materials are acceptable for the FT straws, taking into account the expected accumulated charges on the level of 1 C/cm.

4.2 Straw Tube Modules

4.2.1 Assembly of Straw Modules

In the tracking stations, the straw tube detectors are grouped into modules constituting independent mechanical and electrical units. Assembly of the straw tube module is performed on a reference grooved plate, which defines precisely tube to tube distance of 10.1 mm. First, a series of 16 straws is placed on the plate and the end-plugs with the aluminum rings are inserted in openings in an aluminum bracket at the side for the FEE (see Fig. 4.8). To ensure the durability of the electrical contact between the rings and the bracket, an electrically conductive adhesive (MG Chemicals 8331S [12]) is applied. Then the straws are con-

nected to a gas supply and pressurized to the nominal overpressure of 1 bar. The individual tubes are aligned with high precision also from the top by smaller reference plates (see Fig. 4.9). Then, each tube is glued to the two adjacent ones at several defined points along its length. The glue used here is an instant cyanoacrylate adhesive (Loctite 408 [20]). After that, a second layer of straws is precisely positioned on top of the first one. Their aluminum rings are inserted and glued with the conductive glue to the bracket, and after the straws are pressurized to the nominal overpressure, the single tubes are glued to the adjacent ones in the same layer and in the lower one.

4.2.2 Module Description

The module consists of a planar double layer of 32 straw tube detectors supported by two end-pieces (see Fig. 4.10). Connections of the straws to the front-end electronics (FEE) cards and to the high voltage (HV) supply are made in one end-piece, whereas the gas mixture is supplied to the straws through the other.

The end-piece on the FEE side is shown in Fig. 4.11. It consists of an aluminum bracket with an attached PCB needed for connecting the straws to the HV supply and the FEE cards. The bracket contains two rows of $\phi = 8$ mm openings in which the straw end-plugs with aluminum rings are inserted to provide electrical contact between the rings (and thus also the cathodes) and the bracket. One side of the PCB, fully coated with copper, contacts the bracket and serves as a common ground for the straws (cathodes) as well as for the FEE and the high voltage supply.

The connection between the anode wires and the PCB is done with ≈ 2 cm long isolated cable with miniature plugs which are fitted onto pins soldered to the PCB.

The PCB contains a pair of connectors for two 16-channel FEE cards. The connection of the straws to the HV supply and to the FEE is done as shown in the circuit diagram presented in Fig. 4.12. In this diagram, resistor $R_1 = 10\text{ k}\Omega$ and capacitor $C_1 = 1\text{ nF}$ are used as a low pass filter to filter out noise coming from the HV supply. The filter is one common for the 32 straws in the module. The resistor $R_2 = 1\text{ M}\Omega$ limiting the short circuit current to 2 mA at a voltage of 2000 V, and the decoupling capacitor $C_2 = 0.3\text{ nF}$ are separate for each straw.

The end-piece on the gas supply side consists of

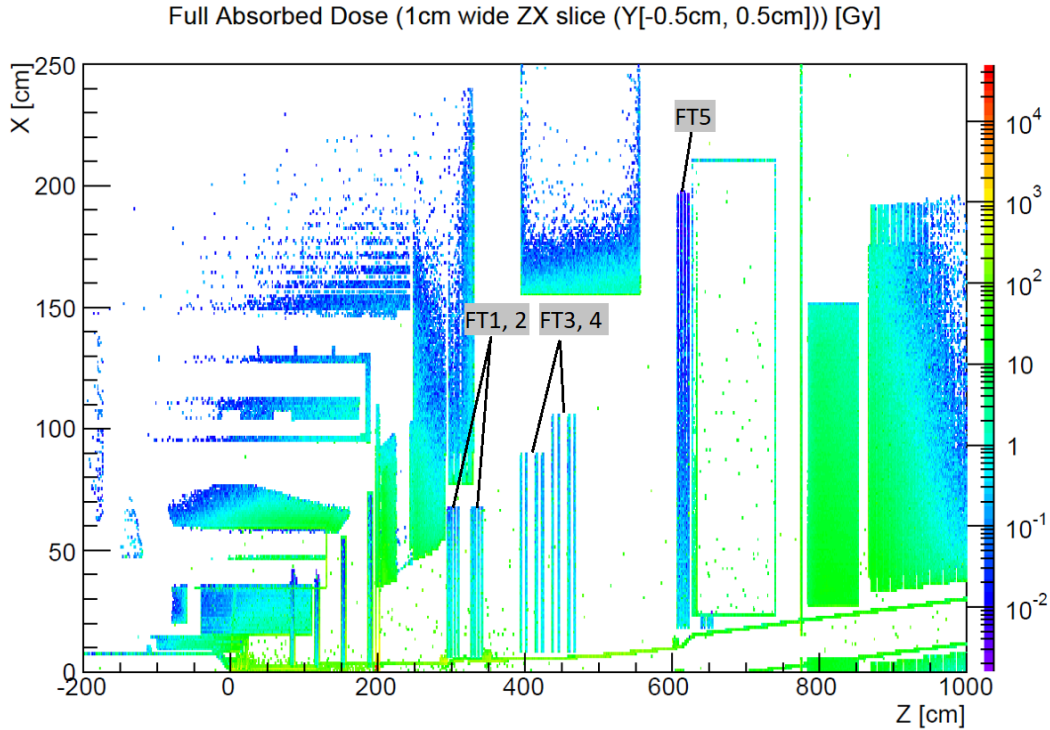


Figure 4.7: Full absorbed dose in 1 cm wide zx slice ($y \in [-0.5 \text{ cm}, 0.5 \text{ cm}]$) of the Forward Spectrometer, calculated for one year of the nominal operation of $\bar{\text{P}}\text{ANDA}$ (net half a year of data taking) in the high luminosity mode and with the 15 GeV/c antiproton beam. In the picture, indicated are tracking stations FT1..FT5.

Material	Outgassing properties	Other experiments
Aluminized Mylar (straw tubes)		FINUDA, COSY-TOF, PANDA-STT
ABS plastic (end-plugs)	For various types of ABS listed in [18] TML ranges from 0.33 to 1.13 and CVCM from 0.01 to 0.16	FINUDA, GLUEX, COSY-TOF, PANDA-STT
2-component epoxy adhesive UHU endfest 300		COSY-TOF, PANDA STT
PVC pipe medical quality grade, contains TEHTM plasticizer (no DOP)		COSY-TOF, PANDA STT
Stainless steel capillary tube	no outgassing	standard use in gas detectors worldwide
Aluminum alloy PA6 (gas manifold)		
Polyamide pipe (gas supply)	Result on detector OK according PH-DT-DI Gas Project [19]	

Table 4.2: List of materials in contact with gas mixture, outgassing properties and other experiments/detectors using these materials in straws detectors.

an aluminum bracket with attached gas inlet and outlet manifold (see Fig. 4.13). The inlet manifold

distributes the gas mixture from the supply line to 16 gas circuits, each consisting of two straw tubes



Figure 4.8: Single layer of 16 straw tubes placed on a reference grooved plate.

connected in series. The gas mixture flows from this manifold through one layer of straws to the opposite end of the module and returns through the second layer, where the outlet manifold collects it and leads it to the exhaust line. Connection between straw tubes in each pair is done at the FEE side of the module by coupling the PVC gas pipes connected to the end plugs with a help of 10 mm long and 0.55 mm in outer diameter steel capillaries. The same tubes are used for connecting the straw tubes to the gas manifolds. For connecting the manifolds to the gas supply and exhaust line, $\phi = 4$ mm outer diameter polyamide pipes are used. The $\phi = 7$ mm noses of the end-plugs are inserted in openings in the aluminum bracket and can freely slide in the openings. This allows undisturbed elongation of the straw tubes when the gas pressure in the straws is increased to the working value of 2 bars. This elongation equals 0.6 mm for 1.25 m long straw tubes in the FT5 and FT6 tracking stations.

In the prototype modules, for connecting the gas inlet and outlet manifold to the gas supply lines we used push-in fittings produced by Parker-Legris [21]. These fittings allowed fast gas connections, which was important in the prototyping



Figure 4.9: Gluing of straw tubes to double layer.

phase. However, they contain o-rings made of Buna Nitrile rubber, which, due to out-gassing properties, can cause accelerated aging of the straws. Therefore, in the modules produced for the FT we plan to use the Serto [22] fittings containing only stainless steel parts.

The modules show a strong rigidity when the straws are pressurized to the nominal overpressure of 1 bar. No stretching from a mechanical frame to sustain the wire tension or reinforcements for the tube shape are needed. Due to the high overpressure the thin-wall tubes have a cylindrical shape and the modules are self-supporting.

4.2.3 Layer Arrangement

Straw modules closely arranged next to each other and mounted on a support frame form a double layer of straw tube detectors. One frame is used for two double layers attached on its both sides. Thanks to the appropriate shape of the end-pieces, each module can be mounted and dismounted from the support frame without the need to remove neighboring modules. This allows for fast repair and/or replacement of the modules suffering from aging effects or broken straws during the detector lifetime. The number of modules in one double layer and the length of the straw tubes in the modules

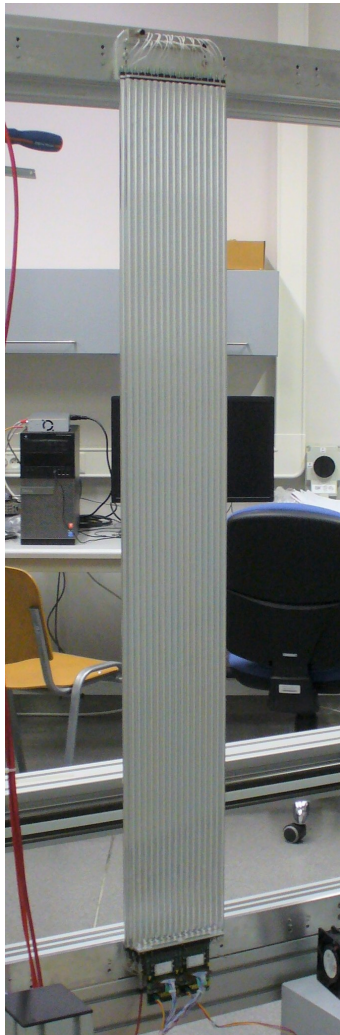


Figure 4.10: Straw tube module for the FT5, FT6 tracking stations. The FEE cards are connected to the module in the lower end-piece and the upper end-piece contains the gas manifold with gas inlet and outlet connector.

are adapted to the dimensions of the active area in a tracking station. The number of modules in one double layer ranges from 10 in the tracking stations FT1, FT2 to 27 in the stations FT5, FT6.

4.2.4 Precision of Positioning Anode Wires

Expected precision of positioning the anode wires with respect to the support structure of the tracking station is determined by the following factors:

- Precision of position the anode wire with respect to the straw by means of the wire locator

Positioning of	Precision along	
	x-axis	z-axis
wires in straws	0.05 mm	0.02 mm
straws in modules	0.05 mm	0.05 mm
modules on frame	0.05 mm	0.02 mm
frame on support	0.1 mm	0.1 mm

Table 4.3: Expected precision of relative positioning of mechanical elements determining the positioning precision of the anode wires with respect to the support frame of the tracking station.

with the V-groove.

- Precision of positioning the straws with respect to the end-pieces dominated by the mechanical tolerance of the openings for the end-plugs in the end-pieces.
- Accuracy of positioning the end pieces with respect to the frame using the dowel pins (x-direction), and the precision of machining of the end-pieces (z-direction).
- The accuracy of mounting the rails for the frame on the support structure.

The values of these contributions to the positioning precision of the anode wires are given in Table 4.3

4.2.5 The Grounding Scheme

The grounding scheme of the straws has a single point structure and is made according the following assumptions:

- Each frame supporting the modules is made of aluminum and is isolated from the support structure of the corresponding tracking station. The ground of the straw tubes and the FEE cards in a module, defined by the aluminum bracket with the FEE, is electrically connected to the frame. Thus, the frame constitutes a ground reference point for the modules mounted on it.
- Each aluminum frame supporting the modules is connected to the safety ground.
- For the high voltage supply and low voltage supply of the FEE cards we use supplies with floating outputs.
- The ground of the FEE cards (the aluminum frame supporting modules) and the ground of

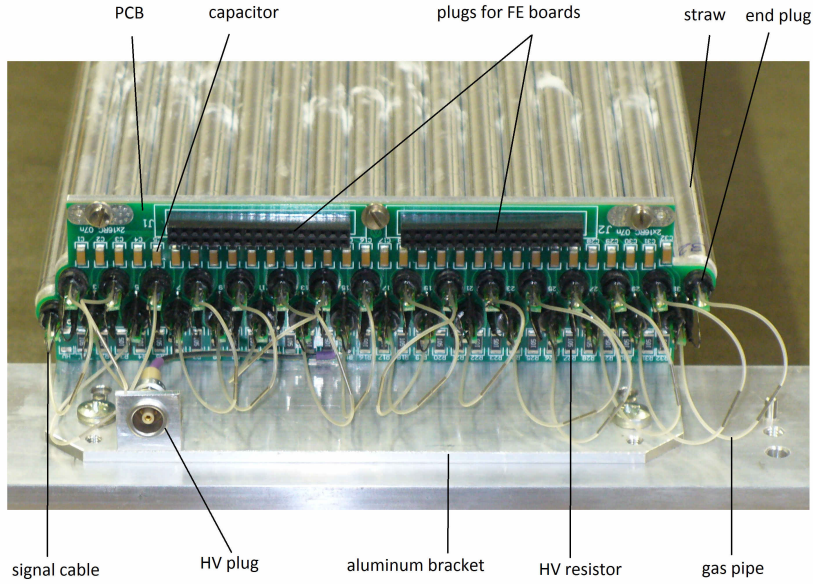


Figure 4.11: View of the end-piece for connecting the FEE cards to the module.

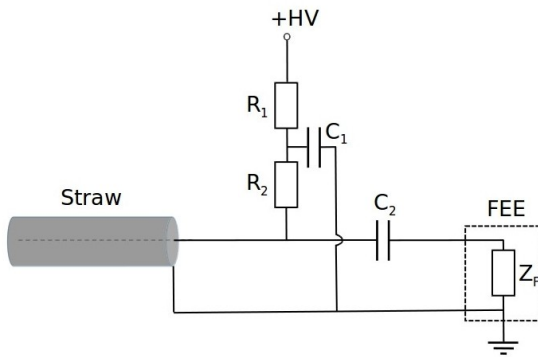


Figure 4.12: Scheme of connecting the straw to the HV supply and to the FEE.

the digitizing electronics are separated, since we use the differential LVDS signal connections.

are identical. Each one comprises four double layers composed of straw tube modules which are mounted on two rectangular aluminum frames. One frame supports on one side modules oriented vertically (0°) and modules inclined at $+5^\circ$ on the other side. The second frame is identical but is rotated by 180° around the vertical axis. In this way, the inclination of straw tube modules in consecutive double layers of one tracking station is $0^\circ, +5^\circ, -5^\circ, 0^\circ$. The distance of successive double layers is 5 cm.

Modules are mounted on a frame with the FEE cards placed along the upper arm of the frame and the gas manifolds arranged along the lower arm. Only the short modules coming below the beam pipe are mounted in reversed orientation with the gas manifold placed in the vicinity of the beam pipe and the FEE cards located at the lower arm of the frame. In this way the FEE cards are exposed to smaller radiation doses and the amount of material in the vicinity of the beam pipe is smaller.

The positions of the straw tube modules mounted on the frames are defined by means of trapezoidal cutouts machined in the frames which fit the corresponding elements in the aluminum end-pieces of the modules. The positioning accuracy of the modules with respect to the frame is better than 0.05 mm. The fixation of each module on the frame is secured by means of two pairs of screws. A view of a double layer with vertical straw tube modules mounted on the support frame is shown in Fig. 4.14.

4.3 Tracking Stations before the Dipole Magnet

4.3.1 Support Frames

The first pair of tracking stations (FT1, FT2) will be installed in the space between the Target Spectrometer (TS) forward door and the yoke of the dipole magnet. The tracking stations FT1 and FT2



Figure 4.13: View of the end-piece with the gas manifold.

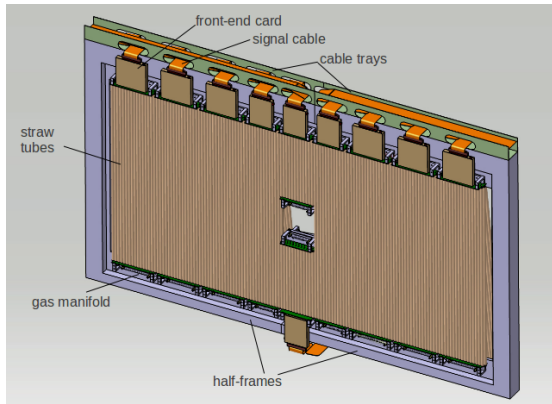


Figure 4.14: Double layer with vertical straw tube modules mounted on the rectangular support frame.

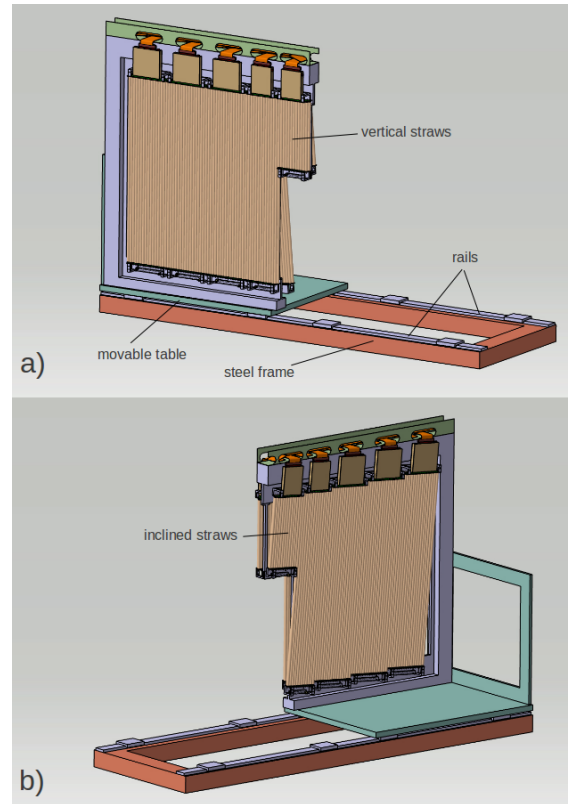


Figure 4.15: View of a half frame from the side with vertical straws (a) and from the side with inclined straws (b). The frame is mounted on a horizontal platform which is described in the text.

Each of the rectangular support frames consists of two half-frames having "C" shape. This solution allows to split the tracking stations into two parts - the left and the right one with respect to the beam direction - which is necessary for their installation on the beam line. A view of the half frame with straw tube modules is shown in Fig. 4.15.

The ends of the two horizontal arms of each half-frame are connected by means of two vertical bars linked by a horizontal bar (see Fig. 4.16). The bars have a rectangular cross section and are made of ABS plastic. The horizontal bars are also used to fix the free ends of the two short modules.

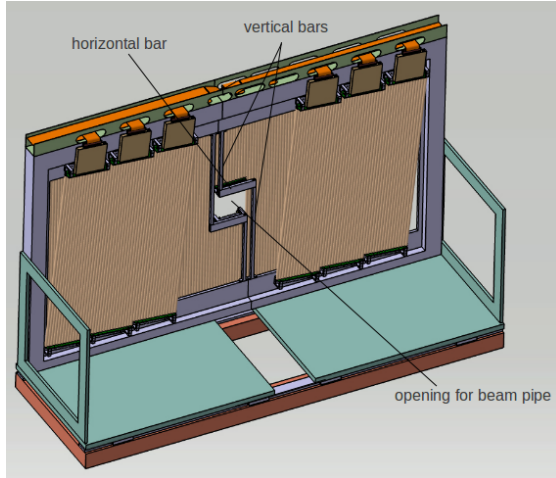


Figure 4.16: Support frame with straw tube modules. The most central modules in the double layer with inclined straws are removed in order to show the plastic bars which connect the arms of the half-frames and are used to create openings in the detection planes for the beam pipe.

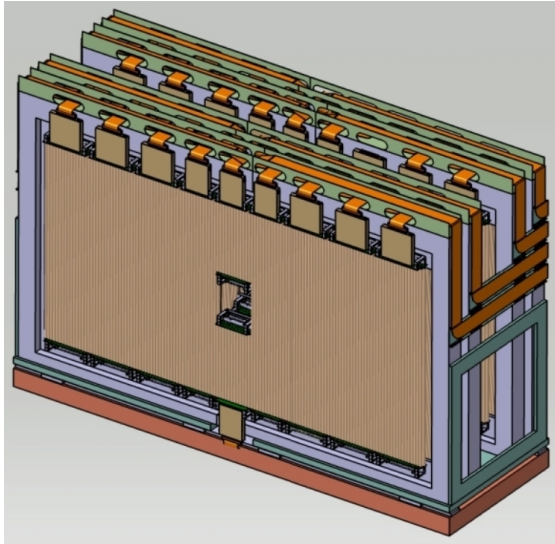


Figure 4.17: Tracking stations FT1, FT2 mounted on the common platform.

4.3.2 Platform with Movable Tables

For supporting tracking stations FT1, FT2 in their working place, a common platform will be used. It consists of a rectangular frame made of steel profiles which is attached to the dipole magnet, and of two aluminum tables independently movable left-right on linear bearings sliding along two parallel rails fixed to the frame. The half-frames with modules are mounted on the two tables (see Fig. 4.15). The position of each half-frame with respect to the table is defined by two dowel pins. To guarantee perpendicularity between the frames and the tables, two rectangular elements are mounted on the left and right side of the frames. The positioning accuracy of the half-frames with respect to the table is better than 0.1 mm in all directions

The two tracking stations mounted on the common platform are shown in Fig. 4.17 and a side view of the stations is presented in Fig. 4.18. The total extension of each station along the z-direction is 20 cm. The spacing between geometrical centers of the stations is 32 cm which leaves a 12 cm gap between them. The full setup of the tracking stations, including the platform and the cable trays, fits in a rectangular opening in the Forward Muon Filter having a width $x = \pm 770$ mm and a height $y = \pm 520$ mm, with 5 mm tolerance at each side.

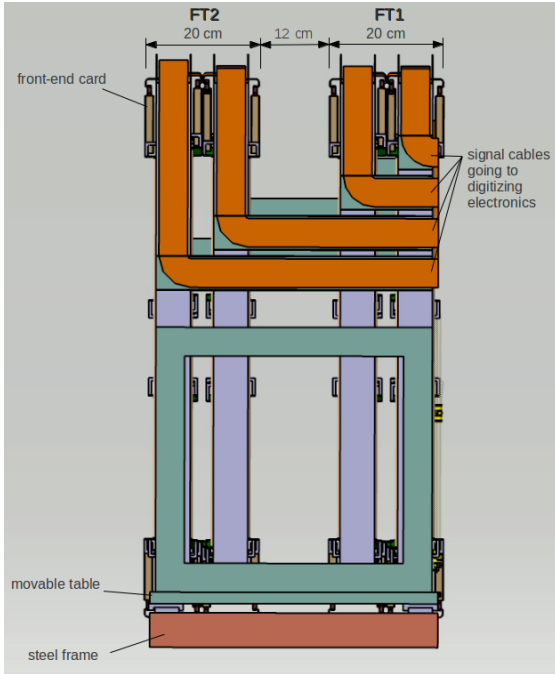


Figure 4.18: Side view of the tracking stations FT1, FT2.

4.3.3 Supply Lines

Signal cables from the FEE cards are led in cable trays mounted on the top of each C-shaped frame (see Fig. 4.14). The trays are also used for placing high voltage supply cables and low voltage power supply cables for the FEE cards. Two gas supply

lines for the straw tube modules and two exhaust lines are attached on both sides of the bottom arm of each frame. Proper connectors allow to disconnect easily the cables and gas supply lines from the module, and the module itself, if necessary, can be dismounted from the frame.

4.3.4 Installation

During the installation of the tracking stations, the TS downstream door and the two halves of the Forward Muon Filter have to be opened. In the first step, the steel frame with two movable tables has to be fixed to the dipole magnet yoke. After this, individual half-frames with modules can be placed on the tables and secured with screws. Next, the tables with half-frames will be moved towards the beam line to the defined position in which the left and right halves of double layers are joined and the beam line passes through the centers of the double layers. Afterwards, the cables will be placed in the trays mounted on the top and the gas pipes will be connected to the gas distribution system. Finally, the two halves of the Forward Muon Filter surrounding the stations and the TS downstream door can be closed.

To access the stations for a repair, the Forward Muon Filter has to be opened. The movable table with a half-frame containing a broken module has to be retracted from the beam pipe. The cables and gas pipes have to be disconnected from the half frame containing the broken module and the half-frame has to be removed from the table. The module can be then dismounted from the frame and repaired or replaced with a new one and the procedure can be completed analogously to the installation of the tracking station.

For moving the Target Spectrometer from the experimental hall to the parking position, the TS downstream door and the Forward Muon Filter have to be opened. Next, the two movable tables with FT1 and FT2 half-frames have to be drawn aside creating access to the flange connection of the beam line at the position between the TS downstream door and the Forward Muon Filter. Opening of this connection is necessary for relocation of the TS.

4.4 Tracking Stations inside the Dipole Magnet Gap

4.4.1 Space Available for the Tracking Stations

The tracking stations FT3, FT4 are placed between the poles of the $\bar{\text{P}}\text{ANDA}$ dipole magnet. The width of the magnet aperture equals 3.1 m and is larger respectively by 1.3 m and 1.0 m than the horizontal extension of the active area of the FT3 and the FT4 station. This leaves sufficient space for the mechanical support structures.

In the vertical direction the magnet aperture opens according the $\pm 5^\circ$ vertical acceptance of the FT from 0.80 m to 0.98 m. For detector frames and other passive elements, cutouts of $\Delta y = 5.5$ cm in the upper and lower pole of the magnet is foreseen (see Fig. 4.19). A relatively small depth of the cutouts is dictated by the necessity to limit the magnet cost and the operating cost which strongly depend on a distance between the magnet poles.

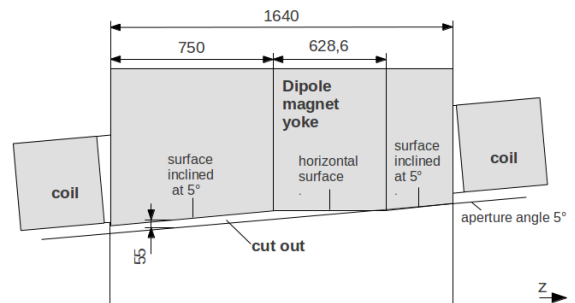


Figure 4.19: Sketch of the pole shoe geometry in the z-y plane with indicated the cutout for the detector frames. The vertical dimension of the cutout is 55 mm.

4.4.2 Support Frames with Straw Tube Modules

Due to a limited space in vertical direction, FEE cards in FT3 and FT4 are oriented horizontally while in the stations FT1, FT2, FT5, FT6, they are oriented vertically. A schematic view of a straw tube module designed for the tracking stations FT3 and FT4 is shown in Fig. 4.20. To create space in the horizontal direction for the FEE cards, the spacing between the two frames in one tracking station is increased to 20 cm with respect to 10 cm in FT1, FT2 and FT5, FT6 stations.

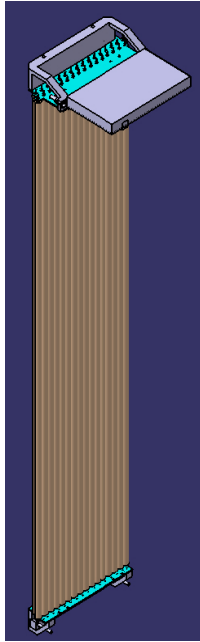


Figure 4.20: Straw tube module for tracking stations FT3, FT4.

Support frames for the modules in tracking stations FT3, FT4 have a rectangular shape and are made of aluminum profiles with square cross section (40 mm x 40 mm) (see Fig. 4.21 a). For each station two frames are used. They have the same width of 2876 mm and the height depends on the location of the frame inside the magnet gap. It ranges from 785 mm, for the first frame in FT3, to 905 mm, for the second frame in FT4. The modules are attached at both ends to the horizontal bars in the frames. For a precise positioning of the modules, the bars contain trapezoidal cutouts which fit with the corresponding elements in the aluminum end-pieces of the modules.

Each support frame contains in the center a square element made of ABS plastic, attached to the frame with two vertical beams. This element surrounds the beam pipe and is used to fix the ends of two short modules mounted above and below the beam pipe, respectively. One frame is used for supporting two double layers of straw tubes mounted on opposite sides as it is shown in Fig. 4.21 b).

4.4.3 Base Frame

The rectangular support frames, with straw tube double layers, will be mounted on a base frame, having a trapezoidal shape, fitting the aperture of the magnet. A side view of the tracking stations

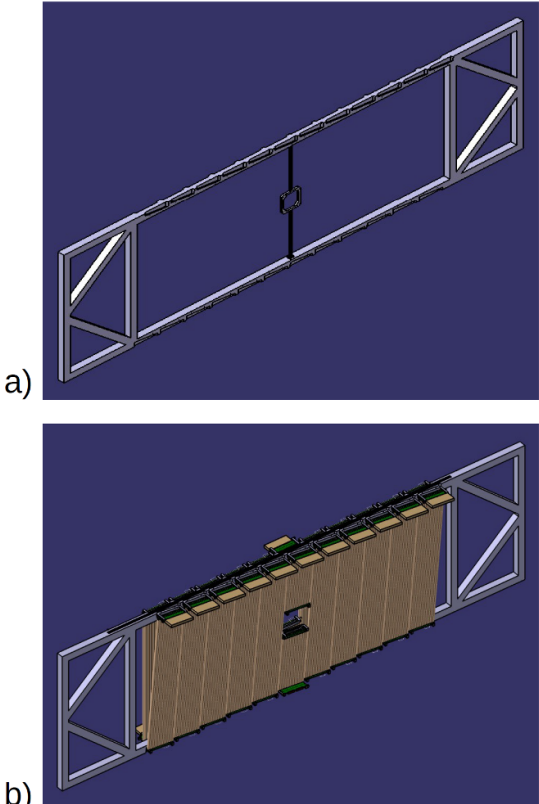


Figure 4.21: Rectangular frame, supporting two double layers of straw tube detectors, designed for the tracking station FT3, shown without modules (a) and with modules (b).

installed inside the dipole magnet gap is presented in Fig. 4.22 and a perspective view of the stations is shown in Fig. 4.23. The base frame will be supported by two rails mounted on the side walls of the magnet gap. The rails will be used for sliding the frame in the gap during the installation. The frame is foreseen to support the tracking stations FT3 and FT4 as well as the two TOF side walls. It will be also used for hanging trays for signal cables going from the FEE cards to the digitizing electronics and for supporting the 3 m long part of the beam pipe crossing the magnet gap.

4.4.4 Installation Procedure

The installation of tracking stations FT3, FT4 on the base frame will be done with the frame rolled outside the magnet gap. The positions of the rectangular support frames with modules with respect to the base frame will be fixed with a precision better than 0.05 mm by means of reference pins. The

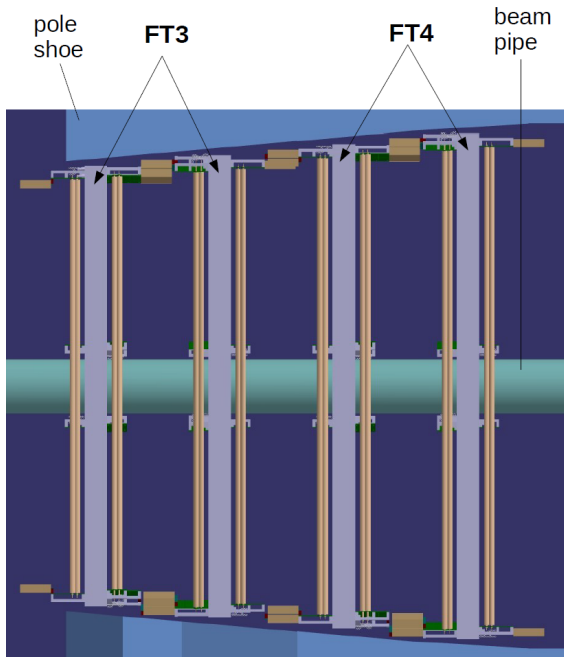


Figure 4.22: Side view of the tracking stations FT3 and FT4 installed inside the dipole magnet gap.

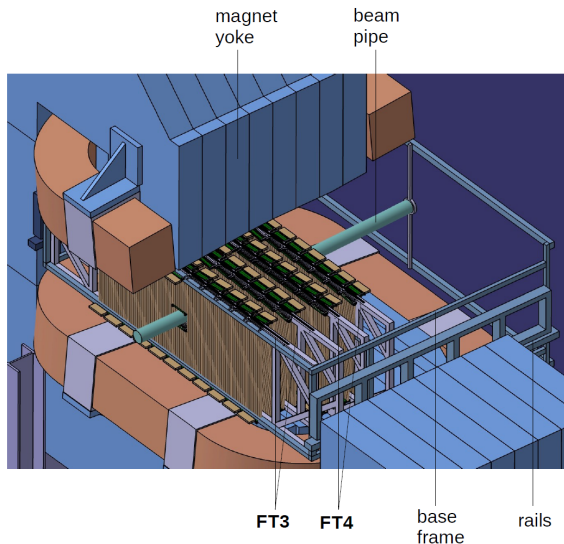


Figure 4.23: Tracking station FT3 and FT4 installed inside the dipole magnet gap.

beam pipe will be inserted in the central openings in the tracking stations and subsequently it will be hanged on the base frame by means of two vertical bars. Afterwards, the tracking stations will be cabled and connected to the gas supply lines. The gas distribution system, the digitizing electronics and the low-voltage power supply for the tracking sta-

tions will be placed below the dipole magnet yoke. The installation of the whole assembly inside the gap of the dipole magnet will be accomplished just by rolling it inside the gap. Excesses of the detector cables and the supply lines should allow for a free movement of the structure during the installation. The movement of the frame inside the magnet gap will be limited by a mechanical blockade. Positioning pins mounted on the blockade system will be used to fix precisely the position of the support frame with respect to the magnet.

4.5 Tracking Stations after the Dipole Magnet

4.5.1 Support Frames for Straw Tube Modules

The tracking stations FT5, FT6 have identical layout. With an active area of about $3.9 \times 1.2 \text{ m}^2$ they are the largest ones in the Forward Tracker. Double layers in the FT5 and FT6 are composed of 27 straw tube modules. The distances between successive double layers are equal to 5 cm as in FT1, FT2. Also the spacing between the geometrical centers of the stations, equal to 32 cm, is the same as in the FT1-FT2 pair.

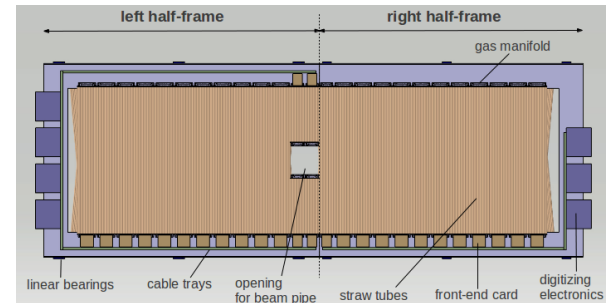


Figure 4.24: Rectangular support frame with straw tube modules for the FT5 and FT6 tracking stations. The division of the frame into two halves is indicated with a vertical dashed line.

As for the FT1, FT2 stations, the support frames for the FT5 and FT6 have a rectangular shape and consist of pairs of half-frames. Modules are mounted on a support frame with FEE cards placed along the lower arm of the frame and gas manifolds are located along the upper arm. Only the short modules, placed above the beam pipe, are mounted with reversed orientation with the gas manifold placed in the vicinity of the beam pipe and the FEE

cards located at the upper arm of the frame. Signal cables, from the FEE cards to digitizing electronics cards, are led in cable trays mounted on the side bars of the half-frames (see Fig. 4.24). The trays are also used for the high voltage supply cables and for the FEE low voltage power supply cables. The gas supply lines are laid in trays attached to the upper arms of the half-frames. The gas distribution system and the low voltage supply units are placed on a shelf which is attached to the FS platform directly below the FT5, FT6 stations.

4.5.2 Stand for the Stations

The tracking stations FT5, FT6 are placed on a common stand made of steel profiles (see Fig. 4.25). The stand contains two horizontal platforms -upper and lower one. The platforms contain four pairs of high precision rails - two pairs for mounting FT5 and another two for FT6. A rectangular frame with modules comprising two half-frames is guided by a pair of rails - upper and lower one. It slides on the rails by means of linear bearings. The half-frames can be independently slidden sideways with respect to the beam line. Fixation of the rails to the platforms allows for their leveling.

In case of module failures, the corresponding half-frame can be drawn out, and the module can be repaired or exchanged. This operation can be done when the *PANDA* detector is in the parking position, as well as in the experimental hall which is wide enough (9.5 m) to fully extract the half-frame. Detailed description of the module replacement procedure is given in Sec. 4.5.4.

The basic lateral dimensions of the tracking stations placed on the stand are indicated in Fig. 4.26. In the z direction, the pair of tracking stations FT5, FT6 occupies 52 cm.

The stand with the tracking stations FT5, FT6 stays on the Forward Spectrometer platform directly after the dipole magnet. For moving the platform from the experimental to the parking position (or vice-versa), the beam pipe has to be disconnected (or connected) directly before the FT5 station. In order to access the connection flange placed downstream the dipole magnet, the half-frames of the FT5 and FT6 stations have to be moved apart.

4.5.3 Concept of Self-supporting Half-frame

The basic design of the half-frames and the stand for FT5, FT6 stations is based on the assumption

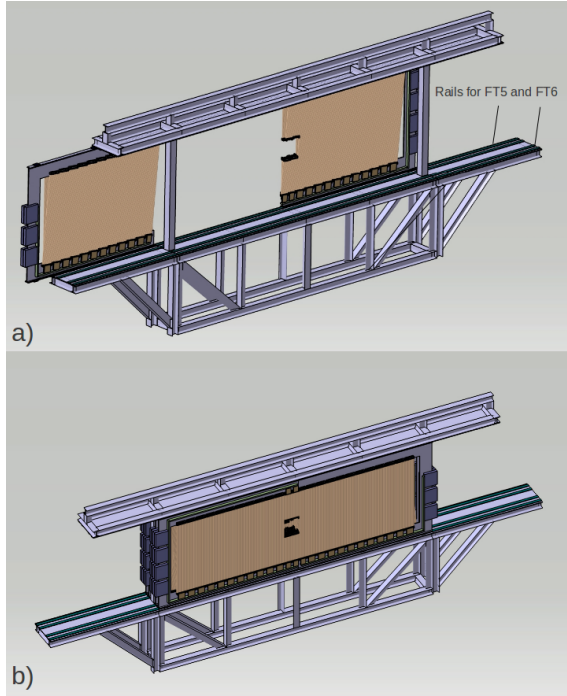


Figure 4.25: (a) Stand for FT5 and FT6 tracking stations with two half-frames equipped with straw tube modules. One half-frame is drawn aside and the other is located in the working position. (b) Tracking stations FT5 and FT6 mounted on the stand.

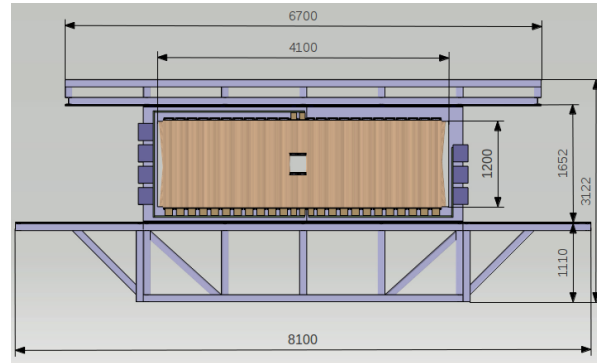


Figure 4.26: Front view of the tracking stations FT5, FT6 placed on the common stand, basic dimensions are also indicated.

that each half-frame is guided by two parallel rails - lower and upper one, as described in the previous section. This solution requires a very precise alignment of the rails and a high rigidity of the mechanical structures in the stand that hold both the lower and upper rails.

Taking this into account, we also studied an alternative solution that uses only the lower rail. This

rail supports the weight of the half-frame together with the attached modules. In this case, the vertical position of the half-frame is determined by positioning elements placed on both sides of the upper arm of the half-frame. The frame should have sufficient rigidity to minimize the deformation under its own weight. In other words, it should be self-supporting.

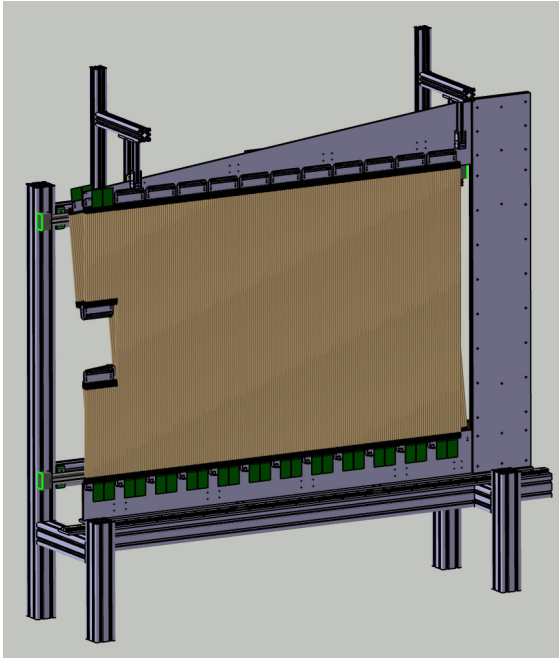


Figure 4.27: 3D model of self-supporting half-frame placed on a rail and equipped with modules. The half-frame is mounted on a test stand.

We have prepared the technical design of the half-frame (see Fig. 4.27). The shape and dimensions of the half-frame have been optimized, using the finite element method (FEM), to minimize the deformation under its own weight and the weight of the attached modules. The optimization was done under assumption, that the half-frame is made of aluminum alloy type 5083. The maximum deformation reaches only 0.44 mm at the end of the upper arm of the half-frame (see Fig. 4.28). This deformation has no mechanical effect on the straws in the modules, since the straws can move freely in the holes of the aluminum brackets attached to the upper arm of the half-frame (this feature is implemented to account for the elongation of the straws due to the gas overpressure - see Sec. 4.2.2).

Recently, a prototype of half-frame has been manufactured and equipped from one side with modules (see photograph presented in Sec. 5.1, Fig. 5.4). The half-frame is mounted on a rail placed on a test

stand, built to measure the positions of the straws with a collimated X-ray beam. The mounting of the frame is identical to that foreseen in the FT5, FT6 stations. We have checked, that the half-frame slides easily on the rail, which means, that it can be extracted from the tracking station as expected. The measured deformation of the upper arm of the half-frame equals 0.5 ± 0.1 mm and agrees with the FEM calculation result (0.44 mm). The modules can be mounted on the frame without problems which confirms the proper mechanical precision of the system. We plan to measure the positions of the straw tubes in the modules, in order to check their precision and their reproducibility after reinstalling the half-frame. Results of these tests will be the basis for the decision to use or not the self-supporting half-frames in place of the more conservative solution with the pair of rails. After selecting the frame type, the design of the common stand for the tracking stations FT5, FT6 will be optimized and its detailed technical drawings will be prepared.

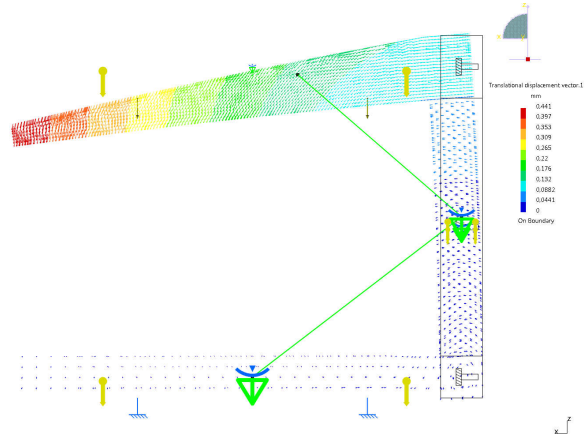


Figure 4.28: Deformation of the self-supporting half-frame under its own weight and the weight of attached straw tube modules, determined using the finite element method. The maximum deformation, represented by red color, is 0.44 mm.

4.5.4 Module Exchange Procedure

In case of module failures, the corresponding half-frame can be drawn out, and the module can be repaired or exchanged. This operation can be performed both in the **PANDA** parking position and in the experimental hall.

The foreseen procedure of module exchange in the FT stations is as follows:

1. Extraction of the frame with the module to be exchanged from tracking station.
2. Disconnecting the HV cable and the FEE cards from the module.
3. Cutting off the inflow and outflow of gas to the double layer containing the module to be exchanged. For this, the valves marked as V1 and V2 in Fig. 4.29 should be closed.
4. Releasing the connections between the input and output gas manifold in the module and the fittings of the T-type on the gas input and output line. For example, for the module 3 in Fig. 4.29, these connections are marked as 1 and 2. The gas overpressure in the modules in the double layer is released and air from atmosphere gets inside the input and output line through the two T-fittings. However, the entry of air in the straws is hindered by the PVC pipes connecting the straws to the gas manifolds.
5. Unscrewing the upper and lower aluminum bracket and removing the module from the frame.
6. Placing the new module on the frame, screwing it to the frame and connecting it to the gas input and output line.
7. Connecting the HV cable and the FEE cards to the module.
8. Purging the input and output line with the gas mixture by opening the valves V1, V2 and V3. After that, closing the valve V3 and pressurizing the double layer to the nominal pressure of 2 bars.
9. Checking the gas tightness of the double layer.
10. Starting the routine gas flow through the double layer.
11. Inserting the frame in the station.

Extraction of the half-frame from the tracking station (point 1 on the above list) is very easy in the case of FT5, FT6, thanks to the possibility of moving the half-frame aside. In the case of FT1 and FT2 the corresponding procedure is more complicated and time consuming since it requires opening the Forward Muon Filter (see Sec. 4.3.4). The most complicated and time consuming is the extraction of the frame with modules from the stations FT3, FT4 (see Sec. 4.4.4). In particular, it can only be done with the Forward Spectrometer platform with the

corresponding detectors removed from the experimental position. The replacement of the module itself (points 2-7 on the list) with the frame extended from the station is relatively fast - it takes about 10 minutes. The operation of pressurizing the double layer, checking the gas tightness and establishing proper gas composition in the double layer (points 8-10 on the list) takes roughly 10 hours.

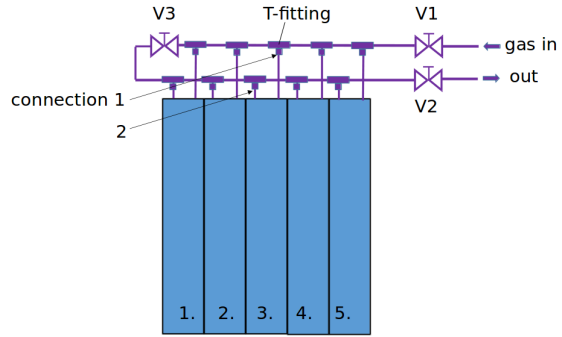


Figure 4.29: Scheme of connecting a layer of modules to the gas supply.

4.6 The Readout Electronics

4.6.1 Requirements and General Concept

The input characteristics of the front-end electronics have to match the electrical properties of the straw tubes, which are listed in Table 4.4.

From the point of view of the pulse propagation, the straw tube acts as a coaxial transmission line with loss, with an impedance given by the formula:

$$Z = \sqrt{\frac{R + i\omega L}{i\omega C}}, \quad (4.1)$$

where R is the electrical resistance, L is the inductance, C is the capacitance and ω is the angular frequency. For high frequencies (> 100 MHz), the impedance of the straw tubes tends to the limit $Z \rightarrow \sqrt{\frac{L}{C}} = 373 \Omega$ (see Fig. 4.30).

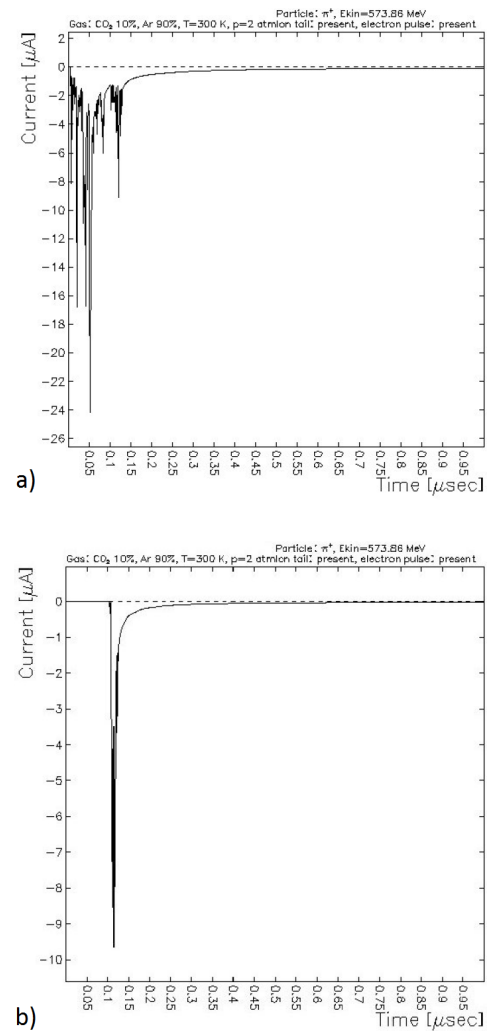
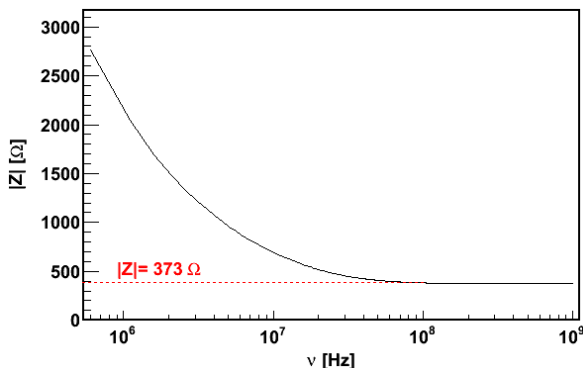
The shape of the current signal, generated in a straw detector, depends on the distance of a particle track from the anode wire. For tracks passing close to the wire, the first part of the signals, corresponding to the maximum drift time of ionization electrons, exhibits fluctuations resulting from statistical distribution of ionization clusters along the track. For longer times, the signals have a long tail

Capacitance	8.9 pF/m
Sense wire resistance	258 Ω /m
Inductance	1.24 μ H/m
Impedance	373 Ω
Analog cross talk	< 1 %

Table 4.4: Straw tube electrical properties.

extending to many hundred microseconds, resulting from a movement of positive ions from the region near the anode wire, where the charge multiplication occurs, to the cathode surface. This long ion tail needs a special treatment in high rate applications of straw tubes, as it is in the case of $\overline{\text{PANDA}}$. An example of a signal shape, simulated with the GARFIELD code [23] for a minimum ionizing pion passing near the anode wire of the FT straw, is shown in Fig. 4.31 (a). For tracks passing close to cathode surface, the ionization electrons reach the anode wire almost simultaneously, and the fluctuations in the signal disappear, however, the ion tail remains (see Fig. 4.31 (b)).

As shown in Fig. 3.4, the maximum counting rate of 1400 kHz is expected for the straws in the vicinity of the beam pipe in the first tracking station (FT1) at the highest beam momentum of 15 GeV/c and at $\overline{\text{pp}}$ interaction rate of $2 \times 10^7/\text{s}$. The counting rate decreases quickly with increasing distance from the beam axis. The maximum drift time of electrons in the straw tubes placed outside the region of magnetic field (tracking stations FT1, FT2, FT5 and FT6) is 130 ns. In the straw tubes working in the magnetic field of the dipole magnet, reaching up to 0.9 T, (tracking stations FT3 and FT4) it extends to about 150 ns. The requested

**Figure 4.31:** Example of signal shape generated in the FT straw detector by a $E_{kin} = 420$ MeV pion passing close to the anode wire (a) and close to the cathode surface (b). The signals are simulated with the GARFIELD program [23].**Figure 4.30:** Straw tube impedance as a function of frequency $\nu = \omega/2\pi$ (solid black line). The high frequency limit is indicated with the red dashed line.

electronic time resolution should be around 1 ns and the intrinsic noise level below 1 fC. The maximum analog pulse duration should be comparable to the maximum drift time of 150 ns. The front-end electronics should withstand a maximum radiation dose of 5 krad which will be accumulated during the lifetime of the $\overline{\text{PANDA}}$ experiment of 10 years (see Sec. 4.1.3). Basic requirements of the front-end electronics are summarized in Table 4.5.

To fulfill all these requirements, the proposed straw tube readout chain comprises 3 stages:

1. Analog Front-End Electronics (FEE) cards hosting 16 channels for the read out of straw tube modules. A FEE card based on es-

Peaking time	≤ 40 ns
Double pulse resolution	~ 100 ns
Intrinsic electronic noise	<1 fC
Discrimination threshold	≈ 5 fC
Max. drift time	150 ns
Max. counting rate	1400 kHz
Radiation dose (10 years)	5 krad

Table 4.5: Front-end electronics requirements.

pecially designed ASICs, PAndaStrawTube-TRackerEleCtronics (PASTTREC) [24].

2. Digital Board (DB) containing a multichannel TDC for time measurements, local logic resources for noise suppression, fast hit detection, memory buffer for hit storage, serial Gbit optical links for data transmission and slow control.
3. Detector Concentrator Board (DCB) (optional) receiving and merging inputs from several DBs in local memory buffer and sending it to the $\bar{P}ANDA$ DAQ system.

The data from the DB (or DCB) will be transferred via fast optical links to Compute Nodes (CN) for on-line pattern recognition and track reconstruction and subsequently, after merging with the information from other $\bar{P}ANDA$ detector systems, for the event selection. It will be possible to perform some local correlations on the data inside the single DCB to suppress noise and reduce the amount of data sent from the board. Time window search (e.g. 300 ns wide) can be performed in order to find particle track candidates and reject hits that are not correlated in any way. Cuts on TOT are also possible and can also help reducing background.

The $\bar{P}ANDA$ data acquisition and filtering systems will implement a trigger-less architecture. Instead of having a hardware trigger signal, which indicates the occurrence of a valid event, each DB will receive a precise clock signal distributed centrally from a single source: the Clock and Timing Distribution System (CTDS) called SODANet (Synchronization of Data Acquisition Network). The DB will continuously monitor the detector channels and will generate data packets whenever the number of input signals exceeds programmed thresholds. These data will be tagged with time-stamps obtained from the CTDS.

The data acquisition system will profit from the structured running mode of the HESR operation. Periods of $2\ \mu s$ with antiproton interactions will be interleaved with periods of 400 ns of idle time. The

Table 4.6: Main parameters of the PASTTREC-v.1 (see text for more details).

Technology	$0.35\ \mu m$ CMOS
Number of channels	8
Equivalent (delta) input range	0-200 fC
Variable gain	$\sim 1.8\text{-}10.5$ mV/fC
Variable peaking time (for delta)	10-35 ns
Noise ENC	< 1 fC
Baseline tuning	-32 - 32 mV
Output standard	LVDS and analog
Power consumption	~ 35 mW/channel

information on the accelerator activity will be distributed to DCBs via the CTDS. The data recorded during the interaction intervals will be grouped together in DCB to form a burst which will be then uniquely tagged. Grouping of data from many bursts into predefined epochs (e.g. $500\ \mu s$), called Super Bursts, inside DB is also considered in order to reduce the network traffic. Data from all $\bar{P}ANDA$ detectors, tagged with the same burst identification number, will be grouped together and will be made accessible to filtering algorithms implemented in the Compute Nodes. Decisions produced by these algorithms will thus be based on the complete detector data with full granularity.

4.6.2 Analog Front-End Electronics

The PASTTREC has been developed in $0.35\ \mu m$ CMOS technology in order to read out the straw tube detectors in the Forward Tracker as well as in the Straw Tube Tracker. The main specifications of this chip are summarized in Table 4.6.

The block diagram of the designed readout channel is shown in Fig. 4.32. The ASIC's channel comprises a charge sensitive preamplifier (CSP) stage, a pole-zero cancellation network (PZC), a shaper stage, a tail cancellation network, a baseline holder (BLH), a discriminator circuit, a fast differential LVDS output and an analog output.

Two versions of the PASTTREC chip have been produced. The prototype containing 4 readout channels was fabricated in 2011 and was extensively tested with straw tubes illuminated with radioactive sources and proton beams. The first version (PASTTREC-v.1) was produced in 2014 and features 8 channels and integrated DAC for the ad-

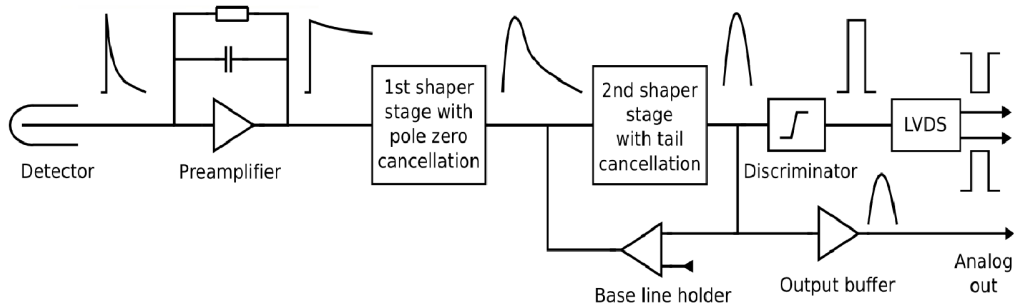


Figure 4.32: Block diagram of a single channel of the PASTTREC ASIC.

justment of the baseline for each channel and one common threshold.

Several parameters of the chip (see Table 4.7) including the preamplifier gain, the discrimination threshold, the baseline setting, the shaping time and the tail cancellation are programmable via slow control.

The total number of various PASTTREC configurations is 65530. The search of the optimal setting was performed for pulses of a straw tube illuminated with an ^{55}Fe source. The search was automated and performed analyzing the analogue output signal shape, in order to find the set of settings that result in minimal under and overshoot, high amplitude and shortest rise time [25]. Sample output signals are presented in Fig. 4.33

In the FT only the measurement of the drift time in the straw tubes is required, however in the STT also the amplitude information is needed for particle identification using the dE/dx method. Therefore, the solution for the FEE should provide both, the timing and the amplitude information. Since it is still under study whether the Time-over-Threshold (TOT) technique or the analog amplitude information will be used for the energy-loss measurement, the ASIC prototypes provide both the amplitude and the TOT information.

The baseline is adjustable for each channel with 5 bit DAC ($\pm 32\text{ mV}$ with 2 mV step) and there is one global threshold setting per ASIC set by 7 bit DAC ($2\text{ mV}/\text{LSB}$). The typical settings for straw tube operation are the gain of $1\text{ mV}/\text{fC}$ and $20\text{--}30\text{ ns}$ shaping. Measurements of the baselines uniformity and stability have been performed and are presented on Fig. 4.34. Standard deviation of the distribution amounts to $\sigma = 7\text{ mV}$ without any tuning. This can be further reduced by the application of settings to individual channels with the help of DACs. Baseline stability is essentially important

for TOT measurements.

The gain characteristics have been measured with a step-like voltage pulse injected into the ASIC channel via a capacitance ("delta-like" pulse). The obtained gain curve Fig. 4.35 is the correlation between the input charge and the amplitude of the analogue output, collected for the four preamplifier gain (K) settings. The uniformity of the gain between channels is presented in Fig. 4.36. The respective RMS distribution of the extracted gains, obtained from linear fits to the characteristics is about 1%.

The charge vs. TOT behavior of the ASIC is shown in Fig. 4.37. The input charge was obtained by calculating the number of primary electrons and the gas gain in the straw. The TOT values were extracted from Gaussian fits to distributions collected with ^{55}Fe source.

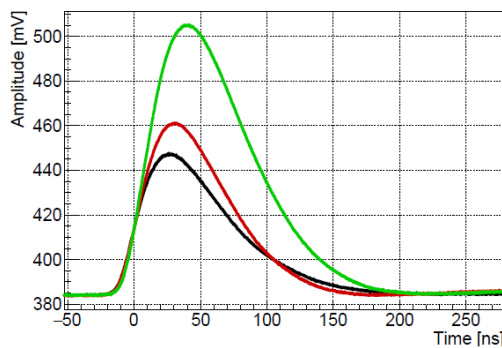
One of the main requirements for the PASTTREC chip is the capability of processing hit rates reaching 1-2 MHz. In view of the expected large counting rate and long time constant related to the ion propagation, it is very important to demonstrate that the ion tail cancellation and the baseline holder circuits work according to the design. Signals from an ^{55}Fe source measured with the ASIC connected to the illuminated straw tube, for different settings of the ion cancellation network, are shown in Fig. 4.38. It can be seen that, with optimized parameters of the network, the long tail can be eliminated.

In order to verify the chip performance in time domain a delta pulse was used. A pulse of 2 MHz frequency has been directed to the chip and the analogue output is presented in Fig. 4.39. Even under heavy load, a clear pulse separation is visible and the baseline remains stable, which is important for the TOT measurements.

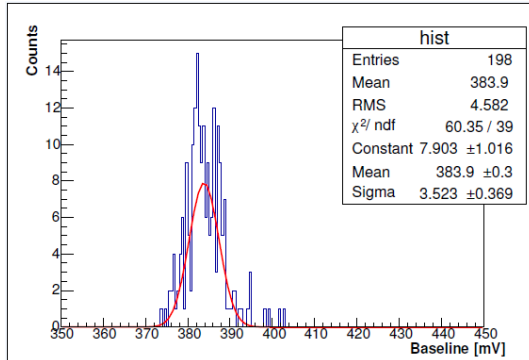
Other measurements, with FT prototypes equipped with FEE cards containing PASTTREC-v.1, were

Table 4.7: PASTTREC available settings

<i>Register^{channel}_{bits}</i>	Setting	Values
$K_{1:0}$	Gain	4, 2, 1, 0.67 mV/fC
$Tp_{1:0}$	Peaking time	10, 15, 20, 35 ns
$TC1C_{2:0}$	1 st stage tail cancellation constant capacitance	6-16.5 pF, step 1.5 pF
$TC1R_{2:0}$	1 st stage tail cancellation constant resistance	3-31 k Ω , step 4 k Ω
$TC2C_{2:0}$	2 nd stage tail cancellation constant capacitance	0.6-1.65 pF, step 0.15 pF
$TC2R_{2:0}$	2 nd stage tail cancellation constant resistance	5-26 k Ω , step 3 k Ω
$Vth_{6:0}$	Common discrimination threshold	0-254 mV, step 2 mV
$Bl_{4:0}^{0-7}$	Baseline fine tuning	0-62 mV, step 2 mV
$Ch_{2:0}^{on}$	Channel input enable	0 - 7
$LVDS_{2:0}^{on}$	Channel LVDS output enable	0 - 7



black: $TC_{C1} = 10.5\text{pF}$, $TC_{R1} = 27k\Omega$, $TC_{C2} = 0.9\text{pF}$, $TC_{R2} = 20k\Omega$;
red: $TC_{C1} = 6\text{pF}$, $TC_{R1} = 23k\Omega$, $TC_{C2} = 0.6\text{pF}$, $TC_{R2} = 11k\Omega$;
green: $TC_{C1} = 16.5\text{pF}$, $TC_{R1} = 11k\Omega$, $TC_{C2} = 0.9\text{pF}$, $TC_{R2} = 5k\Omega$;

Figure 4.33: Three optimal settings for preamplifier gain (K) equal 1 mV/fC and peaking time (T_p) equal 20 ns.**Figure 4.34:** Distribution of the baseline levels accumulated from 192 channels.

performed with a high-intensity proton beam from the COSY-Juelich accelerator. As an example, Fig. 4.40 shows the analog output of the FEE recorded by an oscilloscope. No baseline distortion and a clear separation of the four individual signals can be seen within a time window of about 700 ns, which corresponds roughly to a proton rate of 6 MHz in the single straw.

The second version of the FEE card shown in Fig. 4.41 uses two PASTTREC-v.1 chips and allows for readout of 16 detector channels. The FEE parameters such as the baseline or the gain are adjusted by means of integrated DAC controlled via dedicated lines of the cable connecting the FEE board to the DB (described in more details below).

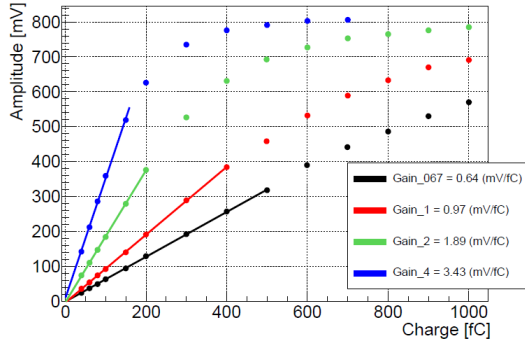


Figure 4.35: Gain measurements for delta pulses for four settings of preamplifier gain (K).

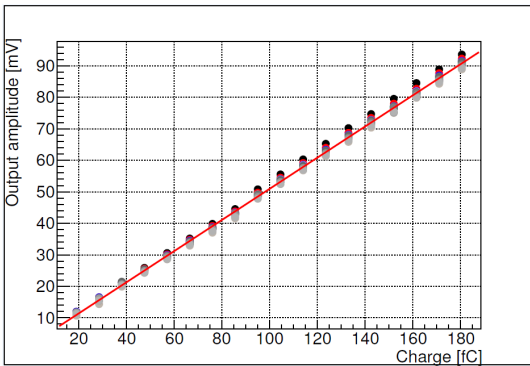


Figure 4.36: Amplitudes of 16 output signals versus input charge for the same ASIC configuration.

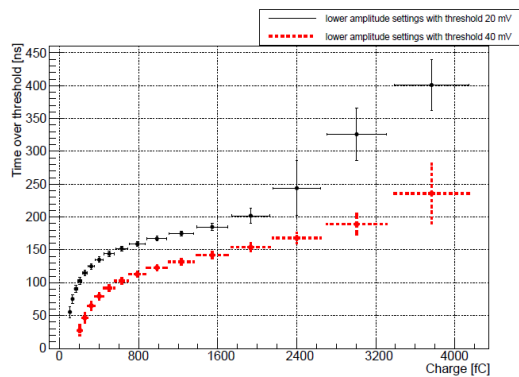


Figure 4.37: Time-over-Threshold vs charge correlation collected with ^{55}Fe source.

The FEE cards are equipped with analog output buffers that make it easier to observe the analog output pulses. The price for this is much higher power consumption and the need for air cooling of the cards. In our prototype detectors, we use small fans for this purpose. In the FT stations we plan to use FEE cards with removed analog output buffers. The first series of such cards is being produced. We plan to check if these new cards require air cooling,

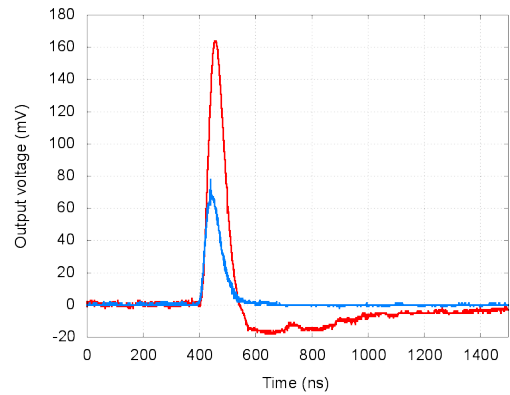


Figure 4.38: Examples of front-end pulses for not optimized (red) and optimized (blue) settings of the ion cancellation network.

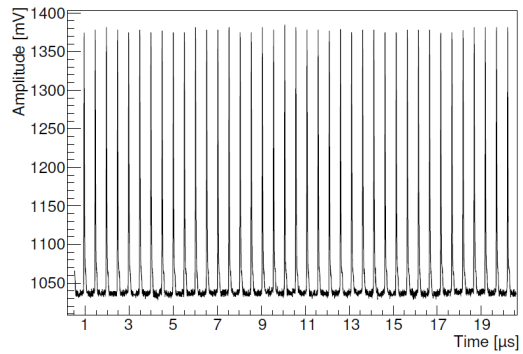


Figure 4.39: The analogue output of the PASTTREC responding to the 2 MHz pulse coupled to the FEE test input.

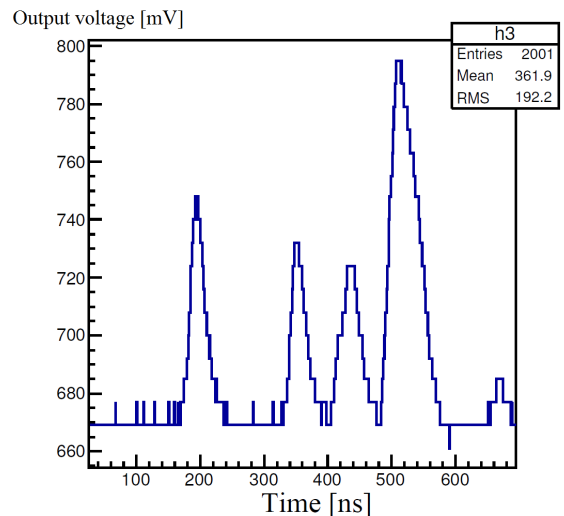


Figure 4.40: Example of the ASIC analog signal output measured at a high (few MHZ) hit rate.

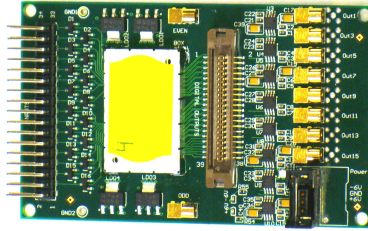


Figure 4.41: 16-channel FEE card comprising two PASTTREC-v.1 ASICs.

and if so, what is the necessary air flow. Depending of the results obtained, appropriate cooling will be applied in the FT.

Another issue is possible heat accumulation inside the dipole magnet gap, due to the power dissipated by the FEE cards in the station FT3 and FT4 (140 W in total). To counteract this, we plan to apply forced air exchange inside the gap.

The FEE cards will be mounted on the frames of the tracking stations and thus will be exposed to the radiation originating from the interaction point and from secondary reactions occurring in the material of the detection system. The expected accumulated dose in the FEE cards is on the level of a few krad (see Sec. 4.1.3), and is significantly smaller than the radiation hardness of a few hundred krad typical for the 350 nm CMOS technology, which was used for the production of the PASTTREC chips.

During the design phase of the new ASIC, several FEE prototypes, based on the CARIOCA chips [26], were built. They are described in Appendix B. They were tested with prototype straw detectors and showed less stable performance characterized by higher sensitivity to pick-up noise and a tendency to oscillate. Therefore, for the FT we decided to use the FEE cards based on the PASTTREC chips.

4.7 The Readout System

4.7.1 Development Policy

For the development of the readout system of the FT, two modes of operation of the \bar{P} *ANDA* experiment are under consideration: the High Resolution and the High Luminosity mode (see Sect. 2.1.2). Depending on the tracking station location, the estimated average hit rate per straw in the High Resolution mode are as follows: FT1, 2: 35 kHits/s, FT3, 4: 31 kHits/s, FT5, 6: 9 kHits/s. In the High Luminosity mode, those values should be multiplied

by a factor 10.

The PASTTREC based FEE modules can cope with a few MHz hit rates and therefore they can be used in both operation modes. The design of the readout system included the existing and well tested Trigger Readout Board (TRB) platform and the TRBv3 boards as the base modules. Such approach allows to perform early evaluation of the detector and the FEE modules on a stable and widely used platform with TDCs and integrated readout. The tests show that the readout system for the entire detector can be constructed out of existing hardware for High Resolution mode.

However, the hardware developed in 2011 has not enough throughput to handle data rates in the High Luminosity mode and requires an upgrade, which is ongoing. It is important to stress that only hardware upgrade is performed and the TRB platform that combines readout procedure, used data transmission standards and protocols remains the same. Therefore, we describe two solutions: one for the High Resolution mode, based on TRBv3 boards and one for the High Luminosity mode with the upgraded concept.

4.7.2 Time-to-digital Converters and TRBv3

The main part of the DB is a multi-hit TDC measuring the time of arrival of leading and trailing edges of the FEE digital signal with respect to the external clock provided by the PANDA CTDS. TRBv3 has been developed by GSI, University of Frankfurt and Jagiellonian University for the HADES experiment [27]. It is based on the Lattice ECP3 FPGA family and it has been chosen as the prototype for the detector DB. A block diagram and a photograph of the TRBv3 are shown in Fig. 4.42 and Fig. 4.43, respectively.

TRBv3 hosts five FPGAs. Four, located along the edges of the board, implement the TDC functionality. The TDC firmware used in the test measurements provided 64 channels for leading and trailing edge measurements with 10 ps binning. The implementation of the TDC functionality in FPGA is achieved by using its internal architecture elements - carry chains [28], [29], [30]. As presented in Fig. 4.44, the time measurement is based on the information from the carry chain - START signal, saved in the flip-flops ($Q_1 - Q_n$) on the rising edge of the system clock - STOP signal. Each carry chain element delays the signal on average by 12 ps.

Time measurements done at GSI demonstrate a

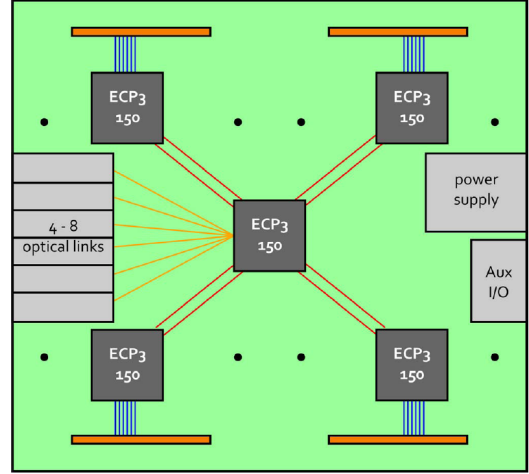


Figure 4.42: Block diagram of TRB-v.3.

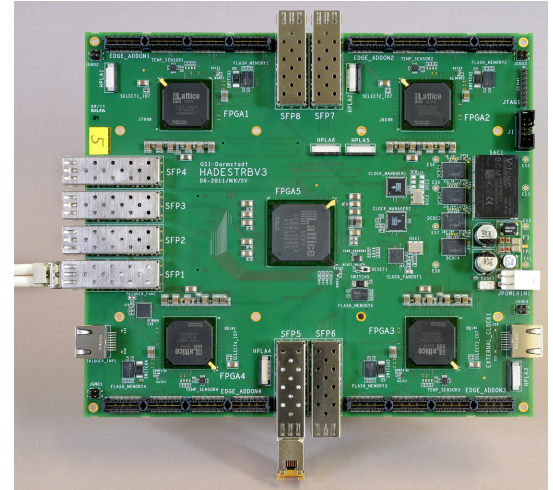


Figure 4.43: Produced TRB-v.3 board.

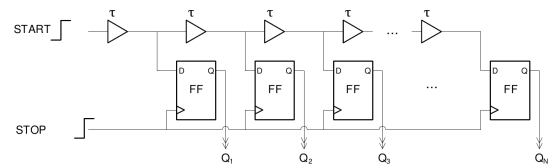


Figure 4.44: Scheme of TDC-FPGA implementation with carry chain usage.

~ 14 ps resolution [27]. For the straw tubes, a 100 ps binning is sufficient. The TDC features multi-hit detection with 5 ns double pulse resolution and internal buffer for hit storage. It can operate with a few MHz hit rate. The fifth FPGA, located in the center of the TRBv3 board, reads out data from the buffers of edge TDCs and provides communica-

cation with the data acquisition system via digital links. The links are accomplished by up to eight optical SFP connectors with a maximum transmission speed of 3.2 Gbps. Besides the data transmission, the links can be used also for slow control (like setting the PASTTREC) and synchronization with the CTDS.

The TRB is equipped with input/output connectors to plug in a mezzanine card which can extend board functionality. The connectors contains 188 general purpose lines and 6 high speed serial connections between edge FPGA and the mezzanine board. Eight lines are connected to the central FPGA from each connector. The design of the mezzanine card is left for future TRBv3 applications as for example multichannel ADC to analyze the analog signal provided by PASTTREC. A set of two connectors is placed on the bottom side of the TRBv3 allowing for connecting another mezzanine card. All 160 general purpose lines from the bottom connectors are controlled by the central FPGA. Both top and bottom connectors provide a power and ground for mezzanine cards.

Recently, a DB with 48 TDC channels in FPGA, each featuring leading edge and TOT measurement and giving the total number of 192 channels per board, has been tested. With such a board one can collect data from six straw tube modules with 32 channels each.

4.7.3 High Resolution Mode Data Rates

The estimated data rate is presented taking into account the existing firmware for the TDC and the DB that define the data format, buffering and throughput capabilities of the TRBv3 platform. One registered hit in the TDC (leading and trailing edge of a signal for TOT) is represented by two 32-bit words, which include the channel number and a value containing encoded time measured in the range up to $10.24\ \mu s$. Additionally, after each $10.24\ \mu s$ period, another 32-bit word containing epoch counter is added on individual channels. In a free-running measurement system (time counters are not initialized at the beginning of the measurement window), it is assumed that the epoch counter words will appear on each active channel with a frequency close to 100 kHz.

The buffering is performed on several data processing stages. Each TDC channel can store up to 40 hits between consecutive readouts. Output buffer from one TDC module can store up to 2048 hits

from all the channels. Assuming uniform hit distribution over all channels, the TRBv3 is capable to process up to 55 kHits/s on all 192 channels. When needed, one can limit the amount of hits stored per channel in order to gain buffer space for additional epoch counters (for lower readout frequencies) or higher channel density at the cost of lost hits.

In the High Resolution mode the average load on channels is below 55 kHits/s (see Table 4.8). Straws close to the beam pipe can have a much higher hit rate, reaching 140 kHits/s. Such effect can be compensated by mixing straws from various detector regions on one TRBv3 and therefore achieve balanced, aggregated data volumes per DB.

A setup with 69 TRBv3 boards with 192 channels each is needed to read all 12 224 channels of the FT (see Fig. 4.45). 65 TRBv3 provide enough channels for the time measurement and are called slaves. 4 additional boards are required to construct a tree-like architecture. One module, called master is a root and controls the readout process of the entire system. It also acts as a gateway for Slow-Control commands. The remaining 3 modules provide connectivity and synchronization of the slaves. The setup requires 13 SFP Addons, which are used to connect the boards between themselves.

The expected hit rate differs between FT stations, but so does the number of straws. Stations FT1 and FT2 are constructed out of 1152 straws each and expect 35 kHits/s in the High Resolution mode. For such number of channels 12 TRBv3s are required, each generating 81 MBps summing up to total of 0.927 GBps. Stations FT3 and FT4 have 3328 channels with which a setup of 18 TRBv3s has to deal with, generating 1.242 GBps data stream. Stations FT5 and FT6 have higher channel number (6592) but significantly lower hit rate. 35 TRBv3s are needed and a 0.7 GBps data stream will be generated. All those values are presented in Table 4.8 and sum up to a total of 2.914 GBps out of the system in the High Resolution mode.

4.7.4 High Luminosity Mode Readout Scheme

In the High Luminosity mode, the expected hit rates per channel are ten times higher than in the High Resolution mode. The readout system described above is not capable to cope with such data volumes and, therefore, development of a new hardware platform is planned.

The concept is to develop a new version of the TRB board (conventionally named TRB5G), equipped

Tracking station	Number of channels	Average hit rate	Maximum hit rate	Number of TRBv3s	Bandwidth	Total bandwidth
FT 1,2	2304	35 kHits/s	140 kHits/s	12	81 MBps	972 MBps
FT 3,4	3328	31 kHits/s	90 kHits/s	18	69 MBps	1242 MBps
FT 5,6	6592	9 kHits/s	39 kHits/s	35	20 MBps	700 MBps

Table 4.8: Estimated data rates per tracking station in High Resolution mode.

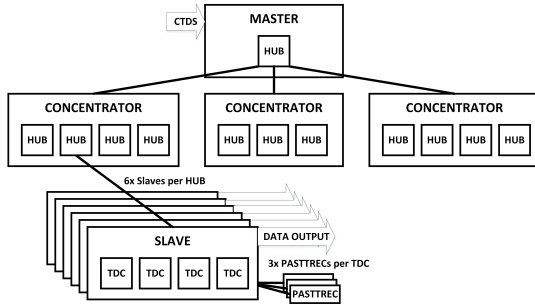


Figure 4.45: Schematic view at the TRBv3 system for High Resolution mode.

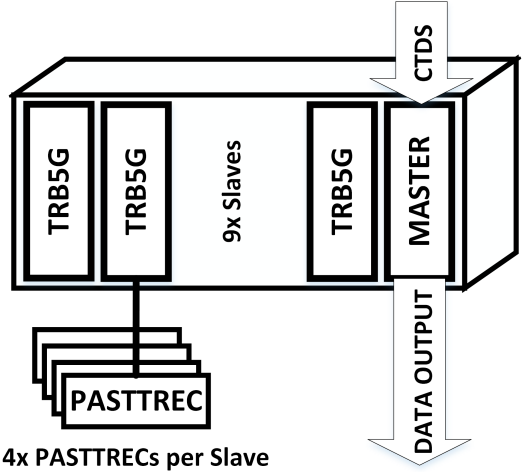


Figure 4.46: Schematic view at the TRB5G crate system for the High Luminosity mode.

with more advanced and up-to-date FPGA devices, mountable in a crate system that includes backplane with power supply and communication features. It is an evolution of the already existing TRB3SC system based on ECP3 FPGA, the same as in TRBv3 platform.

Resources available in the proposed ECP5G-45 FPGA devices allow to implement up to 64 low-resolution (below 0.5 ns) TDC channels sufficient for readout of 4 FEE modules. A new implementation of the time measurement component allows also to redefine its output data format. One 32 bit word is enough to combine channel number, leading time (relative to the burst update signal from CTDS) and its width for the TOT measurement. It is a significant (more than factor 2) reduction of the data volume as compared to the system for the High Resolution mode.

One crate can house up to 9 DB modules. One master module (DCB) will interface with CTDS and propagate the timing information to the remaining 9 slave modules (Fig. 4.46). In order to reduce the amount of physical links, the master will also concentrate the measurement data from the slaves, through the backplane and transfer collected data further to the CN for event building. The master module has to be equipped with a different FPGA device (e.g. Artix or Kintex) because ECP5G has not enough high-speed transceivers to accommodate 9 data streams from slaves and handle output links.

In the High Luminosity mode, the rate of 350 kHits/s is expected in stations FT1 and FT2. Under such conditions, one DB module with 64 channels will generate 90 MBps (0.72 Gbps). Chosen ECP5G FPGAs are equipped with 5 Gbps transceivers, both for backplane connections and for data transmissions out of the system. Fully-loaded crate with 9 slave and one master modules, will generate 6.5 Gbps data stream to the CN farm.

The proposed solution will be constructed out of 191 new DB slave modules. In order to house them, 22 crates will be needed and the same amount of master modules. Each crate can be connected directly to the CTDS for time synchronization and to the CN farm for event building and further processing. In Table 4.9 are presented the values of expected hit rates, required hardware and generated data volumes. They can be compared with those quoted in the previous section. All stations summed up will produce 9.6 GBps in the High Luminosity mode.

Tracking station	Number of channels	Average hit rate	Maximum hit rate	Number of TRB5Gs	Bandwidth	Total bandwidth
FT 1,2	2304	350 kHits/s	1400 kHits/s	36	90 MBps	3240 MBps
FT 3,4	3328	310 kHits/s	900 kHits/s	52	79 MBps	4108 MBps
FT 5,6	6592	90 kHits/s	390 kHits/s	103	23 MBps	2369 MBps

Table 4.9: Estimated data rates per tracking station in High Luminosity mode.

4.7.5 System Integration and Synchronization

The Forward Tracker readout system, composed out of TRB modules (actual TRBv3 or new version described in the previous section) as Data Concentrator Boards is a subsystem that has to be integrated with the PANDA data acquisition and synchronization system. Measured data have to be delivered to data processing farm of Compute Nodes and each DB module has to be connected to the SODANet system providing time stamps for data packets and slow control for configuration and monitoring.

The link to the Compute Nodes is a point-to-point optical connection. Since no packet routing is required for such connections, the low-level 8b/10b encoding with defined comma characters as data delimiters is sufficient in order to achieve maximum throughput over 3.2 Gbps transceivers for TRBv3 or higher for the new module. The Compute Node farm performs event building, which is reassembling data packets from all inputs, tagged with the same time stamp.

Time stamp distribution is realized by the SODANet system. The system consists of one central point, which is SODANet Source. This module generates a periodic signal, which is used as measurement start for TDC and also provides time stamp, a unique identifier of current measurement window for the DCB. Both are transmitted through optical connections and distributed with the use of SODANet Hubs to the Data Concentrator Boards. Upon receiving such message, the DCB starts the TDC measurement, collects the gathered data, constructs a packet including header with the time stamp and transmits such unit to the Compute Node farm.

In the High Resolution mode, the readout system based on TRBv3 modules requires in total 69 boards. Each TRBv3 has a direct output link, which has to be connected point-to-point to the Compute Node for event building and further processing. The existing CN prototype has 4 input links per FPGA Mezzanine Card (FMC) and 16 links per full ATCA module (one ATCA carrier

module with 4 FMC modules plugged in). In order to collect the data from all tracking stations, 18 Compute Node FMC modules are required, housed in 5 full size ATCA carrier boards. The upgraded TRB modules will be organized in a crate, where data from 9 TDC modules are transmitted out by one master module. In High Luminosity mode, 22 crates will be used, therefore there will be 22 output links. It is a significant reduction of the processing required to handle output data streams. Only 6 Compute Node FMC modules are needed, housed into 2 carrier boards. It is important to note, that the Compute Node hardware is currently under upgrade and will feature recent and more advanced FPGA devices, capable of handling higher number of input links.

After receiving data fragments from all the TRB modules, the Compute Node farm has to perform event building. All parts containing the same Super Burst update number, delivered by CTDS, have to be reassembled into a single data unit. The Compute Node modules have to exchange (route) the data between them in a way that all fragments from a particular Super Burst end up on a particular FPGA device. In parallel, on-line tracking algorithms can be executed on specific data parts. Especially, tracklets from station pairs FT1, 2, FT3, 4 and FT5, 6 can be reconstructed during the event building and the calculated results replacing or appended to the raw data fragments. Finally, when all parts arrive to a single device, tracklets can be assembled into a fully reconstructed track.

4.8 Quality Control

4.8.1 Gas Tightness

Each stage of construction of the tracking station construction will undergo a proper quality control procedure. Individual straws will be tested for gas tightness and mechanical tension of the anode wire. The gas tightness will be checked by means of an automatic test stand shown in Fig. 4.47. It tests simultaneously up to 16 straws. The straws are being filled with argon at 2 bar absolute pressure and, af-

ter closing the gas supply, variation of the pressure is registered for a specified period of time, typically few hours. Straws with gas leaks exceeding the acceptable limit of $\Delta p/p/t = 0.3\%/\text{h}$ are rejected.

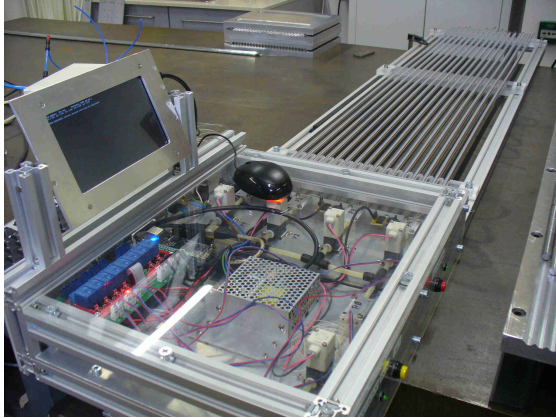


Figure 4.47: Test stand for checking the gas tightness of straws.

Results of the measurement of the gas leak in straws produced for 13 prototype modules for FT5 and FT6 are shown in Fig. 4.48. Only data for the straws considered as tight are presented. We did not record the pressure loss for the leaky straws, but its value was typically of $\Delta p/p/t \sim 50\%/\text{h}$ and, thus, was drastically different from values measured for the tight straws. The percentage of not tight straws between those produced for the first 4 modules was 16%. After finding the cause of the gas leaks, which was an overlap between consecutive turns of the Mylar strip in the straw, and by rejecting the straws with the overlap, for straws produced for the next 9 modules, only one was not tight. Thus the straw yield, as far as the gas tightness is concerned, was $324/325=99.7\%$ for the 9 modules.

The gas tightness is also checked for complete straw tube modules. A typical rate of the gas pressure loss measured with the Ar/CO₂ (90:10) gas mixture at 2 bar pressure is about 11 mbar/day ($\Delta p/p/t = 0.55\%/\text{day}$). This loss is negligible compared to the planned flow of the gas mixture through the FT stations on the level of a few gas volumes exchanges per day to refresh the gas mixture and to prevent aging effects. We measured also gas leakage for straws filled with pure Ar and pure CO₂ at 2 bar and we observed the pressure drop of about 7 mbar and 46 mbar per day, respectively. The observed difference in the gas loss rate for argon and CO₂ is characteristic for the different permeation of the specific gas molecules through the Mylar film [31].

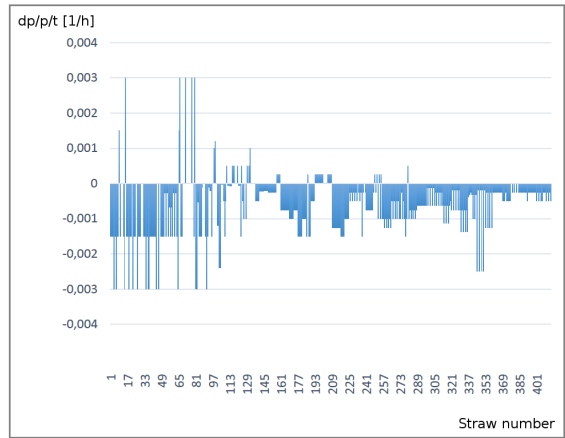


Figure 4.48: Gas leak measured for individual straws produced for 13 modules for FT5, FT6.

4.8.2 Wire Tension

For measuring the wire tension, the straw is placed in a field of a permanent magnet and a short (1 ms) current pulse is applied to excite vibrations of the wire. The tension is determined evaluating the frequency of the first harmonic of alternative current induced in the vibrating wire (see Fig. 4.49). The tension is measured with an accuracy of about 0.5 g. We accept deviations from the nominal tension of 50 g smaller than $\pm 5\text{ g}$.

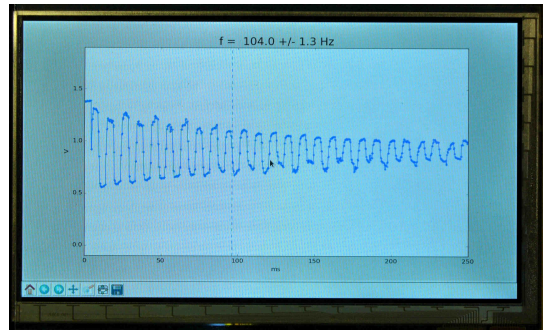


Figure 4.49: Waveform showing alternative current induced in straw tube wire vibrating in magnetic field.

This requirement is met for all 416 straw produced for the 13 prototype modules for FT5, FT6. Wire tension measured for consecutive produced straws is presented in Fig. 4.50 (top panel). Visible systematic changes of the wire tension with the straw number are presumably caused by variations of temperature and humidity in the assembly room in the course of the production. To check this hypothesis, we will monitor the temperature and the humidity

during the further production of straws.

The average value of the measured wire tension (see Fig. 4.50-bottom panel) equals 47.9 g and lies below the foreseen nominal wire tension of 50 g. The reason for this was too high pretension of the straws applied during the assembly equal 300 g. After producing the straws for the 13 prototype modules we checked, that reduction of the straw pretension to 160 g results in the wire tension close to the foreseen value of 50 g. For a better understanding of this effect (increase of the wire tension with reduced pretension of the straw) we performed calculations of the wire tension using the available data for the Young's modulus for the Mylar film and for the wire, as well as the Poisson's ratio for the Mylar. We reproduced the measured value of the wire tension of 50 g with the straw pretension of 160 g (see Sec. 4.1.1 and Appendix A).

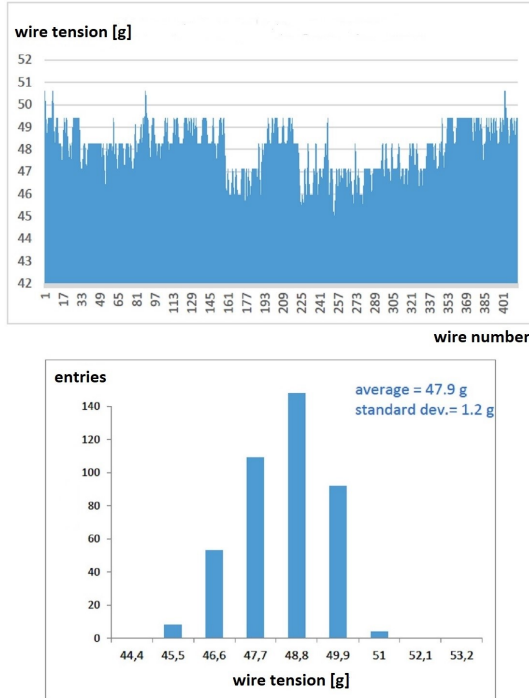


Figure 4.50: Wire tension measured for 416 straws (13 modules) with a length of 125 cm produced for FT5, FT6 in function of straw number (top panel) and a histogram of wire tension (bottom panel).

In the near future, we plan to start a measurement of the long-term stability of the wire tension in the straws. For this, we prepare a test setup comprising one straw tube module, a gas system stabilizing the pressure in the module at the level of 2 bars, sensors measuring the humidity and the temperature in the vicinity of the module and a setup for the measurement of the wire tension. The tension will

be measured in each straw every few days. The test will be carried out for about one year.

4.8.3 Control of the Module Geometry

The most extended quality tests will be conducted on straw tube modules. They will include checks of:

- gas tightness,
- dark current after conditioning at the HV working point,
- geometry of module including the straightness and width of the module, as well as positioning of individual wires and straws in the module,
- high voltage characteristics with an ^{55}Fe source measured for each straw tube,
- uniformity of gas flow through the straws in the module.

For inspection of the geometry of produced modules, we built a motorized positioning stage with a range of 2.0 m horizontally and 1.3 m vertically and a positioning precision of 0.05 mm (see Fig. 4.51). This range is sufficient to inspect not only in a single module, but also the group of modules mounted on the half frame of the FT5 and FT6 stations, the largest ones in the FT.

Inspection of the geometry of the module is performed in two steps. First, we check the straightness of the module and its width using an optical scan with a digital microscope mounted on the stage. In the second step, we measure positions of individual straws and wires in the module using a scanning technique with a collimated X-ray source.

To check the straightness of a module, we take a series of pictures along its edges using the digital microscope. The applied test setup is shown in Fig. 4.52. The straightness of the module is checked for three different settings of the microscope, corresponding to its optical axis directed to the left, right and a side edge of the module, as shown in Fig. 4.53. The microscope is used to take a series of pictures of a selected module edge along its length. The pictures are then stacked one above the other to form one continuous image of the edge. An example of an image of the side edge of a module, containing 125 cm long straws, is shown in Fig. 4.53. This image was obtained by taking 117 pictures of the module edge with a step of 1 cm along the y axis oriented along the straws, and then by arranging the pictures one above the other and squeezing



Figure 4.51: x-y stage with a positioning area of about $2.0 \times 1.3 \text{ m}^2$.

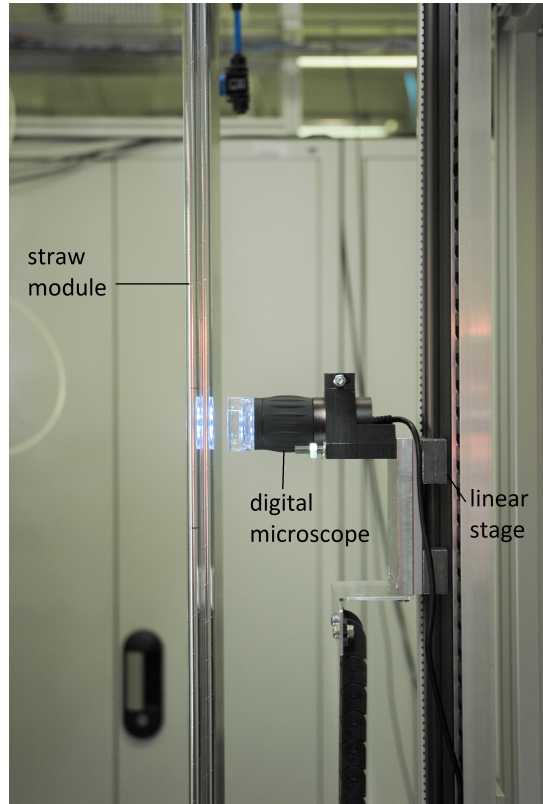


Figure 4.52: Digital microscope mounted on positioning stage and a straw tube module seen from the side.

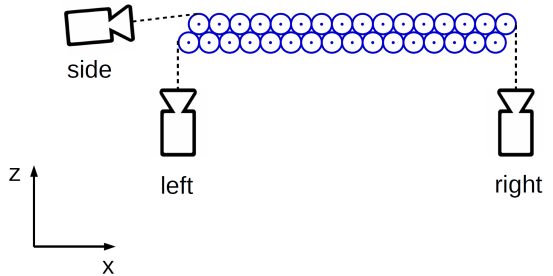


Figure 4.53: Three settings of the microscope used for imaging the left, right and side edge of the module.

them in the y-direction by a factor of about 50 for presentation and analysis.

For measuring positions of individual straw tubes in the module, we will use a scanning technique with a collimated X-ray beam from an ^{55}Fe source. By adding admixture of electronegative component to the working gas, it is possible to restrict the sensitive volume of the straw tube to a small region with a high electric field around the anode wire, and, in this way, the position of the anode wire can be measured. This method, proposed in Ref. [32], allows to determine the locations of the straw tubes and of the wires in the direction of with a high accuracy on the level of $25 \mu\text{m}$. We plan to extend this method in order to measure the straw and wire positions in three dimensions by taking stereoscopic scans with two different directions of the X-ray beam.

The tested modules will be mounted vertically (y-axis), with the active area parallel to the scanner plane (x-y plane). We will measure positions of wires in the x-z plane for two y-coordinates, close to the ends of the wires. A displacement of the anode wire from the straw axis results in a systematic error of the measured track-to-wire distance. The systematic error corresponding to the wire positioning precision of 0.1 mm is smaller than the expected statistical accuracy of the distance mea-

surement ($\sigma \sim 0.15 \text{ mm}$). Therefore, we will accept straw tube modules with the wire locations differing from the nominal ones by not more than 0.1 mm.

We will also inspect the position of the center of each straw in the x-z plane and the diameter of the straw for a few locations along its length. Under assumption, that the anode wire is mounted in the nominal position in the straw, a displacement of the straw in the x-direction significantly affects the measurement of the track-to-wire distance only at distances close to the straw radius. This is because

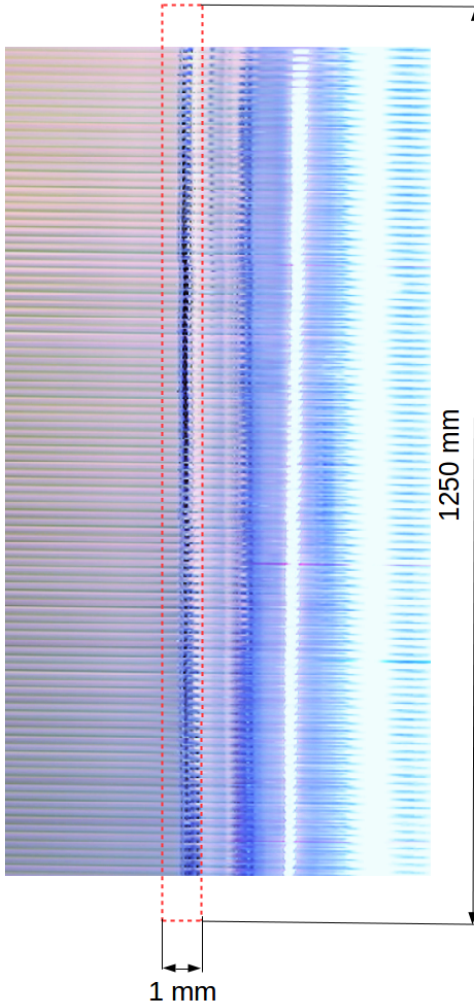


Figure 4.54: Image of a side edge of straw tube module.

the drift time - distance relation $t(x)$ remains approximately symmetric between the left and right side of the wire, as presented in Fig. 4.55, showing results of calculations made with GARFIELD [23]. The red curve in the figure corresponds to the nominal position of the straw and the blue one to a straw displaced by 0.2 mm. The difference δx between the two curves for $x = 2$ mm, 4 mm and 5 mm is 0.00 mm, 0.04 mm and 0.06 mm, and is negligible. Based on this result we will accept deviations of the straw straightness in the x-direction - parallel to the active area of the module - smaller than 0.2 mm.

A displacement of the straw center in the z-direction, in the first approximation, does not affect the measurement of the track-to-wire distance for tracks oriented in the z-direction. Since the

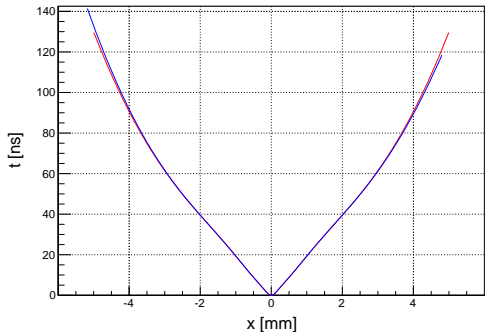


Figure 4.55: Distance- drift time relation calculated with GARFIELD for straw located centrally with the anode wire (red curve) and for straw displaced by 0.2 mm (blue curve) along the x-direction (blue curve). Simulated tracks are oriented perpendicularly to the x-axis.

tracks measured in the FT are oriented around the z-axis (the forward direction), displacements of the straws in this direction resulting e.g. from buckling of modules, are less critical than in the x-direction. Based on simulations with GARFIELD, we set the limit for an acceptable deflection of straws in the z-direction equal to 0.5 mm.

The measurements of positions of anode wire and straws will be automatized and their results will be stored in a data base including all produced modules.

An example of a scan of 32 straws in a module is presented in Fig. 4.56. The scan was done by moving the collimated X-ray beam transversely to the direction of the straws in the module with a step of 1 mm. The width of the beam at the position of the first and second straw layer was about 2 mm and 3 mm, respectively. For each step, the number of detected X-rays was measured for each straw for 10 seconds. The upper panel of Fig. 4.56 shows distributions of the number of registered X-rays in individual straws as a function of the beam position. Each of these distributions was fitted with a Gaussian function and the center of the fitted function was taken as the reconstructed coordinate of the straw. Differences between the reconstructed and nominal coordinates of straws in the module do not exceed $150 \mu\text{m}$, as shown in the lower panel of Fig. 4.56.

The scanner will also be used for illuminating individual straws with X-rays from ^{55}Fe in order to measure the plateau curve. This measurement is based on the registration of the number of straw tube pulses exceeding a fixed discrimination thresh-

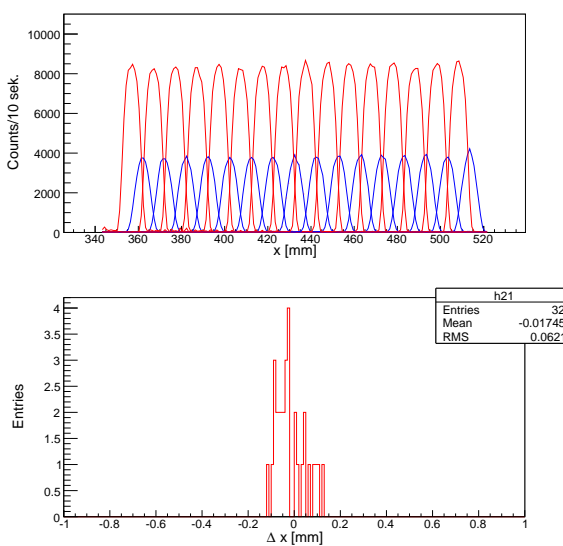


Figure 4.56: (Upper panel) Number of counts in individual straws in the tested module as a function of position of the X-ray beam. Response of the first and the second straw layer, when looking in direction of the X-ray beam, is represented with red and blue line, respectively. (Lower panel) Deviations between the measured and nominal positions of straws.

old of the front-end electronics, as a function of the high voltage applied to the anode wire. An example of the plateau curve is shown in Fig. 4.57. The main step on the curve visible slightly above 1500 V corresponds to the registration of pulses produced by the total absorption of the 5.9 keV X-rays from ^{55}Fe . The smaller step visible at higher voltage, around 1600 V, results from the argon escape peak and corresponds to the registration of an energy deposit of 2.9 keV. The data points are very well described by fitting with a sum of two cumulative distributions given by the error functions and representing the probabilities of registering the energy deposits of 5.9 keV and 2.9 keV (see Ref. [33]).

The measurement of the plateau curve is very useful to evaluate the overall module quality [34] thanks to the following properties:

- Increased level of counts at voltages below the main edge of the curve can indicate for pick up of noise signals.
- The slopes of the edges on the plateau curve are related to the noise level in the electronic channel (see Ref. [33]).
- The position of the slope depends on the gas gain and its deviation from the expected value

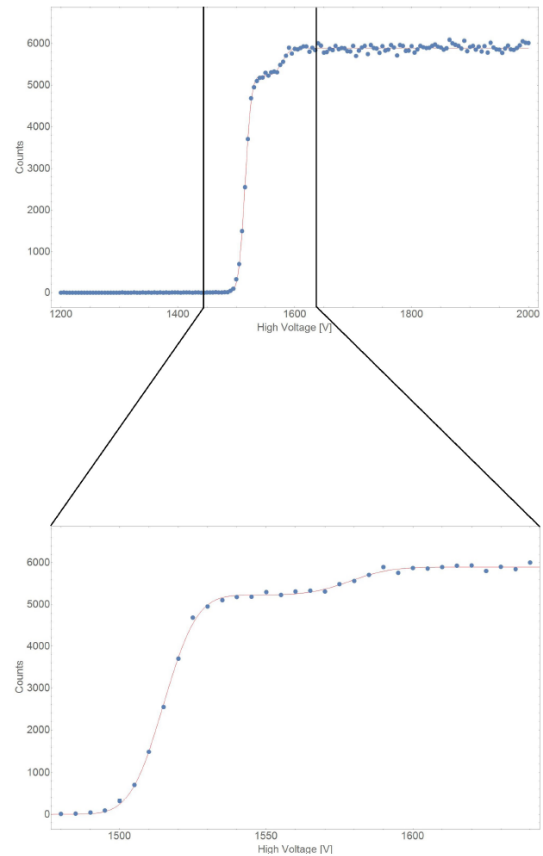


Figure 4.57: (Upper panel) Plateau curve measured for straw illuminated with X-rays from ^{55}Fe (full circles) and the fit to the data with a sum of two error functions (solid line). (Lower panel) Zoomed edge region of the curve.

can indicate impurities in the gas mixture, improper gas pressure or displacement of the anode wire from the central position.

- The width of the plateau region defines the range of the straw working voltages. A rapid increase of the measured counts, at the upper end of the curve, can indicate discharges or after-pulses.

The measurement of the plateau curve will also be used to check uniformity of the gas flow through the straws in the modules, in order to identify straws with a lower gas flow caused, for example, by a partially blocked gas supply tube. To check this, the gas composition has to be changed at some time (e.g. from Ar-CO₂ (90:10) to (80:20)) and a shift of the edge of the plateau curve has to occur [34]. The edge shifts to higher (lower) voltages for reduced (increased) argon contents. Anomalous gas

flow in a straw results in a slower movement of the edge.

Fig. 4.58 shows the plateau curves registered for 32 straws of a tested module, directly before changing the gas mixture composition from Ar-CO₂ (90:10) to (80:20), and after 60, 120 and 180 minutes from the change. Two groups of curves with higher and lower counts are visible, and correspond to the first and second straw tube layer in the module looking from the source side.

The input gas manifold of the module distributes the gas mixture to 16 gas circuits, each consisting of two straws connected in series - one from the first and the other from the second layer. The tested module was connected to the gas system in such a way that the gas was fed first to the second layer and then to the first. As a result, the movement of the plateau curves corresponding to the second layer (group of curves with the lower counts in Fig. 4.58) is faster than that of the curves for the first layer. About three hours after the change of the gas mixture (time corresponding to about 1.5 gas exchange at the flow rate applied), both edges again overlapped and end at a higher voltage of about 1650 V (see the bottom panel in Fig. 4.58).

In order to demonstrate that this measurement is sensitive to the gas flow in individual straws, we deliberately reduced the gas flow by a factor of about two in a pair of straws in one gas circuit. For this purpose, a pipe with a length of 50 cm and an inner diameter of 0.5 mm was used to increase the impedance of the gas circuit. The corresponding two plateau curves, presented with black color in Fig. 4.58, move towards the higher voltage much slower than the curves for the remaining straws with undisturbed flow, shown in red.

After the assembly of a layer of modules on the support frame, the relative positions of the consecutive modules will be checked using the X-ray scanner.

The high voltage conditioning of the straws in the modules will be done in two phases. First, each module will be conditioned during the quality tests after its assembly. The conditioning will be continued for a few weeks after mounting a layer of modules on support frame and connecting it to the supplies.

Fully assembled tracking stations, equipped with the read-out electronics, will undergo the following tests at the production site:

- long term test (~1 month) under high voltage in order to verify stability of operation of the station,
- measurement of Time-over-Threshold (TOT) spectra with ⁵⁵Fe in order to check uniformity

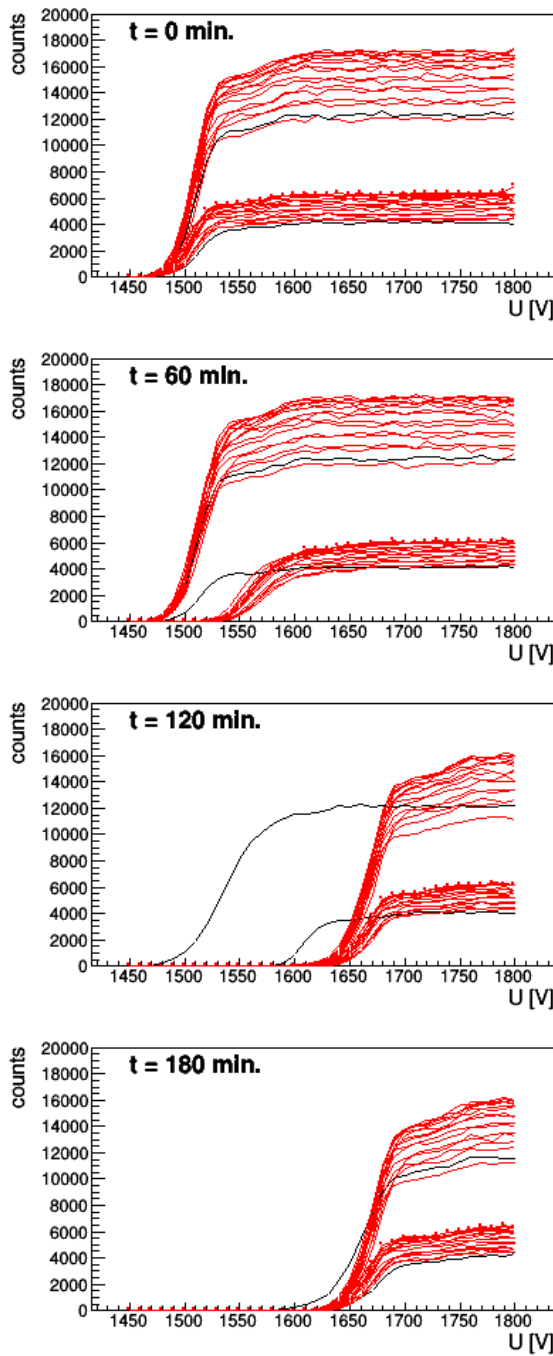


Figure 4.58: From top to bottom: Plateau curves registered for 32 straws in a tested module just before changing the gas mixture composition from Ar-CO₂ (90:10) to (80:20), and after 60, 120 and 180 minutes from the change. The two black curves correspond to a pair of straws with a gas flow deliberately suppressed by a factor of two compared with the others.

- of the height of signals in individual channels,
- measurement with cosmic rays triggered by auxiliary scintillators in order to inspect the drift time spectra in individual channels and to check the quality of the track reconstruction and the alignment of the double layers.

4.9 Detector Integration

The supplies for the FT can be placed either in the counting house or in the experimental hall. Each of these possibilities has advantages and disadvantages. An advantage of the location in the counting house is an easy access to the supplies and negligible radiation doses. Its drawback are long cables and gas pipes, in the order of 50 m, for connecting the supplies to the detector, which can result in additional electronic noise and lead to an increase of the detector costs.

Taking this into account, we plan to place the high voltage supply and the gas mixing system in the counting house. The gas distribution systems, the digitizing electronics and the low voltage supplies will be located in the experimental area, in the vicinity of the FT. They will be placed in racks indicated schematically as R1 and R2 in Fig. 4.59. The racks R1 will serve tracking station installed before and inside the dipole magnet (FT1, ..., FT4). In turns, the racks R2 will be used for tracking stations FT5 and FT6 which are placed on the Forward Spectrometer platform. The racks R2 will be fixed to the platform in order to avoid disconnecting cables and gas pipes when moving the platform between the parking and the experimental positions. R2 will contain only the gas distribution and the low voltage supply for the FT5, FT6 since the digitizing electronics will be mounted directly on the frames of the stations. The signal cables, high voltage cables, low voltage cables, cables for test signals and the gas pipes are led between the tracking stations and the racks in cable trays indicated schematically as L1, L2 and L3 in Fig. 4.59.

4.10 Infrastructure

4.10.1 The Gas System

The preferred gas mixture for the FT is argon with an admixture of about 10% CO₂ (90:10) as the quenching component. The same mixture was chosen for the $\bar{\text{P}}\text{ANDA}$ -STT. The details that brought to this choice are illustrated in Sec. 4.1.2. This gas

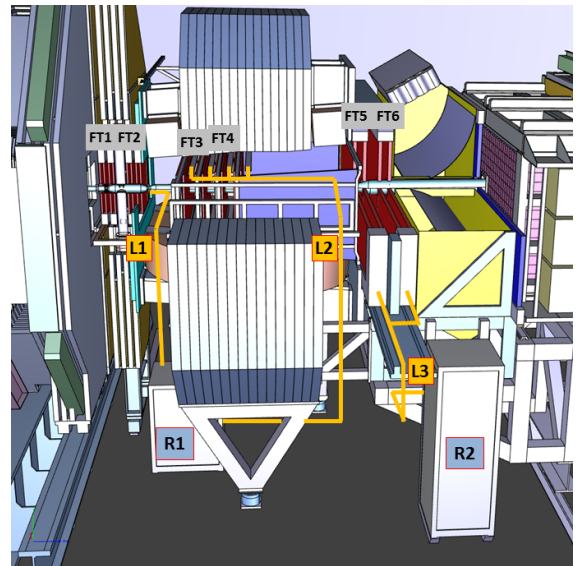


Figure 4.59: Scheme of cable and gas tubes routing for the FT.

mixture has capability to tolerate high irradiation levels since no deposits on the straw tube electrodes from polymerization reactions occur. It is required, however, that there is a clean gas environment including all materials and parts of the detector and gas supply system in contact with the gas. For both gas components a high purity grade is required (argon with grade 5.0, CO₂ with 4.8). The supply lines consist of polished stainless steel pipes and thermoplastic (PA) tubing where a higher flexibility is needed. Since argon and CO₂ are non-flammable, not expensive, and components of the atmosphere, no recirculation and containment of the gas mixture is needed, and the gas supply of the detector is done in flushing mode. The FT will be operated at a gas pressure of 2 bar (absolute) and preferably at room temperature. The total FT gas volume of about 9121 l is exchanged typically every six hours with a flow rate of about 2.5 l/min to refresh the gas mixture and to prevent an accumulation of contaminants in the detector and gas system.

The gas system of the FT is analogous to the one designed for the STT. It consists of supply gas bottles for each mixture component, cleaning filters in the gas lines, a mixing section with ratio-based mass flow controllers and a gas distribution system for supplying gas mixture to separate sections of the FT. Each line of the gas distribution comprises a mass flow controller regulating the flow, and an outlet valve which regulates the absolute pressure in the FT sector to 2 bar based on data from pressure sensor connected to the sector volume. After

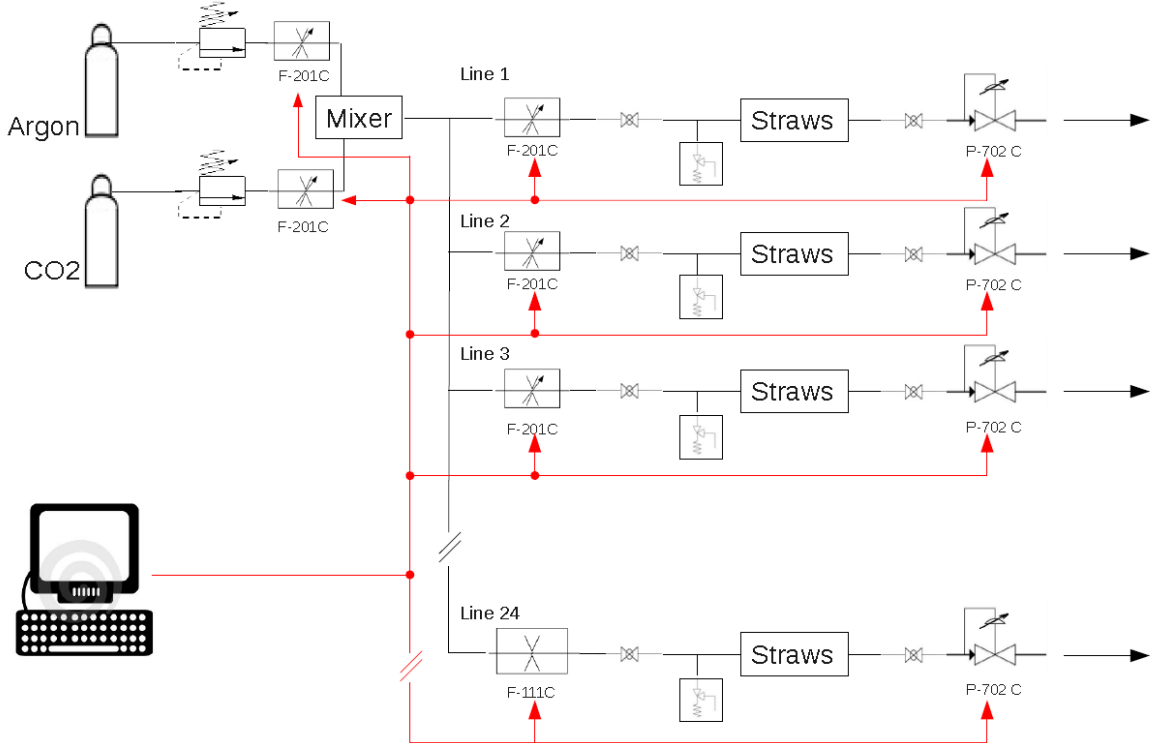


Figure 4.60: Scheme of the gas system.

the outlet valve, gas flows to a dedicated exhaust line at the $\bar{\text{P}}\text{ANDA}$ experimental area. The scheme of the gas system is shown in Fig. 4.60. For the Ar/CO₂ gas mixture the required accuracies of the settings and control have to be better than 0.3% (absolute) for the mixture ratio, about 1-2 mbar for the pressure, and 1 K for the temperature. Monitoring of the gas system will be included in the FT slow control (see Sec. 4.10.3).

The $\bar{\text{P}}\text{ANDA}$ FT consists of six tracking stations. Each station contains four double-layers of straw tubes. In the consecutive tracking stations FT1, FT2, FT3, FT4, FT5 and FT6 the double layers have volumes of about 131, 131, 241, 301, 741 and 741, respectively. Each double-layer is connected to individual supply line and thus 24 supply lines are needed. With this choice, the gas flow through each double layer can be controlled individually, and, in case of failure of one line, only one double layer in a tracking station must be turned off. Modules organized as a double layer of straw tubes are connected in parallel to the gas supply line. In each module, the manifold distributes the gas to 16 parallel circuits, each containing two straw tubes connected in series (see Sec. 4.2.2). The impedance of the gas supply lines is dominated by the plastic pipes with

inner diameter of 0.5 mm which are used for connecting the straw tubes to the gas manifold and for interconnecting the two straws in each pair. The impedance of the plastic pipes provides balanced flow among all straws in a module.

For testing straw tube detectors, we built a gas system (see Fig. 4.61) which can be considered as a prototype of the gas system for the FT. It contains two mass flow controllers for mixing argon with CO₂ and a third one for automatic pressure stabilization in the straw tubes based on the pressure measured in the gas inlet to the straw modules. For the pressure stabilization, the proportional-integral-derivative algorithm implemented in the control software is applied. The pressure stabilization works with a precision better than 0.5 mbar. The system contains three pressure sensors. One measures the pressure at the inlet, the second - at the outlet from the modules, and the third one is used for monitoring the atmospheric pressure. The sensors are placed in a temperature stabilized box, in order to get rid of uncertainties connected with non zero temperature coefficients of the sensors. The system is controlled with the National Instruments PXI controllers and the LabVIEW software [35]. In order to avoid an uncontrolled rise of a pres-

sure in the straws caused e.g. by computer crash, we use an autonomous system consisting of a pressure sensor and an electromagnetic valve, which, in case of excess of the pressure, cuts out the gas supply to the straws. We protect also the gas system against an uncontrolled turning on after a power failure by using a contactor on the power line.

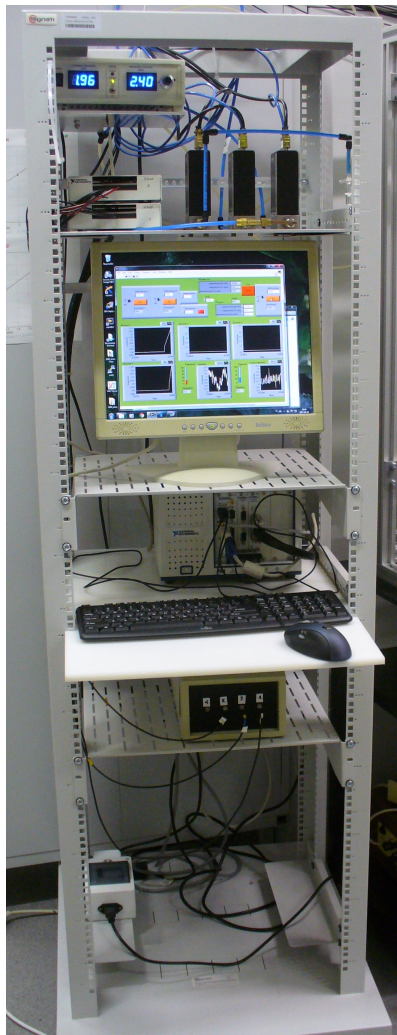


Figure 4.61: Gas system used in tests of prototype straw tube modules.

4.10.2 The Power Systems

4.10.2.1 High-Voltage System

Each straw tube module will be connected to a separate high voltage supply channel. This will allow to avoid unacceptably large loss in the active area, if one of the HV channels has to be turned off e.g. due to a straw tube failure. The high voltage sup-

ply units will be placed in the counting house. The length of HV cables leading to the tracking stations will be about 50 m.

In order to estimate the maximum current that can flow in one HV channel, we assume that the straw tubes are operated at the nominal voltage of 1800 V. With the selected gas mixture the gas gain is then $5 \cdot 10^4$. The current produced by minimum ionizing particles at the highest expected counting rate of 1.4 MHz/straw is $2.2 \mu\text{A}$. In one module comprising 32 straws, the current can thus reach $70 \mu\text{A}$. Including an additional safety factor of 2, accounting for a background of low energetic - highly ionizing particles, and another factor of 5 to allow the possibility of a higher working voltage, we come to the conclusion that the HV supply should be able to provide currents of at least $700 \mu\text{A}$ per channel.

The high voltage supply system will possess all necessary features required for a safe operation of the FT including over-current protection and reduction of high voltage to a lower level e.g. when needed during the beam injection phase. Monitoring of the high voltage units will be included in the FT slow control system.

4.10.2.2 Low-Voltage System

The FT read out electronics comprising 800 FEE cards and 69 TRBv3 boards demands about 1.4 kW of power. One 16-channel FEE card requires a supply voltage of 3.3 V and a current of 0.17 A. In turns one TRBv3 board needs 49 V and 0.3 A.

Each group of FEE cards reading out one layer of straw tube modules in the tracking stations FT1, 2, 3, 4 will possess individual power supply line. In FT5 and FT6, each double layer will be served with two supply lines. The total number of supply lines for the stations FT1..6 will be 32 ($=4+4+4+4+8+8$). The current in the supply lines will be 6 A for FT1, FT2 and about 9 A for FT3, FT4, FT5, FT6. Applied fine granularity of supply lines allows an easy registration of variation in a drawn current which can result from a failure of a FEE card.

The TRBv3 boards used for the read out of one of the tracking stations, will be connected to one power supply line in the case of FT1..4 and to two lines in the case of FT5 and FT6. Thus, the total number of low voltage channels will be 8 and the current in a channel will be at most 2.7 A.

The low voltage supply units will be placed in the same location as the gas distribution racks (see previous section). A feedback system will be used to

compensate for the voltage drop on the cables. The FEE cards are equipped with linear regulators, and, therefore, it is acceptable that the supply voltage exceeds slightly the nominal value. Monitoring of the low voltage power supply units will be included in the FT slow control system.

4.10.3 Detector Control System

The Detector Control System (DCS) of the FT is one branch of the general \bar{P} A N DA Experiment Control System (ECS). The control system has to continuously collect the actual parameters from the supply and electronic readout systems and compare them with their set values and predefined tolerances. In addition, parameters of the detector environment, like for instance temperatures and humidities at several locations must be monitored.

In case of big deviations, a specific alarm message should be generated to inform the detector operators. Some of the data must be stored on disk and added to the experiment data for possible off-line corrections of the detector measurements. The DCS system will manage a database with the mapping of the physical channel source (voltage, current, temperature, etc.), the label and the relevant calibration constants.

The parameters which have to be considered for the FT are:

- gas supply system: gas mixture composition, pressure and temperature at several locations in the in- and outlet lines, gas flow;
- high and low voltage supply systems: voltage, current and status (trip, ramp, on, off) values for every supply line;
- electronic readout system: settings of the FEE boards including gain, discriminator thresholds, baseline levels and pulse shaping constants for every readout channel, supply, reference voltage and temperature of every readout board;
- detector environment: temperature and humidity at several locations.

The gas supply system will be controlled by the user via Graphical User Interfaces (GUI). An example of such interface, prepared for the prototype gas system, using the LabVIEW environment is shown in Fig. 4.62. The GUI for the final gas system will be prepared based on the Control System Studio (CSS) framework, which provides an interface to EPICS.



Figure 4.62: Graphical User Interface prepared with the LabVIEW environment for the prototype gas system.

For the high and low voltage distribution, multi-channel power supply systems like CAEN SY1527 will be used. This system consists of a main frame allowing the housing of a wide range of boards providing high and low voltages. High voltage supplied, current, ramp up and down times, will be the parameters to be controlled by the DCS system using a dedicated bus or Ethernet connection.

For the FEE a few channels of low voltages can be housed in the same main frame. This system allows an easy communication with the mainframe through Ethernet using an OPC server software which can be easily integrated in the DCS.

For a stable FT operation, remote access and monitoring of the FEE cards is mandatory. Therefore, the DCS will be connected to the FT FEE cards via a dedicated bus. The software will permit addressing via read-write operations the status and control registers of the FEE ASIC chips. Moreover, through the slow control software interface, various test and/or calibration pulses will be generated.

The present version of the Graphical User Interface for controlling the working parameters of the FEE cards (see Fig. 4.63) is prepared in HTML 5 with the use of CSS styles. Java Script instructions are used to prepare the command word and forward it, over the Ethernet, to the TRB-v3 boards. The received word is then decoded and sent to the FEE cards using 4 line custom protocol.

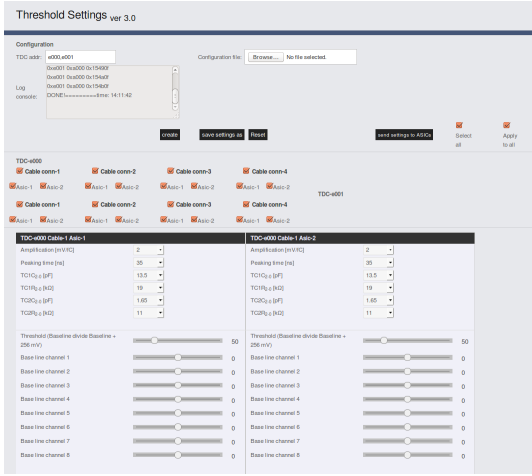


Figure 4.63: Graphical User Interface for controlling the working parameters of the FEE cards.

4.11 Alignment and Calibration Methods

4.11.1 Alignment

Accuracy of the track reconstruction obtained with position sensitive detectors, depends not only on the intrinsic position resolution of the detectors, but also on the accurate knowledge of their locations in space (alignment). Alignment of the Forward Tracker stations will be done after the first installation as well as after each re-installation. It will proceed in two steps. First, the positions of the tracking stations will be measured using optical survey instruments (e.g. Leica laser tracker [36]). The measurements will be used for introducing corrections in the FT geometry files used in the data analysis software.

In the second step, further corrections to the FT geometry will be determined based on reconstruction of tracks of cosmic rays and of particles produced in the \bar{p} -p collisions (track-based alignment). For this, one of existing least square formalisms, such as the Millepede algorithm [37], can be used. The track-based alignment will be done for correcting the six coordinates of each tracking station (three Cartesian coordinates and three inclination angles). It will also be used for correcting relative positions of components of the tracking stations such as the double layers of straw tubes.

The measurement with the cosmic rays will be performed with the magnetic field in the PANDA solenoid and dipole magnet turned off. The registered straight tracks will be used for relative align-

ment of tracking stations in each pair (FT1, FT2), (FT3, FT4) and (FT5, FT6). Switching off the dipole magnet for conducting the alignment with straight tracks origination from the \bar{p} -p collisions is not feasible, since it leads to a loss of the HESR beam. Therefore, the alignment with the tracks originating from the interactions in the target will be done with the magnetic field turned on and it will be used for correcting the relative positions of the three pairs of the tracking stations.

4.11.2 $r(t)$ Calibration Curve

The calibration of the FT includes a determination of the characteristic relation between the measured drift time and the isochrone radius. The calibration benefits from the mechanical properties of the pressurized, thin-wall ($27\ \mu\text{m}$) straw tubes, having a perfect cylindrical shape and precise diameter. The experience from the COSY-STT with 2700 straw tubes, also pressurized and with a similar thin film wall ($32\ \mu\text{m}$), showed that a global isochrone calibration for all straws together is sufficient. The individual time offsets from the electronic readout system have to be corrected only once.

The calibration proceeds in two steps. First, an approximate calibration is determined based on the drift time spectra registered during data taking. For this, the so-called uniform irradiation method is applied. In the second step, reconstruction of registered tracks is used to calculate corrections to the calibration based on systematic deviations between the measured and fitted track distance to the wire. In the following, the calibration procedure is described in details.

Fig. 4.64 shows an example of a measured time spectrum for a uniformly illuminated straw tube, with some particular noise contribution from the electronic readout system. The analysis of the time distributions of individual straws allows the monitoring of the data quality: the minimum and the maximum drift times, t_0 and t_{max} , correspond to a track traversing the tube close to the wire and close to the cathode wall, respectively. The value of t_0 depends on the signal cable length, discriminator threshold, high voltage setting and delays in the readout electronics. Nearby tubes sharing the same front-end electronics are expected to have a similar value of t_0 ; on the contrary, the drift time $\Delta t = t_{max} - t_0$ depends only on the drift properties of the tubes. The number of events outside the drift time window gives an estimate of the random, constant noise level over time range (see Fig. 4.64) [38].

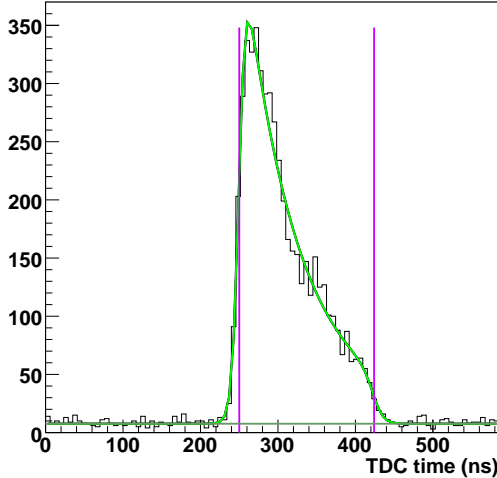


Figure 4.64: Example of a fitted TDC spectrum. The light green line is the fit of the distribution; the violet vertical lines correspond to the t_0 and t_{max} values determined by the fit. The dark green horizontal line indicates the noise level.

For each tube, the parameters of the drift time distribution are derived from a fit performed with the following empirical function [38, 39, 40]:

$$\frac{dn}{dt} = P_1 + \frac{P_2 [1 + P_3 \exp((P_5 - t)/P_4)]}{[1 + \exp((P_5 - t)/P_7)][1 + \exp((t - P_6)/P_8)]} \quad (4.2)$$

where P_1 is the noise level, P_2 is a normalization factor, P_3 and P_4 are related to the shape of the distribution, P_5 and P_6 are the values of t_0 and t_{max} . P_7 and P_8 describe the slope of the leading and trailing edge of the distribution, so they are indicators of the drift tube resolution close to the wire and to the tube wall, respectively. The fit result of Fig. 4.64 shows as an example the fit of the function (green line) to a measured TDC spectrum. In order to do a common calibration for all the tubes, their time spectra must have approximately the same shape and the same maximum drift time Δt . A quality check on the uniformity of the tubes, as well as on the quality of the fit, can be done by looking at the distributions of the fit parameters.

After the selection of the similar spectra, their specific time offset t_0 is corrected and their noise level is subtracted; then, they are added into a sum spectrum, each in its Δt range. Under the hypothesis of a uniform illumination of the tube and a constant efficiency over the tube volume, the isochrone radius – drift time relation ($r(t)$) relation in the following) can be obtained by the following integration:

$$r(t) = \frac{R_{\text{tube}}}{N_{\text{tot}}} \int_0^t \frac{dn}{dt'} dt' \quad (4.3)$$

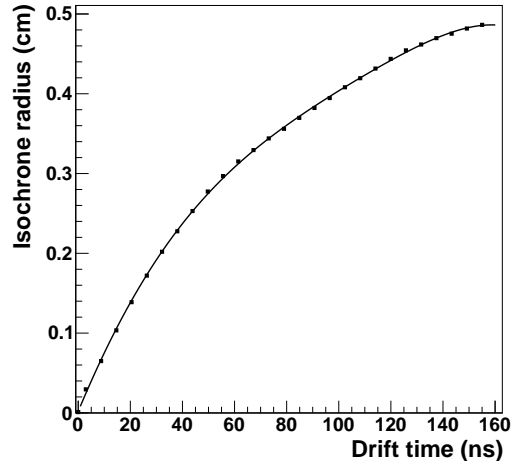


Figure 4.65: Isochrone radius – drift time relation ($r(t)$), parametrized using a combination of Chebyshev polynomials of the first kind, up to the fifth order.

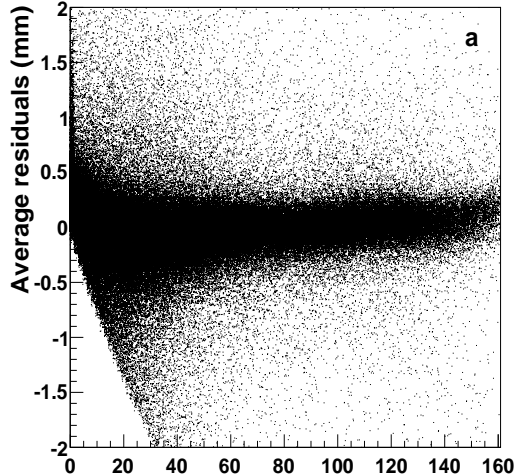


Figure 4.66: Distribution of the average residuals as a function of the drift time at the first iteration.

where n is the number of tracks, N_{tot} is the total number of tracks and R_{tube} the tube radius.

Taking into account the finite TDC resolution (bin size) and the wire radius R_{wire} , Eq. 4.3 becomes:

$$r(t_i) = \frac{\sum_{i=1}^{i_t} N_i}{N_{\text{tot}}} \cdot (R_{\text{tube}} - R_{\text{wire}}) + R_{\text{wire}} \quad (4.4)$$

R_{wire} is the wire radius and N_{tot} is the sum of all bin entries N_i . The obtained space–time relation is then parametrized as a polynomial function.

An example of the $r(t)$ curve is shown in Fig. 4.65; in this case, the space–time relation has been parametrized with a combination of Chebyshev

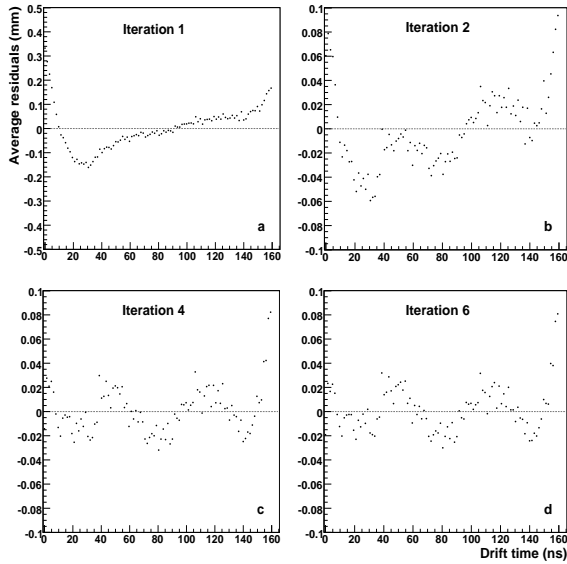


Figure 4.67: Distribution of the average residuals as a function of the drift time after one (a), two (b), four (c) and six (d) iterations of the autocalibration procedure.

polynomials of the first kind up to the fifth order:¹

$$\begin{aligned} r(t) = & p_0 + p_1 t + p_2(2t^2 - 1) + p_3(4t^3 - 3t) \\ & + p_4(8t^4 - 8t^2 + 1) + p_5(16t^5 - 20t^3 + 5t) \end{aligned} \quad (4.5)$$

Once the space-time relation is known, the isochrone radius of a certain tube is computed by substituting in Eq. 4.5 the measured drift time. This is calculated by subtracting from the measured drift “raw” time the time offset t_0 of that tube, obtained from the fit of Eq. 4.2.

Once the calibration curve has been derived, it is possible to proceed with the track reconstruction. In order to perform a good track fitting, it is necessary to know with high precision the relation between the measured drift time and the distance of closest approach of the particle trajectory to the wire. This implies an accurate knowledge of the $r(t)$ relation, that can be achieved with an iterative procedure called **autocalibration**, since it makes use of just the information from the tubes under investigation.

The autocalibration works as follows: at each step of the procedure, the $r(t)$ relation derived in the previous iteration is used to convert the measured drift times into drift radii, which will be used in the track fitting. At the first step, the $r(t)$ relation obtained directly from the integration of the drift time spectra is used. Once a track candidate has been identified through dedicated pattern recogni-

tion algorithms, the track is reconstructed by using a track fitting algorithm. It allows to extract the (x, y) hit coordinates from the drift times and the (x, y) coordinates of the firing wires, which are the observables measured by the straw tubes. The fitting algorithms implemented for the **PANDA-FT** will be described in detail in Sec. 6.2; the tracking procedure used for the test systems will be briefly presented in Sec. 5.5.4. In this last case, in general tracks are reconstructed as straight lines $y = a + bx$, where the parameters a and b are obtained by a least squares fit (χ^2) that minimizes the track residuals, i.e. the difference of the distances of closest approach of the best fit lines to the centers of the firing tubes and the corresponding isochrones calculated from the measured drift times using the $r(t)$ relation. For each tube of the pattern associated with a track, the residuals are then computed and represented as a function of the N bins the drift time interval is divided into. If the $r(t)$ relation was exact, the average residuals would be zero at all radii.

An example of a residual distribution is shown in Fig. 4.66: at this step, the mean value of the residuals varies from a minimum of $\sim 160 \mu\text{m}$ to a maximum of $\sim 320 \mu\text{m}$ for small radii. These deviations from zero indicate a miscalibration in the $r(t)$ relation, which is then corrected by taking the average deviation. The track reconstruction and the $r(t)$ calibration with the residuals as input are then repeated until the corrections become negligible and the mean value of the residuals is close to 0, as shown in Fig. 4.67.

To study the speed and stability of the convergence of the method, the following quantity (mean square correction):

$$\Delta_k^2 = \frac{\sum_{i=0}^N \delta_{ik}^2}{N} \quad (4.6)$$

where δ_{ik} is the mean value of the residuals in the i^{th} time bin and N is the total number of bins, can be used as figure of merit (Fig. 4.68).

The recalibration procedure is iterated until the mean square correction has converged to a stable solution [41].

1. The Chebyshev polynomials of the first kind are defined by the recurrence relation:

$$\begin{aligned} T_0(x) &= 1, \\ T_1(x) &= x, \\ T_{n+1}(x) &= 2xT_n(x) - T_{n-1}(x). \end{aligned}$$

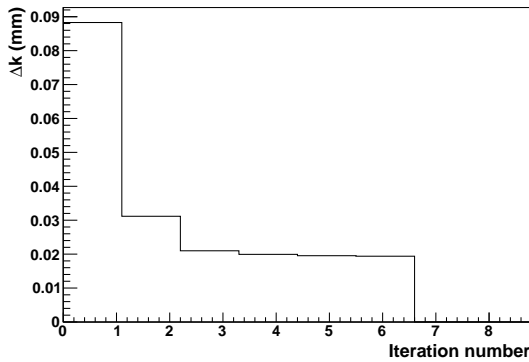


Figure 4.68: Root mean square correction from the autocalibration procedure.

References

- [1] P. Wintz, *A large tracking detector in vacuum consisting of self-supporting straw tubes*, in *Intersections of Particle and Nuclear Physics: 8th Conference CIPANP2003*, volume 698 of *Issue 1*, pages 789–792, AIP Conf.Proc., (2004).
- [2] W. Erni et al., Eur. Phys. J. **A49**, 25 (2013), <http://arxiv.org/abs/1205.5441>.
- [3] Mylar, polyester film, registered trademark of DuPont, www.dupont.com.
- [4] <http://luma-metall.com/servizi/gold-plated-tungsten-rhenium-wire/>.
- [5] <http://www.doganak.com/wp-content/uploads/2014/07/Mylar-%C2%AE-A-12-36mic.pdf>.
- [6] <http://usa.dupontteijinfilms.com/resources/technical-information/>.
- [7] B. Schmidt, Nucl. Instrum. Methods **A515**, 364 (2003).
- [8] *ATLAS Inner Detector Technical Design Report*, CERN/LHCC/97-17, ATLAS TDR 5.
- [9] RM-no DOP-Tube, RAUMEDIC,, <https://www.raumedic.com/>.
- [10] Thermo-plastic,
Acrylonitrile-Butadiene-Styrene.
- [11] UHU endfest 300, UHU GmbH & Co. KG - P.O. Box 1552, D-77813 Bühl, www.uhu.de.
- [12] MG Chemicals 8331S, MG Chemicals, www.mgchemicals.com.
- [13] K. Makonyi, *DIY Radiation Mapping for the PANDA detector*, Status Report, January 12, 2015.
- [14] S. Spataro (for the PANDA collaboration), J. Phys.: Conf. Ser. **331**, 032031 (2011).
- [15] A. Capella et al., Phys. Rept. **236**, 225 (1994).
- [16] C. Guarino, F Hauviller and M. Tavlet, *Compilation of Radiation Damage Test Data, Part IV: Adhesives*, CERN 2001-006 (2001).
- [17] P. Beynel, P Maier and H. Schonbacher, *Compilation of Radiation Damage Test Data, Part II: Materials used around high-energy accelerators*, CERN 82-10 (1982).
- [18] NASA Outgassing Data for Selecting Spacecraft Materials, <https://outgassing.nasa.gov>.
- [19] PH-DT-DI Gas Project, CERN, <http://detector-gas-systems.web.cern.ch/detector-gas-systems/HomePage/homePage.htm>.
- [20] Loctite 408, Henkel Loctite Europe, Gutenbergstr. 3, 85748 Garching, www.henkel.com.
- [21] Parker-Legris, www.legris.com.
- [22] SERTO, www.serto.com/chen/.
- [23] R. Veenhof, *GARFIELD, Simulation of gaseous detectors*, version 7.04 edition, CERN Program library write-up W 5050.
- [24] D. Przyborowski et al., JINST **11**, P08009 (2016).
- [25] P. Strzempek, *Development and evaluation of a signal analysis and a readout system of straw tube detectors for the PANDA spectrometer*, Ph.D. Thesis, Jagiellonian University, Krakow, Poland (2017).
- [26] W. Bonivento et al., Nucl. Instrum. Methods **A491**, 233 (2002).
- [27] M. Traxler et al., JINST **6**, C12004 (2011).
- [28] J. Kalisz, IEEE Trans. Instr. and Measurement **46**, 55 (1997).
- [29] J. Wu, *The 10-ps wave union TDC: Improving FPGA TDC resolution beyond its cell delay*, pages 1082–3654, IEEE Nuclear Science Symposium Conference Record, (2008).

- [30] E. Bayer, IEEE Trans. on Nuclear Science **58**, 1547 (2011).
- [31] M. Mapes et al., Journal of Vacuum Science and Technology **A12**, 1699 (1994).
- [32] C. Kendziora et al., *A straw drift chamber for operation in vacuum*, NUIMA FERMILAB-PUB-02-241-E, <http://inspirehep.net/record/600324/files/fermilab-pub-02-241-E.pdf?version=1>.
- [33] M. Morales, *Straw characterization based upon ^{55}Fe plateau*, sist.fnal.gov/archive/2003/Morales/Paper.doc.
- [34] K. Ziemek, *Quality control of straw tube detectors for the PANDA experiment*, Master Thesis, Jagiellonian University, Krakow, Poland (2016).
- [35] National Instruments, ni.com.
- [36] Leica, http://www.leica-geosystems.com/en/Laser-Tracker-Systems_69045.htm.
- [37] V. Blobel and C. Kleinwort, *A new method for high-precision alignment of track detectors*, Conference of Advanced Statistical Techniques in Particle Physics, Durham, (2002), <http://arxiv.org/abs/hep-ex/0208021>.
- [38] G. Avolio et al., Nucl. Instrum. Meth. **A523**, 309 (2004).
- [39] A. Biscossa et al., Nucl. Instrum. Meth. **A419**, 331 (1998).
- [40] M. Bellomo et al., Nucl. Instrum. Meth. **A573**, 340 (2007).
- [41] S. Costanza, *Design of the Central Tracker of the $\bar{\text{P}}\text{ANDA}$ experiment*, PhD thesis, Università degli Studi di Pavia, (2010).

5 Prototype Results

5.1 Test Systems

The experience from different straw test systems and dedicated test measurements have been taken into account in the design of the $\bar{\text{P}}\text{ANDA-FT}$. The Straw Tube Tracker of the COSY-TOF experiment (COSY-STT) is considered to be a global test system, due to the similar mechanical layout of close-packed, self-supporting straw modules and its operation in the experimental environment of proton-proton collisions with a proton beam momentum around 3 GeV/c. COSY-TOF is a non-magnetic spectrometer (see Fig. 5.1) and the tracks are reconstructed as straight lines instead of the bent trajectories measured in the FT. Nevertheless, the cal-

straws, arranged in 8 close-packed layers is shown in Fig. 5.2. Different studies of prototypes including energy-loss measurements and tests of detector performance with high intensity proton beams are presented in the Technical Design Report for the $\bar{\text{P}}\text{ANDA STT}$ [1]. Here we concentrate on the results of the aging tests which are some of the most critical issues for the FT. They are summarized in Sec. 5.3.

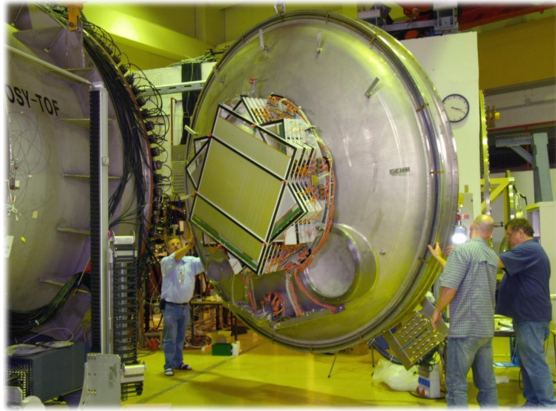


Figure 5.1: Mounting of the COSY-STT in the time-of-flight barrel of the COSY-TOF spectrometer.

ibration method of the COSY-STT, the obtained spatial resolution and the mechanical precision of the detector, which consists of 2700 straw tubes, are of interest for the $\bar{\text{P}}\text{ANDA-FT}$ design and expected performance. The COSY-STT operated in the large (25 m^3) evacuated time-of-flight barrel of the spectrometer for about 5 years. The surrounding vacuum was a strong test of all straw materials and assembly techniques, which are the same or similar to the $\bar{\text{P}}\text{ANDA-FT}$. In the next section, the properties and results of the COSY-STT are presented.

The performance of the self-supporting straw detectors has been also intensively studied in order to design the $\bar{\text{P}}\text{ANDA-STT}$. For this purpose, numerous prototype detectors were built and tested. An example of a test system consisting of 128

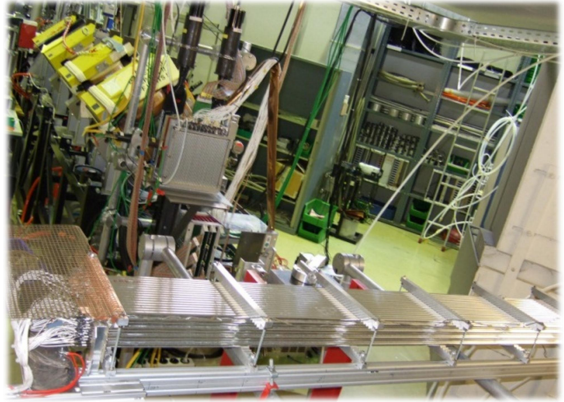


Figure 5.2: Straw setup (in front) for the energy-loss test measurements. The proton beam is coming from the back.

In order to develop the modules for the FT, the group from the Jagiellonian University in Krakow built in total 21 prototype modules: one long module with straws of length 150 cm, 3 short modules with length 68 cm, corresponding to straws in the FT1 and FT2 stations as well as 13 modules with 125 cm straws and 4 modules with 60 cm straws, foreseen for the FT5 and FT6 stations.

The three short modules with 68 cm long straws, arranged one behind the other, as in the course of the performed tests of tracking, are shown in Fig. 5.3. The modules were used to check various aspects of the mechanical construction, for optimization of the read out electronics as well as for tests of performance with radioactive sources, cosmic rays and the proton beam of the COSY-Juelich accelerator. The tests at COSY were done in two measuring periods - in May 2015 and in April 2016 - for a total of about three weeks of beam time. The main aim of the tests was to check the tracking at particle rates, comparable with those expected in the FT at the maximum $\bar{p}\text{-}p$ interaction rate, and to study applicability of the TOT measurement of the straw

pulses for the particle identification. The obtained results are presented in Sec. 5.5.



Figure 5.3: Three prototype modules for the FT1 and FT2 station, mounted on a support frame and equipped with FEE cards.

The aim of constructing the prototype modules for the FT5, 6 tracking stations was to check the developed production procedure and the quality of a larger number of produced straws and modules. Results of the quality tests are presented in Sec. 4.8.

In order to check the concept and technical details of the self-supporting half-frame for the modules described in Sec. 4.5.3, we constructed a prototype half-frame for the tracking stations FT5, FT6 and we equipped it from one side with modules as shown in Fig. 5.4. The mechanical properties of the half-frame, in particular the precision and reproducibility of positioning modules, are currently being checked as discussed in Sec. 4.5.3.

In addition to conducting various quality tests, the prototype modules for the FT5, 6 tracking stations will be used to build the forward tracker for the HADES detection facility [2]. This tracker will be used in selected HADES experiments, dedicated to the spectroscopy of hyperons, in the period before

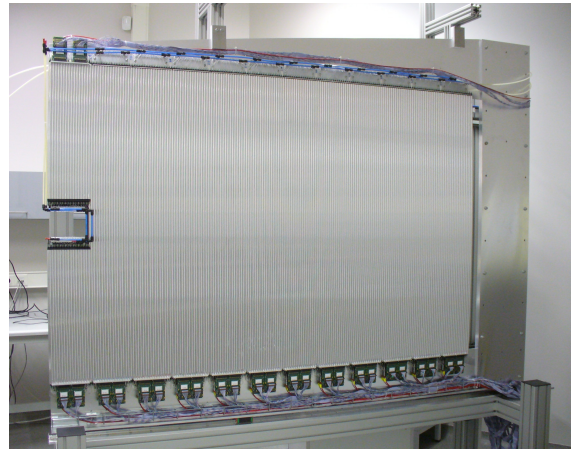


Figure 5.4: Double layer of the straw tube detectors mounted on a prototype half-frame for the tracking stations FT5, FT6. The double layer contains 11 modules with 125 cm long straws and two short modules with 62 cm straws (on the left) used to create an opening for the beam pipe.

the start of the PANDA experiment. In this way, the technology developed for the PANDA STT and FT including the straw detectors and the read-out electronics can be used and tested under realistic conditions.

The HADES forward tracker will consist of two planar tracking stations - STS1 and STS2, covering polar angles below 6.5° . The station STS1 comprises 20 straw tube modules arranged in four layers - two horizontal and two vertical. The modules are compatible with the 3rd and 4th double layer of the PANDA Forward Tracker station FT3. The STS2 station contains 32 modules arranged in four layers with four different views: $0^\circ, 90^\circ, +45^\circ, -45^\circ$, mounted on two quadratic support frames. The modules are compatible with the PANDA FT5, FT6. One STS2 frame fully equipped with modules is already prepared by the Krakow FT group (see Fig. 5.5) and the second one will be built in 2018. The STS1 station is being built by the Juelich STT group. It is planned, that both stations will be ready for installation at HADES at the end of 2018.

5.2 The COSY-TOF Straw Tube Tracker

The technique of pressurized, self-supporting straw tube layers was first developed for the Straw Tube Tracker of the COSY-TOF experiment (COSY-



Figure 5.5: One half of the tracking station STS2 for HADES comprising a pair of double layers of straws mounted on a quadratic frame. The visible double layer contains vertical straws and the second one - mounted on the other side of the frame - contains horizontal straws. The double layers contain a central opening for the beam.

STT) at the COSY-accelerator (Juelich, Germany). The used straw tube materials and dimensions, and the geometry of planar, close-packed multilayers are the same or quite similar to those of the \bar{P} *A*ND*A*-FT. Although the COSY-TOF is a non-magnetic spectrometer, the calibration methods for the straw tube positions and isochrone radius - drift time relation are similar for both detectors. The operation of the COSY-STT, with a gas volume of about 2751 installed in a vacuum tank, is an outstanding technical challenge. The required minimal leakage of the detector in vacuum is a strong and sensitive proof of all straw materials, gluing and assembly techniques, which are also crucial for the \bar{P} *A*ND*A*-FT. Therefore, the COSY-STT can be considered a global test system for the \bar{P} *A*ND*A*-STT and the \bar{P} *A*ND*A*-FT. Its properties and performance results are summarized in the following.

The COSY-STT was installed in 2009 as an upgrade of the COSY-TOF spectrometer, which consists of a large (25 m^3) vacuum barrel with a liquid hydrogen target cell at the entrance, followed by a start detec-

tor, the silicon-microstrip detector, the straw tube tracker (STT), and a scintillator hodoscopes covering the barrel walls and end cap. The apparatus allows to measure the time-of-flight and the spatial directions of the decay products of hyperons produced in proton-proton and proton-deuteron collisions with a polarized proton beam. The vacuum ensures low background produced by the beam and reaction particles with up to 3.5 m track lengths. More details about the experimental program and the STT installation can be found in [3] and [4]. A first data taking to study the hyperon production with polarized proton beam was carried out in 2010.

The COSY-STT consists of 2704 straw tubes, each with a length of 1050 mm, inner diameter of 10 mm, and a thickness of $32\text{ }\mu\text{m}$ of the aluminized mylar film. The tubes are arranged as a vertical stack of 13 close-packed double-layers with three different orientations ($\phi=0^\circ, 60^\circ, 120^\circ$) for a 3-dimensional track reconstruction. A $15\times 15\text{ mm}^2$ beam hole in the center of every double-layer is realized by splitting the 4 central straws into 8 straws with about half length (see Fig. 5.6). The straws are filled with a gas mixture of Ar/CO₂ (80/20%) at a pressure of 1.25 bar. The typical operation voltage is 1840 V. The electronic readout consists of low-power trans-impedance preamplifiers directly connected to each straw in vacuum and feeding the signals through 13 m coaxial signal cables to ASD8B-discriminators and TDCs, which are located outside the vacuum barrel.

The COSY-STT has been used for 5 years in vacuum and no real leakage sources of the detector, caused by dissolving glue spots, brittle materials, or loose gas connections, have been observed. The gas leakage remained at the permeation level, caused by the flow of the gas molecules through the thin mylar film wall. Fig. 5.7 shows the gas loss by measuring the pressure drop inside the straws when the STT is filled with pure argon and pure CO₂. The difference in the gas loss rate for argon and CO₂ of about a factor of 10, is an indication of the different permeation of the specific gas molecules through the mylar film, and it is in accordance with reference measurements by the manufacturer (DuPont Teijin Films, USA). For the used gas mixture of Ar/CO₂ (80/20 %) the total leakage is about 2 % of the STT volume per day. The typical gas flow during the high voltage operation is about four times the STT volume per day (=10001/day).

The calibration of the STT consists in the determination of the isochrone radius - drift time relation and in the adjustment of the straw positions and it is performed with an iterative procedure. First of



Figure 5.6: The COSY-STT mounted at the front cap of the COSY-TOF spectrometer. The detector consists of 2704 straw tubes of 1 m length and 10 mm diameter, arranged as a vertical stack of 13 close-packed double-layers at three different orientations.

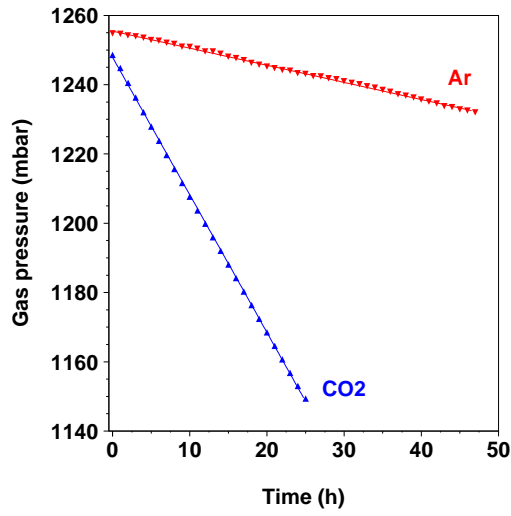


Figure 5.7: Gas leakage of the COSY-STT filled with pure argon (red) and pure CO₂ (blue), measured by the gas pressure drop of the straws in surrounding vacuum.

all, the isochrone - drift time relation ($r_{iso}(t)$ in the following) determined by an integration of the drift time spectrum after having corrected it with the proper time offset, is parametrized as a polynomial

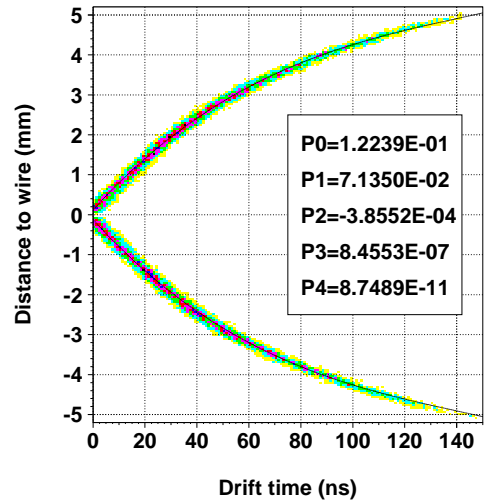


Figure 5.8: Track to wire distances and measured drift times for the reconstructed tracks. The $r_{iso}(t)$ -relation (black line) is parametrized as a polynomial function of 4th order with the parameters P_0 – P_4 .

function of 4th order:

$$r_{iso}(t) = \sum_{i=0}^4 P_i \times t^i. \quad (5.1)$$

Then, tracks are reconstructed as straight lines with a least squares fit (χ^2) to the isochrones calculated from the measured drift times using the defined $r_{iso}(t)$ -relation. Fig. 5.8 shows, for all reconstructed tracks, the distances from the straw wires versus the measured drift times. A systematic deviation in the track distance for single straws or straw groups from the expected $r_{iso}(t)$ -relation is corrected by adjusting the straw position accordingly. Here, the assembly technique of the STT simplifies the calibration procedure to a large extent. Individual displacements of single tubes in the close-packed double-layers are not possible, and only the vertical position of the 13 double-layers have to be adjusted. The track reconstruction is repeated using the new straw layer positions, the distances are checked and the positions are corrected again until the systematic deviations vanish. Finally, also the $r_{iso}(t)$ -relation is verified with a new fit.

The distribution of the finally obtained residuals of the reconstructed tracks is a measure of the spatial resolution of the STT, and it is shown in Fig. 5.9. Only a simple filter for single hits from delta-electrons with large distortions to the fitted track has been applied. No drift time correction due to the signal propagation time along the wire and the particle time-of-flight have been made. The estimated drift time error is about $\Delta t=2$ ns. Also the reconstruction of a straight line track does not take

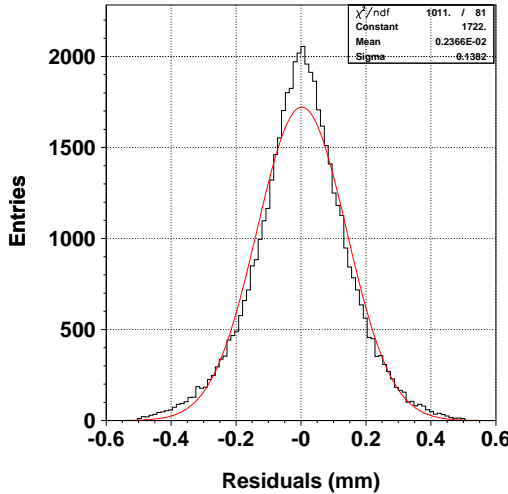


Figure 5.9: Distribution of the residuals of all reconstructed tracks as a measure of the COSY-STT spatial resolution. The width of $138\text{ }\mu\text{m}$ (σ) and mean of $2\text{ }\mu\text{m}$ are the results from the Gaussian fit (red line).

into account multiple-scattering inside the STT which contributes to a maximum of about $100\text{ }\mu\text{m}$ for the first and last layers. The spatial resolution of the STT is given by the width of the residual distribution, which is $138\text{ }\mu\text{m}$ (σ) for the gas mixture of Ar/CO₂ (80/20%) at an absolute pressure of 1.25 bar. The shape of the distribution is nicely symmetric with a mean value of $2\text{ }\mu\text{m}$, pointing out no major systematic errors.

The straw tube spatial resolution is not constant, but varies with the radial distance from the wire, as shown in Fig. 5.10. Close to the wire, the resolution is about $190\text{ }\mu\text{m}$, dominated by the primary ionization cluster spacing that together with higher drift velocities produce a larger time jitter. Both effects are reduced more and more for larger distances and the resolution improves to about $100\text{ }\mu\text{m}$ close to the straw cathode, where the electron diffusion during their drift to the anode is the limiting factor.

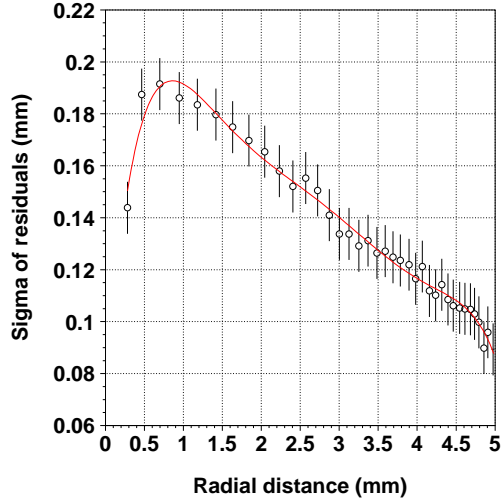


Figure 5.10: Width (sigma) of the residual distributions for different intervals of the radial distances from the wire.

nomenons in gaseous detectors can be found in [5] which is a summary of a dedicated workshop with about 100 detector experts, held at DESY (Hamburg, Germany) in 2001. In the following the main aspects relevant for the \bar{P} *ANDA*-FT are discussed.

Two main sources of aging have been identified in wire chambers. A growth of polymeric deposits on the electrodes which can change the electric field, create sparking, produce dark- or even self-sustaining (Malter) currents. At high irradiation densities and high gas gains already trace contaminations on the sub-ppm level in the gas can lead to such deposits. Another aging source is a possible oxidation of the sense wire. Usually the wire is protected by an outer gold-plating layer which makes the wire highly inert to chemical reactions. If oxygen produced in the amplification avalanche penetrates through the gold-layer to the inner wire by permeation or at imperfection spots (holes), it can oxidize the wire with a swelling of the inner wire diameter and a cracking of the gold-plating layer [6]. The increased wire diameter reduces the gas gain at a given voltage by the lower electric field strength on the wire surface. A quantitative description of the aging process is difficult due to the high complexity with an influence for instance of the gas mixture and purity, trace contaminations, construction materials, gas flow, irradiation area and intensity, ionization density, high voltage setting, particle type and energy.

The proposed Ar/CO₂ gas mixture is known as being one of the best gas mixtures for high-rate hadronic environments due to the absence of polymerisation reactions of the components. Contam-

5.3 Aging Tests

A degradation of the straw tube properties, like a specific gas gain reduction or high voltage instabilities during operation, caused by irradiation is normally called aging. In general, aging is induced by the plasma-chemical processes during the gas amplification processes with a high density of ions, electrons, excitation photons, free radicals and possible molecular dissociations and polymerizations. A complete overview and description of the aging phe-

inations of the gas or detector materials with silicone, e.g. from lubricants, must be avoided, since they produce a strong growth of non-volatile SiO₂ crystals on the wire. An admixture of CF₄ to the gas can remove such SiO₂ deposits, but due to its high additional wire etching capability, special care is needed. Hydrocarbons are better quenching agents compared to CO₂, but they have not been considered for the $\bar{\text{P}}\text{ANDA}$ -FT because of their high polymerisation rate, which can lead to deposits on the electrodes. In particular deposits on the cathode can produce self-sustaining currents with a possible high voltage breakdown (Malter-effect) [5]. In general a moderate gas gain of about 5×10^4 is recommended. This reduces the occurrence of limited streamer mode pulses which increasing the avalanche size accelerate aging [7].

The behavior of the straw tubes under very high irradiation was studied at COSY with a proton beam. The goal was to check the influence of the beam exposure and charge deposition on the straw gas gain, high voltage operation stability and to verify that all assembled materials, including the gas system, do not create harmful pollution, e.g. by out-gassing. Within the short time of about 10 days beam irradiation it was possible to collect a charge deposition in single tubes up to about 1.2 C/cm, comparable to a few years of operation of the $\bar{\text{P}}\text{ANDA}$ detector at full luminosity.

For the aging tests, a dedicated straw system consisting of a close-packed double-layer of 32 tubes was used. The straw design and all materials were the same as used for the COSY-TOF straw tracker, i.e. 30 μm thick mylar film tubes with 10 mm diameter and a length of 105 cm. The straw tube detectors for the $\bar{\text{P}}\text{ANDA}$ FT contain end-plugs constructed differently than those used in the COSY-TOF straws. However, the materials having contact with the working gas are identical in both types of straws, namely:

- straw tube aluminized Mylar film,
- gold-plated tungsten-rhenium anode wires,
- ABS plastic end-plugs,
- adhesive for gluing end-plugs inside straws (UHU endfest 300),
- micro PVC (medical quality grade) pipes for gas supply,
- steel capillary tubes for connecting the gas pipes.

Therefore, we infer, that the presented results of the aging tests of the COSY-TOF straws apply also to the $\bar{\text{P}}\text{ANDA}$ -FT straws.

The aging tests were done with the dedicated straw system installed behind the COSY-TOF apparatus and exposed to the residual proton beam with a momentum of about 3 GeV/c during about 2 weeks. Due to the horizontal placement of the double-layer and a beam spot of about $2 \times 2 \text{ cm}^2$, the particle rate through all tubes was almost the same. The surrounding alignment frame consisted of sandwich bars with a Rohacell core reinforced by Carbon fiber skins [8]. Therefore, interaction of the beam with this low-density foam material ($\rho=0.05 \text{ g/cm}^3$) was negligible.

The gas supply was divided into four parallel lines, each serving eight straws. Thus, it was possible to test at the same time straws filled with four different gas mixtures and gas gains with the same particle rates. The chosen gas mixtures were argon based, with different fractions of CO₂ (10 % and 30 %) and one mixture with 10 % ethane. The gas pressure for all mixtures was 1650 mbar. The typical gas flow was one volume exchange per hour. In total, 16 high voltage supply channels (one channel per two straws) allowed to operate the straws at different voltage levels and gas gains. The current of every voltage channel was monitored with a resolution of 2 nA. All straws were equipped with preamplifiers and 30 m long signal cables ending in the counting room. Therefore, it was possible to check analog signal shapes and signal rates during beam irradiation for every straw. Table 5.1 lists the straw settings during the beam test.

The total live-time with beam on the straws was 199 hours after correcting the COSY spill time structure and beam breaks. All straws were exposed to the proton beam at the same longitudinal position, in the middle of each tube. The beam rate and cross section profile was measured by a scintillating fiber hodoscope placed behind the COSY-TOF apparatus and in front of the straw setup. The derived proton intensity per straw during extraction was about $2.3 \times 10^6 \text{ s}^{-1}$. The slightly lower pulse rate of $\approx 2.0 \times 10^6 \text{ s}^{-1}$, measured for the single straws, could be explained by losses of low amplitude signals due to the damping inside the 30 m long cables.

During the beam time, no high voltage failures, dark currents or broken wires due to the high charge load were observed. A maximum current on single straw wires of up to 2.3 μA was measured.

A possible gas gain reduction, due to the proton beam irradiation, was checked after the beam time

Table 5.1: List of straw settings and charge load during the beam test. The last column shows the normalized gas gain reduction in the irradiated straw region with a measurement resolution of about 2 %. The aging intervals give the minimum and maximum gain reductions, e.g. 0–7 % means that at least one straw showed no gain reduction and one a maximum of 7 %.

Straw no.	Gas mixture	Voltage (V)	$\sum Q$ (C/cm)	Aging $\Delta G/G_0$
1–8	Ar/CO ₂ (10 %)	1750	0.72	0–3 %
9–16	Ar/CO ₂ (10 %)	1700	0.58	0–7 %
17–20	Ar/CO ₂ (30 %)	2200	1.23	no
21–24	Ar/CO ₂ (30 %)	2100	0.79	no
25–32	Ar/C ₂ H ₆ (10 %)	1550	0.87	no

by exposing all straw tubes to a ⁵⁵Fe radioactive source with 5.9 keV γ -emission. In the argon-based gas mixtures the photo-absorption produces a localized ionization spot with a characteristic number of about 220 electrons. Therefore, the recorded signal amplitude height was a direct measure of the gas gain. The amplitude heights were checked for each straw at different longitudinal positions around the beam irradiation spot and normalized to the amplitude heights far from the irradiation spot (see Fig. 5.11). A lower amplitude height indicates a reduction of the gas gain ($\Delta A/A_0 = \Delta G/G_0$). The estimated resolution error of the measurement was about 2 % of the amplitude height.

It can be seen that for all straws filled with 30 % CO₂ or 10 % ethane no gas gain reduction was measured, even for the highest charge loads up to 1.2 C/cm. Some, but not all straws filled with 10 % CO₂ showed a small gas gain loss up to 7 % at the beam irradiation spot. A clean spatial correlation between the reduced gas gain and beam intensity distribution, measured by the scintillating fiber hodoscope in front of the straws, was observed. The results of the gas gain measurement together with the total charge loads for all 32 straws are summarized in Table 5.1.

The absence of any aging in the straws filled with ethane or the higher CO₂ percentage indicated no general problems with the gas purity, and a pollution by the used straw materials or gas system could be excluded. The small gas gain reduction observed only for some of the straws operated with the lower 10 % CO₂ admixture, might be explained by the known poor quenching capabilities of CO₂, together with the very high irradiation perpendicular to the wire and concentrated at a small spot of about 2 cm along the wire during the beam test. Due to the incomplete avalanche quenching the occur-

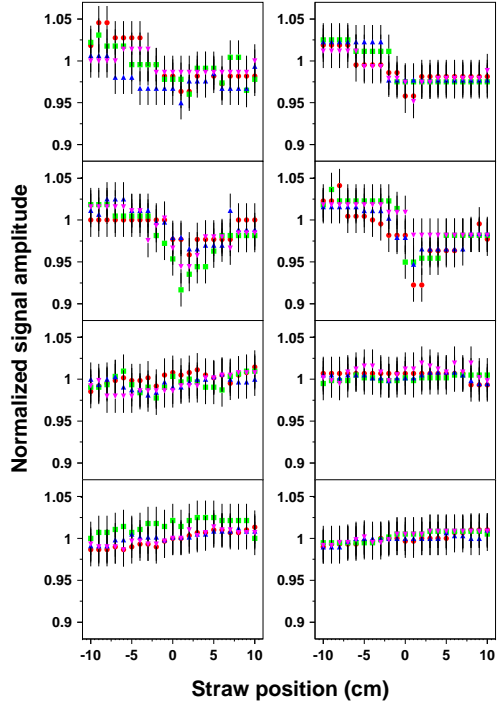


Figure 5.11: Normalized gas gain reduction ($\Delta G/G_0$) measured along the tube for all 32 straws, shown in groups of 4 straws. Straw no. 1–4 (upper left) to straw no 29–32 (lower right). The beam hit all tubes around 0 cm longitudinal position.

rence of limited streamer mode pulses, with the characteristic double-peak signal shape, was higher for that gas mixture. The high ionization density with a large number of produced oxygen ions and radicals increased the probability of oxygen permeation through the gold-layer to the inner wire. The oxidation of the inner tungsten-rhenium wire caused a swelling of the wire diameter, and as a result the electric field strength at the wire surface

was reduced ($E \propto 1/r$). This lowered the gas gain at the same high voltage setting. Since the observed gas gain reduction was very small, the occurring aging processes were rather weak. To clearly identify the sources of aging, dedicated investigations with a higher charge load over a much longer time period would be needed.

The highest particle fluxes in the FT, expected for the maximum $\bar{p}p$ interaction rate of $2 \times 10^7 \text{ s}^{-1}$ and the beam momentum of 15 GeV/c, reach up to $25 \text{ kHz} \cdot \text{cm}^{-2}$ in the vicinity of the beam line, at the position of the FT1 station (see Fig. 3.2). With increasing distance from the beam line they drop rapidly and e.g. at 40 cm distance they lay below $4 \text{ kHz} \cdot \text{cm}^{-2}$ in all FT stations.

The expected accumulated charge in the straw tubes was estimated under the assumption, that the gas gain equals $5 \cdot 10^4$ and the primary ionization amounts to 200 electrons, as expected for minimum ionizing tracks passing close to the anode wire, at right angle with respect to the straw direction. The charge accumulated in one year of the experiment, with foreseen half a year of data taking, in the high luminosity mode, at the highest beam momentum of 15 GeV/c, is presented in Fig. 5.12 as a function of the distance from the beam axis (x -coordinate) for the tracking stations FT1, FT3 and FT5. The highest accumulated charge of 0.63 C/cm/year is expected in the first module of FT1. This module is located directly near the beam pipe. For distances from the beam axis $x > 40 \text{ cm}$, the accumulated charges lie below 0.075 C/cm/year . In ten years of the lifetime of the experiment, this limit corresponds to 0.75 C/cm . Only for the central modules in the tracking stations, the charges are higher and reach the maximum value of 6 C/cm in the FT1. Presumably, some of these modules will have to be replaced after a few years of data taking due to aging effects. In reality, the accumulated charges may be a few times smaller since the PANDA physics program includes, in the dominant part:

- studies at smaller beam momenta than the assumed 15 GeV/c, for which the interaction rate and the multiplicity of produced particles is lower,
- measurements in the high resolution mode with roughly 10 times smaller interaction rate than in the assumed high luminosity mode,
- measurements with nuclear targets, for which the rates in the FT are essentially smaller than for the hydrogen target.

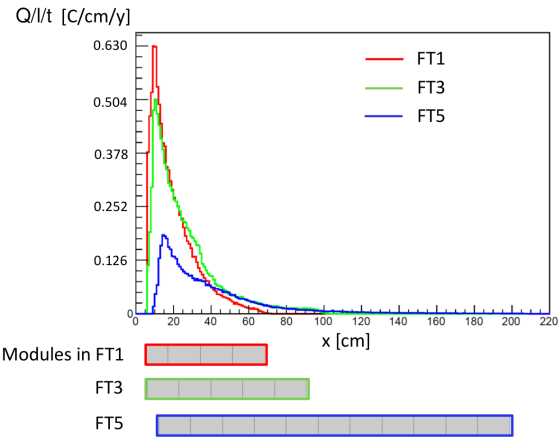


Figure 5.12: The accumulated charge in C/cm/year expected in the high luminosity mode, at the highest beam momentum of 15 GeV/c, presented as a function of the x -coordinate (perpendicular to the beam direction at the target) in the horizontal symmetry plane ($y = 0$), for the tracking stations FT1, FT3 and FT5. Due to the left-right symmetry of the detection system, the accumulated charges are presented only for $x > 0$. Below the plot, the horizontal bars indicate the horizontal range of the active areas in the three tracking stations.

5.4 Laboratory Tests with ^{55}Fe

Some of the basic properties of the prototype straw tube modules have been examined using 5.9 keV X-rays from the ^{55}Fe isotope. The advantage of using the ^{55}Fe source is a point ionization resulting in regular straw tube pulses, not disturbed by the drift time spread occurring in the case of charged particles tracks. The number of the ionization electrons of about 220 is very close to 200 electrons produced by a minimum ionizing particle on a path equal to the straw tube diameter. The performed studies, including determination of the signal-to-noise ratio, variation of signal amplitude along straw length, cross-talk between straws and gas gain drop at high rates, are presented in the four subsequent subsections.

5.4.1 Signal-to-Noise Ratio

The signal-to-noise ratio was measured for the straw tube pulses at the analog output of the FEE. The measurement was done for the gain parameter in the FEE set to 1 mV/fC and three different settings of the peaking time parameter: 15, 20 and 35 ns. These settings were selected as the optimal ones concerning minimal under and overshoot,

high amplitude and shortest rise time (see discussion in Sec. 4.6.2) and are as follows:

- **setting 1:** Gain = 1 mV/fC, Peaking time = 15 ns, $TC_{C1}=13.5\text{ pF}$, $TC_{R1}=19\text{ k}\Omega$, $TC_{C2}=1.5\text{ pF}$, $TC_{R2}=23\text{ k}\Omega$ (see Table 4.7),
- **setting 2:** Gain = 1 mV/fC, Peaking time = 20 ns, $TC_{C1}=10.5\text{ pF}$, $TC_{R1}=27\text{ k}\Omega$, $TC_{C2}=0.9\text{ pF}$, $TC_{R2}=20\text{ k}\Omega$,
- **setting 3:** Gain = 1 mV/fC, Peaking time = 35 ns, $TC_{C1}=6\text{ pF}$, $TC_{R1}=31\text{ k}\Omega$, $TC_{C2}=1.65\text{ pF}$, $TC_{R2}=23\text{ k}\Omega$.

In the following, the abbreviation s1, s2 and s3 will be used for the above three settings, respectively.

The straw tube pulses were registered using CAEN Digitizer DT5742 [9] working at a sampling frequency 1 GHz and a resolution of 0.25 mV. At the applied anode voltage of 1700 V, the straw pulse, shown in Fig. 5.13, have an amplitude of about 160 mV. The observed peaking time of the pulses corresponding to the three settings of the FEE: s1, s2 and s3, is about 25, 40 and 50 ns, respectively, and the rise time, calculated as time taken by a signal to change from 10% to 90% of the height, is about 13, 24 and 33 ns, respectively.

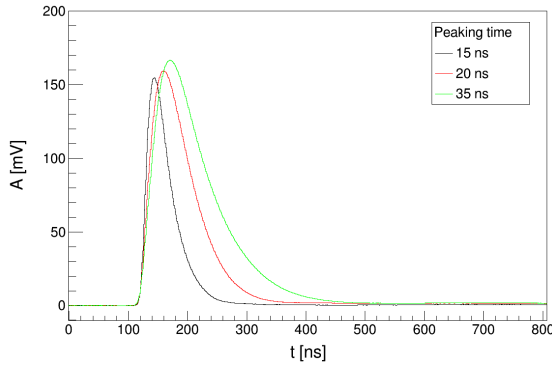


Figure 5.13: Signals registered at analog outputs of the FEE for straws illuminated with X-rays from ^{55}Fe source, for the three selected settings of the FEE parameters described in the text and the anode voltage 1700 V. To reduce statistical fluctuations of the signal amplitude, the presented signals were determined as an average of 500 recorded waveforms.

The average amplitude of pulses corresponding to absorption of the 5.9 keV X-rays from ^{55}Fe was determined from a gaussian function fit to the amplitude spectrum (see Fig. 5.14). For each registered waveform, the baseline level was determined as an average of the first 100 samples preceding the

straw pulse and then was subtracted from all samples in the waveform. A distribution of the first 100 samples corrected for the baseline was fitted with a gaussian function and the standard deviation of the function was taken as the level of noise (see Fig. 5.15). The average amplitude of pulses for the FEE setting s1, s2 and s3 was 162, 168 and 174 mV, respectively, the level of noise was 1.00, 0.84 and 0.80 mV, and the signal-to-noise ratio was 162, 200 and 218.

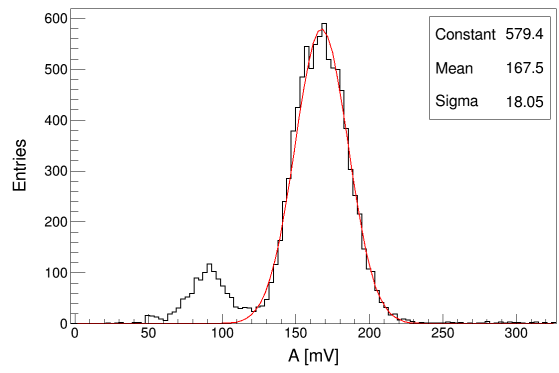


Figure 5.14: Amplitude spectrum registered for X-rays from ^{55}Fe source, for the anode voltage 1700 V and the s2 setting of FEE (black line). A gaussian fit to the 5.9 keV peak is presented with the red line.

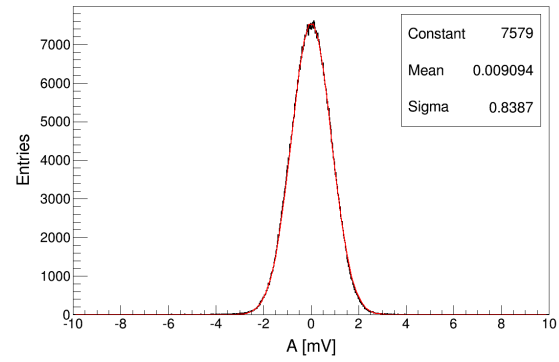


Figure 5.15: Distribution of noise for the s2 setting of FEE (black line) together with a fitted gaussian function (red line).

The signal-to-noise ratio was also determined during tests of the prototype straw tube modules with 3 GeV/c protons (MIPs) from the COSY accelerator. At the anode voltage of 1800 V and the s2 setting of the FEE, the amplitude of pulses was close to the present one observed with ^{55}Fe . However, the level of noise measured in the experimental conditions at COSY was twice as high as in the laboratory tests

discussed here and, therefore, the signal-to-noise ratio was about two times smaller and equal to 80. (see Sec. 5.5.2).

5.4.2 Signal Amplitude Variation Along Straw

Reflection of electric signal from not terminated, "far" end of the straw with respect to the FEE, as well as the signal attenuation in the straw, being a lossy transmission line, introduce dependence of the signal amplitude on the position of the ionization along the straw length. This dependence can be particularly pronounced in the straws for FT5 and FT6, due to their largest length equal to 125 cm. The amplitude and shape of straw tube pulses was determined for 5 positions of a collimated ^{55}Fe source, spaced by 25 cm along the 125 cm straws as shown in Fig. 5.16. The pulses were registered for the three settings s1, s2 and s3 of the FEE (see previous section) and are presented in Fig. 5.17. The position of the source along the straw has no visible effect on the shape of the pulses, but leads to a change in the pulse height by about 20%. With the level of the discrimination threshold in the FEE of 10 mV corresponding to more than 10 times the level of noise, the effect of the time walk due to the 20% change of the amplitude is about 0.07, 0.13 and 0.18 ns respectively for the FEE setting s1, s2 and s3. In the above estimation of the time walk we used the signal rise time determined in the previous subsection. The estimated time walk is negligible compared to the drift time interval of about 5 ns corresponding to the required spatial resolution of about 200 μm , assuming the average drift velocity of 5 mm/130 ns = 0.038 mm/ns.

5.4.3 Cross-Talk

We studied cross talk between pairs of straws in a group of 16 straws out of the 32 straws in one module, connected to one FEE card and arranged as shown in Fig. 5.18. One reference straw - number 7 in Fig. 5.18 - was illuminated with X-rays from an ^{55}Fe source. Pulses from this straw were observed on one channel of an oscilloscope (TELEDYNE LECROY MSO 44MXs-B) and were used for triggering the oscilloscope. The amplitude of these pulses was about 400 mV. Signals induced due to cross talk in the remaining 15 straws in the group were observed on the second channel of the oscilloscope. Based on these observations we have come to the conclusion that if two neighboring straws are connected to two different PASTTREC chips in the

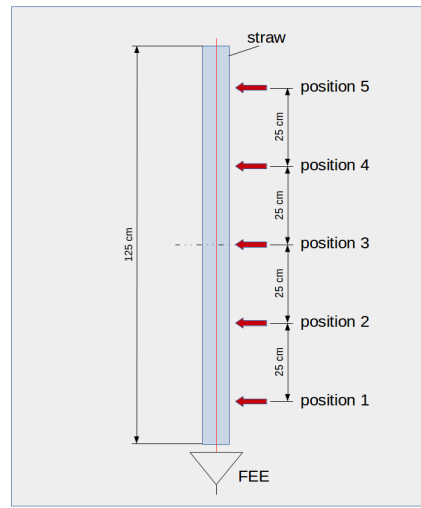


Figure 5.16: Five positions of collimated ^{55}Fe source along straw, selected for the study of signal amplitude variation along the straw length. Spacing between consecutive positions is 25 cm; position 1 is the closest to the end of the straw with attached FEE, and the position 3 corresponds to the center of the straw.

FEE card (one FEE card contains two such chips) than the cross talk pulses have an amplitude of the positive part of the pulse of about 0.6 mV. So the cross-talk is only 0.15%. Pulses registered for such a case, for the pair of straws indicated as 7 and 9 in Fig. 5.18, are presented in Fig. 5.19 (left panel).

Cross-talk between two straws that are not adjacent to each other is several times smaller, provided that the straws are not connected to the same PASTTREC chip. Otherwise we observe cross talk pulses with amplitudes of the positive and negative part of the pulse reaching up to 2.5 mV ($\sim 0.6\%$) and this is not only in the case of adjacent straws but also for not adjacent ones. An example of cross talk pulses registered for a pair straws 7 and 5 connected to one PASTTREC chip (see Fig. 5.18) is presented in Fig. 5.19 (right panel).

We compared the levels of cross-talk for the three selected settings of the FEE - s1, s2 and s3, and we did not observe a significant difference between them. We conclude, that the cross-talk between neighboring straws due to the capacitive coupling between them is of only $\sim 0.1\%$. Higher cross-talk - on the level of 0.6% - occurs due to coupling between the electronic channels in the PASTTREC chips. However, this level of cross-talk is still acceptable, since for the minimum ionizing particle and the nominal working voltage of 1800 V, the pulses have an amplitude of about 200 mV and the corresponding cross-talk pulses have a height

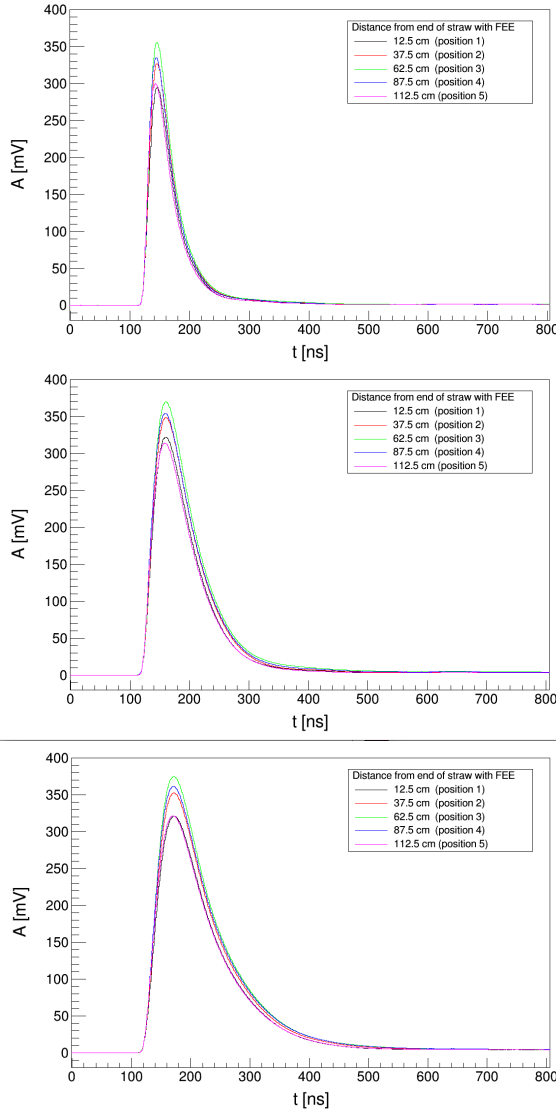


Figure 5.17: Signals registered for the five selected positions of the ^{55}Fe source along the straw and the s1 setting of the FEE parameters (upper panel), s2 setting (middle panel) and s3 setting (lower panel). The applied anode voltage was 1800 V. To reduce statistical fluctuations of the signal amplitude, the presented signals were determined as an average of 500 recorded waveforms.

of roughly 1 mV, which is ten times smaller than the foreseen discrimination threshold of roughly 10 mV. Only at much higher energy losses in the straws, the cross-talk pulses may exceed the discrimination threshold, but due to their low amplitude and adequately low Time-over-Threshold registered with the readout electronics, it will be easy to filter them out.

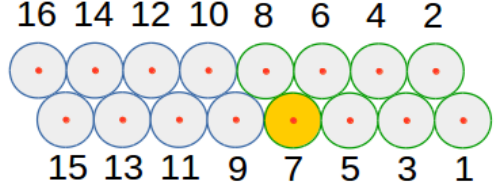


Figure 5.18: Sixteen straws (out of 32 in one module) read out by one FEE card and used in the study of the cross-talk between straws. The straws numerated from 1 to 8, indicated with green circles, are read out by one PASTTREC ASIC, and the straws 9 to 16 marked in blue are read out by the second ASIC on the same FEE board. The straw number 7 indicated in yellow was illuminated with X-rays from ^{55}Fe source and the cross-talk pulses were registered in the remaining 15 straws.

5.4.4 Gain Drop due to Space Charge

In the FT, the particle fluxes reach up to about 25 kHz/cm² in the first four tracking stations, in the vicinity of the beam pipe (see Sec. 3.1). In order to determine the gas gain drop due to the space charge of positive ions accumulated in the straw tube volume at the expected high particle rates, we illuminated locally a straw with a strong (1 GBq) collimated ^{55}Fe source (see Fig. 5.20) and we measured the amplitude of straw tube pulses as a function of the rate of pulses. For this, the analog pulses from the FEE were sampled with the CAEN DT5742 Digitizer and the position of the 5.9 keV peak in the amplitude spectrum determined by fitting a Gaussian function was used as a measure of the gas gain. The rate of pulses was varied by changing the distance between the source and the straw. It was measured at the digital output of the FEE with the TRB-v3 board. Results of the measurement of the pulse amplitude as a function of the rate per unit length of straw, performed for three different anode voltages: 1700, 1750 and 1800 V, are presented in Fig. 5.21. At the highest measured rates of about 260 kHz/cm, the pulse amplitude drops by a factor of about two compared to the lowest measured rate of 4 kHz/cm. The amplitude drop at a rate of 25 kHz/cm - the highest expected in the FT - is about 10%. This amplitude variation is acceptable from the point of view of the required precision of the drift time measurement (~ 1 ns) since the corresponding time walk is about 0.1 ns (see the estimation presented in Sec. 5.4.2).

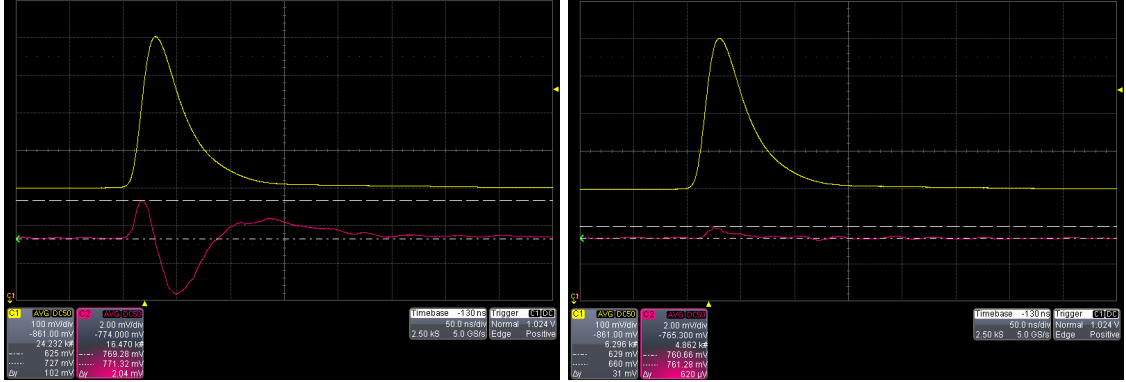


Figure 5.19: (Left panel) Oscilloscope screen shots presenting signal corresponding to the registration of the 5.9 keV X-ray from ^{55}Fe in one straw (yellow trace) and a cross-talk signal in a neighboring straw (pink trace), for a pair of straws connected to the same PASTTREC chip (left panel) and two different chips (right panel). The sensitivity setup in the oscilloscope was 100 mV per division for the X-ray signal and 2 mV per division for the cross-talk signal. The time base was 50 ns per division. To eliminate fluctuation of the cross-talk signal due to the noise, the presented signals were averaged over 500 recorded waveforms.

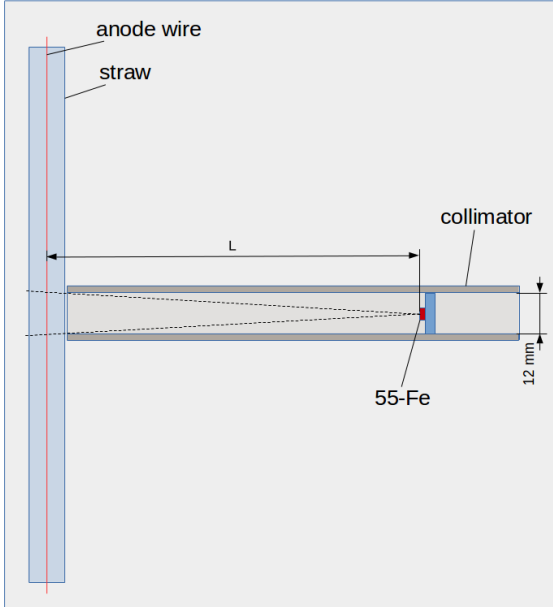


Figure 5.20: Setup applied in measurement of gas gain drop at high particle flux.

5.5 Tests with Proton Beams

5.5.1 Experimental Setup

The three prototype modules for the FT1 and FT2 station were tested with an external proton beam of the COSY-Juelich synchrotron. The tests were carried out in two measuring periods, each lasting about two weeks, in May 2015 and April 2016. The

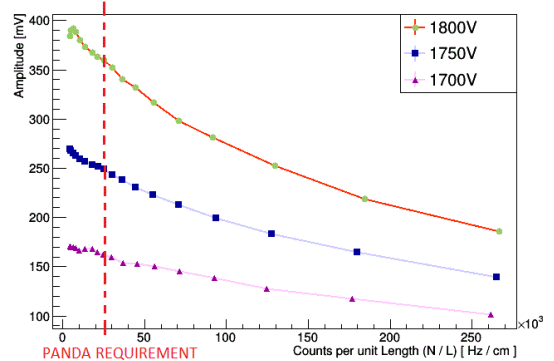


Figure 5.21: Amplitude of straw tube pulses corresponding to absorption of the 5.9 keV X-rays from the ^{55}Fe isotope, as a function of counts per unit length of the straw tube, measured for three voltages of the anode wire. The highest rate per unit length expected in the PANDA FT is indicated by the red dashed line.

tests were performed for a few beam momenta in the range from 0.55 to 3.0 GeV/c. During the tests, the modules were oriented vertically and they were arranged one after the other with a pitch of 11 cm (see Fig. 5.22). The beam was passing through all of them at approximately right angle.

Upstream of the modules, a triggering scintillator was placed, and downstream, a position sensitive GEM detector, for monitoring the beam profile, was located. A width of the beam spot was about 2 cm horizontally and 5 cm vertically. Due to the small horizontal width, the beam was illuminating mainly 1-2 straws in each layer (see Fig. 5.23).

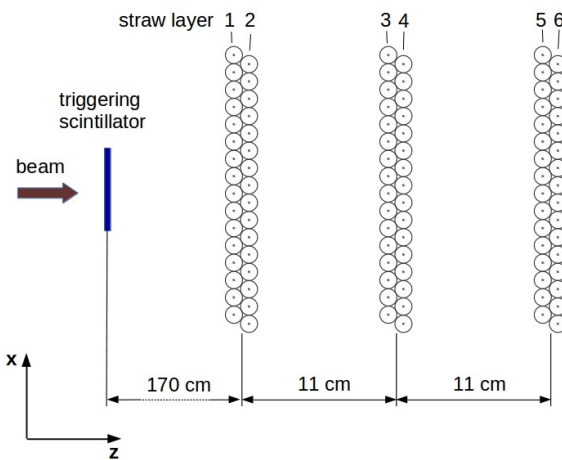


Figure 5.22: Arrangement of the prototype modules and of the triggering scintillator placed upstream of the modules.

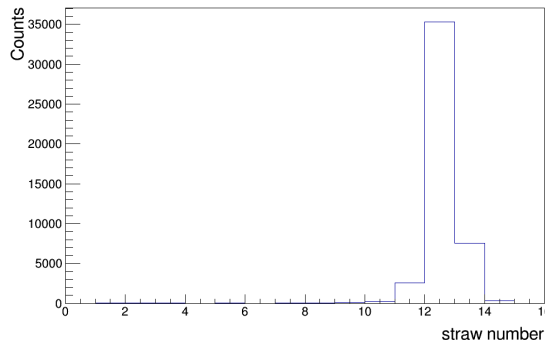


Figure 5.23: Counts on individual straw tubes in one layer illuminated with 3.0 GeV/c beam.

The tests in May 2015 were performed for two beam momenta of 0.6 and 3.0 GeV/c, and a beam intensity reaching up to 500 kHz and 200 kHz, respectively. The average counting rate in the straws illuminated by the 3 GeV/c beam was in the order of 200-400 kHz, but due to the beam bunching the instantaneous rate was reaching 800 kHz. This rate was smaller than the maximum rate expected in the central modules of the FT1 and FT2 (1.4 MHz), however, it was higher than an average rate in the FT stations ranging from 500 kHz in FT1 to 150 kHz in FT6 (see Sec. 3.2, Fig. 3.4). The flux of protons in the beam region was about 40-50 kHz/cm² and thus was roughly two times higher than the one expected in the hottest spots of the FT1 (see Sec. 3.1, Fig. 3.2).

The tests in April 2016 were performed for four beam momenta 0.55, 0.75, 1.0 and 3.0 GeV/c, cor-

responding to the ionisation densities in the range of about 2.5 ÷ 1 of the ionisation minimum, in order to study the applicability of the TOT measurement of the straw tube pulses for determining the specific energy loss and thus for particle identification. The hit rate was about 20 kHz/straw, and was roughly one order of magnitude smaller than in the May 2015. This lower rate was chosen in order to avoid loss of the detection efficiency of the straws due to the space charge effect.

5.5.2 Adjustment of Baselines and Threshold in FEE

The time of arrival as well as the width (TOT) of the digital pulses from the PASTTREC FEE cards and from the triggering scintillator were registered in the TRB-v3 board. As it was pointed in Sec. 4.6.2, the PASTTREC chip contains 8 channels with baseline levels adjustable separately for each channel by means of internal DAC circuits. The discrimination threshold is common for the 8 PASTTREC channels and can also be adjusted. Since the baseline levels may differ among the PASTTREC channels, they were fine tuned before the beam tests using the following iterative procedure. The first step of the procedure implies collection of the TOT spectrum of the ⁵⁵Fe isotope for all the system channels (96). Then the median of the position of the TOT peaks is established. The baseline levels are shifted for the channels which have different TOT peak position than the calculated median value. If the peak is below the median then the baseline is augmented by 2 mV else it is reduced by the same value or left untouched if its position is close to the median. After completion of all the mentioned steps next iteration of the procedure starts. In Fig. 5.24 the result of the iterative baseline tune procedure is shown. The same method can be adapted to be used with MIPs from in-beam operation or cosmic rays instead of the iron source. Once the baseline configuration was found it remains stable over time.

During the tests with the proton beam, for a few selected analog outputs of the PASTTREC, we observed pulses on a scope. Fig. 5.25 shows examples of pulses observed for two selected settings of the pulse shaping in the PASTTREC: a "slow" shaping corresponding to the s2 setting and a "fast" shaping corresponding to the s1 setting. The measured peaking time for the "slow" and "fast" setting was about 40 ns and 20 ns, respectively. The duration time of the "slow" and "fast" pulses was about 200 ns and 150 ns, respectively. The ampli-

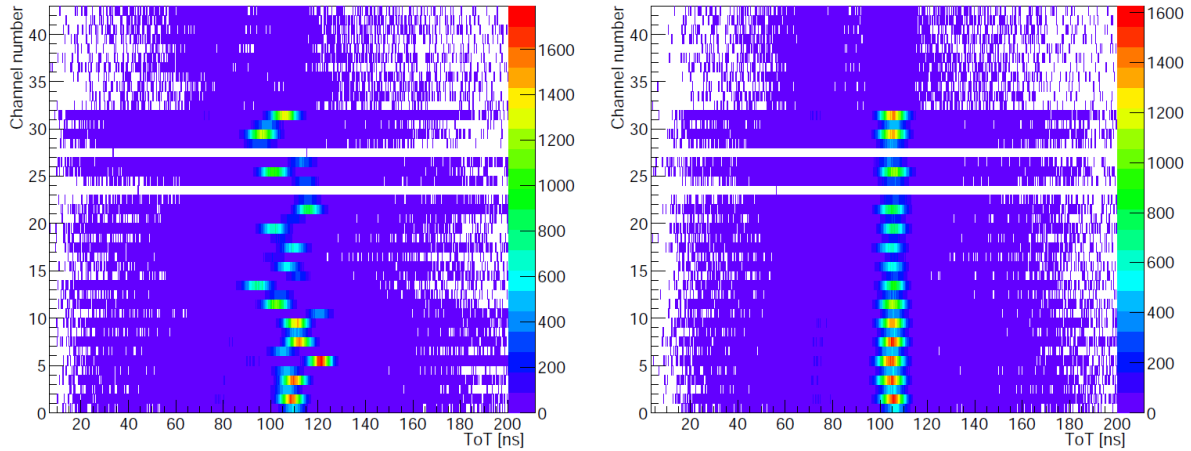


Figure 5.24: Left: TOT spectrum versus channel number for selected channels of the detector before the baseline tune procedure was applied. The white bars corresponds to disconnected straw tubes. Right: TOT spectrum versus channel number for selected channels of the detector after the baseline tune procedure was applied. The channels above 32 have less statistics as they belong to the second module of the straw tubes which was located 10 cm farther from the iron source

tude of pulses was about 160 mV for a high voltage on the straws of 1800 V and the 3 GeV/c protons (MIPs). For the 0.6 GeV/c protons the amplitude was roughly two times higher in accordance with the higher ionization density. The noise level was about 2 mV (see Fig. 5.25 (b)), which is equivalent to 2 fC with the chosen setting of the FEE. The lowest value of the discrimination threshold set in the PASTTREC was 10 mV (5 times the noise level), but we also collected data at higher thresholds of 20, 30 and 40 mV, which was of particular interest for the studies of PID based on the TOT measurements. The saturation of pulses with amplitude higher than 1V was happening rarely (see Fig. 5.26) and no baseline distortion was observed even at the highest measured rates.

5.5.3 Drift Time Spectra

An exemplary distribution of the time difference between pulses of straws in one layer and the triggering scintillator pulse, registered in a 2500 ns time window in a measurement at a beam momentum of 3.0 GeV/c performed in April 2016, is shown in Fig. 5.27, left. The prominent peak visible on the left side of the distribution, around $t = -500$ ns, corresponds to the sum of the drift time spectra for the chosen straws. A cyclic structure visible on the right side of the peak has a period equal to the period of the beam bunching (600 ns) and corresponds to accidental coincidences between the scintillator pulse and the straw pulses coming in consecutive

beam bunches. Based on the ratio of counts of the accidental coincidences and the real coincidences in the drift time spectrum we estimated, that the pile-up of two tracks hitting the straw layers within the drift time represents about 4% of all events. Due to the small width of the beam, which was illuminating 1-2 straws in each layer, the pile-up tracks pass in large part through the same straws. This leads to an inefficiency in the track reconstruction.

The left edge of the drift time distribution presented in Fig. 5.27, right, corresponds to short drift times related to tracks passing in the vicinity of the anode wire. A width of the distribution of about 130 ns gives the maximum drift time corresponding to drift path equal to the straw radius (5 mm). A hump visible on the drift time distribution in the range (-540, -510 ns) corresponding to distances from the wire of about 0.1–0.3 cm is explained by the peak in the dependence of the drift velocity on the distance from the wire at around 0.2 cm, calculated with Garfield-9 simulation program [10] and the Magboltz code, version 8.9.5 [11] (see Fig. 5.28).

The numbers of fired straws for all registered tracks and for successfully reconstructed tracks are shown in Fig. 5.29. Events with the multiplicity of hit straws larger than 6 are mainly caused by noise pulses appearing in addition to pulses of typically 6 straws that respond to a particle track, and by pile-up of two or more proton tracks in one event. In the case of two well-separated tracks, the number of hit straws is 12 ($= 2 \times 6$). However, due to the relatively small width of the proton beam,

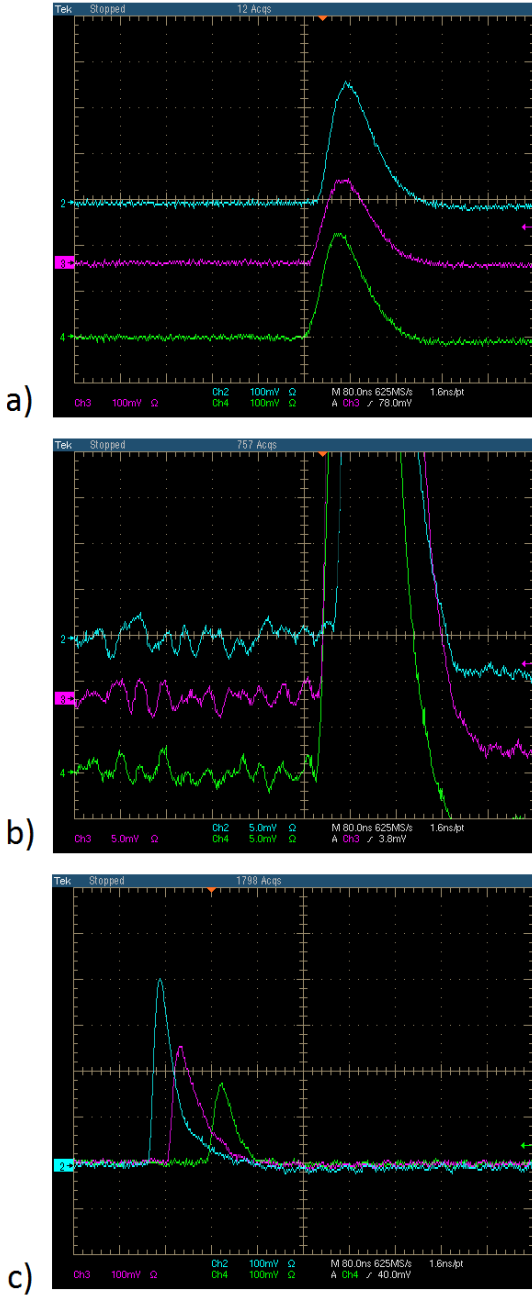


Figure 5.25: Oscilloscope screen shots presenting typical signals from three consecutive straws located in the beam for a "slow" shaping of the front-end pulses (a), observed noise (b) and signals for "fast" shaping in the front-end (c). The sensitivity setup in the oscilloscope was 100 mV per division for (a) and (c) and 5 mV per division for (b). The time base in all three cases was 80 ns per division.

comparable to the diameter of the straw, in some layers the tracks pass through the same straw and, therefore, the multiplicity of hits is less than 12 and ranges between 6 and 12.

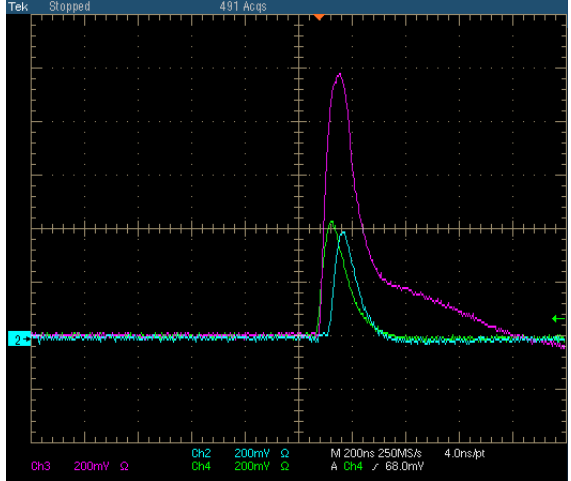


Figure 5.26: Distortion of a pulse (shown in magenta) due to saturation of amplifier in the front-end. The two remaining pulses (green and blue one) in the presented oscilloscope screen shot are undistorted. The sensitivity in the oscilloscope was 100 mV and the time base was 200 ns per division.

5.5.4 Track Reconstruction

The registered proton tracks were reconstructed using the least χ^2 fit to the measured track to wire distances with the χ^2 value calculated as:

$$\chi^2 = \sum_{i=1}^N \frac{(r_i^e - r_i^f)^2}{\sigma_a^2}, \quad (5.2)$$

where the summation is carried out over the hit straws taken for the fit, r_i^e and r_i^f is the measured and fitted distance to the wire and σ_a is an average spatial resolution per straw, determined as shown below. In the reconstruction procedure, the distance-drift time relation, obtained using the uniform irradiation method, and corrected in two iterations using the autocalibration procedure, was applied.

In the first step of the reconstruction procedure, straw layers with at least one straw response were identified. Only events with at least three responding layers (out of six) were used in the reconstruction. Then, a straight line was fitted to all possible combinations of hits containing one hit from each responding straw layer. Finally, a combination of hits corresponding to the lowest χ^2 value was selected.

In the following we present results of the reconstruction of 3 GeV/c proton tracks registered during the tests in April 2016 at the anode voltage of 1900 V, the peaking time in the PASTTREC set to 20 ns

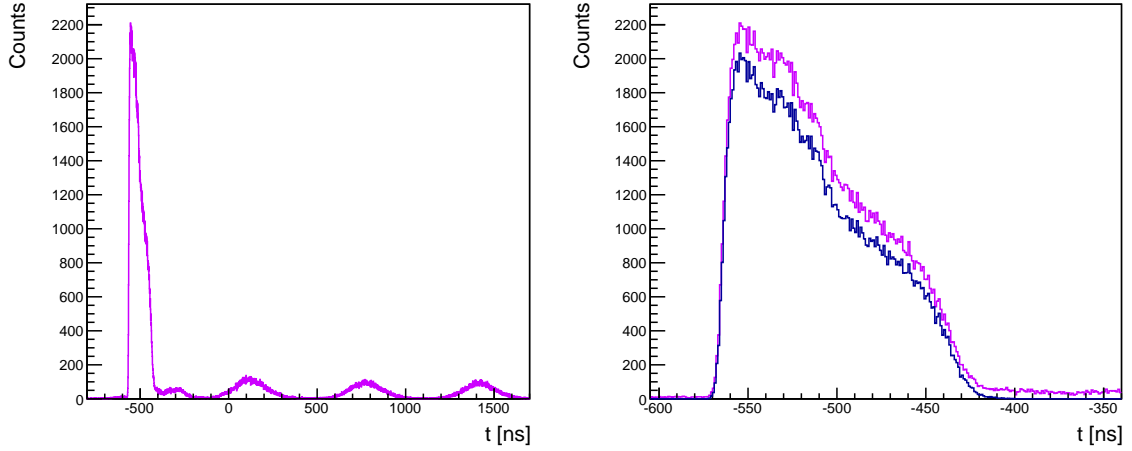


Figure 5.27: Time difference between straw tube pulses and the reference pulse from the triggering scintillation detector registered in a 2500 ns window (left), and in a 265 ns window zoomed in on the drift time spectrum (right). The violet line represents raw data, and the blue line in the right panel corresponds to straw tube hits successfully reconstructed by the track reconstruction procedure. The high voltage of the anode wires was 1900 V and the discrimination threshold was 10 mV.

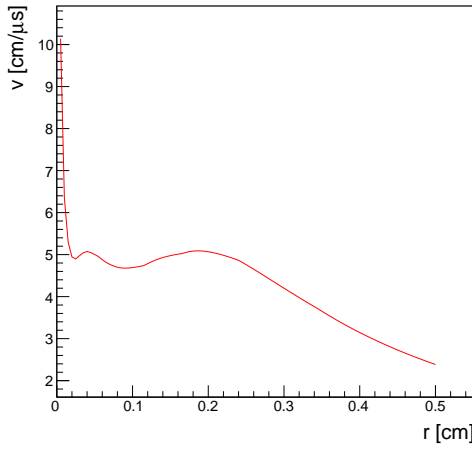


Figure 5.28: Drift velocity of electrons as a function of the distance from the anode wire calculated for the straw tube filled with the 90% Ar+ 10% CO₂ gas mixture at 2 bar pressure and the anode wire voltage of 1900 V.

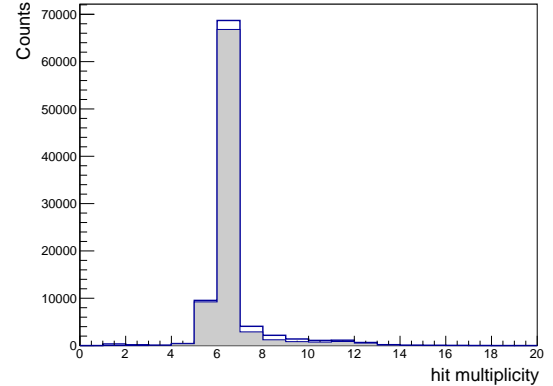


Figure 5.29: Multiplicity of hit straws for 3.0 GeV/c protons. The solid line includes all registered tracks and the fill area represents successfully reconstructed tracks.

and the discrimination threshold of 10 mV. Distribution of differences between the measured and reconstructed track distance from the wire ($r_i^e - r_i^f$), hereinafter referred to as residuals, and of the χ^2 values obtained for events with 6 and 5 fit straws is presented in Fig. 5.30, in the top and bottom part, respectively. The standard deviations of the distributions of residuals, obtained from a fit of a gaussian function, are about 0.11 mm. The χ^2 distributions obtained in the reconstruction procedure are compared with theoretical χ^2 distributions, respectively for 4 and 3 degrees of freedom (see Fig. 5.30,

right). To obtain the best possible agreement between the experimental and theoretical χ^2 distributions, we adjusted the value of σ_a in eq. 5.2 to 0.130 mm. This value is the spatial resolution of a single straw averaged over the distance from the wire.

Fit results with χ^2 value per degree of freedom smaller than 10 were accepted as a successful reconstruction. The efficiency of the track reconstruction, calculated as the percentage of the successfully reconstructed tracks, equals 94%. The main contribution to the lack of efficiency comes from events with the hit multiplicity higher than 6 (see Fig. 5.29). Therefore, we conclude, that the inefficiency in the track reconstruction is mainly due

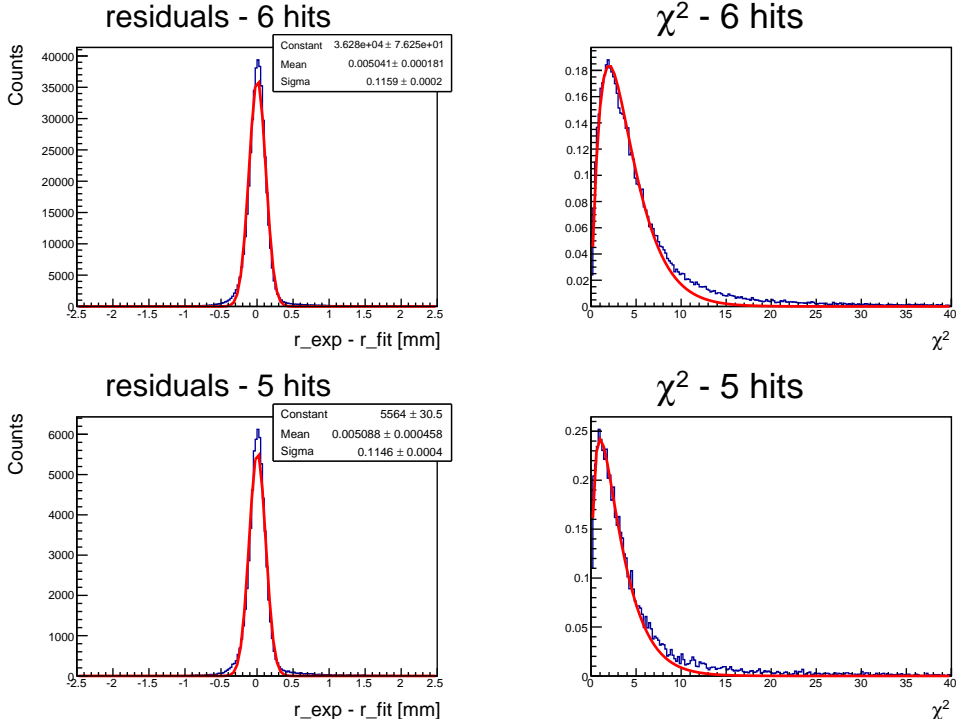


Figure 5.30: Distribution of the residuals (left) and χ^2 values (right) obtained in the track reconstruction with 6 fit hits (top) and 5 hits (bottom), shown with solid blue line. The red line on the two panels on the left presents a gaussian fit to the distribution of residuals, and on the top right and bottom right panel - the χ^2 distribution with 4 and 3 degrees of freedom, respectively.

to the pile-up of the proton tracks.

The single straw spatial resolution was also determined in a different way, based on the distances between a reference track reconstructed with two modules - the first and third one in the test setup (layers (1, 2) and (5, 6) in Fig. 5.22) and the track position measured in the second module, in layer 3 (not included in the fit). The precision of the coordinate of the reconstructed track at the position of the 3rd layer, determined from the distributions of the residuals, is about 0.07 mm (σ) and it does not depend on the position along the layer (x-coordinate in Fig. 5.22). Distribution of the position measured with the 3rd layer with respect to the reconstructed track has the standard deviation of 0.144 mm. After subtraction in quadrature the precision of the track position in the 3rd layer, a spatial resolution of 0.126 mm is obtained, which is very close to the one determined above by the method based on the analysis of the χ^2 distributions.

We have also reconstructed tracks registered at lower voltages of the anode wires: 1800 V and 1700 V, as well as for different settings of the FEE parameters. With the s1 setting of the FEE and the anode voltage reduced to 1800 V (gas gain $\sim 5 \cdot 10^4$)

the reconstruction efficiency does not change significantly but the spatial resolution deteriorates to about 180 μm per straw. This lower resolution is still satisfactory from the point of view of the FT requirements and the lower voltage has the important advantage of lower aging due to the smaller gas gain. Further reduction of the voltage from 1800 V to 1700 V (gas gain $\sim 2 \cdot 10^4$), investigated only for the s2 FEE setting, leads to a reduction of the reconstruction efficiency from about 95% to 93% and a deterioration of the spatial resolution from about 220 to 330 μm per straw.

Studies of the track reconstruction precision at the voltage 1800 V, for different settings of the FEE parameters (s1, s2 and s3) and different values of the discrimination threshold (10, 20, 30 and 40 mV), are presented in the next subsection. The main conclusion of these studies is that best spatial resolution can be achieved for the shortest peaking time parameter of 15 ns (FEE setting s1) and for the lowest applied threshold of 10 mV.

We currently consider the 1800 V working voltage, the s1 setting of the FEE and the discrimination threshold 10 mV as the most optimal for the PANDA FT. If we manage to reduce the noise

level by considered electronic shielding of the FEE cards and the straw layers, then the discrimination threshold and the working voltage will be reduced accordingly.

5.5.5 PID Based on the TOT Measurement

The data collected in April 2016 have been used to check the applicability of the Time-over-Threshold (TOT) measurement of the straw tube pulses for the determination of the specific energy loss and thus for the particle identification. The tests were done for four different proton beam momenta of 0.55, 0.75, 1.0 and 3.0 GeV/c corresponding to the ionisation densities in the range of about $2.5 \div 1$ of the ionisation minimum.

The drift time and the Time-over-Threshold was measured for three different PASTTREC settings, referred to as: s1, s2 and s3 (see Sec. 5.4.1), corresponding to three different values of the peaking time parameter in the PASTTREC: 15, 20 and 35 ns. For each of the settings, the data were collected with the discrimination threshold of 10 mV. For the setting s2, data were acquired for 4 different thresholds: 10, 20, 30 and 40 mV. For each configuration, one million events were saved. The high voltage applied to the anode wires was 1800 V. The performed tests, the data analysis and the obtained results are described in detail in [12]. Here we focus on presenting the most important ones.

Examples of drift time and TOT distributions, registered at the beam momentum of 0.75 GeV/c for each of the 96 read-out channels (32 channels per module) are shown in the upper part of Fig. 5.31. There are three high intensity spots (one per each module) reflecting the spatial beam distribution with the number of channels corresponding to the beam width. An exemplary drift time spectrum, shown in the lower panel in the figure has a sharp edge at small drift times corresponding to the vicinity of the anode wire and a width of about 140 ns, in agreement with the simulations described in Sec. 6.1.2. The distributions of TOT have the maximum at around 200 ns (see upper-right panel of Fig. 5.31). The positions of the maximum for the different channels are consistent, which confirms the good alignment of the baseline levels in individual channels of the FEE.

In order to reconstruct the proton tracks, the distance-drift time relation in the straw tubes was determined using the uniform irradiation method. The tracks were fitted as straight lines tangent to

drift circles defined by the drift radii of contributing straws. Distribution of the residuals, obtained in the fitting procedure, is presented in Fig. 5.32. The distribution is symmetric around the residual zero value indicating that the determined distance-drift time relation was correct.

The spatial resolution of a single straw, determined as the variance of the residual distribution, is presented as a function of the proton beam momentum for different settings of the peaking time and different values of the discrimination thresholds in the FEE, respectively, in top and bottom panel of Fig. 5.33. For all presented distributions, the best resolution was obtained for the lowest beam momentum and the worst one for the highest momentum. With the discrimination threshold set at 10 mV, the best resolution is obtained for the shortest peaking time of 15 ns and it changes from 100 μm to 165 μm for the beam momentum increasing from 0.55 GeV/c to 3.0 GeV/c. For the peaking time of 20 ns, the best resolution is achieved for the lowest discrimination threshold of 10 mV.

A study of the TOT resolution was done for tracks with 6 hit straws (one straw in each layer). The TOT measured at given momentum of the proton beam shows a dependence on the drift time (see Fig. 5.34 (top panel)). To correct for this dependence, the measured values of TOT were normalized to the mean TOT observed for small drift times as shown in Fig. 5.34 (bottom panel).

Next, a truncated mean was calculated from the 6 hits belonging to a single track by rejecting the highest TOT. The TOT truncated mean spectra clearly depend on the beam momentum as shown in Fig. 5.35.

The TOT truncated mean spectra corresponding to a pair of momenta (p_1, p_2) were used to calculate the separation power defined as:

$$S = \frac{|\langle M_{p1} \rangle - \langle M_{p2} \rangle|}{(\sigma_{p1} + \sigma_{p2})/2}, \quad (5.3)$$

where $\langle M_{p1} \rangle, \langle M_{p2} \rangle$ are the means of TOT over the simulated tracks and σ_{p1}, σ_{p2} are the corresponding standard deviations. The separation power for the 0.55, 0.7 and 1.0 GeV/c protons with respect to the 3 GeV/c protons (MIPs) calculated for three different peaking times and the discrimination threshold of 20 mV is presented in Fig. 5.36 (top panel). The best separation power is obtained for the peaking time of 20 ns. The separation powers for this peaking time and the three discrimination thresholds 10, 20 and 30 mV have similar values, as shown in Fig. 5.36 (bottom panel). The separation power for the 0.55 and 3.0 GeV/c protons is about 5.

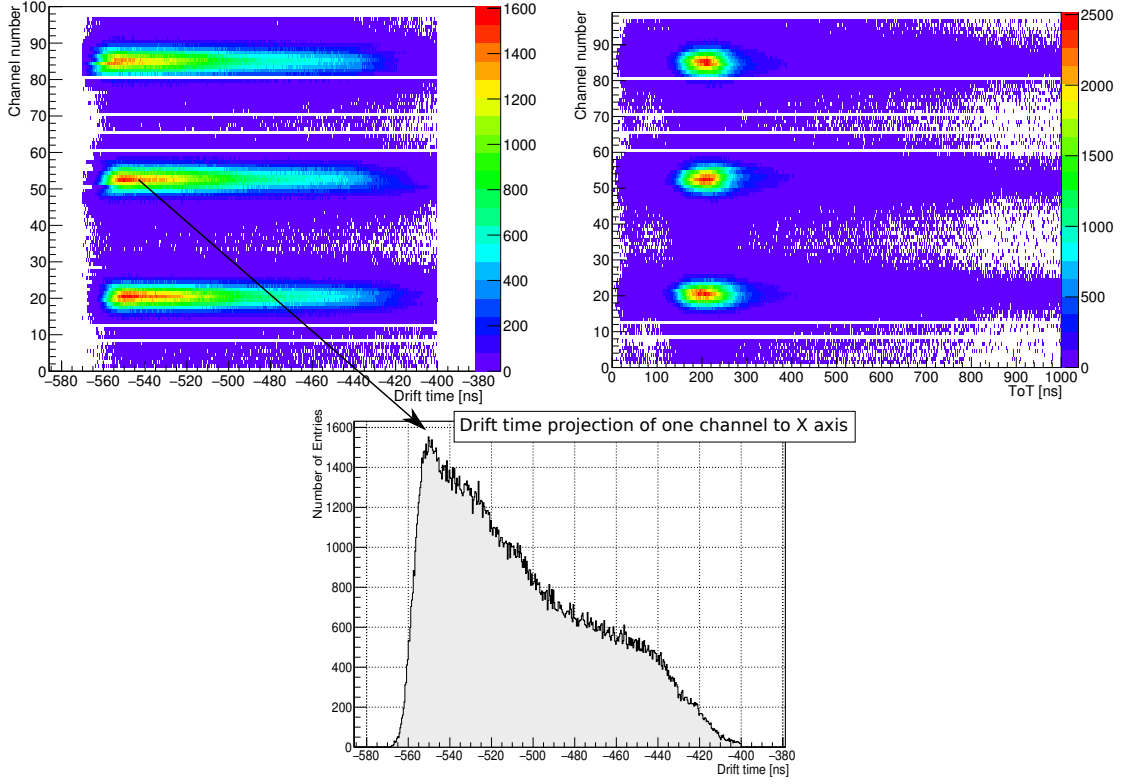


Figure 5.31: Drift time spectra (upper-left) and TOT spectra (upper right) for all 96 channels of the three prototype modules. The white horizontal lines in the spectra correspond to defective channels. The lower panel shows drift time spectrum for one selected straw tube.

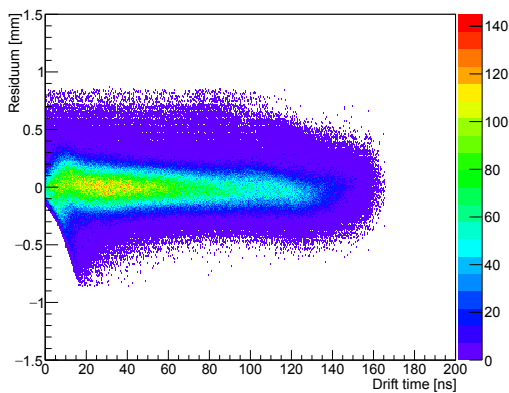


Figure 5.32: Distribution of residuals as a function of drift time for reconstructed proton tracks (proton momentum $0.75 \text{ GeV}/c$).

One can expect that the separation power for $0.55 \text{ GeV}/c$ protons and pions should be very close to the one for the 0.55 and $3.0 \text{ GeV}/c$ protons, since the $0.55 \text{ GeV}/c$ pions are in the ionisation minimum as the $3.0 \text{ GeV}/c$ protons. Corresponding value of

the separation power obtained in the simulations presented in Sec. 6.1.4 equals about 13 but for 24 layers of straws. The measured and simulated separation powers differ by a factor of 2.6 which can be explained, at least in part, by smaller number of straw layers available in the experiment (6 instead of 24). Consequently, an improvement in the determination of mean TOT by a factor $\sqrt{24/6} = 2$ can be expected.

The present results demonstrate that the TOT measurement of the straw tube pulses is useful for the particle identification. Obtained results are in reasonable agreement with the simulations presented in Sec. 6.1.4. According to the results of these simulations, in the FT comprising 24 double layers of straws (48 single layers) the TOT measurement should allow to separate pions, kaons and protons for momenta below $1 \text{ GeV}/c$. This measurement can complement the main way of identifying low momentum charged particles based on the registration of the time-of-flight with the Forward TOF-Wall.

The TOT measurement turned out to be very useful for setting the baseline levels in the FEE and for tests of straws with ^{55}Fe source. It can also be used

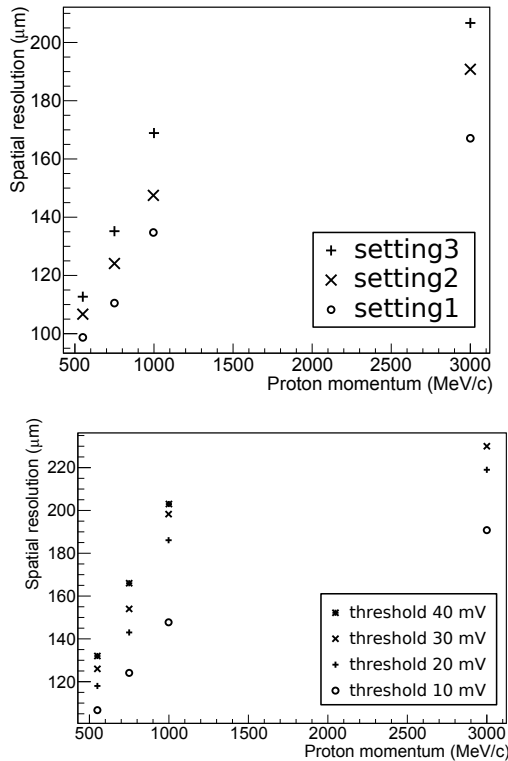


Figure 5.33: (Upper panel) Distribution of residuals for the three different PASTTREC settings and the discrimination threshold set to 10 mV as a function of the beam momentum. (Lower panel) Distribution of residuals for four different discrimination thresholds and the peaking time equal to 20 ns.

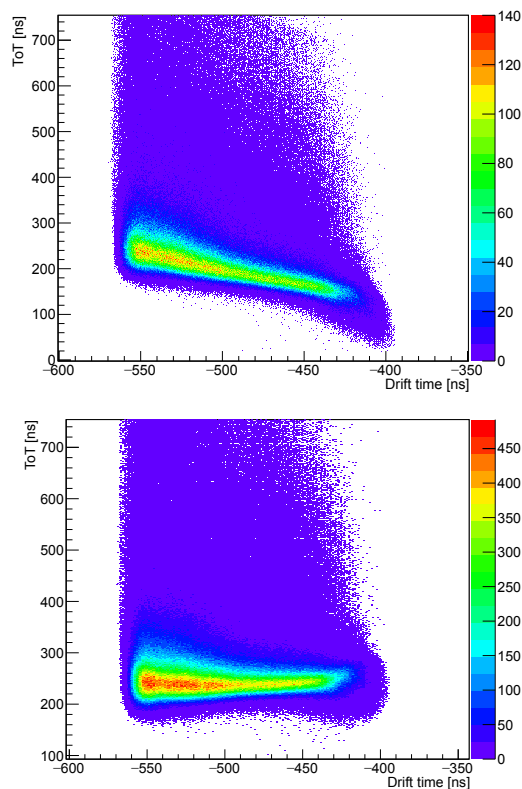


Figure 5.34: TOT versus drift time for reconstructed tracks before correction for the drift time (top) and after correction (bottom).

for rejection of noise pulses from the data stream. Therefore, we plan to measure the TOT besides the drift time.

References

- [1] W. Erni et al., Eur. Phys. J. **A49**, 25 (2013), <http://arxiv.org/abs/1205.5441>.
- [2] www-hades.gsi.de.
- [3] A. Gillitzer et al., *Strangeness Physics at COSY-TOF*, Technical report, Forschungszentrum Jülich, (2007), COSY Proposal no. 178.
- [4] P. Wintz, *Commissioning of the COSY-TOF Straw Tube Tracker and the silicon-microstrip Quirl*, Technical report, Forschungszentrum Jülich, (2007), COSY Proposal no. 179.
- [5] M. Hohlmann, C. Padilla, N. Tesch, and M. Titov, Nucl. Instrum. Methods **A494**, 179

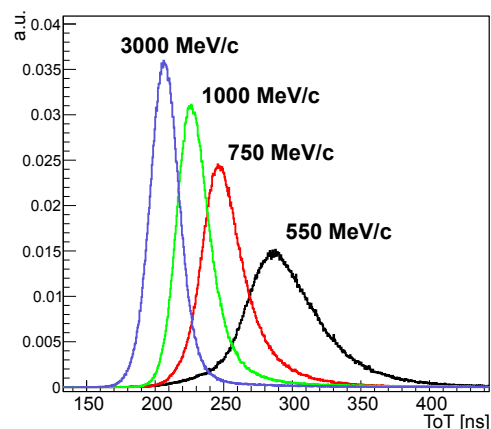


Figure 5.35: Distribution of the truncated mean of TOT for four different proton momenta. The discrimination threshold was set to 10 mV and the PASTTREC parameters were set to the configuration s2.

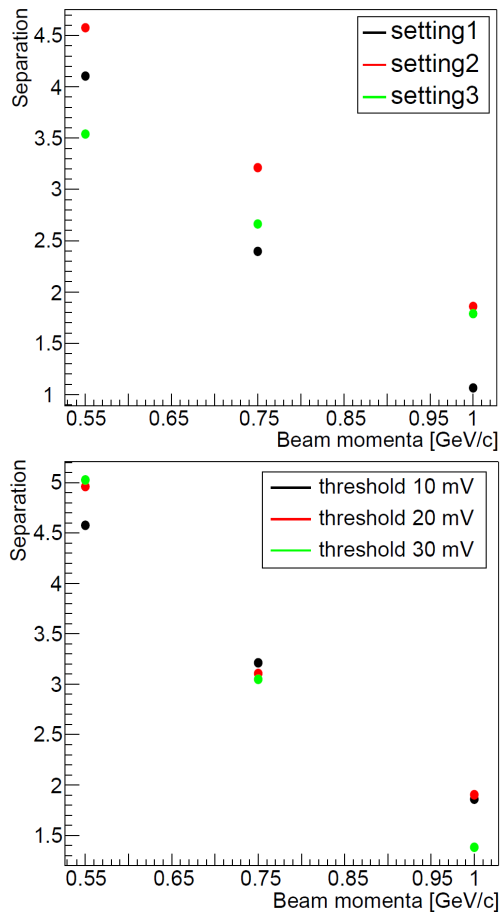


Figure 5.36: Separation power for the three settings of PASTTREC corresponding to the three different peaking times (top) and for the three discrimination thresholds (bottom) presented in a function of the proton beam momentum.

(2002).

- [6] T. Ferguson et al., Nucl. Instrum. Methods **A478**, 254 (2002).
- [7] M. Titov, arXiv:physics/0403055v2 (2004).
- [8] P. Wintz, A large tracking detector in vacuum consisting of self-supporting straw tubes, in *Intersections of Particle and Nuclear Physics: 8th Conference CIPANP2003*, volume 698 of *Issue 1*, pages 789–792, AIP Conf.Proc., (2004).
- [9] CAEN, DT5742 Digitizer,
[http://www.caen.it/cssite/CaenProd.jsp?
parent=14&idmod=651](http://www.caen.it/cssite/CaenProd.jsp?parent=14&idmod=651).
- [10] Garfield - simulation of gaseous detectors,
<http://garfield.web.cern.ch/garfield/>.

- [11] S. Biagi, Nucl. Instrum. Methods **A421**, 234 (1999).
- [12] P. Strzempek, *Development and evaluation of a signal analysis and a readout system of straw tube detectors for the PANDA spectrometer*, PhD Thesis, Jagiellonian University, Krakow, 2017.

6 Computer Simulations and Expected Performance

6.1 The Single Straw Tube Simulation

6.1.1 The Charge Released into the Tube

We have performed a detailed simulation of the charge generation and collection in a single straw tube.

In correspondence of an incident charged particle, we sample from an exponential distribution the point where an electron cluster is generated and from the proper distribution (see below) the number of electrons in the cluster. By stopping when the particle leaves the tube, we have the number of free electrons generated from a poissonian number of clusters. The mean number of clusters/cm is taken from ref. [1] (25 for Ar and 35.5 for CO₂). For the reliability of the simulation, it is crucial to know the cluster size distribution, that is the number of electrons per cluster. We use the theoretical calculations of [2] for Ar and the experimental data on Ar and CO₂ from [3]. The comparison with some available results in gas has shown that this choice is in reasonable agreement with data (see Fig. 6.1).

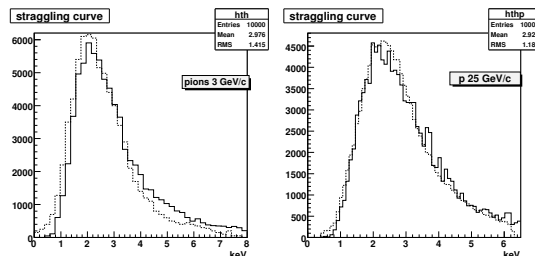


Figure 6.1: Comparison between the simulation of the energy lost in a 1.5 cm Ar/CO₂ layer (line) and the experimental values of Allison et al. [4] (dotted line).

As a further check, we compared the energy lost in the tube, for a variety of projectiles and energies, with the Urban model [5], which is used in GEANT3 and GEANT4 in the case of gaseous thin absorbers [6, 7]. The results, reported in Fig. 6.2, show good agreement with our simulation.

By multiplying the number of clusters with the mean number of electrons per cluster, an average number of ionization electrons can be calculated.

For a minimum ionizing particle passing close and perpendicular to the anode wire in the $\bar{\text{P}}\text{ANDA}$ straw tubes filled with the Ar+CO₂ (90:10) gas mixture at 2 bar pressure, the number of ionization clusters is about 60, the number of ionization electrons is of about 200 and the average energy loss is of about 5 keV. An average distance between consecutive ionization clusters is about 170 μm . This sets a limit on the position resolution in the straw tube for tracks passing in the vicinity of the anode wire.

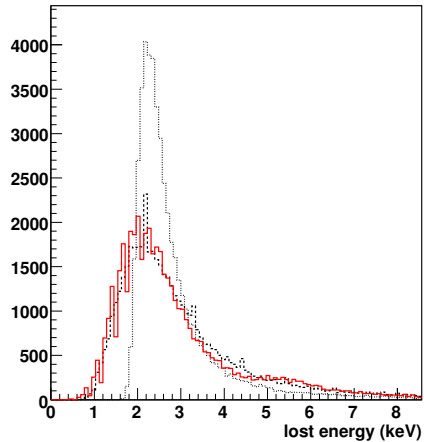


Figure 6.2: Energy loss of 1 GeV pion traversing a 1 cm of 90 % Ar 10 % CO₂ gas mixture at NTP. Solid line: Urban distribution; dashed line: specific simulation model; dotted line: Landau distribution.

6.1.2 Simulation of the Electron Drift

We performed studies of a single straw tube performance using the Garfield program version 7.40 [8]. As an input for Garfield we used simulations of the gas ionization by traversing charged particles with the Heed program version 1.01 [9]. In turns, the electron transport properties were calculated using the Magboltz code versions 7 and 8.9.5 [10]. A detailed description of our studies is presented in Ref. [11].

The computed drift velocity of electrons in argon mixed with various fractions of CO₂ is shown in Fig. 6.3 as a function of the electric field strength. For the electric field in the order of 1 kV/cm, adding small fraction of CO₂ leads to a significant increase

of the drift velocity and e.g. at $E = 1 \text{ kV/cm}$, the drift velocity for pure argon is of about $0.3 \text{ cm}/\mu\text{sec}$ and for mixture of Ar/CO₂ (90:10) it increases to $4.5 \text{ cm}/\mu\text{sec}$. For higher CO₂ concentration, it drops again and for example for mixture of Ar/CO₂ (80:20) it equals to $2.2 \text{ cm}/\mu\text{sec}$ at $E = 1 \text{ kV/cm}$. The reduction of the electron drift velocity with higher CO₂ concentration is also visible in the space-time relation calculated for two CO₂ percentages: 10 % and 20 %, presented in Fig. 6.4. From the point of view of the high rate applications at PANDA, the Ar/CO₂ (90:10) mixture is more appropriate than the mixtures with higher CO₂ content due to the higher drift velocity.

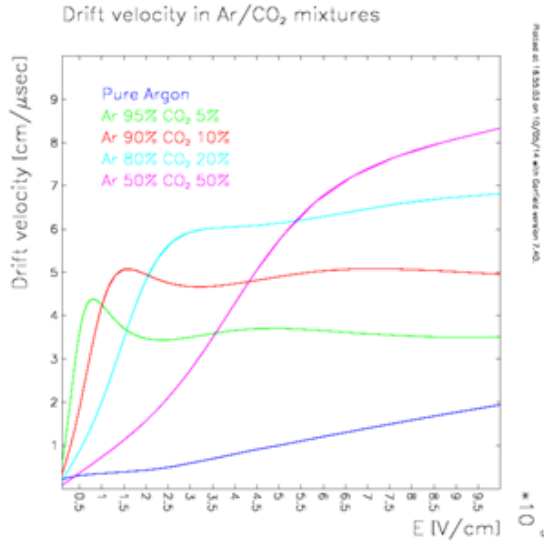


Figure 6.3: Drift velocity of electrons in Ar-CO₂ gas mixture at 2 bar for various CO₂ concentrations.

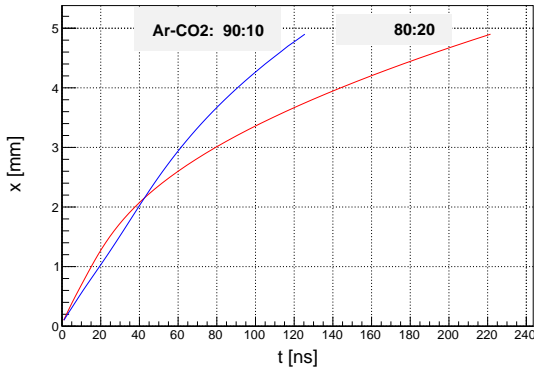


Figure 6.4: Space-drift time relation calculated for Ar-CO₂ gas mixture at 2 bar for CO₂ concentration of 10% and 20%. The potential of the anode wire is 1800 V.

Computed standard deviation of longitudinal and transverse diffusion for 1 cm drift in argon with

different admixtures of carbon dioxide at 2 bar is presented in Fig. 6.5. With increasing CO₂ content, the transverse diffusion is strongly reduced (see Fig. 6.5 (b)). This effect is less pronounced in the case of the longitudinal diffusion (Fig. 6.5 (a)). For the Ar/CO₂ (90:10) mixture, the calculated standard deviation of the longitudinal and transverse diffusion at $E = 1 \text{ kV/cm}$ are about $170 \mu\text{m}$ and $190 \mu\text{m}$, respectively. For the Ar/CO₂ (80:20) mixture, the diffusion is roughly by 20-30% lower which results in higher position resolution of the straw tubes. However, the resolution provided by the (90:10) mixture is fully sufficient from the point of view of the requirements for the FT and we choose it as a faster one.

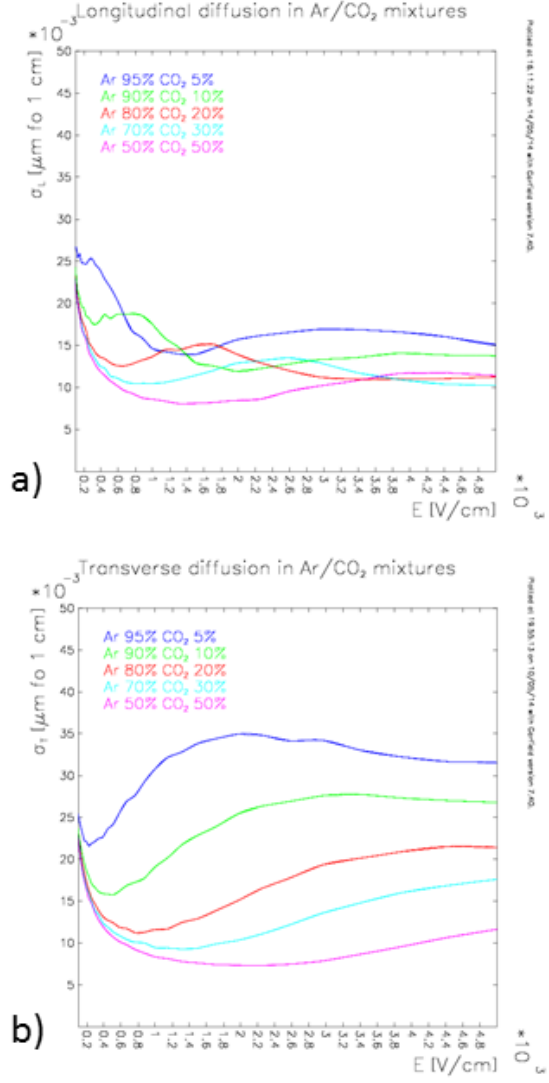


Figure 6.5: Standard deviations of longitudinal (a) and transverse (b) diffusion for 1 cm drift pass of electrons in Ar-CO₂ gas mixture at 2 bar for various CO₂ concentrations.

6.1.3 The Gas Gain

One of the basic issues in the simulation of the straw detectors is the gas amplification, that is the multiplication factor of the avalanche which is formed in the last tens of microns of the primary electron path in its drift to the anode wire. Results of our measurements and of simulations of the gas gain are shown in Fig. 6.6 as a function of the anode voltage. The experimental gain was determined by measuring simultaneously the current of a single straw tube and the count rate from the ^{55}Fe source. In a range of the working voltage considered for the FT straw tubes, lying between 1700 and 1800 V, the gain rises from $2 \cdot 10^4$ to $5 \cdot 10^4$. The gain computed with the Magboltz program with inclusion of only the direct ionization underestimates the experimental results. They are reproduced by adding a contribution of 34% from the Penning effect connected with a transfer of excitation energy of D-level in Ar (14 eV) to CO₂ molecules leading to their ionization.

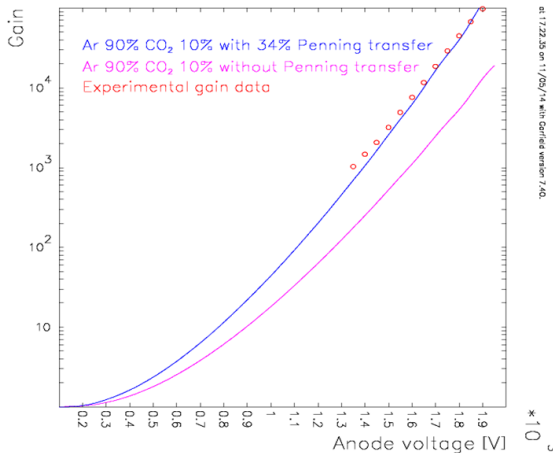


Figure 6.6: The gas gain curves for Ar+CO₂ (90:10) without and with 34% Penning transfer rate represented by purple and blue curve, respectively. The experimental data are shown with open circles.

The results of the gas gain measurements are compared with the Diethorn parametrization [12] in Fig. 6.7. For anode voltages in a range from 1350 to about 1850 V, the data are well reproduced by the Diethorn formula, but for higher voltages the agreement is lost probably due to impact of the space charge effect.

6.1.4 Detector Pulses

Simulations of straw tube pulses with Garfield were used for optimizing of the front-end electronics design. An example of such pulses is presented in Sec. 4.6.1, Fig. 4.31. Simulations of pulses were

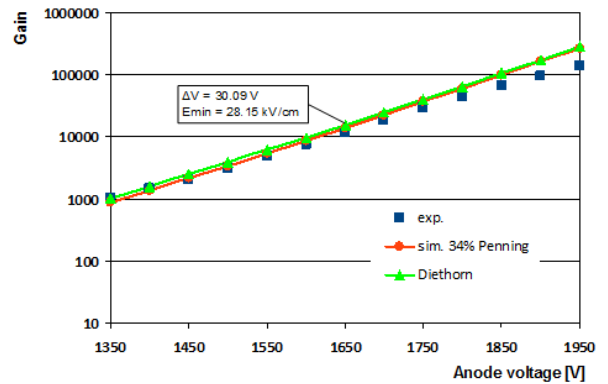


Figure 6.7: Experimental data and results of simulations with Garfield for the gas gain in straw tube filled with Ar-CO₂ (90:10) gas mixture at 2 bar, compared with the Diethorn parametrization (green). Parameters used in the Diethorn formula are indicated in the figure.

also used for studies of applicability of the Time-over-Threshold (TOT) measurements in straw tube detectors for particle identification in the $\overline{\text{PANDA}}$ Straw Tube Tracker [13]. In the Forward Spectrometer, identification of charged pions, kaons and protons with momenta below 1 GeV/c will be based on Time-of-Flight (TOF) measurement using the Forward TOF Wall. The TOT will be registered in order to have a control on the amplitudes of the straw tube pulses and, in particular, it will be applied for the rejection of electronic noise. It can be also used to improve the PID based on the TOF information. For the TOT measurement, shaping of pulses in the front-end electronics (FEE) is of primary importance. In order to account for the FEE in the simulations, the straw tube pulses were convoluted with the transfer function of the FEE. This function was determined as the response to a "delta-like" pulse injected into the FEE channel (see Fig. 6.8).

Results of the TOT simulations have been compared with the results of the TOT measurement performed with the ^{55}Fe radioactive source. A good agreement between the simulations and tests was observed (see Fig. 6.9).

The simulations of the particle identification in the straw tubes were performed using pseudo-tracks created by randomly combining 24 hits generated with Garfield, assuming a uniform distribution of the track distance to the sense wire. The chosen number of hits equals the number of straw tube layers in the first three tracking stations (FT1, FT2, FT3) of the FT, and it corresponds to detection of low momentum tracks in these stations.

Simulated TOT values were corrected for the dis-

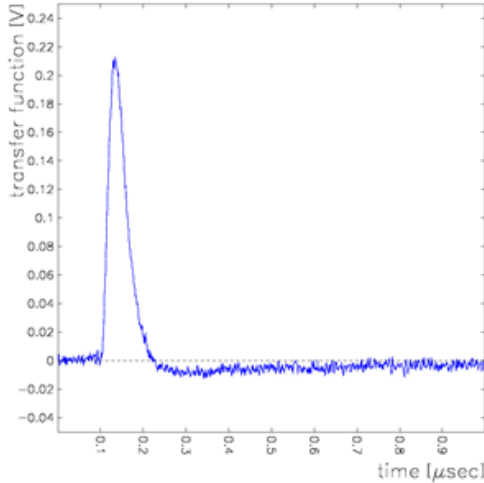


Figure 6.8: Transfer function of the FEE determined as a response to a very fast (~ 1 ns) "delta-like" pulse.

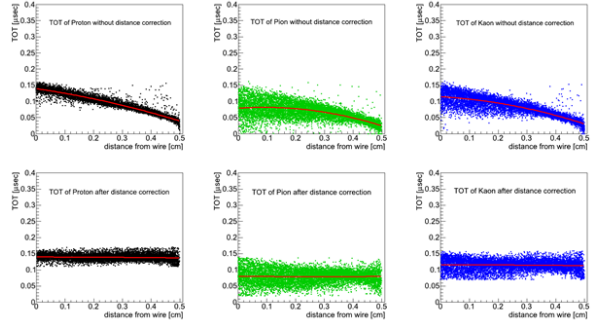


Figure 6.10: TOT vs. distance between the track and the anode wire for protons (left), pions (middle) and kaons (right) at $0.5 \text{ GeV}/c$, before (top) and after applying the distance correction (bottom). The simulations are done for the anode wire at $+1800 \text{ V}$ and a discrimination threshold for the TOT measurement equivalent to 20 primary electrons. The solid red lines indicate the second order polynomial fits to the TOT distributions.

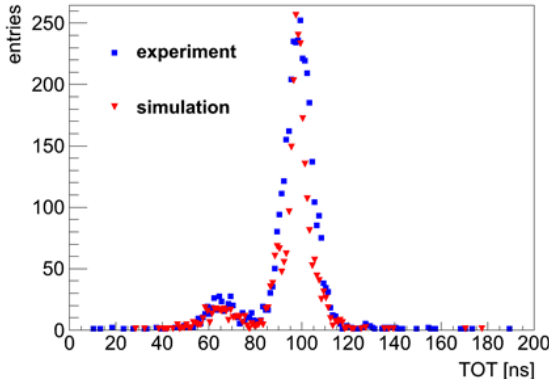


Figure 6.9: Time-over-Threshold spectrum measured (blue squares) and simulated (red triangles) for ^{55}Fe source. A peak corresponding to the full absorption of the 5.9 keV X-rays from ^{55}Fe is clearly separated from the 2.9 keV argon escape peak. In the simulations, electronic noise with a level observed in the measurements, was added to the signals.

tance to the anode wire (see Fig. 6.10), and subsequently, a truncated mean was calculated for each track by discarding 30% of the largest values. The distributions of the corrected TOT values and of the mean values for $0.5 \text{ GeV}/c$ pions, kaons and protons are presented in Fig. 6.11. The values of the truncated mean were then used for calculating the separation power for two particle species, defined in Sec. 5.5.5, Eq. 5.3.

Fig. 6.12 presents a comparison of the separation power determined for $p - K$, $p - \pi$ and $K - \pi$ pairs using the TOT of the straw tube pulses and the integrated charge of the pulses. In the studied particle momentum range $0.3\text{-}1.0 \text{ GeV}/c$, the TOT measure-

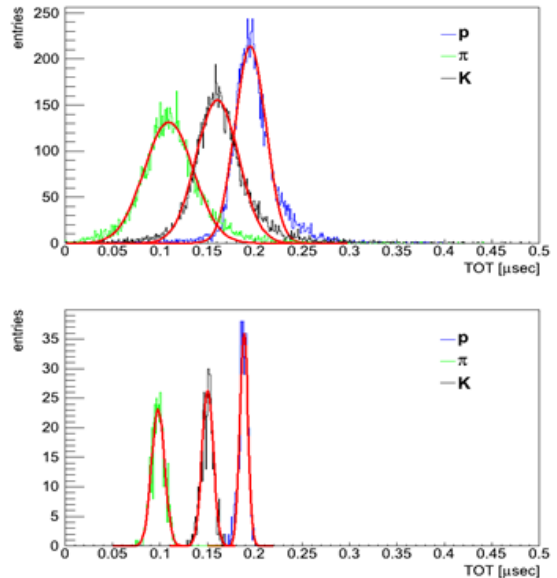


Figure 6.11: TOT simulation with single straw response (top) and truncated mean over 24 straws (bottom) for protons and charged pions and kaons with $0.5 \text{ GeV}/c$ momentum. The solid red lines show the Gaussian fit to the distributions.

ment gives similar separation power as the charge integration of the pulses and it can be used for identification of charged pions, kaons and protons.

6.1.5 Performance in Magnetic Field

Drift of electrons in the straw can be considerably influenced by magnetic field components perpendicular to the electric field lines. The trajectories of the electrons have in this case a form of spirals and

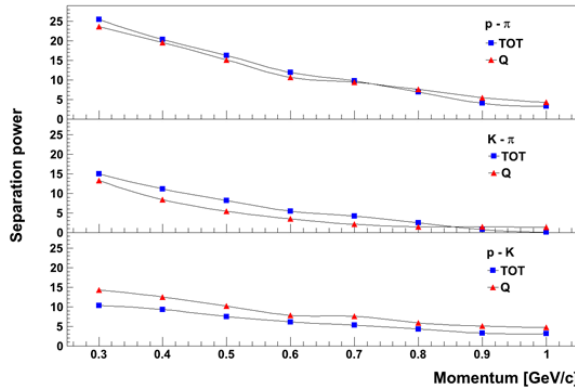


Figure 6.12: Separation power for $p-\pi$, $k-\pi$ and $p-K$ pairs based on Time-over-Threshold (blue squares) and charge measurements (red triangles).

the drift time is longer compared to the case of absence of the magnetic field. Therefore, for a precise reconstruction of particle trajectories, corrections to the distance-drift time relation - $r(t)$ might be needed. In order to estimate these corrections we performed simulations of the drift of electrons in the straw tube placed in a uniform magnetic field. The simulations were done with the Garfield code for the straw tube oriented vertically (y -direction) and particle tracks going in the z -direction. Results of these simulations are shown in Fig. 6.13 in the form of the distance-drift time relation calculated for various values of magnetic field components in the range from 0 to 1 T. The largest variations in the $r(t)$ relation is caused by the vertical magnetic field B_y . For distances from the sense wire close to the straw radius (5 mm) turning on the 1 T field prolongs the maximum drift time from about 140 ns to 160 ns. The corresponding change of the drift path $\Delta r = dr/dt\Delta t$ is about 0.5 mm. Much smaller effect is caused by the horizontal field component B_x (see Fig. 6.13 (bottom)).

In order to estimate the effect of the magnetic field on the $r(t)$ relation in the FT straws we use 3-dimensional field maps calculated for the PANDA solenoid and dipole magnet. An example of the magnetic field distribution in the horizontal symmetry plane ($y = 0$) is shown in Fig. 6.14 together with indicated active volumes of the tracking stations. The stations FT1, FT2 and FT5, FT6 stay in the stray magnetic field of the solenoid and the dipole magnet. In the active volumes of these stations the x -, y - and z -components of the magnetic field are smaller than 0.35 T and the resulting corrections to the $r - t$ relation lie below 0.05 mm and can be neglected compared to the expected position resolution of about $\sigma = 0.15$ mm. For the tracking stations FT3 and FT4 located inside the dipole

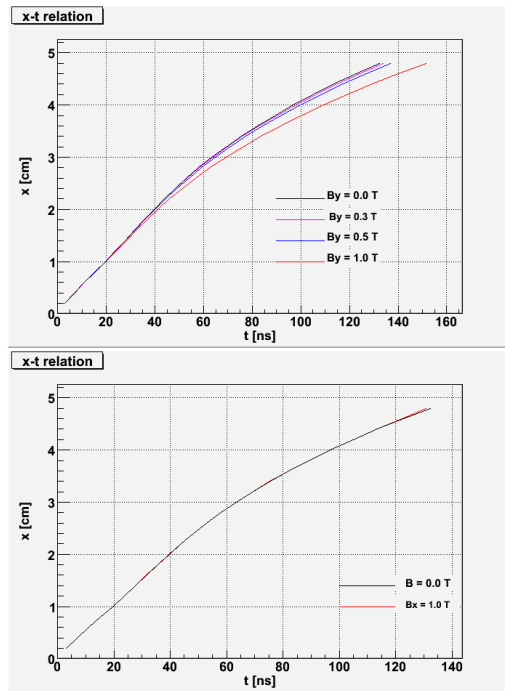


Figure 6.13: Distance-drift time relation for magnetic field in the y -direction (top) and x -direction (bottom).

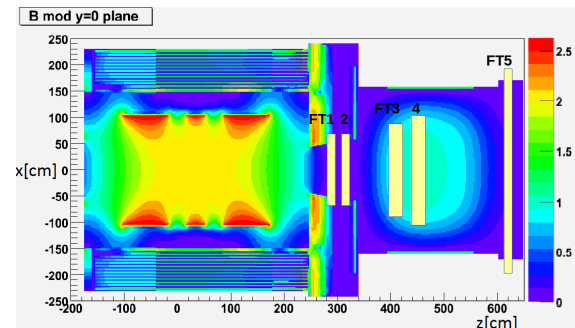


Figure 6.14: Magnetic field distribution in the Target Spectrometer and in the Forward Spectrometer in teslas in the horizontal symmetry plane ($y = 0$) for the maximum setting of the field in the magnets.

magnet gap, for the maximum setting of the magnet field of 2 Tm, the corrections to the $r - t$ relation resulting from the non-uniformity of the field lie in the range up to 0.35 mm. These corrections will be parametrized as a function of x - and y - coordinate for each straw layer and will be applied during the track reconstruction.

6.2 Track Reconstruction in the Forward Tracker

6.2.1 Simulation and Reconstruction Software

The simulation and reconstruction code for the FT is fully integrated in the *PANDA* code framework *PandaRoot* [14]. *PANDA* shares the base classes of a wider framework called *FairRoot* [15] with other FAIR experiments (CBM [16], HADES [17], R3B [18]) and adds its own specific tasks.

The FairRoot framework is based on the Virtual Monte Carlo (VMC) [19, 20], a tool developed at CERN by the ALICE collaboration, which allows the user to change the engine for the transport of particles in matter (*geant3*, *geant4*) at runtime without the need to change the input/output structure and to adapt the geometry description of the detector. The VMC classes decouple the user classes from the Monte Carlo classes and act as an interface allowing the interchange of the Monte Carlo codes. This grants high flexibility: the user can change the implementation of the detector and the algorithm of reconstruction and/or analysis independently from the core code.

A full simulation chain can be characterized by four main steps: simulation, digitization, reconstruction and analysis.

6.2.1.1 Simulation and Digitization

During this step, realistic data, resembling the ones that will be available from the operating system, are generated, ready for the reconstruction. It can be divided in two parts, concerning, respectively, the tracker setup and its response to the passage of the particles.

The **detector description** is contained in the *PndFt* class, where the geometry is loaded and the sensitive material is set to collect signals from charged particle traversing it. The straw tubes are built and positioned in an ASCII geometry file; for each tube, the coating, the filling gas mixture and the wire materials are implemented. The passive elements of the tube such as the plugs have not been implemented yet. It is however foreseen to insert all the information on passive elements in the future. Moreover, since the presence of many details will slow down the simulation, it is foreseen that the final geometry description will contain only *average* materials to take into account the correct material budget but be fast enough to grant good time per-

formances. At the simulation stage the geometrical parameters of the tube are saved in the parameter file in order to be retrievable at any stage of the reconstruction.

After the collection of MC points from charged particles, the detector response of the FT is simulated as described in Sec. 6.1 during the **digitization** step which provides the collection of realistic hits. These hits contain the information on the drift radius and the energy deposit: it must be pointed out that actual hits coming from the detector will contain only the time information together with the deposited energy, but in the present code the conversion from time to drift radius, which will be later part of the reconstruction, is inserted directly in the simulation of the single straw response (i.e. there is no separation between a “digi”, with the time information, and a “hit” with the reconstructed drift radius).

6.2.1.2 Reconstruction

In a tracking detector, the aim of the reconstruction is to collect the hits, assign them to the different track candidates and then fit the obtained track candidates to get the momentum of each particle. The FT does not provide the x, y, z spatial coordinates of the point where the particle passed. When a tube is hit by a particle, the only available information for the track reconstruction is the measured drift radius, together with the position and orientation in space of the tube itself. A specific track finding (described in Sec. 6.2.2) and fitting (described in the following subsection) procedure have been developed relying only on this information.

6.2.1.3 The Kalman Filter

The track fitting step is performed through the Kalman filter procedure, using the hits coming from FT, MVD and GEM where available and, as starting position and momentum, the values inferred by the pattern recognition backtracked to the point of closest approach to the interaction point in case of primary particles. In this section a short summary of the Kalman fit procedure [21, 22] is reported. A more detailed description of this topic can be found in [23] and [24] and references quoted therein. The package devoted to the Kalman fit procedure is *genfit* [25].

The Kalman fit is an iterative procedure which, unlike global methods such as the helix fit, takes into account the energy loss, the magnetic field inhomogeneities and the multiple scattering. The aim of

the Kalman filter is to find the best estimation of the true track point f_i on the i -th detector plane by minimizing the χ^2 :

$$\chi^2(\mathbf{f}) = \sum_i [(\mathbf{e}_i[\mathbf{f}_{i-1}] - \mathbf{f}_i) \mathbf{W}_{i-1} (\mathbf{e}_i[\mathbf{f}_{i-1}] - \mathbf{f}_i)] + (\mathbf{x}_i - \mathbf{f}_i) \mathbf{V}_i (\mathbf{x}_i - \mathbf{f}_i) \quad (6.1)$$

where $\mathbf{e}_i[\mathbf{f}_{i-1}]$ is the extrapolated point on the i -th detector plane starting from the true point on the $(i-1)$ -th plane and \mathbf{x}_i is the measured one; \mathbf{W} and \mathbf{V} are the weight matrices containing respectively the tracking and the measurement errors. The Kalman filter is a method to minimize the χ^2 of Eq. 6.1 to find the true points \mathbf{f}_i . Usually this is done through three steps [26, 27]:

- *extrapolation*: the status vector on the i -th plane is predicted starting from the knowledge gained up to the $(i-1)$ -th plane;
- *filtering*: this is a preliminary evaluation of the track parameters on plane i , making a “weighted mean” between the measured and the predicted values on the same plane;
- *smoothing*: on each plane, the Kalman point solution of the second step is refined to get the final estimate of its value. This last step is often substituted by an alternative option: the so-called “backtracking”, which consists in repeating the first two steps while extrapolating in backward direction, from the last point of the track to the first one.

The Kalman filter algorithm is a standard tracking procedure, but its use in the case of the FT has some peculiarities: the extrapolation method, the use of virtual detector planes and the z-reconstruction.

The track follower used during the extrapolation step is GEANE. The standard ways of extrapolation made available by this tool are the one to a volume, to a plane and to a track length. Though the extrapolation to a plane was useful and easily applied to planar detectors as MVD and GEM, it was not suitable for the FT. None of the standard functions was and so a fourth method has been developed: The propagation to the point of closest approach to a line or to a space point. In particular, for the straw detectors, the propagation to the point of closest approach to the straw wire is used (see Fig. 6.15). This method combines the propagation to a track length and to a plane: An extrapolation is performed, calculating the distance from the wire step by step, the minimum is found and a plane containing the wire and the point of closest

approach is built there (see Fig. 6.16). Eventually a standard extrapolation onto this plane is made. As already pointed out, the straw tube is not a pla-

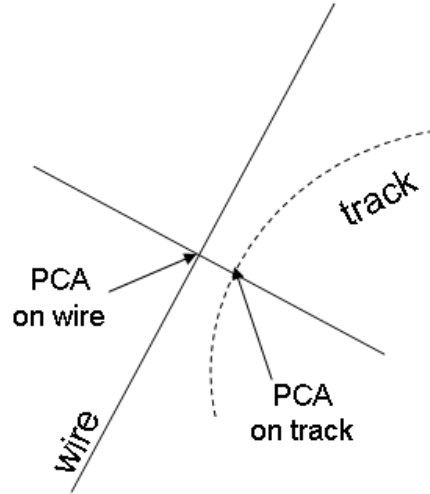


Figure 6.15: Sketch of the positions of the point of closest approach (PCA) on the track and on the wire.

nar device, thus no real measurement plane can be identified. The chosen detector planes are virtual and are built during the extrapolation step. Each plane is spanned by the axes v and w as shown in Fig. 6.16: The w axis is along the wire and the v axis orthogonal to it, through the found point of closest approach. The z coordinate of each single

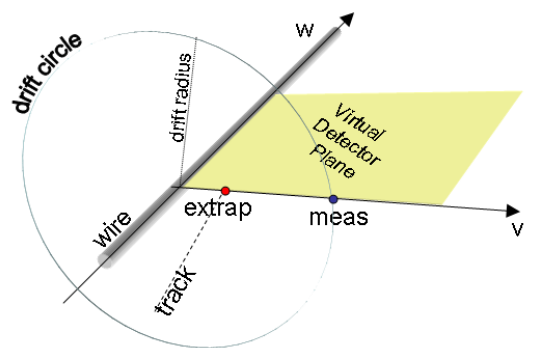


Figure 6.16: Sketch of the virtual detector plane at the point of closest approach to the wire.

hit is unknown at this stage since no reconstruction of this coordinate has been done so far and it is not measured directly. It is reconstructed by the Kalman filter using the skewed tubes. In fact, given a starting position and direction (which con-

tains also the z information) the extrapolation to the point of closest approach to the skewed tubes takes into account their position in tridimensional space and thus, indirectly, the z coordinate. When performing the filtering step on the virtual planes associated to the skewed tubes, all the track parameters are modified at the same time, taking into account the z information provided by the skewed tubes themselves.

6.2.2 Pattern Recognition in the Forward Tracker

The pattern recognition (PR) algorithm expects as input a set of IDs of straws which recorded a hit with associated drift distance. It produces as output a number of sets of straws' IDs identified as belonging to a single track. The algorithm also assigns impact parameters of every identified track at the first straw layer of the tracking stations. These parameters are used to initialize the Kalman filter as a subsequent step in the full track reconstruction.

A charged particle originating from the interaction point and moving through the FT system is measured in three sections of the FT corresponding to the three pairs of the tracking stations (FT1, FT2), (FT3, FT4), (FT5, FT6) and, in the following, referred to in short as FT12, FT34 and FT56, respectively. The first (FT12) and the last section (FT56) are located outside the magnetic field of the dipole magnet and in the proposed PR algorithm we assume that the particle trajectory in these sections can be approximated by a straight line in 3D space. The middle section (FT34) is located in the magnetic field B of the dipole magnet and with no multiple scattering and negligible bremsstrahlung radiation the trajectory in this section can be described by a helix in 3D space. In our model of the track in the FT34 we assume a constant strength of the field B within a defined range along the z-axis (the nominal beam direction at the target point). Based on this assumption, the PR approximates tracks in FT34 in projection on the horizontal plane ZOX as part of a circle. The projection of the track on the vertical plane ZOY is approximated by a straight line.

The PR algorithm was tested using simulated tracks of muons emitted isotropically from the target at polar angles smaller than 5° . The tests were performed for three different muon momenta: 0.55, 2.55 and 5.55 GeV/c and three different track multiplicities per event: 1, 3 and 5. The magnetic field in the dipole magnet was set to the maximum nominal value corresponding to the field integral of 2 Tm.

6.2.2.1 Track Recognition in the ZOX Plane Using the Vertical Straws

The layers with vertical straws are used to determine the particle track in the ZOX projection. The respective consecutive straw layers 1, 2, 7, 8, 9, 10, 15 and 16 are analyzed in the tracking section FT12 and for FT56 the corresponding layers are 33, 34, 39, 40, 41, 42, 47 and 48. The procedure to identify track candidates is the same in both sections.

The algorithm searches the list of straws to identify all pairs of the straws (S_1, S_2) located at the entry and the exit of the FT12 (FT56) section, where the straw $S_1(z_1, x_1)$ with the drift radius r_1 belongs to the layer 1 or 2, and $S_2(z_2, x_2)$ with the drift radius r_2 belongs to the layer 15 or 16. The coordinates (z_i, x_i) refer to the intersection of the anode wire (i) with the ZOX plane. Next, the straight line L: $x = a \cdot z + b$ passing through these points is constructed. The algorithm then looks for all vertical straws $S_i(z_i, x_i)$ from the inner vertical layers, whose distance from the constructed line is smaller than a predetermined value $d = \max(r_1, r_2) + 0.5$ cm (the constant 0.5 cm is the radius of the straw tube) - see Fig. 6.17.

For a given pair (S_1, S_2), the number of straws located closer than d to the constructed line is calculated and, if it is greater than 6, the set of straws is preserved for further processing. The search for the track line continues with creation of four lines tangent to the two circles $c1(S_1, r_1)$ and $c2(S_2, r_2)$ defined by the drift radii r_1 and r_2 , respectively (see Fig. 6.18). For each tangent line a new straw search is performed and the absolute value of the difference ds between the track line distance from the straw center $d(S, \text{tangent})$ and the drift radius rs is calculated for each straw (see Fig. 6.18):

$$ds = |d - rs| . \quad (6.2)$$

Hereinafter, the difference ds is called the residuum. If ds is smaller than assumed limit value $\Delta l = 0.5$ cm (the radius of the straw tube), then the straw is accepted and added to the straw list associated with a hypothetical track and the sum dd of residua for all straws from the list is calculated:

$$dd = \sum ds . \quad (6.3)$$

If more than 6 straws meet this criterion then the tangent is treated as a candidate for the track. From all the candidate tangent lines the one characterized by the smallest value of dd is accepted as the track candidate.

The approach which allows preserving track candidates based on the two outermost layers leads

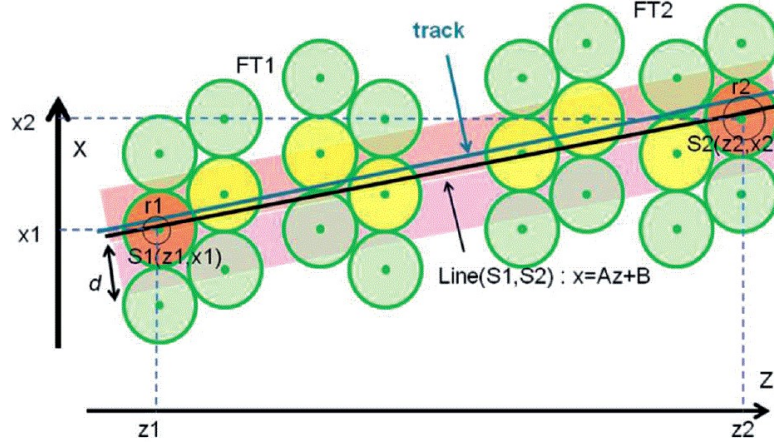


Figure 6.17: Straw candidates to the track in the ZOX plane in the FT12 (or FT56) station. Yellow colored straws inside pink band fulfill the distance requirement.

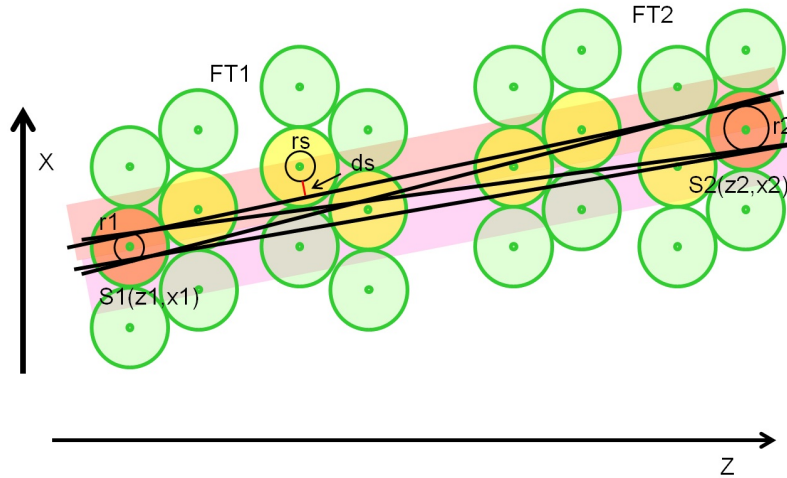


Figure 6.18: Four tangent lines considered in the search for the track line in the FT12 (or FT56) station.

to creation of duplicate sets with the same straws. Two track candidates are considered to be a "track repetition" if they contain the same straws in at least 7 out of 8 layers or if out of 7 straws no more than 4 have adjacent numbers. The candidate with a larger number of hit straws or, if the numbers of straws are equal, with a smaller value of dd is selected and the other is considered as a ghost and discarded.

Distributions of the residua ds for the accepted track candidates in the sections FT12 and FT56 are shown in Fig. 6.19 (upper panel). The widths of the distributions are close to the spacial resolution of a single straw tube detector of $\sigma = 0.015$ cm assumed in the simulations. This confirms, that the assumed model of the track in the FT12 and FT56

section in the form of a straight line is correct and the bending of the track in the stray field of the dipole magnet is negligible.

6.2.2.2 Track Recognition in the ZOY Plane Using the Skewed Straws

In the next step, the layers with skewed straws in the sections FT12 and FT56 are used to determine the projection of the particle trajectory in these sections on the vertical plane ZOY. For each track found in the horizontal plane ZOX, a vertical plane Z' OY containing this track is constructed (see Fig. 6.20).

Then for the anode wire in each skewed input straw (described by equation $y = a \cdot (x - x_0) + y_0$) the point

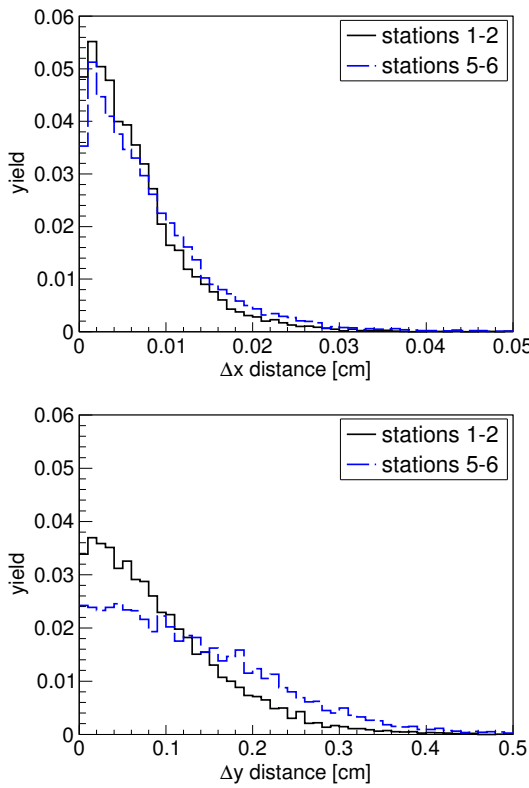


Figure 6.19: Distribution of residua ds for the track projections on the horizontal plane (upper panel) and on the vertical plane (lower panel) in the FT12 section (black line) and FT56 section (blue line).

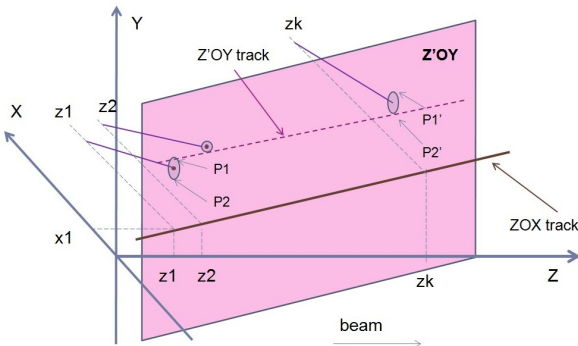


Figure 6.20: The vertical Z'OX plane constructed with the track candidate found on ZOX. The points P1 and P2 correspond to the intersection of a skewed straw at z_i with the Z'OX plane.

$P(z, y)$ of the intersection of the wire with the Z'OX plane is calculated. The drift radius associated with the hit straw defines a cylindrical surface with the wire being the symmetry axis. The intersection of the cylindrical surface and the Z'OX plane is an el-

lipse. For each ellipse the y coordinates of the vertex points $P_1(z, y_1)$ where $y_1 = y + cc$, $cc = r \cdot \sqrt{1+a^2}$ and $P_2(z, y_2)$ where $y_2 = y - cc$, lying in the anode wire plane described by a fixed value of the z coordinate, are determined (see Fig. 6.20). The algorithm then uses these points in search for track candidates utilizing the same approach as for the plane ZOX. For every pair of points from the outermost double layers of skewed straws the four lines are constructed and the distances from the skewed straws from the internal layers to these lines are calculated. The tangent line consistent with at least 6 straws and having the smallest sum of the residua is then selected as a projection of the track candidate on the ZOY plane.

Distributions of the residua ds for the projections of the track candidates on the vertical plane ZOY in the sections FT12 and FT56 are shown in Fig. 6.19 (lower panel). The widths of the distributions are roughly 0.15 cm and are comparable with the expected spatial resolution σ_y in the vertical direction. This resolution is about 10 times worse than the one in the horizontal plane ($\sigma_x \sim 0.015$ cm) since the ratio of the resolutions σ_y/σ_x depends on the inclination angle θ of the straws as $\cot(\theta)$ and for the present inclination $\theta = 5^\circ$, $\sigma_y/\sigma_x \approx 11$.

6.2.2.3 Track Recognition in the ZOX Plane in Magnetic Field with Vertical Straws

The PR in the FT34, in the presence of the magnetic field, continues with the set of track candidates found in the section FT12. For every track candidate from FT12 the algorithm calculates coordinates of a circle being tangent to the track projection on the horizontal plane at position, where the track curvature starts (z_Bstart). Furthermore, it is required that the circle is passing through the anode wire of at least one fired straw of the two outermost vertical layers in FT34 (layer 31 or 32) depicted as dashed line P32 in Fig. 6.21. For each circle the sum of residua for the internal vertical straws in FT34 is calculated and the circle with minimal value of such sum is identified as the continuation of the track originating from FT12.

The z -coordinate of the beginning of the constant magnetic field (z_Bstart) was found, using a sample of single muon tracks passing through all the FT sections, in the following procedure. Alternating the beginning of the magnetic field in the z direction in 11 steps of 5 cm, the sum of residua for the vertical straws was calculated for every step. The sum was then histogrammed as function of z for three different muon momenta (see Fig. 6.22).

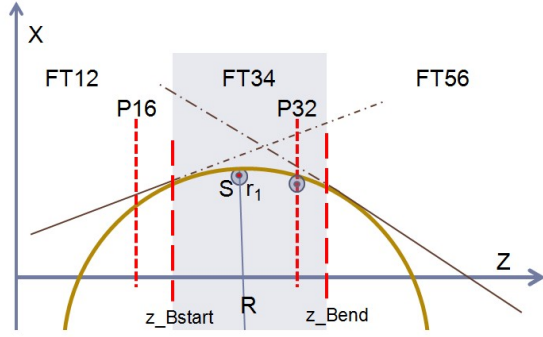


Figure 6.21: The constant magnetic field spans between z_Bstart and z_Bend . The circle is tangent to track candidate from FT12 at point z_Bstart and passes through a straw from the layer number 32 (P32 in the figure) or 31.

A clear minimum in the histograms was found at $z_Bstart = 368$ cm for each of the three momenta. This coordinate was chosen as optimal for connecting the straight track segments determined in the FT12 section with the circular segments in the FT34 section. As one could expect, z_Bstart lies in the range of the rising slope of the magnetic field distribution in the dipole magnet gap presented in Fig. 3.7 (Sec. 3.2) as a function of the z-coordinate.

Fig. 6.23 (upper panel) shows distributions of the residua for the circular track segments in the FT34 section for three different muon momenta: 0.55, 2.55 and 5.55 GeV/c. The residua are on the level of a few millimeters and thus are much larger than the assumed position resolution of the straws (~ 0.15 mm). This results from the applied approximation of the particle trajectories in the inhomogeneous magnetic field inside the dipole magnet gap with the circular track models corresponding to the homogeneous field.

6.2.2.4 Track Recognition in the ZOY Plane in the Magnetic Field

The PR algorithm assumes that the ZOY projections of tracks in FT34 are straight lines being prolongations of the tracks from FT12. As the horizontal projections of the tracks from FT12 are now associated with the circles in FT34, the PR uses the circle equation to calculate x coordinate of a point on the circle at given z-coordinate of a layer with skewed straws (see Fig. 6.24). This point defines a plane containing it and parallel to ZOY. In this plane, distances between its intersections with the skewed straws and the projection of the straight line

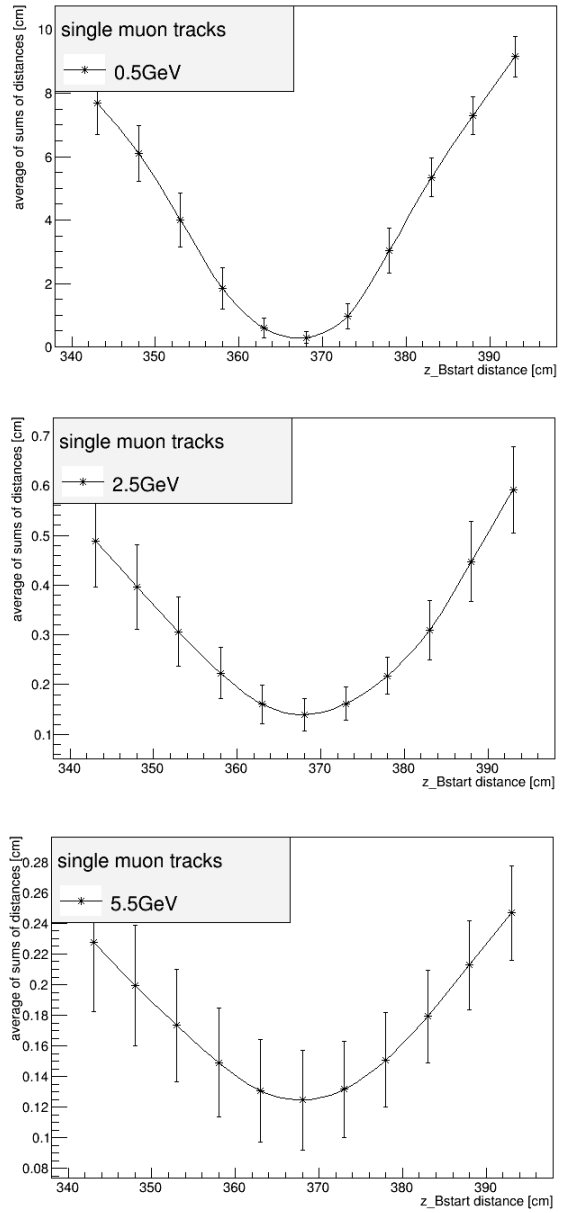


Figure 6.22: Average sum of residua of the vertical straws in the FT34 section with respect to the circular tracks, determined as a function of the z-coordinate of the matching point between the straight line trajectory in the FT12 section and its prolongation as a circle within the FT34. The distributions are presented for the three momenta of muon tracks.

from FT12 are calculated. The straw with the intersection at minimal distance to the straight line projection is then assumed to contribute to the track.

Fig. 6.23 (lower panel) shows distributions of residua for the inclined straws in the FT34 section with respect to the track projection on the ZOY

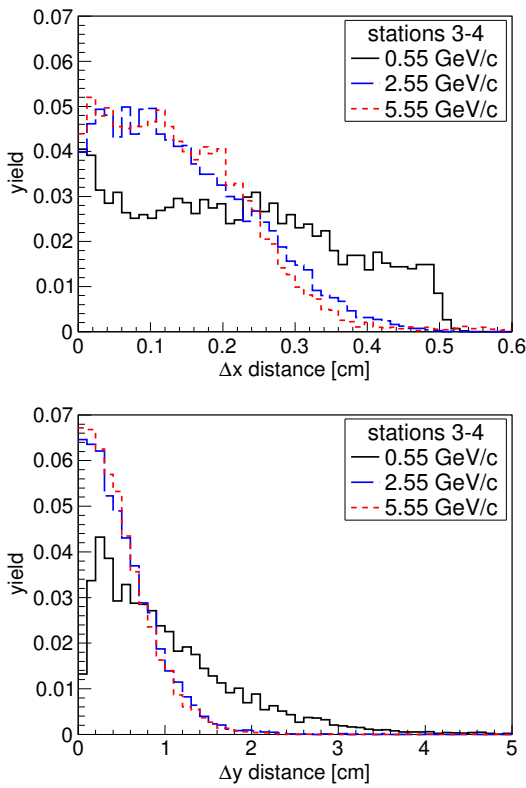


Figure 6.23: Distribution of residua ds for the track projection on the horizontal plane (upper panel) and on the vertical plane (lower panel) in the FT34 section, for the three muon momenta.

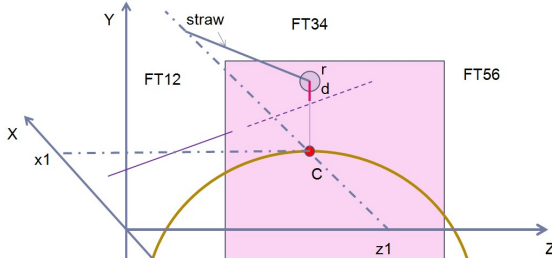


Figure 6.24: The x_1 coordinate of point C for a given z_1 (as z_1 coordinate of the layer with skewed straws is taken) is calculated from the circle equation corresponding to the projection of the track on ZOX plane. The distance d is used in calculation to find straw corresponding to the track.

plane. The relatively large widths of the distributions, in the order of 1 cm, result from the approximate nature of the track model in the FT34 section (a circular in the horizontal projection and a straight line in the vertical projection).

6.2.2.5 Matching Track Segments from FT12 and FT34 with Tracks from FT56

In the final step, the PR algorithm attempts to match track candidates identified in the section FT12 and their prolongation to FT34 with the track candidates found in FT56. Some of the low momentum particles may not enter the FT56 section, hence the number of candidates found in FT56 may not correspond to the number of tracks identified in FT12+FT34.

In order to find an optimal matching point z_Bend between the circular track segments in FT34 and the linear segments in the FT56, we applied a procedure analogous to that used for determining the matching point z_Bstart between FT12 and FT34. For this, a sample of single muon tracks was used to scan the position of the z_Bend with a 5 cm step. Sum of the residua for the vertical straws in the FT34 segment was histogrammed as a function of the z-coordinate (see Fig. 6.25). Position of the minimum visible at $z_Bend = 560$ cm was chosen as the optimal matching point. The point z_Bend lies approximately in the middle of the z-coordinate range corresponding to the falling slope of the magnetic field distribution in the dipole magnet gap (see Fig. 3.7, Sec. 3.2).

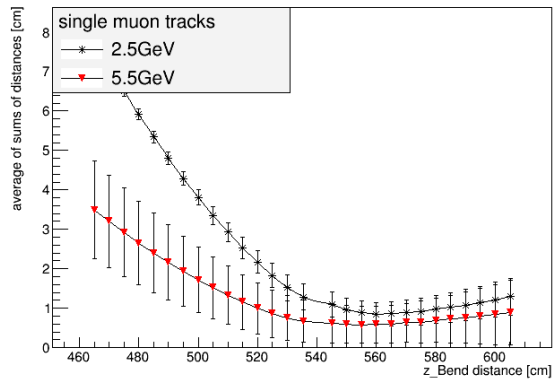


Figure 6.25: Sum of distances in plane ZOX from points in tracks to positions of anode wires reduced by the drift distance from a sample muon tracks at different energies as function of z_Bend .

For every track candidate identified in the section FT12 and the FT34 the PR algorithm calculates sums of two distances to every track candidate identified in the FT56. The two distances are calculated at the z_Bend coordinate. The first distance d_{ZOX} (see Fig. 6.26) is calculated between the track segment reconstructed in FT56 and the circle in the ZOX plane (for an ideal match it should be 0). The

other distance d_{zoy} is determined between the track segment reconstructed in FT12 and FT34, and the track segment reconstructed in FT56 in the ZOY plane. The match between track segment from FT12 continued in FT34 and FT56 is declared for the combination with the minimal value of the sum of these distances.

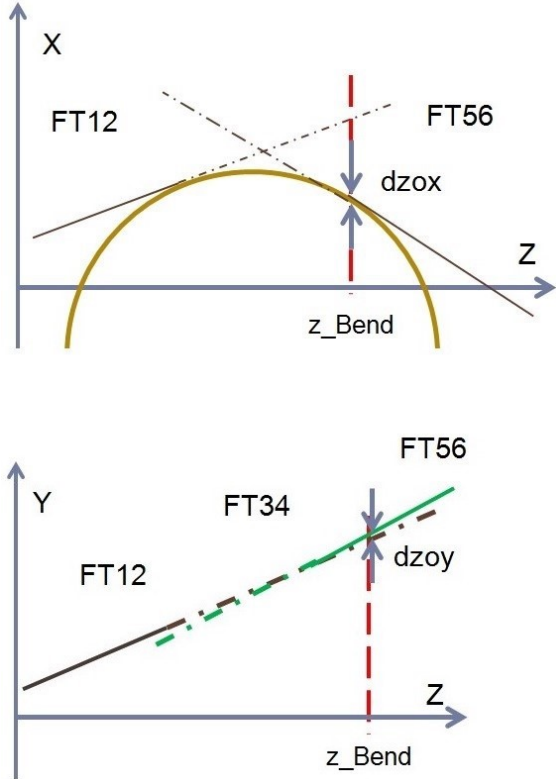


Figure 6.26: Definition of the distance d_{zox} in the horizontal XOZ plane (upper panel) and d_{xy} in the vertical YOZ plane (lower panel) calculated by the PR algorithm when matching track fragments from FT12+34 with track fragments from FT56.

Distribution of d_{zox} and d_{xy} for 2.55 GeV/c and 5.55 GeV/c muon tracks is shown in Fig. 6.27. The widths of the distributions, both the horizontal (d_{zox}) and the vertical one (d_{xy}), are of about 1.5 cm and are mainly due to the approximate nature of the track model in the magnetic field section of tracking system.

6.2.2.6 Efficiency of the Pattern Recognition Algorithm

Each set of n_s straws corresponding to the simulated track was compared to the sets of n_r straws indicated by the PR algorithm as track candidates.

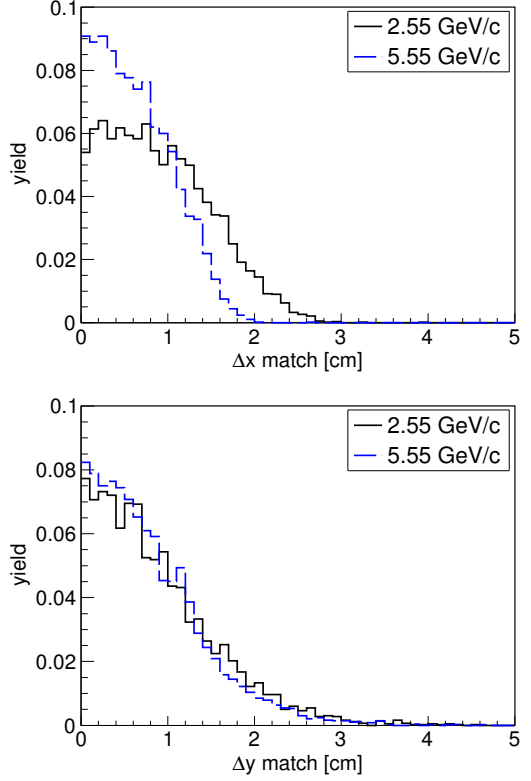


Figure 6.27: Distribution of the distance d_{zox} (upper panel) and d_{xy} (lower panel).

The track candidate with the highest number n_c of straws common with the simulated track was selected for determination of PR efficiency. The number n_c can be viewed as a number of correctly recognized straws in the simulated track. Fig. 6.28 shows distributions of straw multiplicity for simulated tracks and for the PR track candidates with the highest number n_c , for simulations with the track multiplicity per event of 5.

For the momentum of 0.55 GeV/c (top panel in Fig. 6.28), both distributions have a peak around the straw multiplicity of 32 expected for the low momentum tracks passing only through the FT12 and FT34 sections, but, besides, the distributions corresponding to the track candidates have a long tail at the side of the low multiplicities. The origin of this tail is being investigated. For the particle momenta of 2.55 and 5.55 GeV/c (middle and lower panel in Fig. 6.28), both distributions are very similar and are concentrated around the straw multiplicity of 48, corresponding to tracks passing through all of the tracking stations.

The efficiency of the PR algorithm was defined as

the ratio of the number of simulated tracks with more than 28 recognized straws ($n_c > 28$) for the low momentum tracks passing through FT12+34 and 40 for tracks with higher momenta, passing through all the stations, to the number of all simulated tracks. The PR efficiency is presented in Fig. 6.29 as a function of momentum for the three different track multiplicities. For the muon momentum of $5.55 \text{ GeV}/c$, the efficiency is close to 100%, for $2.55 \text{ GeV}/c$ is slightly above 90% and for $0.55 \text{ GeV}/c$ equals roughly 94%, 86% and 79% for the track multiplicities of 1, 3 and 5, respectively. We expect, that the efficiency can still be improved, since the PR algorithm has been finished very recently and contains several parameters and conditions which can be optimized.

6.2.2.7 Momentum Estimation

The PR algorithm also provides the information about the approximate value of the particle momentum. For high momentum tracks reaching the FT5, 6 stations, the momentum determination is based on the angle between the straight track segments measured in the FT12 and FT56. In the calculations, the nominal field integral in the dipole magnet (2 Tm at $p_{beam} = 15 \text{ GeV}/c$) is assumed. For lower momentum tracks measured only in the FT12 and FT34 stations and not reaching the FT56, the momentum determination is based on the radius of the circular trajectory of the particle in the stations FT34. For this, we assume, that the integral of the uniform magnetic field in the range between z_Bstart and z_Bend equals the integral of the real (non-uniform) field of the dipole magnet equal 2 Tm at the maximum field setting. Fig. 6.30 shows the distributions of the reconstructed momenta of 0.55, 2.55 and $5.55 \text{ GeV}/c$ muons, with variances σ_p corresponding to the momentum resolution σ_p/p of 2.2%, 1.8% and 1.6%, respectively. Since the momentum resolution is quite good, close to the required precision of 1-2%, and the developed PR algorithm is relatively simple from the point of view of the computational complexity, we propose to use it for online momentum reconstruction in the FT. We have already started to work on the implementation of this algorithm in FPGA.

6.2.3 Momentum Reconstruction

The PR algorithm delivers track candidates (sets of IDs of straws with associated drift radii, identified as belonging to a single track) which are then used for the reconstruction of tracks with the Kalman

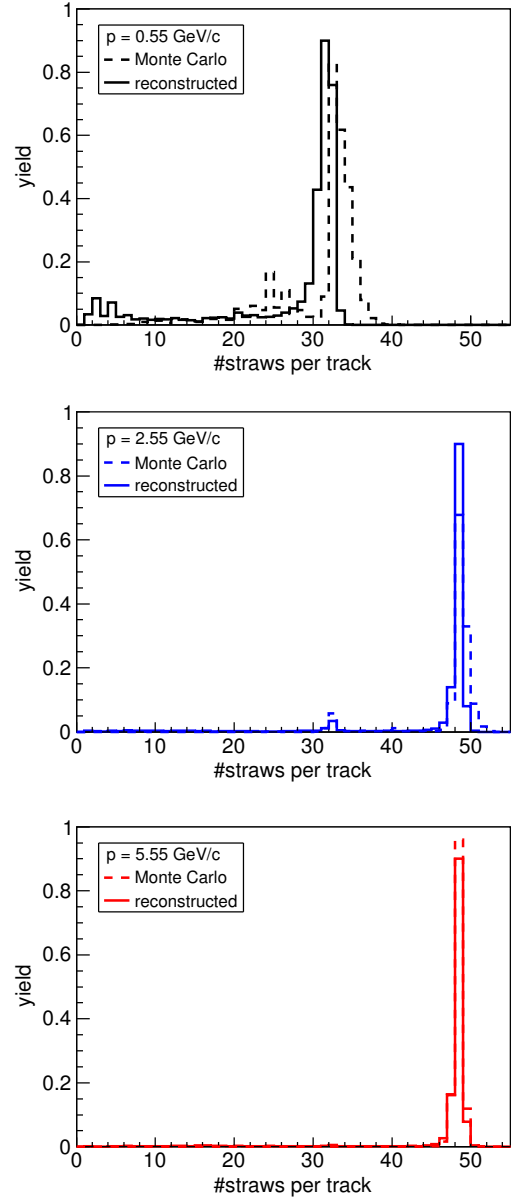


Figure 6.28: Straw multiplicity in the simulated tracks (dashed line) and the track candidates with the highest number of recognized straws n_c (solid line) for muon momentum of $0.55 \text{ GeV}/c$ (upper panel), $2.55 \text{ GeV}/c$ (middle panel) and $5.55 \text{ GeV}/c$ (lower panel).

filter. One of the basic quantities provided by the Kalman filter is the reconstructed momentum vector \vec{p}_{rec} at the target point, or strictly speaking, at the point of intersection of the reconstructed trajectory with the plane $z=0$ (the plane contains the target point: $x=y=z=0$). To assess the precision of the particle momentum reconstruction, we introduce two quantities: Δp - the difference be-

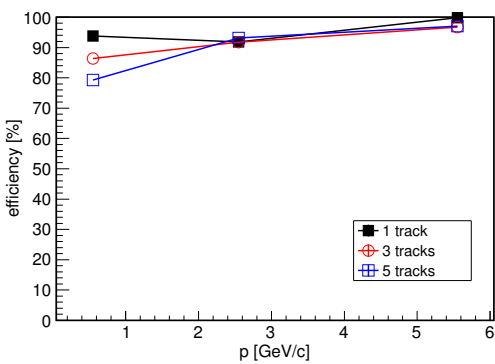


Figure 6.29: Efficiency of the PR algorithm for three different muon momenta 0.55, 2.55 and 5.55 GeV/c and track multiplicities 1, 3 and 5.

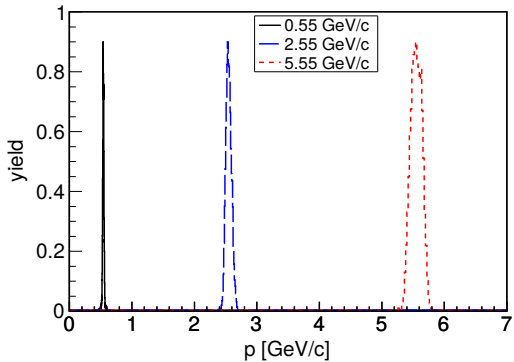


Figure 6.30: Distributions of muon momenta determined using the radius of the circular trajectory in the magnetic field of the dipole magnet for 0.55 GeV/c muons and the deflection of the trajectory measured with the FT12 and FT56 stations for 2.55 and 5.55 GeV/c muons.

tween the magnitude of the momentum vector of the reconstructed track and of the simulated track: $\Delta p = |\vec{p}_{rec}| - |\vec{p}_{ideal}|$ and

$\Delta\Theta$ - the opening angle between the momentum vector of the simulated track and the reconstructed track.

Fig. 6.31 (left part) presents distributions of Δp for reconstructed single muon tracks (corresponding distributions for the track multiplicity 3 and 5 are very similar and, therefore, are not presented). The distributions of Δp are symmetric with respect to $\Delta p = 0$, and, apart from small tails, fit well within a range of roughly $\Delta p = \pm 0.1$ GeV/c. The variance of the Δp distribution divided by the magnitude of the momentum is a measure of the mo-

mentum resolution. For the studied momenta of 0.55, 2.55 and 5.55 GeV/c, the obtained momentum resolutions are 3.1%, 1.1% and 0.6%, respectively. The momentum resolution is limited not only by the performance of the FT tracking stations, but also by the energy straggling and the multiple scattering at small angles on the elements of the PANDA setup in the particle path. An essential contribution comes from the elements of the beam pipe. After removing the beam pipe from the simulated setup, the momentum resolution determined for 0.55, 2.55 and 5.55 GeV/c improves to about 2.5%, 0.7% and 0.4%, respectively (see Fig. 6.31 (right part)).

The effect of the multiple scattering on the elements of the PANDA system, has even greater impact on the angular smearing $\Delta\Theta$. Fig. 6.32 (upper panel) presents distributions of $\Delta\Theta$ for reconstructed single muon tracks (corresponding distributions for the track multiplicity of 3 and 5 are again very similar and, therefore, are not presented). The largest smearing $\Delta\Theta$ of a few tenths of degree is visible for the smallest momentum of 0.55 GeV/c. This smearing is dominated by the multiple scattering on the elements of the beam pipe. After removing the beam pipe from the simulated setup, the smearing is reduced by a factor of 3-4 (see Fig. 6.32 (lower panel)).

For the study of the reconstruction efficiency, we select the muon tracks generated in the Monte Carlo simulations (MC-tracks) emitted at polar angles in the range $2.5^\circ - 5^\circ$. This condition ensures that the tracks pass through the active layers of the FT and not through the central openings in the layers and, thus, the tracks can be considered as "reconstructible".

The MC-track is considered to be successfully reconstructed if at least one track reconstructed by the Kalman filter has the momentum vector very close to the momentum vector of the MC-track. We express this condition in quantitative way by the requirement, that Δp should lie in the range ± 0.2 GeV/c and the opening angle $\Delta\Theta$ for the momenta of 0.55, 2.55 and 5.55 GeV/c should be smaller than 0.5, 1.0 and 2.5 degrees, respectively.

We calculate the track reconstruction efficiency as the fraction of successfully reconstructed tracks:

$$e = \frac{N_{REC}}{N_{MC}}. \quad (6.4)$$

With the assumed condition defining the successful reconstruction, the reconstruction efficiency is of 95-98% as given in Table 6.1.

The reconstructed tracks which do not fulfill this condition (are not consistent with any of the MC-

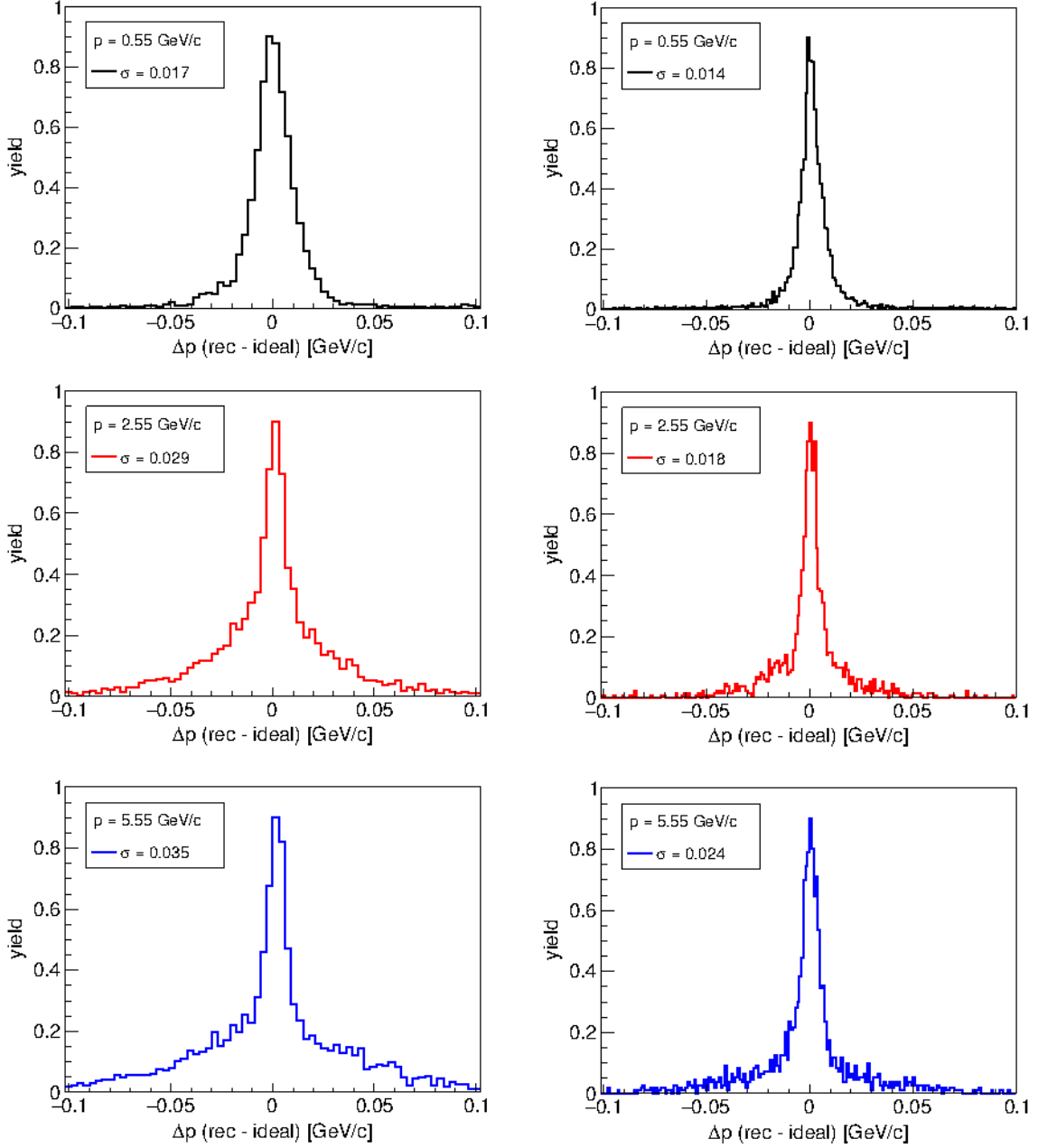


Figure 6.31: Difference between the absolute value of the reconstructed momentum and the simulated momentum of single muon tracks in simulations including the full PANDA setup (left) and the PANDA setup with removed beam pipe (right).

tracks within the given limits) are called the ghost tracks. The fraction of ghost tracks is calculated as:

$$e = \frac{N_g}{N_{MC}}. \quad (6.5)$$

The largest ghost fraction of 9% observed for the lowest momentum of $0.55 \text{ GeV}/c$ results mainly from the tail in the $\Delta\Theta$ distribution exceeding the limit

$$\Delta\Theta < 2.5^\circ.$$

The last column of Table 6.1 gives the fraction of the so-called clone tracks, which correspond to MC-tracks consistent with two or more successfully reconstructed tracks. The clone fraction is calculated as:

$$c = \frac{N_c}{N_{MC}}. \quad (6.6)$$

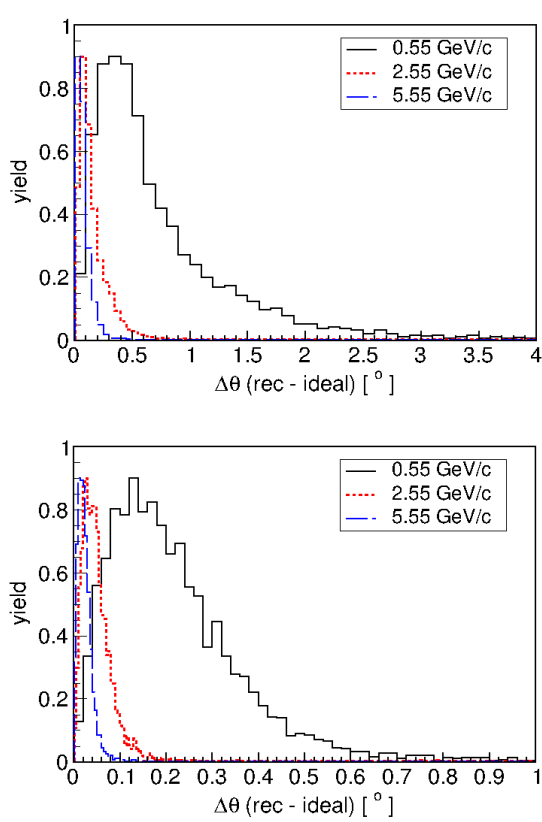


Figure 6.32: Distribution of the opening angle between the reconstructed and simulated momentum vector of single muon track in simulations including the full PANDA setup (top) and the PANDA setup with removed beam pipe (bottom). Note that the range of the angular scale in the top figure is four times wider than in the lower one.

For the momenta 2.55 and 5.55 GeV/c, this fraction is smaller than 1%. It has the highest values of 9% and 17% for the 0.55 GeV/c muon tracks with the multiplicity 3 and 5, respectively. This high clone fraction does not result from multiple track candidates produced by the PR algorithm (clone fraction of single muon tracks is 0%) but it corresponds to pairs of close MC-tracks and the corresponding pairs of successfully reconstructed tracks being consistent with more than one MC-track.

6.3 Optimization of the Tracking System

The simulations of tracking were used to optimize some of the key parameters of the FT. In the following three subsections we present results of searching

p (GeV/c)	Track mult.	Recon. eff.	Ghost fract.	Clone fract.
0.55	1	96%	9%	0%
	3	97%	9%	9%
	5	98%	9%	17%
2.55	1	95%	3%	0%
	3	96%	2%	2%
	5	95%	2%	3%
5.55	1	97%	2%	0%
	3	96%	3%	0%
	5	95%	3%	1%

Table 6.1: Reconstruction efficiency, ghost fraction and clone fraction determined for three momenta and three multiplicities of the simulated muon tracks.

for optimal (i) setting of the stations FT5, FT6 and the Forward RICH relative to each other, (ii) inclination angle of the straws and (iii) active areas of the tracking stations. In the simulations, the distances of the simulated tracks from the anode wires in the hit straws were smeared according the assumed position resolution of $\sigma = 200 \mu\text{m}$ per straw. Thus the simulations did not include the measurement of the drift time. We applied the so-called ideal tracking, i.e. the pattern recognition was not used and the information about track candidates was taken directly from the simulation code. The tracks were reconstructed with the Kalman fit.

6.3.1 Short versus Long Distance Scenario for Arrangement of FT5-FT6

For the forward tracking stations two different scenarios have been studied: the long and short distance configuration for the arrangement of the FT5 and FT6.

In the long distance scenario, shown in Fig. 6.33 (a), the RICH detector is placed between the FT5 and the FT6. The distance between the two tracking stations is 140 cm and the FT6 is two meters bigger in width and 30 cm in height than the FT5.

In the short distance scenario, shown in Fig. 6.33 (b), the RICH detector is moved after the FT stations. The distance between the FT5 and FT6 is reduced to 32 cm and both stations have the same dimensions.

In order to check the momentum resolution for these two scenarios, we simulated tracks of positive pions emitted from the target point in the polar angle range $\theta \in [0^\circ, 10^\circ]$, uniformly in $\cos \theta$ (isotropic distribution), and in the full azimuthal angle range

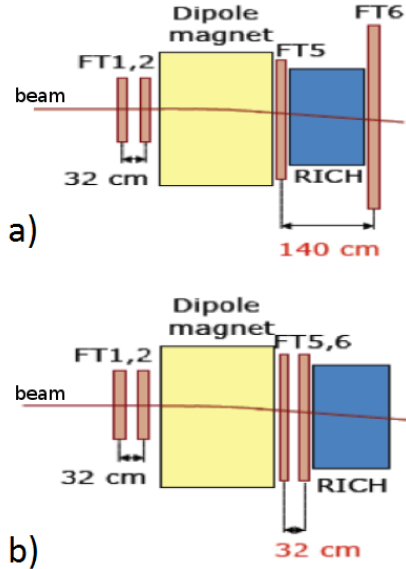


Figure 6.33: Long distance (a) and short distance (b) scenario for arrangement of FT5 and FT6. Details are described in the text.

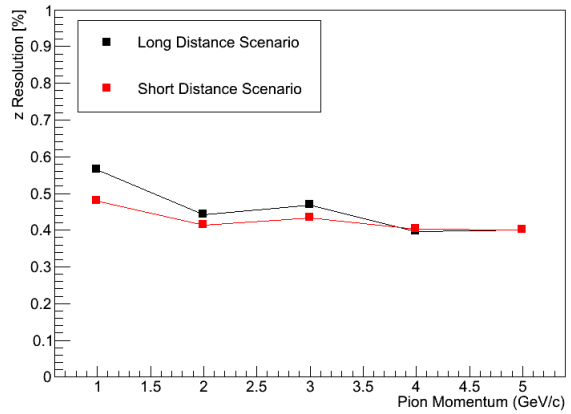


Figure 6.34: Momentum resolution (%) as function of pion's momentum for the two different geometry scenarios.

6.3.2 Inclination Angle of Skewed Modules

$\phi \in [0^\circ, 360^\circ]$. The simulations were done for a few pion momenta in the range 1–5 GeV. The magnetic field in the dipole magnet was set to the maximum of 2 Tm foreseen for operation of the HESR at the highest antiproton beam momentum of 15 GeV/c. We used the ideal tracking with 10% of momentum smearing and a vertex smearing of (0.1, 2.0, 0.1) cm in x, y, and z direction, respectively. We selected only the successfully reconstructed tracks from the Kalman fit. We studied the difference between the z component of the reconstructed momentum and the Monte Carlo generated momentum divided by the Monte Carlo one. The distribution was then fitted with a double Gaussian function in order to extract the z momentum resolution. The resolution is slightly better for the short distance scenario, especially for pion's momentum below 3 GeV/c, as shown in Fig. 6.34. The worsening of the resolution in the case of the long distance scenario results from the multiple scattering on components of the RICH detector.

For the Forward Tracker, the short distance scenario was chosen due to the better momentum resolution and a lower cost resulting from smaller active area of FT6. This is the scenario which has been discussed so far in this TDR.

The inclination angle of straw tubes in the double layers with skewed modules was determined based on simulations of the momentum and position resolution for muon tracks at different momenta. Fig. 6.35 shows the resolution of the vertical momentum component p_y divided by the longitudinal component p_z for 0.5 GeV/c muons, determined as a function of the straw inclination angle. The resolution deteriorates for angles below roughly 5° and for higher angles it remains almost constant. Similar behavior is visible for the position resolution of the vertical track coordinate at the location of the tracking station FT1, presented in Fig. 6.36 as a function of the inclination angle, for four different muon momenta. The presented dependence flattens for inclination angles greater than 5°, for which the resolution is better than 1 mm.

For the tilted layers in the FT we chose the inclination angle 5°, as the optimal one. Angles larger than 5° improve slightly the position resolution in the vertical direction, however, this improvement is not relevant for the precision of the determination of the scattering angle at the target, due to the dominance of the multiple scattering effect. Inclination angles larger than 5° are also unfavorable due to problems with mounting the modules in the vicinity of the beam pipe in the case of the split frames.

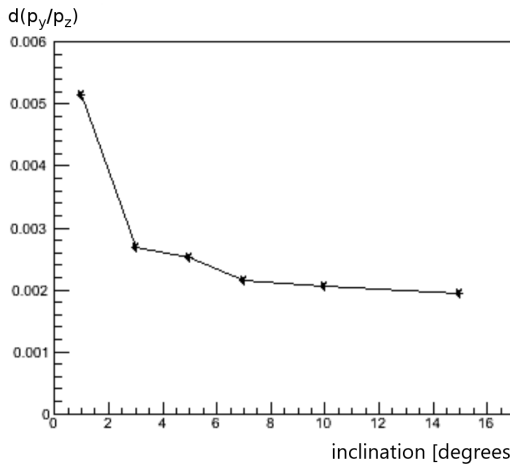


Figure 6.35: Resolution of the vertical momentum component p_y divided by the longitudinal momentum component p_z as a function of the inclination angle, determined for $0.5 \text{ GeV}/c$ muons.

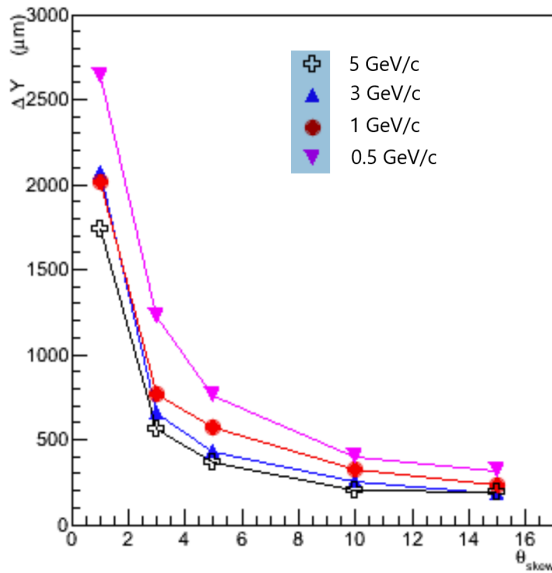


Figure 6.36: Spatial resolution of the vertical track coordinate (y) at the position of the FT1 tracking station as a function of the inclination angle, determined for four different muon momenta.

6.3.3 Active Areas of Tracking Stations

The required active areas of the tracking stations were studied in the following way. We simulated tracks of 10.000 positive pions emitted in the polar angle range $\theta \in [0^\circ, 10^\circ]$, in the full azimuthal angle range $\phi \in [0^\circ, 360^\circ]$, uniformly distributed in $\cos \theta$, selecting only the primary particles and simulating

the full $\overline{\text{P}}\text{ANDA}$ detector. The field in the dipole magnet was set to the maximum value corresponding to the beam momentum of $p_{beam} = 15 \text{ GeV}/c$. The simulations were done for five different pion momenta in a range from 0.3 to $5 \text{ GeV}/c$ corresponding to a fraction of the beam momentum from 2% to 33% .

The intensity distributions for pions in the tracking stations are shown in Fig. 6.37. The white central boxes correspond to the beam pipe holes. The distributions at low momentum have a "rotated" shape compared with the ones at high momentum. This distortion results from a spiraling motion of pions around the TS solenoid field lines. The simulated intensity distributions fit well in the foreseen active areas of the tracking stations.

In order to check numerically which is the acceptance of the tracking stations, we simulated 10.000 pions using the same criteria as described above, but we excluded the beam pipe hole by choosing the polar angle range $\theta \in [2^\circ, 5^\circ]$. We selected only primary tracks and we required that the pion hits all the four double-layers of each station. The pions have been simulated with different momentum: $0.3, 0.5, 1, 2, 3, 4$, and $5 \text{ GeV}/c$.

The acceptance of the tracking stations, calculated as the ratio of the registered and the generated pions, is shown in Fig. 6.38. For the first four tracking stations the acceptance rises rapidly from roughly 20% at the pion's momentum $0.3 \text{ GeV}/c$ ($= 2\% \text{ of } p_{beam}$) to about $80\text{-}85\%$ at $1 \text{ GeV}/c$. The last two tracking stations are not reached by pions with momenta below $1 \text{ GeV}/c$. For the momenta in the range from 1 to $5 \text{ GeV}/c$ the acceptance of the tracking stations lies within $80\text{-}90\%$. An inefficiency in the registration of the pion tracks is due to the interaction with the beam line elements.

The momentum reconstruction with the FT was also studied for different settings of the magnetic field in the dipole magnet, which is scaled according the beam momentum. Fig. 6.39 presents the momentum resolution for $2 \text{ GeV}/c$ muons as a function of the beam momentum in the range from 1.5 to $15 \text{ GeV}/c$. Deterioration of the resolution at low beam momenta results from smaller deflection of the muon tracks in the field of the dipole magnet and thus lower precision of the momentum determination. However, even at the lowest beam momentum of $1.5 \text{ GeV}/c$, the momentum resolution of 2.2% meets the requirements for the FT.

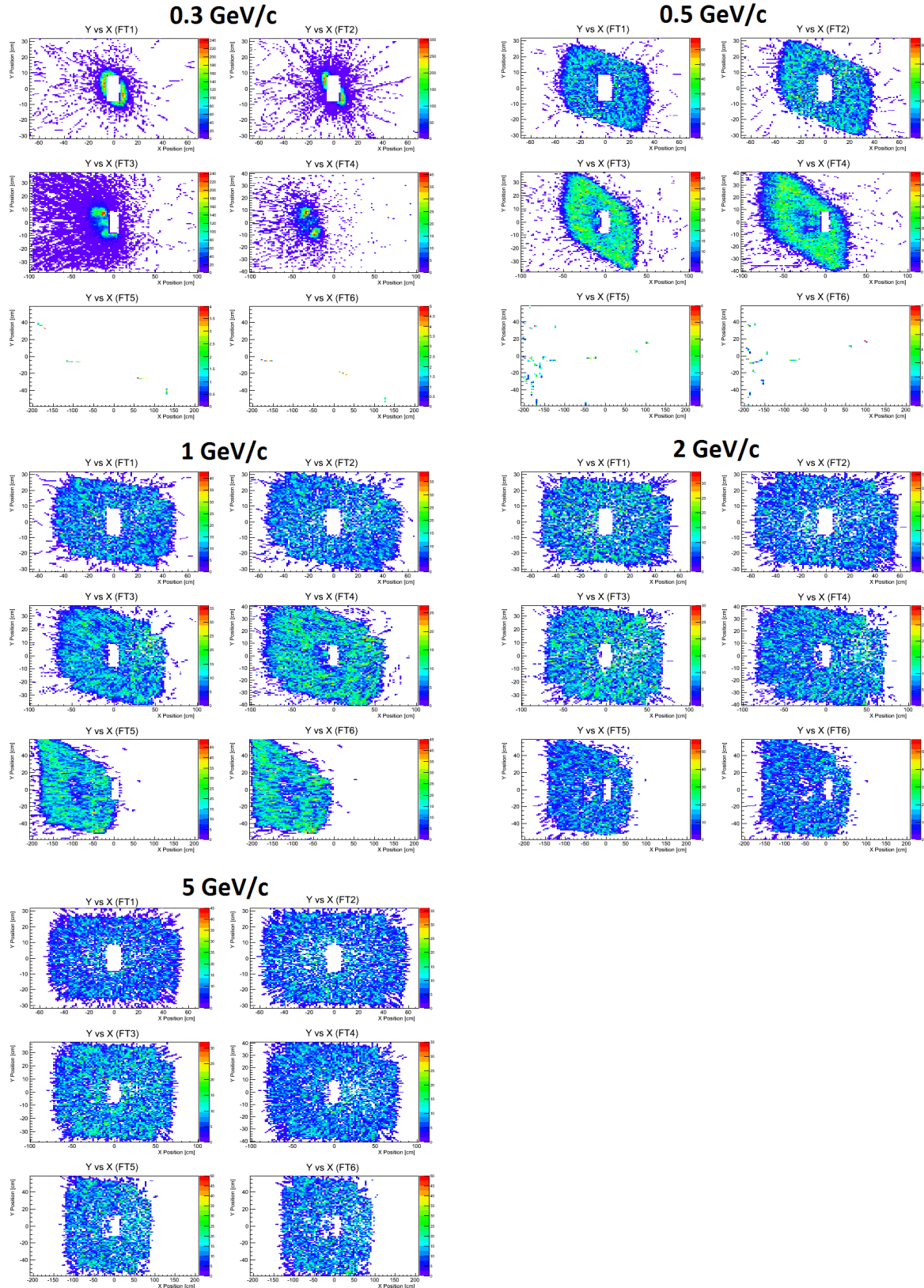


Figure 6.37: Intensity distribution of pions with momenta 0.3, 0.5, 1, 2, 5 GeV/c at the positions of the six FT stations. The x- and y-axis are respectively the horizontal and vertical coordinates of the stations.

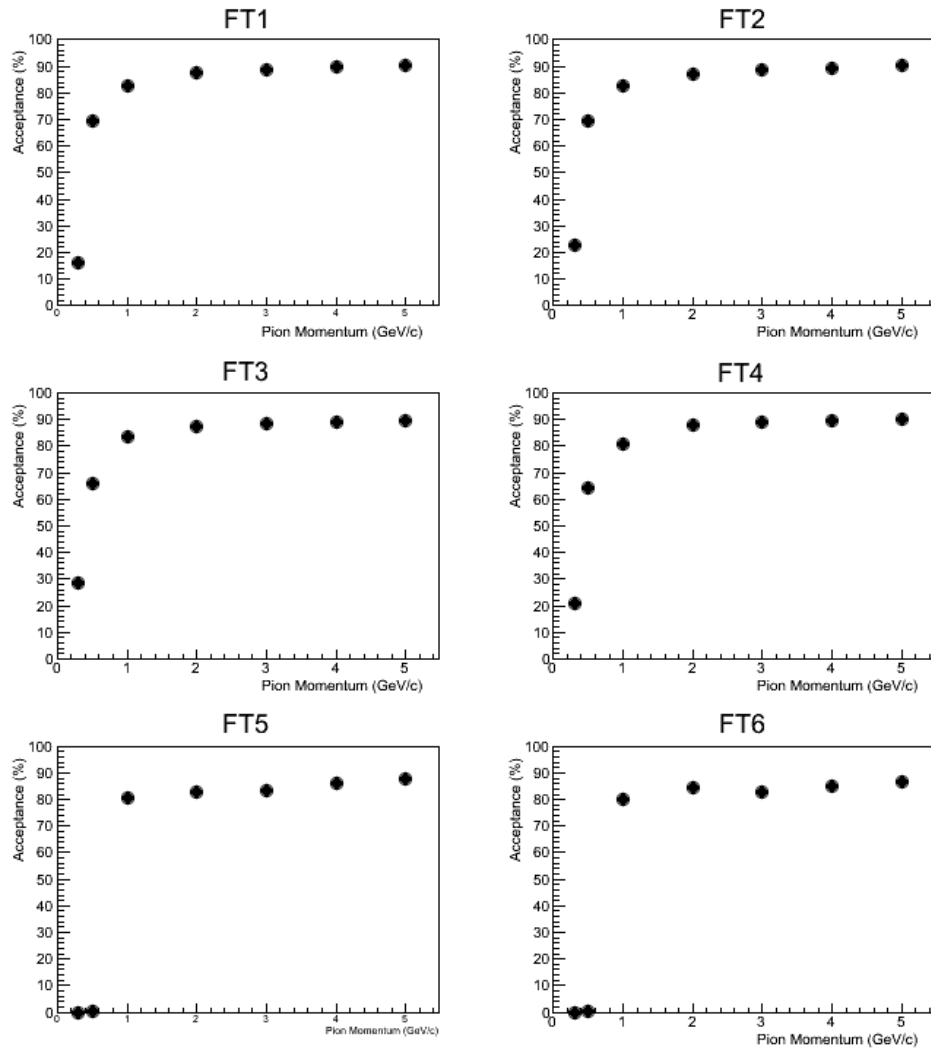


Figure 6.38: The acceptance of the tracking stations in function of the pion's momentum.

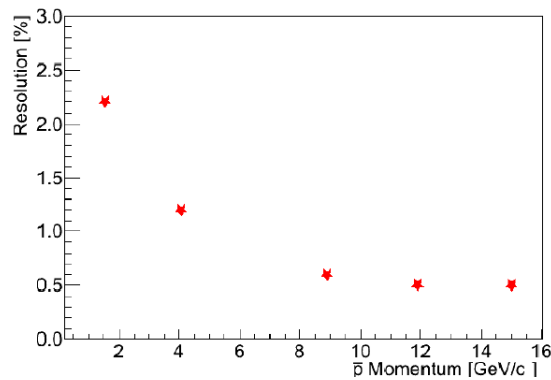


Figure 6.39: Momentum resolution for 2 GeV/c muons as a function of the antiproton beam momentum.

6.4 Physics Channels Analysis

6.4.1 Benchmark Channels

The Forward Tracker plays an essential role in measurements of reactions with angular distributions of produced particles strongly peaked in the forward direction in the laboratory system. The strong forward peaking takes place for processes with low excess energies and consequently low CM velocities of the reaction products. It can result also from a forward peaking of the production cross sections.

In order to check physics performance of the FT, two benchmark channels were selected and simulated:

- $\bar{p}p \rightarrow \Psi(4040) \rightarrow D^{*+}D^{*-}$
- $\bar{p}p \rightarrow \Lambda\bar{\Lambda} \rightarrow p\pi^-\bar{p}\pi^+$

The analysis is performed within the `PandaRoot` framework using the `EvtGen` event generator for the event production, Virtual Monte Carlo with `Geant3` for the simulation, dedicated digitization and reconstruction code, and the `rho` analysis tool for high level analysis. In the Monte Carlo simulations, the primary vertex was generated according to the expected target beam interaction region, with 0.1 cm size in transverse direction and distributed by a Gaussian function with $\text{FWHM} = 0.5$ cm along the z axis. The full \bar{P} *ANDA* geometry has been included in the simulation and, for the tracking, the FT, MVD, STT and GEM detectors have been used. An important remark here is that the analysis is performed with ideal particle identification, i.e. for each reconstructed track its particle type is associated using the Monte Carlo information, in order to avoid possible bias from the detectors used for PID.

6.4.2 $\bar{p}p \rightarrow \Psi(4040) \rightarrow D^{*+}D^{*-}$

The $\bar{p}p \rightarrow \Psi(4040) \rightarrow D^{*+}D^{*-} \rightarrow D_0\pi^+\bar{D}_0\pi^- \rightarrow K^+K^-\pi^+\pi^-\pi^+\pi^-$ was simulated assuming a uniform distribution over phase space accessible for the reaction products. The beam momentum in the simulations was set to 7.71 GeV/c which corresponds to CM energy required for creation of the $\Psi(4040)$ mass in the \bar{p} -p collision. Fig. 6.40 (a) presents distribution of pion θ angle vs momentum for generated events. Due to small excess energy ($Q = 6$ MeV), pions originating from the $D^{*+} \rightarrow D_0\pi^+$ and $D^{*-} \rightarrow \bar{D}_0\pi^-$ decays, are emitted at the most forward angles ($\theta < 10^\circ$) and with low momenta ($p < 0.5$ GeV/c). They are visible

in the presented distribution as a group of counts close to the origin of the coordinate system. In turns, pions resulting from the $D_0 \rightarrow K^+\pi^-$ and $\bar{D}_0 \rightarrow K^-\pi^+$ decays, due to higher excess energy in these decays ($Q = 1232$ MeV), are emitted over the whole angular range. Their momenta are partly correlated with θ and change from roughly 0.3 GeV/c in the backward direction to about 4 GeV/c at the most forward angles. Fig. 6.40 (b) shows the distribution of the pion tracks reconstructed with the full \bar{P} *ANDA* tracking system. With the exception of the most backward angles, not covered by this system, the tracks are registered over the whole angular and momentum range. In particular, the low momentum pions originating from the D^* decays are measured. Fig. 6.40 (c) shows, that these low momentum pions are not registered, if the FT is removed from the \bar{P} *ANDA* tracking system.

The scattering angles of kaons originating from the $D_0 \rightarrow K^+\pi^-$ and $\bar{D}_0 \rightarrow K^-\pi^+$ decays are distributed over the whole forward hemisphere as shown in Fig. 6.41 (a). The FT measures only a small fraction of kaon tracks as one can check by comparing the distribution with included and excluded FT from the \bar{P} *ANDA* tracking system as shown in Fig. 6.41 (b) and (c), respectively.

Reconstructed invariant mass of the D_0 and D^* mesons is presented in Fig. 6.42 (a) and (b), respectively. The black line in the figure represents the distribution of the invariant mass reconstructed with the full \bar{P} *ANDA* tracking system and the red line corresponds to the situation without the FT. Reconstruction efficiency for D_0 equals 51% with the FT and 44% without the FT. In the case of the D^* , the efficiency of reconstruction with the full tracking system equals 25% and is close to 0% without the FT.

Fig. 6.43 (a) shows the distribution of the reconstructed invariant mass of the $\Psi(4040)$ meson. The efficiency of the reconstruction is 8.5%. The invariant mass resolution obtained from a Gaussian fit equals $\sigma = 0.082$ GeV/c² (= 2.0%).

6.4.3 $\bar{p}p \rightarrow \Lambda\bar{\Lambda}$

The $\bar{p}p \rightarrow \Lambda\bar{\Lambda} \rightarrow p\pi^-\bar{p}\pi^+$ reaction was simulated for beam momentum of 4 GeV/c. Delayed decay vertices of the hyperons were taken into account. The angular distribution of the $\bar{\Lambda}$ hyperons was simulated according the LEAR data taken at 1.6 GeV/c [28]. This distribution is strongly peaked at small CM angles leading to emission of the decay pions π^+ and antiprotons at very forward laboratory angles as shown in Fig. 6.44 (a). As one can

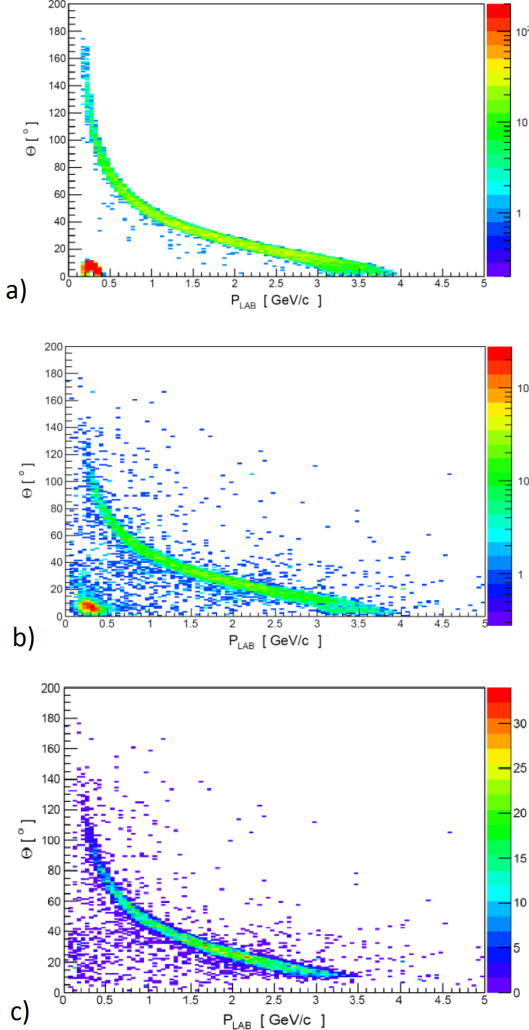


Figure 6.40: Pion scattering angle distribution vs momentum for generated events (a) and for reconstructed events with the FT included in the $\bar{\text{P}}\text{ANDA}$ tracking system (b) and removed from the system (c).

see in the figure, the antiprotons are almost fully confined in the angular range of the FT. The reconstruction efficiency of the antiprotons and the pions in the FT amounts to 65% and 53%, respectively (see also Fig. 6.44 (b)).

Fig. 6.45 shows the distribution of the $\bar{\Lambda}$ invariant mass. The resolution of the invariant mass obtained from a Gaussian fit equals $\sigma = 4.3 \text{ MeV}/c^2$ ($= 0.39\%$). The reconstruction efficiency of $\bar{\Lambda}$ is 34%.

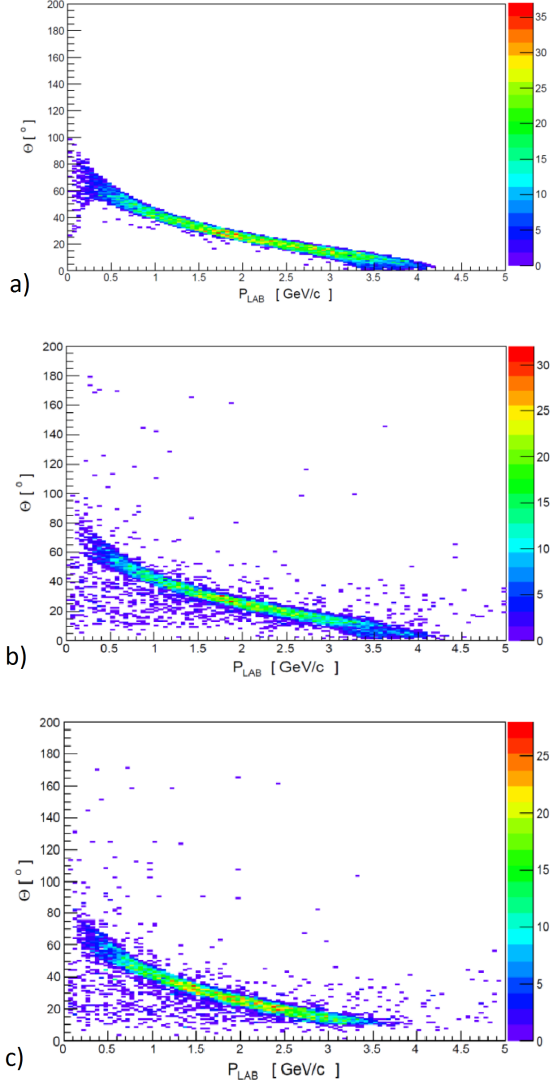


Figure 6.41: Kaon scattering angle distribution vs momentum for generated events (a) and for events reconstructed with the FT included (b) and removed from the $\bar{\text{P}}\text{ANDA}$ tracking system (c).

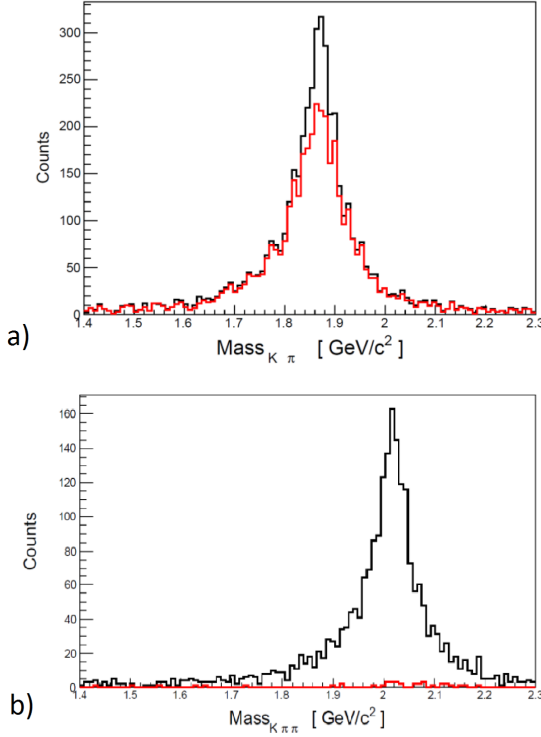


Figure 6.42: Invariant mass of D_0 (a) and D^* mesons (b) reconstructed with the FT included in the \bar{P} ANDA tracking system (black line) and without the FT (red line).

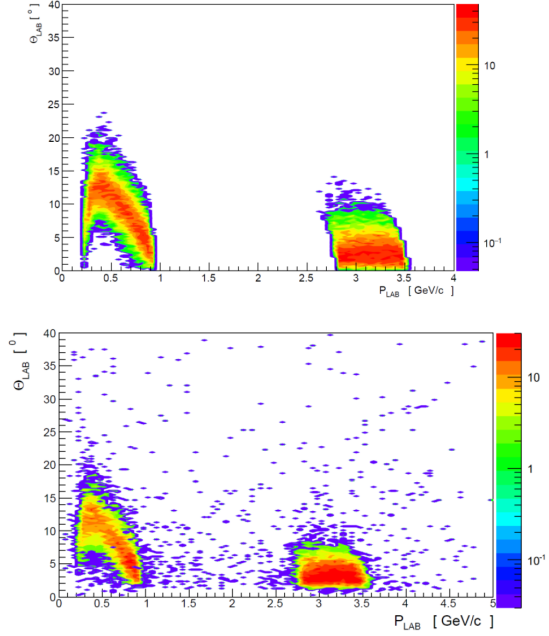


Figure 6.44: Distribution of the scattering angle vs momentum of positively charged pions (up to 1 GeV/c) and antiprotons (around 3 GeV/c) originating from $\bar{\Lambda} \rightarrow \bar{p}\pi^+$ decays and corresponding to generated (top) and reconstructed tracks (bottom).

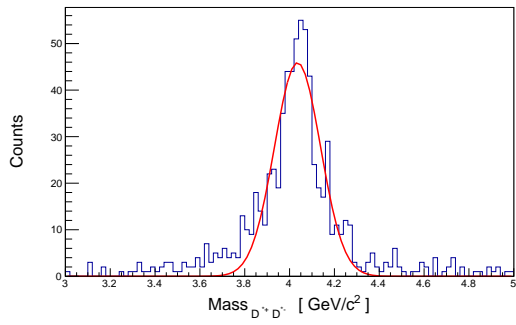


Figure 6.43: Invariant mass of the $\Psi(4040)$ meson reconstructed with the \bar{P} ANDA tracking system including the FT. Corresponding spectrum obtained without the FT contains only one entry and, therefore, is not shown.

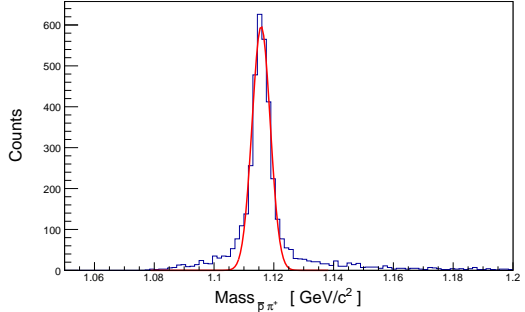


Figure 6.45: Reconstructed $\bar{\Lambda}$ mass.

References

- [1] F. Sauli, *Principles of operation of multiwire proportional and drift chambers*, Technical report, CERN 77-09, Geneva, 1977.
- [2] F. Lapique and F. Piuz, Nucl. Instrum. Meth. **175**, 297 (1980).
- [3] J. Fischle, H. Heintze and B. Schmidt, Nucl. Instrum. Meth. **A301**, 202 (1991).
- [4] J. Allison et al., Nucl. Instrum. Meth. **133**, 325 (1976).
- [5] K. Lassilla-Perini and L. Urban, Nucl. Instr. Meth **A362**, 416 (1995).
- [6] G. Collaboration, *Geant3 manual*, 1993, CERN program library W5013.
- [7] G. Collaboration, *GEANT4: An object oriented toolkit for simulation in HEP*, 1998, <http://geant4.cern.ch>.
- [8] R. Veenhof, *Garfield - simulations of gaseous detectors*, <http://garfield.web.cern.ch/garfield/>.
- [9] I. Smirnov, *Heed - Interactions of particles with gases*, <http://heed.web.cern.ch/heed/>.
- [10] S. Biagi, *Magboltz - transport of electrons in gas mixtures*, <http://magboltz.web.cern.ch/magboltz/>.
- [11] S. Jowzaee, *Self-supporting Straw Tube Detectors for the COSY-TOF and PANDA Experiments*, PhD Thesis, Jagiellonian University, Krakow, 2014, <http://www.fais.uj.edu.pl/documents/41628/b0b3751b-9a81-45b7-94bb-c0cb5a61a9bf>.
- [12] W. R. W. Blum and L. Rolandi, *Particle detection with drift chambers*, Springer Verlag, Berlin, 2008.
- [13] S. Jowzaee et al., Nucl. Instrum. Meth. **A718**, 573 (2013).
- [14] S. Spataro (for the PANDA collaboration), J. Phys.: Conf. Ser. **331**, 032031 (2011).
- [15] M. Al-Turany and F. Uhlig, PoS **ACAT08**, 048 (2008).
- [16] http://www.gsi.de/forschung/fair_experiments/CBM/index_e.html.
- [17] <http://www-hades.gsi.de/>.
- [18] http://www.gsi.de/forschung/kp/kr/R3B_e.html.
- [19] <http://root.cern.ch/drupal/content/vmc>.
- [20] I. Hřivnáčová et al., (2003).
- [21] R. E. Kalman, J. Basic Eng. **82**, 34 (1961).
- [22] R. Fruhwirth et al., Nucl. Instr. and Meth. **A262**, 444 (1987).
- [23] A. Fontana, P. Genova, L. Lavezzi, and A. Rotondi, *Track following in dense media and inhomogeneous magnetic fields*, Technical report, 2007.
- [24] L. Lavezzi, *The fit of nuclear tracks in high precision spectroscopy experiments*, PhD thesis, Università degli Studi di Pavia, 2007.
- [25] C. Höppner et al., Nucl. Instrum. Meth. **A620**, 518 (2010).
- [26] R. Fruhwirth et al., *Data Analysis Techniques For High Energy Physics*, Cambridge University Press, 1990.
- [27] V. Innocente and E. Nagy, Nucl. Instrum. Meth. **A324**, 297 (1993).
- [28] P. D. Barnes et al., Nucl. Phys. **A526**, 575 (1991).

7 Organization

7.1 Production Logistics

The production of the straw tube modules is the most labor-intensive process in the construction of the tracking stations for the FT. The production procedure is divided into a sequence of operations listed in Table 7.1 together with the information on the required amount of work. Each operation is performed on a separate stand using dedicated tooling and thus the operations can be performed in parallel.

The production of one module requires 12 man-days and for the six technicians foreseen in our schedule, the production of one module takes 2 days.

Besides the 400 modules needed in the FT, we plan to build 40 spare modules. Thus the total number of modules which will be built is 440. Taking into account, that one calendar year contains about 220 working days (weekends and holidays excluded), the 440 modules will be produced in four years (4 years \times 220 days / 2 days per module = 440 modules).

The front-end electronics boards and the TRB boards for the FT readout will be produced by external companies and the quality tests will be conducted by the FT groups.

Operation	Amount of work [man-days]
preparatory works e.g. cutting straws	2
gluing end plugs in straws	2
tensioning wires	2
sealing straws with glue	1
tests of straws: gas tightness, wire tension	1
assembling straws into module	2
tests of module	2
Total	12

Table 7.1: List of operations in production of the standard module containing 32 straws and required amount of work for each operation.

7.2 Timeline

The projected timeline of the FT construction is presented in Fig. 7.1. The production of modules, starting in the middle of 2018 and ending in the middle of 2022, is proceeded by a phase of completion of the conducted R&D and preparation of the final production drawings.

For the production of modules, a production line has already been set up in the Institute of Physics of the Jagiellonian University in Krakow. It includes stands for all of the operations in the production procedure listed in Table 7.1. The assembly of straws will be conducted in a clean-room class M5 with an area of 46 m². Tests of straws and assembly of modules will be conducted in an assembly room of 42 m². Tests of modules will be performed in a test laboratory of 58 m² with stabilized temperature and humidity, shielded as Faraday cage against radio frequencies up to 1 GHz.

Frames and support structures for the tracking stations will be produced by the end of 2020.

The ongoing development of the front-end boards and the TRB boards is scheduled to be finished in the mid of 2018 and by the end of 2019, respectively, and subsequent production is planned to be completed by the end of 2019 and in the middle of 2021, respectively.

The preparation of the services, including the gas system, the HV and LV supplies as well as the slow control system, is planned to be finished by the end of the third quarter of 2020. The supplies will be then used for testing the tracking stations at the production site.

Assembly and tests of the tracking stations will be conducted at the production site in the period from October 2020 to the end of 2022. The assembly will be carried out in a sequence from FT1 to FT6 following the order of the production of corresponding modules.

Transportation of the tracking stations and of the services to FAIR and installation in the PANDA Forward Spectrometer is planned in the period of the first three quarters of 2023. Commissioning of the Forward Tracker with the beam is foreseen for the last quarter of 2023 and throughout 2024. The Forward Tracker will be ready for data taking by the end of 2024.

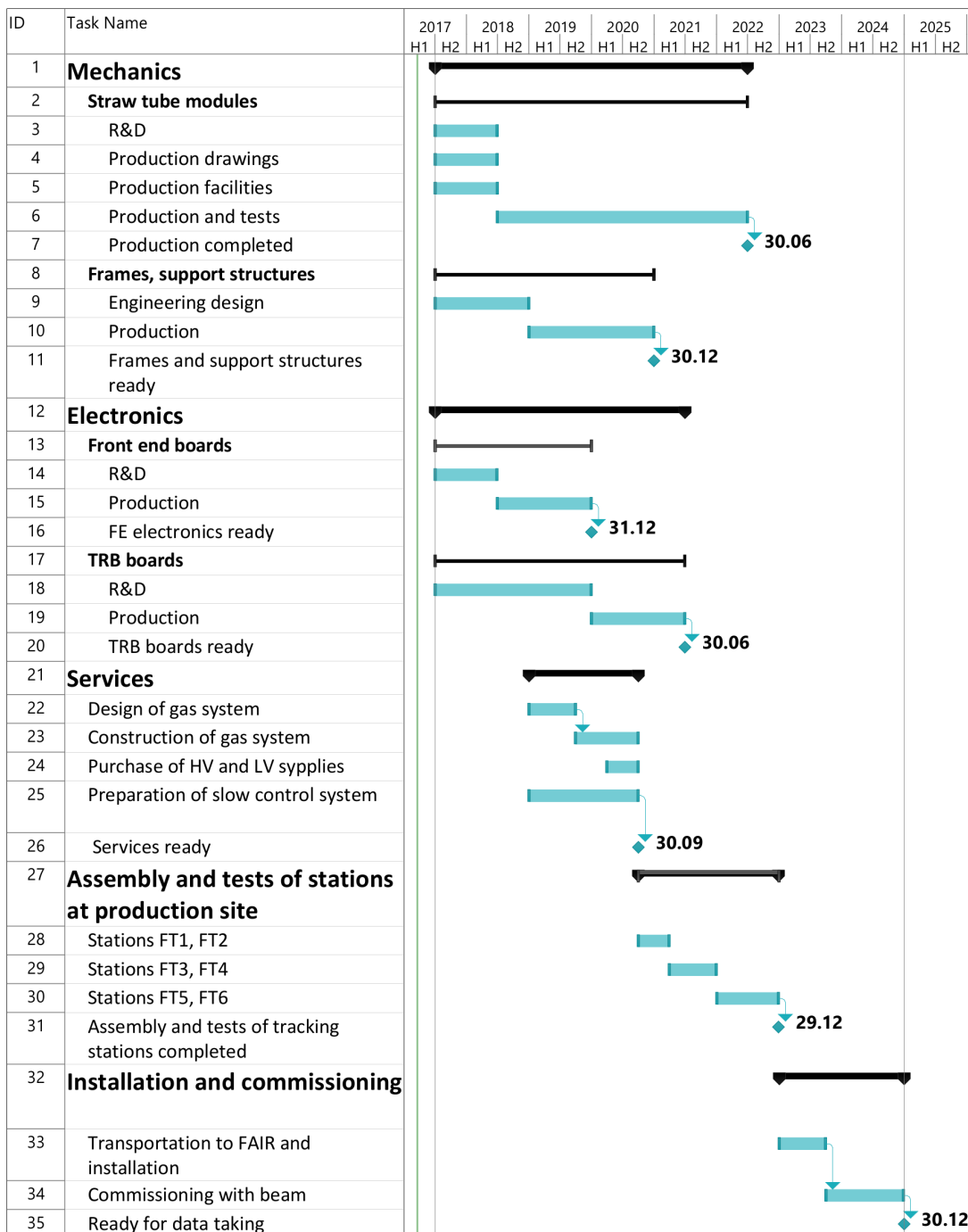


Figure 7.1: Timelines for the Forward Tracker realization.

7.3 Work Packages and Contributing Institutes

The design, construction and installation of the FT will be performed by a number of institutions

which have gained specific expertise in past and ongoing large scale experiments at several accelerator facilities. Construction of the tracking stations will be conducted at the Jagiellonian University. The frames for the tracking stations will be constructed at the Jagiellonian University and at the Krakow

University of Technology. The front-end cards will be produced by the groups from the AGH University in Krakow and at the Jagiellonian University. The digital electronics boards will be constructed at the Jagiellonian University in Krakow and at GSI-Darmstadt. The responsibilities for the various work packages are listed in Table 7.2, in which the coordinating group of the task is denoted by boldface.

A list of the participating groups is as follows:

- AGH, University of Science and technology, Krakow, Poland (T. Fiutowski, M. Idzik, B. Mindur, D. Przyborowski, K. Swientek) (**AGH**),
- Gesellschaft für Schwerionenforschung GmbH, Darmstadt, Germany (M. Traxler) (**GSI**),
- Jagiellonian University, Krakow, Poland (A. Heczko, G. Korcyl, B. Korzeniak, R. Lalik, W. Migdal, A. Malige, P. Moskal, N. Rathod, K. Nowakowski, W. Przygoda, Z. Rudy, P. Salabura, J. Smyrski) (**JU**),
- University of Technology, Faculty of Mechanical Engineering, Krakow, Poland, (P. Brandys, T. Czyżewski, W. Czyżycki, M. Domagała, M. Hawryluk, G. Filo, M. Krawczyk, D. Kwiatkowski, E. Lisowski, F. Lisowski) (**PK-M**),
- University of Technology, Faculty of Physics, Mathematics and Computer Science, Krakow, Poland, (J. Plazek) (**PK-P**),

7.5 Safety

The design details and construction of the FT including the infrastructure for operation will be done according to the safety requirements of FAIR and the European and German safety regulations. All electrical equipment and gas systems will comply with the legally required safety code and concur to standards for large scientific installations to ensure the protection of all personnel working at or close to the components of the \bar{P} *ANDA* experimental facility. Hazardous voltage supplies and lines will be marked visibly and protected from damage by any equipment which may cause forces to act on them. All supplies will be protected against over-current and over-voltage and have appropriate safety circuits and fuses. All cabling and connections will use non-flammable halogen-free materials according to up-to-date standards and will be dimensioned with proper safety margins to prevent overheating. A safe ground scheme will be employed throughout all electrical installations of the experiment. Smoke detectors will be mounted in all appropriate locations. The gas system is based upon non-flammable gases and thus does not pose a fire hazard. The maximum pressure of the gas will be regulated, and the system is designed such that a sudden failure of one tube (operating at maximally 2 bar) can not damage the adjacent tubes (that have equal or higher pressure than the escaping gas), and thus a chain reaction is ruled out. Appropriate measures will be taken during installation and maintenance to avoid damage to or by the FT.

7.4 Infrastructure needed at FAIR

After transporting the Forward Tracker stations to FAIR, but before the installation at PANDA, we plan to perform tests in order to ensure, that the stations were not damaged during the transport. We intend to check the gas tightness of the double layers and the high voltage characteristics of straws with ^{55}Fe source. For conducting the above tests and to store the transported stations prior to the installation, an air-conditioned room with stabilized temperature and low humidity is required. The needed floor area is 40 m².

During the use of the FT stations at PANDA, it may be necessary to perform their repairs. To carry out the repairs, a 30 m² air-conditioned room will be needed.

Table 7.2: Work package list with involved institutions.

Work package	Task	Involved (coordinating) institutes
Straw detectors	Production of straws	UJ
	Quality tests	UJ
Straw tube modules	Assembly of modules	UJ
	Quality tests	UJ
Construction of frames and support structures	Design of frames	PK-M, UJ
	Production of frames	PK-M, UJ
	Design of supports	PK-M , UJ,
	Production of supports	PK-M , UJ
Front-end electronics + signal cables + power supplies	Production of FEE cards	AGH, UJ
	Tests of FEE cards	AGH , UJ
	Preparation of cables and supplies	AGH, UJ
TDCs + power supplies	Production of boards	GSI, UJ
	Development of software	GSI, UJ
High voltage supplies and HV cables	Purchase of HV supply units	UJ
	Production of HV cables	UJ
Slow control	Slow control	UJ
Gas system	Design	UJ
	Production	UJ
Online tracking	Development of software	PK-P , UJ
Assembly, installation and tests at PANDA of tracking stations	Transportation to FAIR	AGH, PK-M, UJ
	Assembly and integration in PANDA	AGH, PK-M, UJ
	Tests and calibration	AGH, PK-M, UJ

A Appendix: Wire Tension vs. Overpressure

The dependence of the wire tension on the overpressure of the gas filling the straw was calculated in two steps. First, we determined the elongation of the wire and of the straw tube under the pretension applied during the assembly (50 g and 160 g, respectively) with the Young's modulus for the wire material of 41800 kg/mm² [1] and for the straw tube material (12 μm Mylar film) of 418 kg/mm² [2]. For the wire and the straw length of 1250 mm, as used in the FT5 and FT6 stations, the elongation equals 4.74 mm and 0.47 mm, respectively. Then we calculated the change in the length of the wire after combining the wire with the straw (soldering the wire to the PCBs in the end-plugs) and releasing the pretensions. This change equals 0.59 mm and it results in the wire tension drop from 50 g to 43.7 g, which agrees with the measurement. Finally, we determined the fractional change in length $\Delta l/l$ of the straw tube detector (straw tube + wire) as a function of the gas overpressure p using the following formula:

$$\frac{\Delta l}{l} = \frac{1}{E_s} \left[\frac{pr_s}{t} \left(\frac{1}{2} - \nu \right) - \frac{\Delta l}{l} \frac{E_w \pi r_w^2}{2\pi r_s t} \right],$$

where E_s and E_w is the Young's modulus for the straw and the wire material, respectively, r_s is the straw tube radius (5 mm), t is the thickness of the straw film (27 μm), ν is the Poisson's ratio for the straw material equal 0.38 according to ref. [3], r_w is the wire radius (10 μm). The first expression in the square bracket describes the elongation of the straw tube under gas pressure (see ref. [4]) and the second term results from the wire elongation. The fractional change in length $\Delta l/l$ multiplied by $2\pi r_w^2 E_w$ gives a change of the wire tension due to a given overpressure. Results of the calculations of the wire tension as a function of the gas overpressure are presented in Section 4.1.1.

References

- [1] <http://luma-metall.com/servizi/gold-plated-tungsten-rhenium-wire/>.
- [2] <http://www.doganak.com/wp-content/uploads/2014/07/Mylar-%C2%AE-A-12-36mic.pdf>.
- [3] <http://usa.dupontteijinfilms.com/resources/technical-information/>.
- [4] D. Roylance, *Pressure vessels*, <http://web.mit.edu/course/3/3.11/www/modules/pv.pdf>.

B Appendix: FEE Cards with CARIOCA Chips

General parameters:	
Number of channels	8
Radiation resistance	20 Mrad
Technology	IBM CMOS 0.25 μ m
Input parameters:	
Input impedance	45 Ω
Range of input charge	2.5 \div 300 fC
Peaking time	14 ns
Sensitivity with detect. capacitance 220 pF for positive input	8.21 mV/fC
negative input	7.7 mV/fC
Width of output pulse for charge < 300 fC at positive input	55 ns
negative input	65 ns
Minimum charge positive input	2.4 fC (rms 0.37 fC)
negative input	2.4 fC (rms 0.24 fC)
Output parameters:	
Standard of pulses	LVDS

Table B.1: Basic technical parameters of the CARIOCA-10 chip.

The CARIOCA is an 8 channel, radiation hard (up to 20 Mrad dose) ASIC, featuring preamplifier, shaper, baseline restorer and discriminator. The basic parameters of the CARIOCA chip - version 10 are collected in Table B.1. We built FEE boards containing four CARIOCA-10 chips for the readout of 32 channels. The FEE boards provide LVDS differential outputs which were connected by a flat cable to the DB. The threshold for the CARIOCA's leading-edge discriminators is set by the on-board DAC, which is controlled by dedicated lines in the cable connection to the DB. The total power consumption per channel of the CARIOCA chip is 25 mW. The FEE board with the CARIOCA chips is shown in Fig. B.1 and its basic parameters are given in Table B.2.

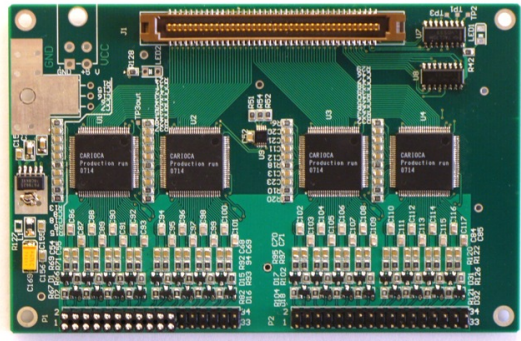


Figure B.1: Prototype board of a 32-channel preamplifier/discriminator based on CARIOCA-10 chips.

Supply voltage	+4.5 \div +12 V DC
Supply current	560 mA
Power consumption	3.3 W
Number of channels	32
Dimensions of board	124 mm x 80 mm x 16 mm

Table B.2: Technical characteristics of the FEE prototype based on CARIOCA.

Acknowledgments

The group from the Institute of Physics of the Jagiellonian University was financially supported by the Polish National Science Center, grant no. DEC-2014/15/B/ST2/01959.

List of Acronyms

ADC	Analog to Digital Converter	FMC	FPGA Mezzanine Card
APD	Avalanche Photo Diode	FPGA	Field Programmable Gate Array
ASIC	Application Specific Integrated Circuit	FRS	FRagment Separator
ATCA	Advanced Telecommunications Computing Architecture	FS	Forward Spectrometer
BLH	BaseLine Holder	FT	Forward Tracker
CBM	Compressed Baryonic Matter	GEM	Gas Electron Multiplier
CERN	Conseil European pour la Recherche Nucléaire	GSI	Gesellschaft für Schwerionenforschung
CM	Center of Mass	HADES	High Acceptance Di-Electron Spectrometer
CN	Computer Node	HESR	High Energy Storage Ring
COMPASS	Common Muon Proton Apparatus for Structure and Spectroscopy	HV	High Voltage
COSY	Cooler Synchrotron	IP	Interaction point
CR	Collector Ring	INFN	Istituto Nazionale di Fisica Nucleare
CSP	Charge Sensitive Preamplifier	KVI	Kernfysisch Versneller Instituut
CSS	Cascading Style Sheets	LEAR	Low Energy Antiproton Ring
CTDS	Clock and Timing Distribution System	LHC	Large Hadron Collider
DAC	Digital to Analog Converter	LSB	Least Significant Bit
DAQ	Data Acquisition	LVDS	Low-Voltage Differential Signaling
DB	Digital Board	MIP	Minimum Ionizing Particle
DCB	Detector Concentrator Board	MVD	Micro Vertex Detector
DCS	Detector Control System	OLE	Object Linking and Embedding
DESY	Deutsches Elektronensynchrotron	OPC	OLE for Process Control
DIRC	Detector for Internally Reflected Cherenkov Light	PASTTREC	PAnda Straw Tube TRAcker EleCtronics
DPM	Dual Parton Model	PCA	Point of Closest Approach
ECS	Experiment Control System	PCB	Printed Circuit Board
EMC	Electromagnetic Calorimeter	PHL	Pellet High Luminosity
ENC	Equivalent Noise Charge	PID	Particle Identification
FAIR	Facility for Antiproton and Ion Research	PMT	Photomultiplier
FE	Front-End	PR	Pattern Recognition
FEE	Front-End Electronics	PVC	Polyvinyl chloride
FEM	Finite Element Method	PWO	Lead Tungstate
		PZC	Pole-Zero Cancellation
		QCD	Quantum Chromo Dynamics
		RESR	Recycled Experimental Storage Ring

RICH Ring Imaging Cherenkov Counter

RMS Root Mean Square

R3B Reactions with Relativistic Radioactive Beams

SciTil Scintillator Tile Hodoscope

SFP Small Form-factor Pluggable

SiPM Silicon Photomultiplier

SODANet Synchronization of Data Acquisition Network

STT Straw Tube Tracker

TDC Time to Digital Converter

TDR Technical Design Report

TOF Time-of-Flight Detector

TOT Time-over-Threshold

TS Target Spectrometer

UrQMD Ultra-relativistic Quantum Molecular Dynamic

VMC Virtual Monte Carlo

List of Figures

2.3 Overview of the \bar{P} ANDA tracking system.	3	4.22 Side view of the tracking stations FT3 and FT4 installed inside the dipole magnet gap.	31
2.4 The Micro Vertex Detector (MVD) of the Target Spectrometer	5	4.23 Tracking station FT3 and FT4 installed inside the dipole magnet gap.	31
2.5 Straw Tube Tracker (STT) of the Target Spectrometer	6	4.31 Example of signal shape generated in the FT straw detector by a $E_{kin} = 420$ MeV pion passing close to the anode wire (a) and close to the cathode surface (b). The signals are simulated with the GARFIELD program [23].	35
2.6 Tracker assembly	6	4.32 Block diagram of a single channel of the PASTTREC ASIC.	37
4.1 Wire tension (weight equivalent) as a function of gas overpressure. Full points represent measurement results and lines correspond to the calculations described in text.	18	4.33 Three optimal settings for preamplifier gain (K) equal 1 mV/fC and peaking time (T_p) equal 20 ns.	38
4.2 Sectional drawing of assembled end-plug.	20	4.34 Distribution of the baseline levels accumulated from 192 channels.	38
4.3 Components of end-plug (lower left) and assembled end-plug with attached connecting cable with plug (upper right).	20	4.35 Gain measurements for delta pulses for four settings of preamplifier gain (K).	39
4.4 Setup for dispensing adhesive inside straws.	21	4.36 Amplitudes of 16 output signals versus input charge for the same ASIC configuration.	39
4.5 Stand for tensioning anode wires in straws.	21	4.37 Time-over-Threshold vs charge correlation collected with ^{55}Fe source.	39
4.6 Sealing of plugs with adhesive.	21	4.38 Examples of front-end pulses for not optimized (red) and optimized (blue) settings of the ion cancellation network.	39
4.7 Full absorbed dose in 1 cm wide zx slice ($y \in [-0.5 \text{ cm}, 0.5 \text{ cm}]$) of the Forward Spectrometer, calculated for one year of the nominal operation of \bar{P} ANDA (net half a year of data taking) in the high luminosity mode and with the 15 GeV/c antiproton beam. In the picture, indicated are tracking stations FT1..FT5.	23	4.39 The analogue output of the PASTTREC responding to the 2 MHz pulse coupled to the FEE test input.	39
4.19 Sketch of the pole shoe geometry in the z-y plane with indicated the cutout for the detector frames. The vertical dimension of the cutout is 55 mm.	29	4.40 Example of the ASIC analog signal output measured at a high (few MHZ) hit rate.	39
4.20 Straw tube module for tracking stations FT3, FT4.	30	4.41 16-channel FEE card comprising two PASTTREC-v.1 ASICs.	40
4.21 Rectangular frame, supporting two double layers of straw tube detectors, designed for the tracking station FT3, shown without modules (a) and with modules (b).	30	4.42 Block diagram of TRB-v.3.	41
		4.43 Produced TRB-v.3 board.	41
		4.44 Scheme of TDC-FPGA implementation with carry chain usage.	41
		4.45 Schematic view at the TRBv3 system for High Resolution mode.	43

4.46 Schematic view at the TRB5G crate system for the High Luminosity mode.	43
4.47 Test stand for checking the gas tightness of straws.	45
4.48 Gas leak measured for individual straws produced for 13 modules for FT5, FT6.	45
4.49 Waveform showing alternative current induced in straw tube wire vibrating in magnetic field.	45
4.50 Wire tension measured for 416 straws (13 modules) with a length of 125 cm produced for FT5, FT6 in function of straw number (top panel) and a histogram of wire tension (bottom panel).	46
4.51 x-y stage with a positioning area of about $2.0 \times 1.3 \text{ m}^2$	47
4.52 Digital microscope mounted on positioning stage and a straw tube module seen from the side.	47
4.53 Three settings of the microscope used for imaging the left, right and side edge of the module.	47
4.54 Image of a side edge of straw tube module.	48
4.55 Distance- drift time relation calculated with GARDFIELD for straw located centrally with the anode wire (red curve) and for straw displaced by 0.2 mm (blue curve) along the x-direction (blue curve). Simulated tracks are oriented perpendicularly to the x-axis.	48
4.56 (Upper panel) Number of counts in individual straws in the tested module as a function of position of the X-ray beam. Response of the first and the second straw layer, when looking in direction of the X ray beam, is represented with red and blue line, respectively. (Lower panel) Deviations between the measured and nominal positions of straws.	49
4.57 (Upper panel) Plateau curve measured for straw illuminated with X-rays from ^{55}Fe (full circles) and the fit to the data with a sum of two error functions (solid line). (Lower panel) Zoomed edge region of the curve.	49
4.58 From top to bottom: Plateau curves registered for 32 straws in a tested module just before changing the gas mixture composition from Ar-CO ₂ (90:10) to (80:20), and after 60, 120 and 180 minutes from the change. The two black curves correspond to a pair of straws with a gas flow deliberately suppressed by a factor of two compared with the others.	50
4.62 Graphical User Interface prepared with the LabVIEW environment for the prototype gas system.	54
4.63 Graphical User Interface for controlling the working parameters of the FEE cards.	55
4.64 Fitted TDC spectrum	56
4.65 Isochrones radius – drift time relation	56
4.66 Distribution of the average residuals as a function of the drift time	56
4.67 Distribution of the average residuals after autocalibration	57
4.68 Root mean square correction from the autocalibration procedure	58
5.1 Mounting of the COSY-STT in the time-of-flight barrel of the COSY-TOF spectrometer	60
5.2 Straw setup (in front) for the energy-loss test measurements. The proton beam is coming from the back.	60
5.6 The COSY-STT mounted at the front cap of the COSY-TOF spectrometer. The detector consists of 2704 straw tubes of 1 m length and 10 mm diameter, arranged as a vertical stack of 13 close-packed double-layers at three different orientations.	63
5.7 Gas leakage of the COSY-STT filled with pure argon (red) and pure CO ₂ (blue), measured by the gas pressure drop of the straws in surrounding vacuum.	63
5.8 Track to wire distances and measured drift times for the reconstructed tracks. The $r_{iso}(t)$ -relation (black line) is parametrized as a polynomial function of 4th order with the parameters P ₀ –P ₄	63

5.9 Distribution of the residuals of all reconstructed tracks as a measure of the COSY-STT spatial resolution. The width of $138\ \mu\text{m}$ (σ) and mean of $2\ \mu\text{m}$ are the results from the Gaussian fit (red line)	64	6.1 Comparison between the simulation of the energy lost in a $1.5\ \text{cm}$ Ar/CO ₂ layer (line) and the experimental values of Allison et al. [4] (dotted line).	81
5.10 Width (sigma) of the residual distributions for different intervals of the radial distances from the wire.	64	6.2 Energy loss of 1 GeV pion traversing a $1\ \text{cm}$ of 90 % Ar 10 % CO ₂ gas mixture at NTP. Solid line: Urban distribution; dashed line: specific simulation model; dotted line: Landau distribution.	81
5.11 Normalized gas gain reduction ($\Delta G/G_0$) measured along the tube for all 32 straws, shown in groups of 4 straws. Straw no. 1–4 (upper left) to straw no 29–32 (lower right). The beam hit all tubes around $0\ \text{cm}$ longitudinal position.	66	6.3 Drift velocity of electrons in Ar-CO ₂ gas mixture at 2 bar for various CO ₂ concentrations.	82
5.27 Time difference between straw tube pulses and the reference pulse from the triggering scintillation detector registered in a $2500\ \text{ns}$ window (left), and in a $265\ \text{ns}$ window zoomed in on the drift time spectrum (right). The violet line represents raw data, and the blue line in the right panel corresponds to straw tube hits successfully reconstructed by the track reconstruction procedure. The high voltage of the anode wires was $1900\ \text{V}$ and the discrimination threshold was $10\ \text{mV}$	75	6.4 Space-drift time relation calculated for Ar-CO ₂ gas mixture at 2 bar for CO ₂ concentration of 10% and 20%. The potential of the anode wire is $1800\ \text{V}$	82
5.28 Drift velocity of electrons as a function of the distance from the anode wire calculated for the straw tube filled with the 90% Ar+ 10% CO ₂ gas mixture at 2 bar pressure and the anode wire voltage of $1900\ \text{V}$	75	6.5 Standard deviations of longitudinal (a) and transverse diffusion (b) for $1\ \text{cm}$ drift pass of electrons in Ar-CO ₂ gas mixture at 2 bar for various CO ₂ concentrations.	82
5.29 Multiplicity of hit straws for $3.0\ \text{GeV}/c$ protons. The solid line includes all registered tracks and the fill area represents successfully reconstructed tracks.	75	6.6 The gas gain curves for Ar+CO ₂ (90:10) without and with 34% Penning transfer rate represented by purple and blue curve, respectively. The experimental data are shown with open circles.	83
5.30 Distribution of the residuals (left) and χ^2 values (right) obtained in the track reconstruction with 6 fit hits (top) and 5 hits (bottom), shown with solid blue line. The red line on the two panels on the left presents a gaussian fit to the distribution of residuals, and on the top right and bottom right panel - the χ^2 distribution with 4 and 3 degrees of freedom, respectively.	76	6.7 Experimental data and results of simulations with Garfield for the gas gain in straw tube filled with Ar-CO ₂ (90:10) gas mixture at 2 bar, compared with the Diethorn parametrization (green). Parameters used in the Diethorn formula are indicated in the figure.	83
		6.8 Transfer function of the FEE determined as a response to a very fast ($\sim 1\ \text{ns}$) "delta-like" pulse.	84
		6.9 Time-over-Threshold spectrum measured (blue squares) and simulated (red triangles) for ^{55}Fe source. A peak corresponding to the full absorption of the $5.9\ \text{keV}$ X-rays from ^{55}Fe is clearly separated from the $2.9\ \text{keV}$ argon escape peak. In the simulations, electronic noise with a level observed in the measurements, was added to the signals.	84

6.10 TOT vs. distance between the track and the anode wire for protons (left), pions (middle) and kaons (right) at 0.5 GeV/c, before (top) and after applying the distance correction (bottom). The simulations are done for the anode wire at +1800 V and a discrimination threshold for the TOT measurement equivalent to 20 primary electrons. The solid red lines indicate the second order polynomial fits to the TOT distributions.	84	6.21 The constant magnetic field spans between z_Bstart and z_Bend . The circle is tangent to track candidate from FT12 at point z_Bstart and passes through a straw from the layer number 32 (P32 in the figure) or 31.	91
6.11 TOT simulation with single straw response (top) and truncated mean over 24 straws (bottom) for protons and charged pions and kaons with 0.5 GeV/c momentum. The solid red lines show the Gaussian fit to the distributions.	84	6.22 Average sum of residua of the vertical straws in the FT34 section with respect to the circular tracks, determined as a function of the z-coordinate of the matching point between the straight line trajectory in the FT12 section and its prolongation as a circle withing the FT34. The distributions are presented for the three momenta of muon tracks.	91
6.12 Separation power for $p - \pi$, $k - \pi$ and $p - K$ pairs based on Time-over-Threshold (blue squares) and charge measurements (red triangles).	85	6.23 Distribution of residua ds for the track projection on the horizontal plane (upper panel) and on the vertical plane (lower panel) in the FT34 section, for the three muon momenta.	92
6.15 Sketch of the positions of the point of closest approach (PCA) on the track and on the wire	87	6.24 The x_1 coordinate of point C for a given z_1 (as z_1 coordinate of the layer with skewed straws is taken) is calculated from the circle equation corresponding to the projection of the track on ZOX plane. The distance d is used in calculation to find straw corresponding to the track.	92
6.16 Sketch of the virtual detector plane at the point of closest approach to the wire	87	6.25 Sum of distances in plane ZOX from points in tracks to positions of anode wires reduced by the drift distance from a sample muon tracks at different energies as function of z_Bend	92
6.17 Straw candidates to the track in the ZOX plane in the FT12 (or FT56) station. Yellow colored straws inside pink band fulfill the distance requirement.	89	6.26 Definition of the distance $dzox$ in the horizontal XOZ plane (upper panel) and $dxoy$ in the vertical YOZ plane (lower panel) calculated by the PR algorithm when matching track fragments from FT12+34 with track fragments from FT56.	93
6.18 Four tangent lines considered in the search for the track line in the FT12 (or FT56) station.	89	6.27 Distribution of the distance $dzox$ (upper panel) and $dxoy$ (lower panel).	93
6.19 Distribution of residua ds for the track projections on the horizontal plane (upper panel) and on the vertical plane (lower panel) in the FT12 section (black line) and FT56 section (blue line).	90	6.28 Straw multiplicity in the simulated tracks (dashed line) and the track candidates with the highest number of recognized straws n_c (solid line) for muon momentum of 0.55 GeV/c (upper panel), 2.55 GeV/c (middle panel) and 5.55 GeV/c (lower panel).	94
6.20 The vertical Z'CY plane constructed with the track candidate found on ZOX. The points P1 and P2 correspond to the intersection of a skewed straw at z_i with the Z'CY plane.	90		

6.29 Efficiency of the PR algorithm for three different muon momenta 0.55, 2.55 and 5.55 GeV/c and track multiplicities 1, 3 and 5.	95	
6.30 Distributions of muon momenta determined using the radius of the circular trajectory in the magnetic field of the dipole magnet for 0.55 GeV/c muons and the deflection of the trajectory measured with the FT12 and FT56 stations for 2.55 and 5.55 GeV/c muons.	95	
6.31 Difference between the absolute value of the reconstructed momentum and the simulated momentum of single muon tracks in simulations including the full PANDA setup (left) and the PANDA setup with removed beam pipe (right).	96	
6.32 Distribution of the opening angle between the reconstructed and simulated momentum vector of single muon track in simulations including the full $\bar{\text{P}}\text{ANDA}$ setup (top) and the $\bar{\text{P}}\text{ANDA}$ setup with removed beam pipe (bottom). Note that the range of the angular scale in the top figure is four times wider than in the lower one.	97	
6.33 Long distance (a) and short distance (b) scenario for arrangement of FT5 and FT6. Details are described in the text.	98	
6.34 Momentum resolution (%) as function of pion's momentum for the two different geometry scenarios.	98	
6.35 Resolution of the vertical momentum component p_y divided by the longitudinal momentum component p_z as a function of the inclination angle, determined for 0.5 GeV/c muons.	99	
6.36 Spatial resolution of the vertical track coordinate (y) at the position of the FT1 tracking station as a function of the inclination angle, determined for four different muon momenta.	99	
6.37 Intensity distribution of pions with momenta 0.3, 0.5, 1, 2, 5 GeV/c at the positions of the six FT stations. The x- and y-axis are respectively the horizontal and vertical coordinates of the stations.	100	
6.38 The acceptance of the tracking stations in function of the pion's momentum.	101	
6.39 Momentum resolution for 2 GeV/c muons as a function of the antiproton beam momentum.	101	
6.40 Pion scattering angle distribution vs momentum for generated events (a) and for reconstructed events with the FT included in the $\bar{\text{P}}\text{ANDA}$ tracking system (b) and removed from the system (c).	103	
6.41 Kaon scattering angle distribution vs momentum for generated events (a) and for events reconstructed with the FT included (b) and removed from the $\bar{\text{P}}\text{ANDA}$ tracking system (c).	103	
6.42 Invariant mass of D_0 (a) and D^* mesons (b) reconstructed with the FT included in the $\bar{\text{P}}\text{ANDA}$ tracking system (black line) and without the FT (red line).	104	
6.43 Invariant mass of the $\Psi(4040)$ meson reconstructed with the $\bar{\text{P}}\text{ANDA}$ tracking system including the FT. Corresponding spectrum obtained without the FT contains only one entry and, therefore, is not shown.	104	
6.44 Distribution of the scattering angle vs momentum of positively charged pions (up to 1 GeV/c) and antiprotons (around 3 GeV/c) originating from $\bar{\Lambda} \rightarrow \bar{p}\pi^+$ decays and corresponding to generated (top) and reconstructed tracks (bottom).	104	
6.45 Reconstructed $\bar{\Lambda}$ mass.	104	
B.1 Prototype board of a 32-channel preamplifier/discriminator based on CARIOCA-10 chips.	111	

List of Tables

3.1 Positions, width and height of the active area, number of modules and number of straw tubes in the Forward Tracker stations. In the second column, z-coordinates of the first and the forth double layer are given. The indicated width and height of the active area correspond to the first double layer with vertical straws.	16	5.1 List of straw settings and charge load during the beam test. The last column shows the normalized gas gain reduction in the irradiated straw region with a measurement resolution of about 2 %. The aging intervals give the minimum and maximum gain reductions, e.g. 0–7 % means that at least one straw showed no gain reduction and one a maximum of 7 %.	66
3.2 Key parameters of the Forward Tracker.	17	6.1 Reconstruction efficiency, ghost fraction and clone fraction determined for three momenta and three multiplicities of the simulated muon tracks.	97
4.1 Mean thickness in radiation lengths of the different straw tube components. The number for the gas mixture is evaluated at temperature of 20° and a pressure of 2 atm.	19	7.1 List of operations in production of the standard module containing 32 straws and required amount of work for each operation.	106
4.2 List of materials in contact with gas mixture, outgassing properties and other experiments/detectors using these materials in straws detectors.	23	7.2 Work package list with involved institutions	109
4.3 Expected precision of relative positioning of mechanical elements determining the positioning precision of the anode wires with respect to the support frame of the tracking station.	25	B.1 Basic technical parameters of the CARIOCA-10 chip.	111
4.4 Straw tube electrical properties.	35	B.2 Technical characteristics of the FEE prototype based on CARIOCA.	111
4.5 Front-end electronics requirements.	36		
4.6 Main parameters of the PASTTREC-v.1 (see text for more details).	36		
4.7 PASTTREC available settings	38		
4.8 Estimated data rates per tracking station in High Resolution mode.	43		
4.9 Estimated data rates per tracking station in High Luminosity mode.	44		